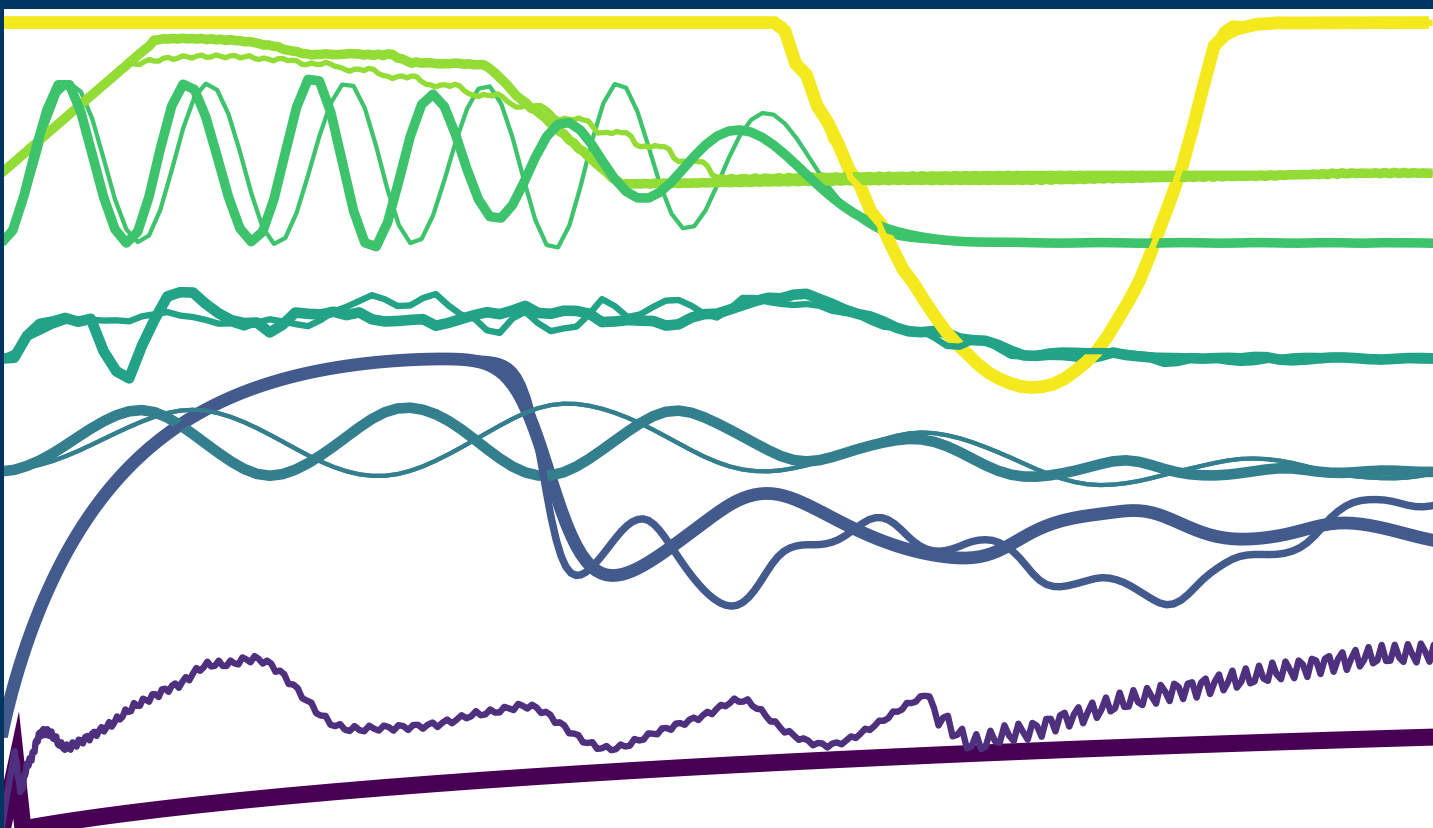


# A Fully Coupled Dynamic Framework for Two-Scale Simulations of SHCC

Erik Tamsen



# A Fully Coupled Dynamic Framework for Two-Scale Simulations of SHCC

Zur Erlangung des Grades  
Doktor-Ingenieur  
an der Fakultät Bauingenieurwesen  
der Technischen Universität Dresden  
genehmigte Dissertation

von

Erik Tamsen

Einreichung der Dissertation: 21.07.2020

Tag der mündlichen Prüfung: 18.09.2021

Erstgutachter: Prof. Dr.-Ing. habil. Daniel Balzani

Zweitgutachter: Prof. Dr.-Ing. habil. Michael Kaliske

Drittgutachter: Prof. Dr.-Ing. Stefan Löhnert

**Mitteilungen aus dem Institut für Mechanik  
Nr. 185**

**Publisher:**

Institute of Mechanics  
Ruhr University Bochum  
D-44780 Bochum

Prof. Dr.-Ing. habil. Daniel Balzani  
Chair for Continuum Mechanics

**Herausgeber:**

Institut für Mechanik  
Ruhr-Universität Bochum  
44780 Bochum

Prof. Dr.-Ing. habil. Daniel Balzani  
Lehrstuhl für Kontinuumsmechanik

---

ISBN 978-3-935892-63-6

---

Copyright © 2021 by Erik Tamsen

All rights reserved.

No part of this work may be reproduced or used in any manner  
without written permission of the copyright holder.

Dieses Werk ist urheberrechtlich geschützt.  
Alle Rechte, einschließlich der Vervielfältigung, Veröffentlichung,  
Bearbeitung und Übersetzung, bleiben vorbehalten.





# Preface

In the spring of 2017, just before starting my graduate thesis at the Technische Universität Dresden, I accepted the offer to be a part of the Research Training Group GRK 2250/1 "Mineral-bonded composites for enhanced structural safety". After just a few months of research work in Dresden, I followed Professor BALZANI to his new position at the Chair of Continuum Mechanics at the Ruhr University Bochum. Looking back on the last three years, I would like to give my sincerest thanks to all the amazing people who have helped me along the way and have thereby contributed to this thesis.

Above all, I want to thank Professor DANIEL BALZANI for his guidance, encouragement and overall excellent academic supervision. As my teacher, advisor and friend, he supported me when I asked, while giving me freedom and his trust to tackle the problems how I saw fit. This environment gave me the possibility to learn from him and grow as a researcher and person.

Being part of the GRK allowed me to meet and learn from many exceptional researchers. Special thanks go out to Professor STEFAN LÖHNERT, for his continuous support of my situation as researcher both in Dresden and Bochum, for his constructive feedback as reviewer and the fruitful discussions regarding multiscale simulations during our workshops. Further, I thank Professor MICHAEL KALISKE for reviewing this thesis and helping me with administrative matters. Then, I would like to acknowledge Professor VIKTOR MECHTCHERINE for making the GRK the success it is. His personal motivation for research in general and the topic of impact safety in particular is an inspiration. Hearty thanks go to Dr. IURIE CUROSU, who has acted as a role model and paved the way for collaborative research within the group. Further, I give thanks to my fellow doctoral researchers in the GRK for all the in-depth discussions, the learning opportunities and for making the overall experience entertaining.

I would like to express my gratitude to Professor CELIA REINA for the opportunity to visit her research group at the University of Pennsylvania and the valuable discussions regarding metamaterials.

My warm words of gratitude and appreciation are addressed to my former colleagues at the Institute of Mechanics and Shell Structures, back when I was still a student in Dresden. Especially to Professor BERND ZASTRAU who supported me from the start and without whom, I probably would have taken a different path. Further thanks go to Professor ANDREAS FRANZE and Professor WOLFGANG WEBER for supervising my first projects and guiding me on my way toward research.

Next, I address all my gratitude to my coworkers. I have been lucky to have had such an amazing group of colleagues who supported me and generally made life in the office enjoyable. I need to thank NIKLAS MISKA in particular, who has been my office roommate from the start. He not only helped me countless times, but was also always there to talk or listen. In addition, I want to thank him for the constructive, amicable and fun work atmosphere.

I want to thank my parents for their unconditional love and support throughout my life. I am grateful to my friends for the welcoming distractions and I thank my girlfriend for her patience and moral support, especially during the last stage of the thesis.



# Abstract

A general numerical two-scale homogenization method for large strains is developed, which consistently takes into account inertia forces at the microscale. The energetic scale coupling of the framework is based on the extended HILL-MANDEL condition of macro-homogeneity. Furthermore, kinematic scale links are discussed and a volume integral displacement constraint is proposed. To enable an efficient algorithm, closed form formulations of four macroscopic tangent moduli are derived. These consistently include the microscale inertia effects as well as the proposed displacement constraint. Two numerical examples are presented, a layered microstructure and a locally resonant material. These examples are used to analyze general properties of the presented framework, namely the macroscopic convergence behavior and the overall match with single-scale reference calculations. In addition, both the displacement constraint and the choice of unit cell as representative volume element are studied with respect to their influence on the macroscopic response. Subsequently, the thesis focuses on the modeling of strain-hardening cementitious composites under impact loading. First, a simplified material model representing the homogenized fiber pullout behavior is calibrated using experimental data. Then, this fiber pullout model is used at the microscale and studied using the proposed dynamic homogenization framework. Finally, a split HOPKINSON bar tension test is numerically replicated and used to showcase the ability of the framework to thoroughly study the dynamic effects of the material and structure.

# Zusammenfassung

In dieser Dissertation wird eine allgemeine zweiskalige Homogenisierungsmethode für große Deformationen entwickelt, welche die Trägheitskräfte der Mikroskala konsistent berücksichtigt. Die energetische Skalenkopplung der Methode basiert auf der erweiterten HILL-MANDEL Bedingung für Makrohomogenität. Darüber hinaus wird die kinematische Skalenkopplung diskutiert und eine Volumenintegrals-Verschiebungsbedingung aufgezeigt, die eine allgemeine dynamische Betrachtung ermöglicht. Um einen effizienten Algorithmus zu gewährleisten, werden vier makroskopischen Tangenten-Module in geschlossener Form hergeleitet. Es werden zwei Rechenbeispiele genutzt, um allgemeine Eigenschaften der Methode zu analysieren. Dazu gehören das makroskopische Konvergenzverhalten und die Übereinstimmung mit einskaligen Referenzsimulationen. Des Weiteren wird der Einfluss der Verschiebungsbedingung und die Wahl der Einheitszelle als repräsentatives Volumenelement auf die Antwort der Makroskala untersucht. Der Fokus der Arbeit wird im Anschluss auf die Modellierung hochduktiler Betone (Engl.: Strain-Hardening Cementitious Composites – SHCC) unter Stoßbelastung gelegt. Zunächst wird anhand von experimentellen Daten ein vereinfachtes Materialmodell kalibriert, welches das homogenisierte Faserauszugsverhalten repräsentiert. Danach wird dieses Faserauszugsmodell auf der Mikroskala eingesetzt und mit der vorgestellten Homogenisierungsmethode untersucht. Schließlich wird ein Split-HOPKINSON-Bar Zugversuch numerisch repliziert. Dieser wird verwendet um die Funktionalität der Methode aufzuzeigen, wie dynamische Effekte des Materials und der Struktur untersucht werden können.



# Contents

<b>1</b>	<b>Introduction</b>	<b>1</b>
1.1	Motivation . . . . .	1
1.2	Background and State of the Art . . . . .	2
1.3	Structure . . . . .	4
<b>2</b>	<b>Fiber-Reinforced Concrete</b>	<b>5</b>
<b>3</b>	<b>Continuum Mechanical Background</b>	<b>11</b>
3.1	Kinematics . . . . .	11
3.2	Stress Measures . . . . .	13
3.3	Balance Equations . . . . .	14
<b>4</b>	<b>Finite Element Method</b>	<b>17</b>
4.1	Variational Problem . . . . .	17
4.2	Linearization . . . . .	18
4.3	Discretization . . . . .	19
4.4	Numerical Time Integration . . . . .	22
4.4.1	Newmark Method . . . . .	22
4.4.2	Application to the FEM Problem . . . . .	23
4.5	Gauss Integration . . . . .	24
4.6	Global FEM Formulation . . . . .	25
<b>5</b>	<b>Material Modeling</b>	<b>27</b>
5.1	Hyperelastic Material Law . . . . .	27
5.1.1	Parameter Study – Young’s Modulus $E$ . . . . .	28
5.2	Stress as a Function of Stretch Rate . . . . .	28
5.2.1	Dynamic Increase Function . . . . .	29
5.2.2	Tangent Modulus . . . . .	30
5.2.3	Parameter Study – Dynamic Increase Factor $\Omega$ . . . . .	30
5.3	Discontinuous Damage . . . . .	31
5.3.1	Damage Approach . . . . .	31
5.3.2	Exponential Damage Function . . . . .	32
5.3.3	Tangent Modulus . . . . .	32
5.3.4	Parameter Study – $D_\infty, D_{\text{rate}}, D_{\text{shape}}, E$ . . . . .	33
5.4	Damage Formulation Combined with a Rate Sensitivity of Stress . . . . .	34
5.4.1	Varying Strain Rates . . . . .	34
<b>6</b>	<b>Homogenization</b>	<b>37</b>
6.1	Analytical Homogenization . . . . .	38
6.2	Computational Homogenization . . . . .	39
6.3	Representative Volume Element . . . . .	39
6.4	Separation of Scale . . . . .	40
6.5	Large Strain Kinematics at Different Scales . . . . .	40

---

6.6	Kinematic Links to the Macroscale . . . . .	41
6.6.1	Deformation Gradient Constraint . . . . .	42
6.6.2	Displacement Constraint . . . . .	43
6.7	Averaging Expressions . . . . .	44
<b>7</b>	<b>Dynamic Homogenization Framework</b>	<b>47</b>
7.1	General Concepts . . . . .	47
7.1.1	Microscale Constraints and Homogenization Operators . . . . .	48
7.1.2	Time Integration . . . . .	48
7.2	The Microscopic Problem . . . . .	49
7.2.1	Microscopic Balance of Linear Momentum . . . . .	49
7.2.2	Kinematic Links to the Macroscale . . . . .	50
7.2.3	Algorithmic Treatment of Kinematic Constraints . . . . .	51
7.2.4	Global Discretized Microscopic Problem Including Constraint . . . . .	52
7.2.5	Coupling of the Deformation Gradient . . . . .	53
7.3	The Macroscopic Problem . . . . .	53
7.3.1	Macroscopic Boundary Value Problem . . . . .	54
7.3.2	Consistent Macroscopic Tangent Moduli . . . . .	55
<b>8</b>	<b>Numerical Study – Layered Structure</b>	<b>63</b>
8.1	Boundary Value Problem . . . . .	63
8.2	Consistency of the Numerical Framework . . . . .	64
8.3	Analysis of the Unit Cell Concept under Dynamic Loading . . . . .	65
8.4	Influence of Displacement Constraints . . . . .	67
<b>9</b>	<b>Numerical Study – Metamaterial</b>	<b>69</b>
9.1	Boundary Value Problem . . . . .	70
9.2	Initial Simulation . . . . .	71
9.3	Macroscopic Mesh Study . . . . .	72
9.4	Sensitivity Regarding the Excitation Frequency . . . . .	73
9.5	Remarks . . . . .	75
<b>10</b>	<b>Fiber-Matrix Bond Properties</b>	<b>77</b>
10.1	Theoretical Background . . . . .	77
10.1.1	Embedment Length . . . . .	78
10.2	Experimental Setup . . . . .	79
10.3	Calibration of the Material Model . . . . .	80
10.3.1	Single-Fiber Tension Test . . . . .	81
10.3.2	Single-Fiber Pullout Test . . . . .	83
10.3.3	Embedment Length . . . . .	86
10.3.4	Complete Fiber Pullout and Boundary Effects . . . . .	87
<b>11</b>	<b>Simplified SHCC Simulation</b>	<b>91</b>
11.1	Boundary Value Problem . . . . .	91
11.2	Pre-Cracked Matrix . . . . .	92
11.2.1	Stretch-Rate Dependent Stress . . . . .	93
11.2.2	Inertia Effects . . . . .	94
11.2.3	Full Dynamic Simulation . . . . .	94
11.3	Matrix Cracking . . . . .	95

---

<b>12 Split Hopkinson Bar Simulation</b>	<b>99</b>
12.1 Quasi-Static SHCC Tensile Experiment . . . . .	99
12.2 Quasi-Static SHCC Tensile Simulation . . . . .	100
12.3 Dynamic SHCC Tensile Experiment . . . . .	101
12.4 Dynamic SHCC Tensile Simulation . . . . .	103
12.4.1 Boundary Value Problem . . . . .	103
12.4.2 Results . . . . .	106
12.5 Discussion . . . . .	108
<b>13 Conclusion and Outlook</b>	<b>111</b>
<b>Appendix</b>	<b>115</b>
<b>A Large Strain Truss Element</b>	<b>115</b>
<b>B Deformation Gradient Constraint</b>	<b>117</b>
B.1 Lagrange Multipliers . . . . .	117
B.2 Variation . . . . .	117
B.3 Discretization . . . . .	117
B.3.1 Global Matrix Notation . . . . .	118
B.3.2 Linearization . . . . .	118
B.4 Residuum . . . . .	118
B.4.1 Full System of Equations . . . . .	118
<b>C Overview – Consistent Tangent Moduli</b>	<b>119</b>
<b>List of Figures</b>	<b>121</b>
<b>List of Tables</b>	<b>126</b>
<b>References</b>	<b>127</b>



---

# 1 Introduction

## 1.1 Motivation

Computer simulations of structures and materials are today a standard procedure in industry as well as in research. To simulate various materials, respective predefined material laws are used to establish a functional relation between for example strains and stresses. When observed at a fine scale, the majority of physical materials exhibit a rather heterogeneous microstructure, with e.g. different crystal orientations in metals, a composition of aggregates, pores and cement paste in concrete, and distinct cellular structures in woods. For general cases, macroscopic material laws can approximate the overall material response reasonably well using effective macroscopic material parameters.

For compound materials that exhibit a wider range of nonlinear effects in their constituents, as for example plasticity, visco-elasticity, rate dependency or fracture, it becomes increasingly difficult to find appropriate constitutive relations. Some examples are reinforced concrete, fiber-reinforced plastics or multi-phase steels. In addition, when using more complex material laws it is difficult to obtain a unique set of parameters for which the respective numerical results match the experimental data. The constitutive equation of the material is therefore often only based on empirical data instead of known physical relationships and possibly only suited for a limited range of applications, reducing the applicability of the model.

One solution is to increase the resolution of the simulation and discretize the microstructure with all its heterogeneities. This way only the material laws of the phases need to be known and the complex behavior of the composite can be simulated. Although when the microstructure gets small in comparison to the analyzed volume, the simulation is more and more computationally expensive, as the number of elements and with that the unknown variables increase. This is where so called multiscale homogenization or coarse-graining methods come into play. Instead of discretizing the full microstructure, a homogenized material is assumed and at each integration point a separate boundary value problem is solved, instead of applying a predefined material law. In the  $FE^2$  method only a small volume of the microstructure is discretized and used to obtain results for an averaged macroscopic response. This way the homogenized elements can be significantly larger than the discretized volume at the microscale, which saves computational time.

The material of interest in this work is fiber-reinforced concrete and specifically its behavior under impact loads. Fiber-reinforced concretes under tension load display a rather ductile behavior, compared with plain concrete. Once the brittle concrete matrix fractures, the fibers engage and bridge the crack. When the bond between fiber and matrix is correctly engineered, this bridge can carry more loads than the uncracked matrix and instead of a pronounced crack opening multiple cracks are formed. This can lead to an overall strain-hardening material behavior, thus giving this class of materials also the name strain-hardening cementitious composites (SHCC). Under

impact loading, SHCC has shown a pronounced energy dissipation which makes it a suitable candidate for reinforcement of structures against dynamic loads.

Material behavior and the corresponding properties can change when loads are applied rapidly. The use of high speed cameras and other modern technology enables the study of materials under high strain rates. However, to be able to accurately measure what is happening inside the material is difficult at best and usually impossible. Generally one can only make assumptions based on the resulting surface deformations or fractures. This is where numerical simulations can offer a possibility to visualize the processes at the microscale at any desired location. In addition it can serve as a virtual lab to study influences of different microscopic material parameters on the overall structure to support further material development.

This work builds a numerical two-scale homogenization framework, consistently including inertia at the microscale. The framework is then used to investigate the contribution of dynamic behavior at the microscale to the overall material response.

## 1.2 Background and State of the Art

Analytical homogenization dates back decades, with HILL [44] being one of the first to do multiscale homogenization with the use of representative volume elements. The rise of computers enabled the growth of the field of numerical homogenization. A work presenting different analytical as well as numerical homogenization methods is GLÜGE [35], also the work of BLANCO et al. [14], which is more focused on RVE-based multiscale models. Nowadays computational homogenization methods are a common tool for material analysis and other applications. A good overview of computational homogenization methods and their history is given in GEERS et al. [32]. Published in 2010, the paper by GEERS et al. [32] still calls dynamic homogenization including inertia forces an open issue. Since then the interest in frameworks for numerical homogenization methods considering inertia effects at the microscale has increased. Most research on simulations regarding dynamic effects arising from microstructures concern the application on locally resonant metamaterials, which can exhibit special properties like band gaps and a negative bulk modulus. The proposed applications cover a broad range of length scales, from cloaking devices in CUMMER and SCHURIG [22] and KADIC et al. [49] over tunable sound attenuation in LI and CHAN [58] and LIU et al. [64] to earthquake protection, c.f. BRÛLÉ et al. [17] and MINIACI et al. [74]. More classical materials are being investigated as well. There is research in metaconcrete, which replaces aggregates by rubber-coated lead inclusions to weaken impact waves, e.g. KETTENBEIL and RAVICHANDRA [51] and MITCHELL et al. [75]. A different approach to impact resistance, which is not primarily based on local resonance phenomena, are strain-hardening cement-based composites, that show a pronounced energy dissipation under dynamic loading, as well as a change in fiber failure and overall crack pattern as investigated by CUROSU et al. [23, 25, 26]. Then there is research on porous materials by MOLINARI and MERCIER [76] and SARTORI et al. [90], which has shown an influence of microinertia on voids under high strain rates. This list is not supposed to be exhaustive but should illustrate the possible influence of the material microstructure on the macroscale response under dynamic loading for a wide range of materials and applications. In general, any material with a large variation in stiffness

or density e.g. rubber-coated particles, pores or cracks at the microscale, can exhibit distinct effective macroscopic properties in a dynamic regime.

To model the before-mentioned effects, the microscale dynamic behavior needs to be somehow accounted for. Computational homogenization methods for quasi-static loading have become a common tool in numerical material analysis. A good overview of multiscale methods is given in GEERS et al. [33]. However with the rise in interest in metamaterials more and more dynamic homogenization frameworks have been published in the last years. There are different approaches to dynamic homogenization. One is the method of asymptotic expansion e.g. CRASTER et al. [21], FISH et al. [31], HU and OSKAY [46], and HUI and OSKAY [47], which are mainly based on the original work of BENSOUSSAN et al. [11]. Then, there is the more general theory of elastodynamic homogenization by WILLIS [114], applied in MILTON and WILLIS [73], NEMAT-NASSER and SRIVASTAVA [79], and WILLIS [115] and others. The two are based on related ideas and their similarities are studied in NASSAR et al. [78]. Both methods are limited to elastic, periodic media. A more general approach is the micro-macro simulation based on a representative volume element (RVE). In RVE homogenization methods, macroscopic quantities as the deformation gradient and the displacements at a macroscale integration point are projected onto a microscale volume element which replaces the constitutive material law by solving the imposed boundary value problem (BVP) and returning the corresponding macroscopic values. As the finite element method (FEM) is often used on both scales this is then usually called the FE<sup>2</sup> method. A comprehensive introduction to this theory including dynamics is given by SOUZA NETO et al. [99], which is the foundation on which this research has been built. The framework of FISH et al. [31] calculates a quasi-static microstructure but then applies an inertia-induced eigenstrain, based on the microstructure, as an extra body force at the macroscale to account for microinertia effects. This was extended by KARAMNEJAD and SLUYS [50] to account for matrix cracking at the microscale under impact loading. Other FE<sup>2</sup> type schemes as LIU and REINA [62], LIU and REINA [63], NULAND et al. [83], PHAM et al. [86], ROCA et al. [88], SRIDHAR et al. [103], and WANG and SUN [113] include the full balance of linear momentum at the microscale. In LIU and REINA [62] an explicit, periodic, small strain framework is presented, which was extended to an implicit time integration method for modeling resonant elastic metamaterials in LIU and REINA [63]. PHAM et al. [86] and ROCA et al. [88] use the assumption of linear elasticity to improve the computational performance, by splitting the problem into a purely static and a special dynamic BVP. In the work of SRIDHAR et al. [103] a FLOQUET-BLOCH transformation is used to build a base of eigenmodes to analyze elastic, periodic metamaterials, to better capture a wider range of applied frequencies. The mentioned frameworks all use at least one of the approximations: small strains, linear elasticity, periodic or symmetric microstructures. In addition many require quite elaborate implementations to run. A recent publication by NULAND et al. [83] does consider finite-strains within a standard FE<sup>2</sup> architecture. However, the derivation of the macroscopic tangent moduli assumes zero fluctuations of some nodes within the RVE. This arbitrarily restricts the translation of the respective nodes, making it applicable only for certain examples.

The aim of this research is to build a multiscale framework for dynamic loading as general as possible, while still being compatible with standard FE architecture. To enable the analysis of micromechanical processes such as plasticity or fiber pullout, as

well as to incorporate effects of geometric nonlinearities, the framework uses a finite-strain formulation. In the analytical example KHAJEHTOURIAN and HUSSEIN [52] of a nonlinear elastic metamaterial, finite strains are shown to be relevant for large wave amplitudes. To permit damage evolution in the RVE without arbitrarily forcing certain crack paths due to periodic boundary conditions COENEN et al. [20], it is proposed to apply the kinematic scale links as constraints on the whole RVE using LAGRANGE multipliers. This allows to model any type of microscopic geometry. In addition it puts no limits on the shape of the RVE. The analysis of e.g. spherical RVEs would be trivial.

## 1.3 Structure

As a coarse structure, this work can be split in three phases. Chapters 1 and 2 give an introduction. This is followed by Chapters 3 to 7 which give the theoretical background, including the proposed dynamic framework. Chapters 8 to 13 then deal with numerical results.

Following this general introduction, Chapter 2 gives an overview of fiber-reinforced concrete and its mechanical properties. The main focus is on strain-hardening cementitious composite, the target material of this project. Chapter 3 provides the basics of continuum mechanics. It covers kinematics, stress measures for large deformations and balance principles. In Chapter 4 the finite element method is presented, which is the method of choice within this work. Then Chapter 5 gives the standard Neo-HOOKEAN material formulation and extends it to include a stretch-rate depended formulation as well as damage. This material model is used to represent the fiber-matrix bond in the fiber pullout simulations. In Chapter 6 the background on numerical homogenization methods is presented. This includes a discussion of consistent scale links and the derivation of macroscopic averaging formulations. The following Chapter 7 then extends the theory to the dynamic regime. The formulation consistently takes into account the inertia forces at the microscale such that a framework is derived which allows the study of dynamic effects on two scales. The derivation of the closed form tangent moduli is presented and a special volume constraint is proposed to kinematically link the microscale to the macroscale. After deriving the dynamic homogenization scheme in detail, first numerical examples are given in Chapters 8 and 9. These are used to analyze general properties of the framework. Chapter 8 uses the example of a layered structure. The quadratic convergence of the norm of the macroscopic residuum during the NEWTON iteration is shown. Initial studies are conducted regarding the choice of RVE for dynamic multiscale problems. In addition, two displacement constraint are compared. Chapter 9 then presents a locally resonant microstructure. Different frequencies are applied and the wave attenuation is studied. Again, the displacement constraint is regarded. Then the focus is shifted to the modeling of SHCC. Chapter 10 deals with the fitting of the effective fiber pullout model to experimental data. In Chapter 11 a simplified SHCC microstructure is analyzed in combination with the proposed framework. Subsequently in Chapter 12, the boundary value problem is chosen to represent an experimental tensile test for dynamic loading. The simulation combines single and multiscale elements at the macroscale. This chapter demonstrates the possibilities the framework offers for analyzing impact events. Finally, Chapter 13 finishes this work with concluding remarks and an outlook.

## 2 Fiber-Reinforced Concrete

Concrete has a low tensile strength and is brittle. For most structural applications like beams or columns, steel bars are introduced as reinforcement to carry the tension loads once the concrete is cracked or to prevent the cracking in the first place. The same mechanism is utilized on a smaller scale when adding fibers to the composite. By introducing discontinuous randomly distributed fibers, the crack width can be controlled and instead of a few major cracks, multiple finer cracks are observed, as e.g. shown in Figure 2.1. This leads to a pseudo-ductile behavior of the composite, where strains of up to 5% prior to failure localization can be reached, an increase of about 500% compared to plain concrete. There are two primary categories of fiber-reinforced concrete. One is textile-reinforced concrete (TRC) where long, continuous fibers, usually woven into a 2D or 3D structure, are applied as laminates. The other category is fiber-reinforced concrete (FRC) which is the target material of this thesis, where chopped fibers are added to the mixture of the concrete and are distributed fairly randomly. In the literature, many different names and abbreviations for specific types of FRC can be found. There is e.g. high-performance fiber-reinforced cementitious composite (HPFRCC) [89], ultra-high performance fiber-reinforced concrete (UHPRC) [59], natural fiber-reinforced concrete (NFRCC) [70], strain-hardening cementitious composite (SHCC) [25], ultra-high-ductile cementitious composite (UHDCC) [120], engineered cement-based composite (ECC) [60], and more. Some are synonyms, others distinguish themselves by their intended use, specific properties or choice of material. They all share the same idea of bridging the emerging cracks to keep the crack mouth from further opening and instead facilitating the formation of multiple cracks. The choice of fiber material is diverse, ranging from steel fibers with different geometries, to carbon or glass fibers, a variety of polymer fibers, all the way to natural fibers, like flax, sisal [2] or curaua [101]. Just as diverse are the possible applications. Using these FRCs allows for lighter structures or more elegant geometries which makes it attractive for architecture and special design purposes. Other favorable properties are the improvement of overall composite properties, like ductility or tensile strength. In addition, it can enhance the durability by reducing crack width and protecting the rebars from chemicals. One very interesting and important property is the enhanced fracture toughness of the composite, meaning more energy is required until total structural failure occurs. This can be attributed to the post-cracking behavior. First, a progressive formation of



**Figure 2.1:** Multiple cracking in SHCC, from ZHAN et al. [120].

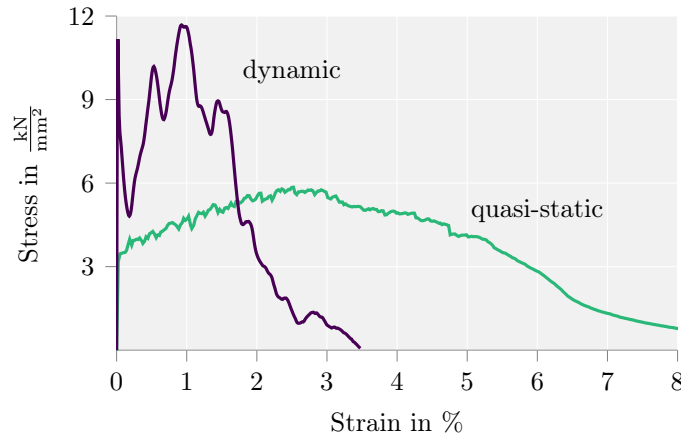


**Figure 2.2:** Tensile stress-strain curves, comparing the quasi-static and dynamic behavior of SHCC, from CUROSU et al. [25].

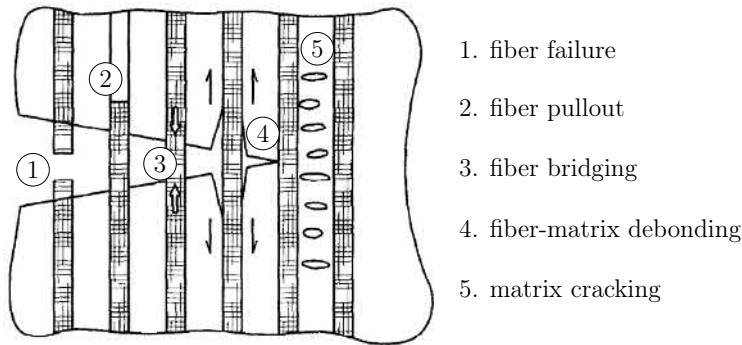


**Figure 2.3:** Energy-absorbing fiber-matrix mechanisms, based on ANDERSON [1] and ZOLLO [121].

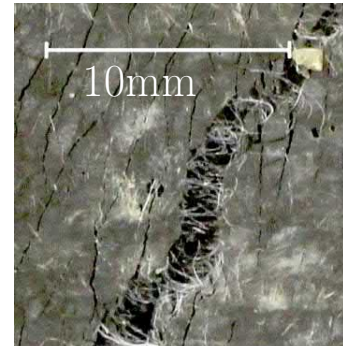


**Figure 2.4:** Global material failure of SHCC, based on CUROSU [24].

steady-state cracks is observed, resulting in a strain-hardening phase before localization occurs. Then instead of a brittle failure a long strain-softening curve is recorded. For correctly adjusted material properties even a pronounced strain-hardening phase is achievable, as depicted in Figure 2.2. These special composites are thus referred to as strain-hardening cementitious composites (SHCC). The micromechanical mechanisms behind this energy absorption are depicted in Figure 2.3. The first mechanism is the breaking of the matrix, forming of cracks and new surfaces. Then, once the fibers are engaged, energy is dissipated by debonding of the fibers, which includes elastic and possible plastic fiber deformations and finally the pullout or even rupture of the fiber. Figure 2.4 shows an SHCC specimen after macroscopic failure. Pulled-out and ruptured fibers are clearly visible, as well as multiple cracking in the surrounding concrete matrix. The micromechanical processes in Figure 2.3 and their role in the effective composite behavior are complex and depend on a number of factors. The first factors are the properties of the concrete matrix, which in itself is a heterogeneous structure. Content, size and distribution of pores as well as the choice of cement, aggregates and admixtures can greatly affect the initialization and propagation of microcracks. The debonding and the subsequent fiber sliding, involving friction between the fiber and the

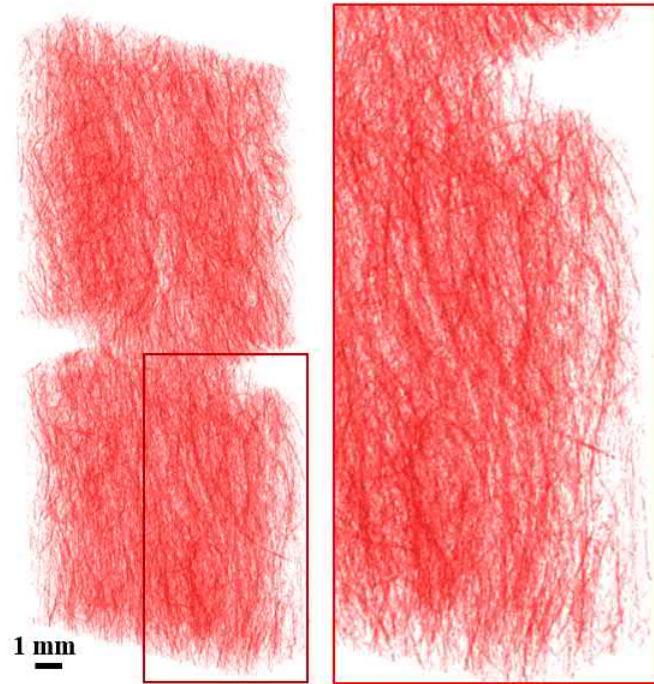


**Figure 2.5:** Segmented fiber for a micro-CT scan in a 3.5 mm thin SHCC specimen, from LORENZONI et al. [66]

matrix, is directly affected by the choice of fiber material as well as the type of concrete matrix. Moreover, additional surface treatment of the selected fibers can influence the composite behavior as well, see DRECHSLER et al. [28] and WÖLFEL and SCHEFFLER [117]. In addition to the material properties, the fiber distribution, spacing and volume fraction play a significant role for the effective composite behavior. Most SHCCs have a volume fraction of about 1–2 %, as higher values can lead to an excessive reduction in workability. Uniformly random distributions are only achieved in thick specimens, since fibers closer to a boundary will be more oriented. Even the molding process influences the distribution. Figure 2.5 shows the segmented fiber data of a micro-CT scan of a special, thin specimen of SHCC with ultra high molecular weight polyethylene fibers. It is evident that the fiber orientation of this specific sample is strongly directional. This must be considered when modeling such composites.

The feature of enhanced energy absorption makes FRCs in general and SHCCs in particular a good candidate for reinforcement against dynamic loads, where an effective energy absorption mechanism can prevent structural failure and reduce possible injuries. The research presented within this thesis was conducted as part of the Research Training Group GRK 2250 “Mineral-bonded composites for enhanced structural impact safety” at the Technische Universität Dresden, whose focus is exactly to investigate this aspect of FRC and TRC under dynamic loading. A general overview of all the projects of the first cohort and the overall goal is given in CUROSU et al. [26] and visualized in Figure 2.6. A summary of the respective results is given in CUROSU et al. [27] and HERING et al. [42]. The projects span different scales, different fiber materials and include both experimental and numerical work. The problem with understanding the dynamic response is the very complex micromechanical behavior combined with the

increased difficulty of precise and meaningful measurements under dynamic loading. This is due to the fact, that higher loading speeds lead to more interference from the testing equipment itself, e.g the shape of the introduced loading wave, reflections at impedance changes or geometric differences due to possible clamping mechanisms. Moreover, the high ductility of the composite makes classical measuring equipment as strain gauges unsuitable. To simply measure overall reactions like stress-strain curves with strain gauges and digital image correlation (DIC), new and advanced testing equipment needs to be designed and manufactured, c.f. HERAVI et al. [41]. As an example, a split HOPKINSON bar, used to measure the data in Figure 2.2, is able to observe and characterize the rate effects on the material response under impact loading. Although this is a good measure of how the effective material response of this specific specimen changes with increased loading rates, it does not answer the more basic questions of what exactly causes this behavior and how to improve it. Many of the before-mentioned micromechanical mechanisms are rate dependent, leading to a change in the macroscale response under impact loading. Micromechanical tests on e.g. single fibers, fibers embedded in matrix c.f. WÖLFEL et al. [116] and pure matrix material can shed light on some of the dynamic material properties. However, just as with the composite, they all suffer from an increased complexity in the experimental setup. In CUROSU [24] some strain-rate effects of e.g. the fiber-matrix bond or the fiber tensile strength are discussed. Notably, even the apparent tensile strength of the concrete matrix increases under high loading rates. Nevertheless, it is difficult to measure to what extent each of the mechanisms contributes to the overall energy dissipation of the composite. Furthermore, when dealing with dynamics there is always the influence of inertia that cannot be easily separated from the pure material response. Inertia is a structural effect that will change with geometry, size and obviously acceleration. Dynamic uniaxial tension tests will always result in an

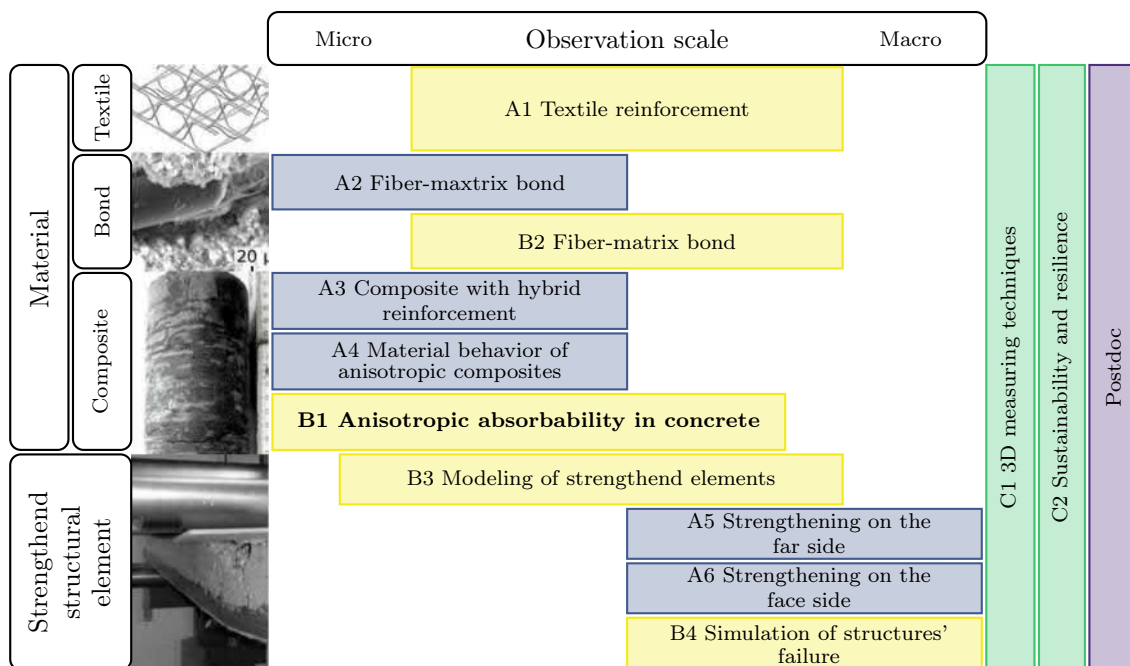


**Figure 2.6:** Overview of the projects within the Research Training Group GRK 2250/1, based on CUROSU et al. [26]. This research is part of project B1.

---

inhomogeneous displacement and stress field in the test specimen. Due to inertia, most material points undergo triaxial stress states. A well-known consequence of this effect is the pronounced overall increase of compressive strength in concrete due to the local confinement. Undoubtedly, inertia plays a significant role at the macroscale, influencing the propagation of the loading wave and making the stress measurement cumbersome due to wave reflections. Yet inertia might also play a significant role at the microscale, e.g. by delaying or changing the crack propagation, reflections at crack surfaces and other wave interferences arising at the small scale. This is one of the questions where a high fidelity numerical material simulation for SHCC might help the further understanding of the fine-scale dynamic effects and their respective influence on the effective composite behavior.



## 3 Continuum Mechanical Background

Continuum mechanics deals with the analysis of the behavior of materials, described by continuous volumes. A complex, real structure is characterized by certain field quantities, like density, displacement, velocity, or stiffness. These are then used to describe e.g. the deformation and the associated internal stress state of the system. Even though matter consist of discrete atoms and is not a continuous mass, this assumption is a good approximation for engineering applications, as the length scale of the atoms and molecules is significantly smaller than the length scale analyzed with the continuum formulations. This chapter gives a brief overview of the continuum mechanical background used in deriving the later presented homogenization method as well as the material models. There is substantial published literature dealing extensively with this topic. Introductions are e.g. found in: BAŞAR and WEICHERT [7], HOLZAPFEL [45], MARSDEN and HUGHES [69], NOTKIN and GULKIN [82], OGDEN [84], and WRIGGERS [118].

### 3.1 Kinematics

Kinematics describe the position and motion of material points over time, as well as the respective strain measures and time derivatives. As a start, an undeformed body  $\mathcal{B}$  is defined in its initial position at time  $t = t_0$ . This is called the reference configuration. However it is also known as the material or LAGRANGIAN description. Each material point in the reference configuration can be described by a position vector  $\mathbf{X}$ . Once loads are applied, the body undergoes deformation and potentially rigid body motion. This is called the current, spacial or EULERIAN configuration and is parameterized by  $\mathbf{x}$ , the deformation. The body in the current configuration is named  $\mathcal{S}$ . Now, the nonlinear deformation map is defined as  $\varphi(\mathbf{X}, t) = \mathbf{x} : \mathcal{B} \rightarrow \mathcal{S}$ . It directly maps for time  $t$  each point  $\mathbf{X} \in \mathcal{B}$  of the reference configuration onto a point  $\mathbf{x} \in \mathcal{S}$  of the current configuration. As depicted in Figure 3.1, the motion of points in the two configurations is linked by the displacement  $\mathbf{u}$  as

$$\mathbf{u} = \mathbf{x} - \mathbf{X}. \quad (3.1)$$

In the following an orthogonal CARTESIAN basis is assumed for both configurations, where  $\mathbf{E}_A$  are the base vectors of the reference configuration and  $\mathbf{e}_a$  the base vectors of the current configuration. In general, values as well as indices related to the reference configuration are denoted with uppercase letters. Conversely lowercase letters are used for the current configuration, unless otherwise stated. To describe the deformation of an infinitesimal environment in the current configuration, the deformation gradient is introduced as

$$\mathbf{F} = \text{Grad}[\varphi(\mathbf{X}, t)] = \frac{\partial \mathbf{x}}{\partial \mathbf{X}}. \quad (3.2)$$

The deformation gradient  $\mathbf{F}$  defines the local stretch and rotations of each point of the continuum. It is a second-order tensor with two different bases  $\mathbf{F} = F_{iA} \mathbf{e}_i \otimes \mathbf{E}_A$ .

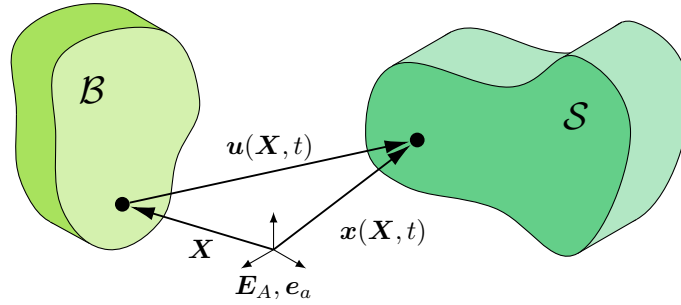


**Figure 3.1:** Motion of the body  $\mathcal{B}$ .

Taking into account the relation (3.1), the deformation gradient can also be formulated as

$$\mathbf{F} = \mathbf{1} + \frac{\partial \mathbf{u}}{\partial \mathbf{X}} = \mathbf{1} + \mathbf{H}, \quad (3.3)$$

where  $\mathbf{1}$  denotes the second-order identity tensor and  $\mathbf{H} = \text{Grad}[\mathbf{u}]$  the displacement gradient. The deformation gradient can be used to map a line element in the initial configuration  $d\mathbf{X}$ , onto a line element  $d\mathbf{x}$  of the current configuration

$$d\mathbf{x} = \mathbf{F} d\mathbf{X}. \quad (3.4)$$

For this mapping to be a one-to-one transformation,  $\mathbf{F}$  cannot be singular. This is ensured by postulating that the JACOBI determinant  $J$  is strictly positive

$$J = \det[\mathbf{F}] > 0. \quad (3.5)$$

From a physical point of view this is logical, as the JACOBI determinant is a direct measure of volume change, linking the reference volume  $V$  to its complement  $v$  in the current configuration as

$$dv = J dV. \quad (3.6)$$

Values of  $J \leq 0$  thus describe a non-existing or self-penetrating volume, which would be non-physical. To project the deformation onto a vectorial area element, the formula of NANSON (c.f. OGDEN [84, p.88]) is applied

$$d\mathbf{a} = \mathbf{n} da = J\mathbf{F}^{-\text{T}} \mathbf{N} dA = J\mathbf{F}^{-\text{T}} d\mathbf{A}. \quad (3.7)$$

Figure 3.2 gives an illustration of the transformation relations of the two configurations. Continuum mechanical equations can be formulated in the reference as well as the current configuration. In practice, different formulations can have advantages regarding the simplicity of the derivations and the efficiency of the selected numerical methods. In addition, some balance equations are only valid in a specific configuration. To describe the strain or stretch in each configuration various strain tensors have been defined. Some examples would be the left and right CAUCHY-GREEN tensors

$$\mathbf{b} = \mathbf{F}\mathbf{F}^{\text{T}} \quad \text{and} \quad \mathbf{C} = \mathbf{F}^{\text{T}}\mathbf{F}. \quad (3.8)$$

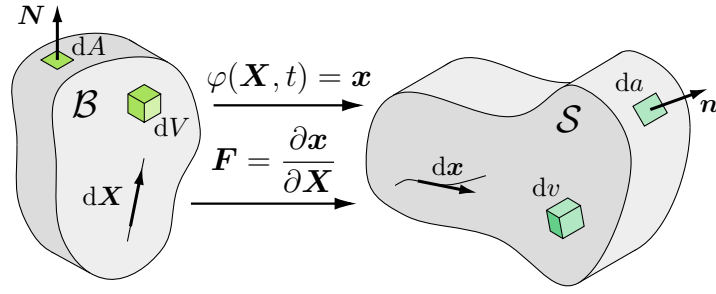


**Figure 3.2:** Infinitesimal elements in the reference and current configuration.

A further popular strain measure for material modeling is e.g. the GREEN-LAGRANGE tensor

$$\mathbf{E} = \frac{1}{2} (\mathbf{F}^T \mathbf{F} - \mathbf{1}). \quad (3.9)$$

In contrast to  $\mathbf{F}$ ,  $\mathbf{E}$  does not contain information about rigid body rotations and both bases are related to the reference configuration. In component form, the strain tensor  $\mathbf{E}$  can be expressed as

$$E_{AB} = \frac{1}{2} (F_{iA} F_{iB} - \delta_{AB}), \quad (3.10)$$

where  $\delta_{AB}$  is the KRONECKER delta, which has the properties of  $\delta_{AB} = 1$  if  $A = B$  else  $\delta_{AB} = 0$ , representing the unit tensor  $\mathbf{1}$ .

The final part of kinematics are the time derivatives. These are applied in problems where the material and structural behavior is time dependent as e.g. in visco-elasticity or obviously in dynamic simulations. The most well-known time derivatives are velocity

$$\mathbf{v} = \frac{d\mathbf{u}}{dt} = \frac{d\mathbf{x}}{dt} = \dot{\mathbf{x}} \quad (3.11)$$

and acceleration

$$\mathbf{a} = \frac{d^2\mathbf{x}}{dt^2} = \frac{d\mathbf{v}}{dt} = \dot{\mathbf{v}} = \ddot{\mathbf{x}}, \quad (3.12)$$

which are defined as the first and second time derivative of the displacement or deformation map. Likewise, other time derivatives are denoted with dots on top as e.g.  $\dot{\mathbf{F}}$ , the second time derivative of the deformation gradient. To maintain the legibility of the formulations in this work, the time dependence of quantities will only be specified for emphasis as e.g. in (3.2) or Figure 3.1. As is mostly dealt with dynamic problems further on, most values will change over time, otherwise it will be clear from context or respective definitions.

## 3.2 Stress Measures

Applying forces to a physical body leads to an internal loading state. This state is described by the concept of stress. The CAUCHY stress  $\boldsymbol{\sigma}$  relates the unit normal

vector  $\mathbf{n}$  of an area  $da$  to the respective stress vector  $\mathbf{t}$  as

$$\mathbf{t} = \boldsymbol{\sigma} \mathbf{n}. \quad (3.13)$$

The stress  $\boldsymbol{\sigma}$  is only related to the current configuration and represents the physical stress inside the deformed body. Thus, it is also called the true stress. Without changing the physical state of the body, other stress measures can be defined. In continuum mechanics it is often convenient to express quantities rather with respect to a reference configuration than to the current configuration, by means of material quantities instead of spatial ones. Applying this to the CAUCHY stress results in the PIOLA-KIRCHHOFF stress. The first PIOLA-KIRCHHOFF stress  $\mathbf{P}$ , sometimes called engineering stress, is defined as the current stress vector acting on an area in the reference configuration. This means, that first PIOLA-KIRCHHOFF stress vector  $\mathbf{T}$  is parallel to the CAUCHY stress vector  $\mathbf{t}$ , but is related to the undeformed area  $dA$ . It follows that  $\mathbf{T} dA = \mathbf{t} da$ . The first PIOLA-KIRCHHOFF stress is expressed as

$$\mathbf{T} = \mathbf{P} \mathbf{N}. \quad (3.14)$$

Using (3.7), the first PIOLA-KIRCHHOFF stress can be written in terms of the CAUCHY stress as

$$\mathbf{P} = J \boldsymbol{\sigma} \mathbf{F}^{-\text{T}} \quad \text{and in index notation} \quad P_{iA} = J \sigma_{ik} F_{Ak}^{-1}. \quad (3.15)$$

Unlike  $\boldsymbol{\sigma}$ ,  $\mathbf{P}$  is not necessarily symmetrical. However it is frequently used, especially in the field of homogenization as shown later in the work at hand. Transforming this mixed basis tensor entirely to the reference configuration results in the second PIOLA-KIRCHHOFF stress tensor  $\mathbf{S}$ . In terms of the other stress measures it can be expressed as

$$\mathbf{S} = \mathbf{F}^{-1} \mathbf{P} = J \mathbf{F}^{-1} \boldsymbol{\sigma} \mathbf{F}^{-\text{T}} \quad \text{and} \quad S_{AB} = F_{Ai}^{-1} P_{iB} = J F_{Ai}^{-1} \sigma_{ij} F_{Bj}^{-1}. \quad (3.16)$$

The second PIOLA-KIRCHHOFF  $\mathbf{S}$  is symmetrical, but does not have a physical interpretation and is a purely mathematical concept.

Each stress tensor has a work conjugated strain measure with which the same scalar-valued potential energy can be expressed. This is especially relevant for material modeling, where the constitutive equations need to be formulated with the corresponding pairs. For the presented stress measures, their work conjugated pairs are  $(\mathbf{S}, \mathbf{E})$  and  $(\mathbf{P}, \mathbf{F})$ .

### 3.3 Balance Equations

To properly represent the real world, balance equations based on fundamental physical observations are used as the basis of simulations. In material modeling, the conservation of mass, conservation of linear and angular momentum, conservation of energy and the entropy inequality form the foundation.

**Conservation of Mass** The first balance principle states, that for an observed system as a whole, the mass does not change over time. At the local level this implies

that the mass  $m$  remains constant, also during a deformation process, with

$$m = \int_{\mathcal{B}} \rho_0 dV = \int_{\mathcal{S}} \rho dv \quad \Rightarrow \quad \rho_0 = J\rho. \quad (3.17)$$

**Balance of Linear Momentum** The balance of linear momentum specifies, that the change of linear momentum  $\mathbf{L}$  over time equals the sum of all external forces. This is usually written as the volume integral of the body forces due to gravity plus the integral of the traction vectors  $\mathbf{t}$  on the boundary  $\partial\mathcal{S}$ ,

$$\dot{\mathbf{L}} = \int_{\mathcal{S}} \rho \mathbf{g} dv + \int_{\partial\mathcal{S}} \mathbf{t} da, \quad \text{with} \quad \mathbf{L} := \int_{\mathcal{S}} \rho \dot{\mathbf{x}} dv, \quad (3.18)$$

with  $\mathbf{g}$  denoting the acceleration by Earth's gravitational field. Written in local notation, here in terms of the first PIOLA-KIRCHHOFF stress, the balance of linear momentum then reads

$$\text{Div}[\mathbf{P}] + \rho_0 \mathbf{g} = \rho_0 \ddot{\mathbf{x}}, \quad (3.19)$$

which will be the start of the derivation of the finite element method.

**Balance of Angular Momentum** Similar to the balance of linear momentum, the balance of angular momentum describes the change of angular momentum for a chosen point, based on the sum of applied moments. From this it can be shown that the CAUCHY stress tensor is symmetrical,  $\boldsymbol{\sigma} = \boldsymbol{\sigma}^T$ . With (3.16), it follows the symmetry of the second PIOLA-KIRCHHOFF stress tensor as well. This property can be exploited to reduce memory and computational cost.

**Balance of Energy** The principle of conservation of energy also referred to as the first law of thermodynamics states that any change of energy in a system equals the power introduced from external sources. In the following work only the mechanical energy in a system is regarded. It should be noted, that in simulations of dissipative processes as plasticity, fracture or damping, part of the strain energy is transformed into a heat source.

**Entropy Inequality** The final axiom, the entropy inequality also called the second law of thermodynamics postulates that the temporal change of the entropy of an isolated system can only increase over time. For an idealized reversible process entropy does not change. However, for irreversible processes entropy increases. In material modeling this is regarded by the CLAUSIUS-DUHEM inequality, as

$$\mathbf{S} : \dot{\mathbf{E}} - \dot{\psi} \geq 0, \quad (3.20)$$

where  $\psi$  is the stored energy.

For more details on balance equations in numerical simulations, see e.g. BAŞAR and WEICHERT [7], BELYTSCHKO et al. [10], HOLZAPFEL [45], and WRIGGERS [118].



## 4 Finite Element Method

The last chapter presented the continuum mechanical equations and respective balance equations used to describe the behavior of a continuous body. For very simple problems, this system of equations might be solved analytically, but for more complex and interesting cases this is not feasible. A possible solution, used in this work, is the utilization of the finite element method (FEM). The main idea is to discretize a body into a finite number of elements, which are defined by a set of discrete points, called nodes, and their respective connections. The elemental field (e.g. displacement, or temperature) can then be described by interpolating between the nodes, using specific ansatz functions, also known as shape functions. To apply the FEM, volume integrals need to be solved. Using GAUSS integration and the isoparametric concept, even complex geometries and higher-order shape functions can be accurately and efficiently integrated. After linearization and incorporation of boundary conditions as well as external loads, the system of equations can be iteratively solved, and thus an approximate solution is found. Due to its flexibility and general robustness FEM is widely used in structural mechanics and material modeling. Here only the conventional finite element method is presented, which solves the system of equations for the nodal displacements. This chapter will briefly outline the basic concepts for the derivation of a finite element formulation in a large strain setting, including inertia. More complex examples can be derived accordingly, c.f. e.g. BATHE [8] and WRIGGERS [118].

### 4.1 Variational Problem

Following the balance equations of linear momentum and angular momentum together with the boundary conditions, a set of differential equations is given whose analytical solution might be difficult. Therefore, variational principles may be applied to obtain the so called weak form of equilibrium. The local form of linear momentum (3.19), here in terms of the first PIOLA-KIRCHHOFF stress tensor, with the body forces expressed as the gravitational force  $\mathbf{f}^b = \rho_0 \mathbf{g}$ ,

$$\text{Div}[\mathbf{P}] + \rho_0 \mathbf{g} = \rho_0 \ddot{\mathbf{x}}, \quad (4.1)$$

together with the boundary conditions

$$\mathbf{u} = \mathbf{u}_{\text{BC}} \quad \text{on} \quad \partial\mathcal{B}_u \quad \text{and} \quad \mathbf{P}\mathbf{N} = \mathbf{t}_{\text{BC}} \quad \text{on} \quad \partial\mathcal{B}_\sigma, \quad (4.2)$$

is referred to as the strong form of equilibrium. Here,  $\mathbf{u}_{\text{BC}}$  are prescribed displacements with the associated surface  $\partial\mathcal{B}_u$ , and  $\mathbf{t}_{\text{BC}}$  are applied tractions on the surface  $\partial\mathcal{B}_\sigma$ . Now the strong form is multiplied with the vectorial test function  $\delta\mathbf{u}$ , which in this case can be interpreted as virtual displacements. Afterwards the integral of the volume is computed, which results in the weak form

$$G = \int_{\mathcal{B}} (\text{Div}[\mathbf{P}] + \rho_0(\mathbf{g} - \ddot{\mathbf{x}})) \cdot \delta\mathbf{u} \, dV = 0, \quad (4.3)$$

where  $G$  is the scalar value of virtual work. By first using  $\text{Div}[\mathbf{P}] \cdot \delta \mathbf{u} = \text{Div}[\mathbf{P}^T \delta \mathbf{u}] - \mathbf{P} : \text{Grad}[\delta \mathbf{u}]$ , then applying the GAUSS theorem  $\int_{\mathcal{B}} \text{Div}[\mathbf{P}^T \delta \mathbf{u}] dV = \int_{\partial \mathcal{B}_\sigma} \delta \mathbf{u} \cdot \mathbf{t}_{\text{BC}} dA$  in combination with the boundary conditions on  $\partial \mathcal{B}_u$ , the equation can be reformulated as

$$G = G^{\text{int}} - G^{\text{ext}} = 0, \quad \text{with}$$

$$G^{\text{int}} = \int_{\mathcal{B}} \mathbf{P} : \text{Grad}[\delta \mathbf{u}] dV \quad \text{and} \quad G^{\text{ext}} = \int_{\mathcal{B}_\sigma} \delta \mathbf{u} \cdot \mathbf{t}_{\text{BC}} dA + \int_{\mathcal{B}} \delta \mathbf{u} \cdot \rho_0(\mathbf{g} - \ddot{\mathbf{x}}) dV. \quad (4.4)$$

Note that equilibrium means  $G = 0$ , or in other terms  $G^{\text{int}} = G^{\text{ext}}$ . Alternatively, the internal virtual work  $G^{\text{int}}$  can be obtained by assuming an internal energy potential  $\Pi^{\text{int}}$ , whose variation results in the equivalent formulation as

$$G^{\text{int}} = \delta \Pi^{\text{int}} = \delta \left( \int_{\mathcal{B}} \mathbf{W}(\mathbf{F}) dV \right) = \int_{\mathcal{B}} \frac{\partial \mathbf{W}}{\partial \mathbf{F}} : \delta \mathbf{F} dV = \int_{\mathcal{B}} \mathbf{P} : \text{Grad}[\delta \mathbf{u}] dV, \quad (4.5)$$

where  $W$  is the respective strain energy density function. Herein, the variation of the deformation gradient  $\delta \mathbf{F} = \text{Grad}[\delta \mathbf{u}]$  is used, c.f. (3.3).

## 4.2 Linearization

There are multiple sources of nonlinear behavior. One example is the use of nonlinear strain measures as e.g. the right CAUCHY-GREEN tensor  $\mathbf{C}$ , the GREEN-LAGRANGE strain tensor  $\mathbf{E}$  or the deformation gradient  $\mathbf{F}$ , as discussed in Section 3.1. Another one is the choice of a nonlinear constitutive equation as e.g. plasticity, rate dependency or fracture. Even microscale inertia can lead to effective nonlinearities. Especially inertia effects as well as strain-rate sensitive constitutive equations will be discussed in the following chapters. To solve such nonlinear systems of equations numerically, iterative solving procedures are employed. The NEWTON-RAPHSON method is applied, as it has the favorable mathematical property of converging quadratically, when sufficiently close to the solution. The definition of sufficiently close obviously depends on the complexity of the problem, but by keeping an eye on the convergence behavior and adapting the load steps accordingly, an efficient solving algorithm can be obtained. The linearization of the weak form is given by

$$\text{Lin}G = G + \Delta G = 0, \quad (4.6)$$

where  $G$  is referred to as the residual. The  $\Delta$  operator is here defined as the difference of a quantity  $\bullet$  between two consecutive iteration steps  $n$ ,

$$\Delta \bullet_{n+1} = \bullet_{n+1} - \bullet_n. \quad (4.7)$$

The definition of the increment of a function  $\bullet(\square)$ , defined in terms of another quantity  $\square$ , holds that

$$\Delta \bullet(\square) = \left. \frac{\partial \bullet}{\partial \square} \right|_{\square_n} \Delta \square. \quad (4.8)$$

Assuming displacement-independent traction forces  $\mathbf{t}_{\text{BC}}$  and neglecting possible gravitational effects  $\mathbf{g}$ , as these do not depend on the local displacements, the incremental virtual work is calculated from (4.4) by

$$\Delta G = \int_{\mathcal{B}} \delta \mathbf{F} : \Delta \mathbf{P} \, dV + \int_{\mathcal{B}} \delta \mathbf{u} \cdot \rho_0 \Delta \ddot{\mathbf{x}} \, dV. \quad (4.9)$$

Following (4.8),  $\Delta \mathbf{P}$  is reformulated as

$$\Delta \mathbf{P} = \frac{\partial \mathbf{P}}{\partial \mathbf{F}} : \Delta \mathbf{F}, \quad (4.10)$$

where  $\partial_{\mathbf{F}} \mathbf{P}$  is referred to as the tangent modulus. In this work the tangent modulus in terms of  $\mathbf{P}$  is abbreviated with  $\mathbb{A}$ , whereas the tangent moduli formulated in the second PIOLA-KIRCHHOFF stress tensor  $\mathbf{S}$  are defined as  $\mathbb{C} = \partial_{\mathbf{E}} \mathbf{S}$  and  $\mathbb{C} = 2 \partial_{\mathbf{C}} \mathbf{S}$ . Now the full linearized weak form can be expressed as

$$\begin{aligned} \text{Lin}G &= \int_{\mathcal{B}} \delta \mathbf{F} : \mathbf{P} \, dV - \int_{\mathcal{B}_\sigma} \delta \mathbf{u} \cdot \mathbf{t}_{\text{BC}} \, dA - \int_{\mathcal{B}} \delta \mathbf{u} \cdot \mathbf{f} \, dV \\ &+ \int_{\mathcal{B}} \delta \mathbf{F} : \mathbb{A} : \Delta \mathbf{F} \, dV + \int_{\mathcal{B}} \delta \mathbf{u} \cdot \rho_0 \Delta \ddot{\mathbf{x}} \, dV, \end{aligned} \quad (4.11)$$

where  $\mathbf{f} = \rho_0(\mathbf{g} - \ddot{\mathbf{x}})$  is the body force vector.

### 4.3 Discretization

Since an analytical solution for the system of partial differential equations is generally not known, the finite element method is applied, in which the real physical body  $\mathcal{B}$  is discretized into nodes and elements, c.f. Figure 4.1. Together the nodes and elements form the finite element mesh. Each element has a certain number of associated nodes  $n_{\text{en}}$ . Specific shape functions are then used to describe the elemental domain  $\mathcal{B}^e$  by

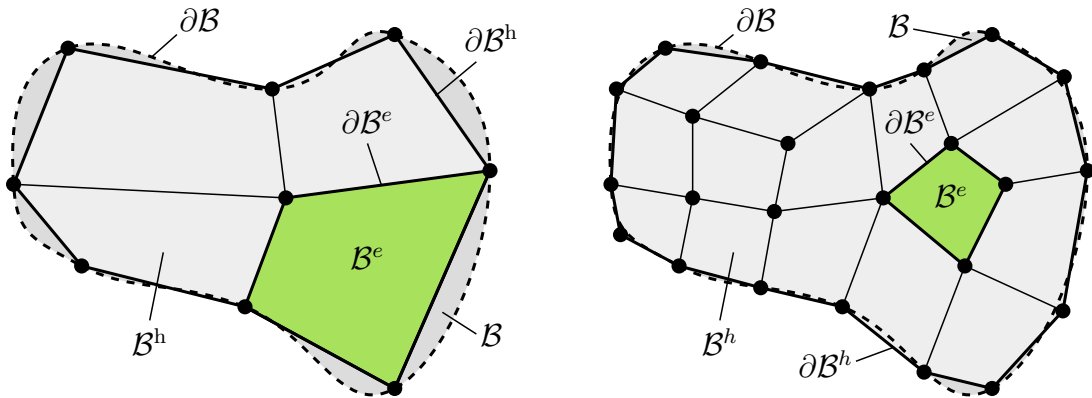


**Figure 4.1:** Example of a finite element approximation  $\mathcal{B}^h$  of the real body  $\mathcal{B}$  for a coarse mesh with  $n_{\text{el}} = 4$  and a finer mesh with  $n_{\text{el}} = 15$ .

interpolating the nodal values. The approximation of the domain  $\mathcal{B}^h$  can be expressed mathematically as the union of all elements

$$\mathcal{B} \approx \mathcal{B}^h = \bigcup_{e=1}^{n_{el}} \mathcal{B}^e, \quad (4.12)$$

where  $n_{el}$  is the total number of elements. As a result, all primary variables, in this work the displacements, can be approximated by using only nodal values. This reduces the infinite number of material points from the continuum mechanical formulation to a finite number, which can be expressed and solved for in a corresponding system of equations. The boundary  $\partial\mathcal{B}$  of the real body is approximated by the boundary of the finite element mesh  $\partial\mathcal{B}^h$ , and the boundary of each element denoted as  $\partial\mathcal{B}^e$ . As illustrated in Figure 4.1, the approximation of the geometry can be improved by using a finer mesh, i.e. a larger number of elements and nodes. On the other hand, a larger number of unknown variables increases the computational costs. A FEM calculation is always a trade-off between accuracy and computational resources as well as calculation time. In the following, the superscript  $\bullet^h$  indicating the approximation is dropped to improve legibility. Unless otherwise emphasized, fields are associated to the approximation. When the same shape functions are used for both the geometry and the primary variables, the isoparametric concept can be adopted. It maps the geometry of an arbitrarily deformed element onto a reference element with a fixed geometry. This drastically facilitates implementation. Both the reference and current configuration, as well as the isoparametric subspace  $\mathcal{B}_\square$  are linked by transformation maps as shown in Figure 4.2 for a quadrilateral element. Using the isoparametric mapping, the current and reference configuration are obtained by

$$\mathbf{X}(\xi, \eta) = \sum_{I=1}^{n_{en}} N_I(\xi, \eta) \mathbf{X}_I \quad \text{and} \quad \mathbf{x}(\xi, \eta) = \sum_{I=1}^{n_{en}} N_I(\xi, \eta) \mathbf{x}_I, \quad (4.13)$$

wherein  $N_I(\xi, \eta)$  are the shape functions in the parameter space. The shape functions have the properties of taking the value of 1 at their respective nodes and that the sum

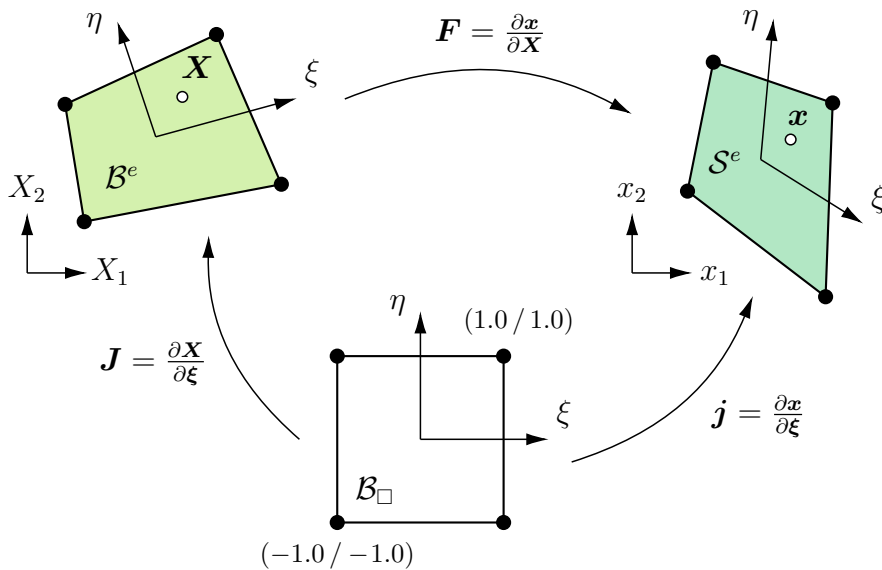


**Figure 4.2:** Isoparametric mapping for a quadrilateral element.

of all equals 1 for every point. The coordinates  $\xi$  and  $\eta$  are generally defined on the interval of  $[-1, 1]$ . To transform a vector to the physical space the JACOBI matrices are defined as

$$\mathbf{J} = \frac{\partial \mathbf{X}}{\partial \boldsymbol{\xi}} \quad \text{and} \quad \mathbf{j} = \frac{\partial \mathbf{x}}{\partial \boldsymbol{\xi}}, \quad (4.14)$$

where  $\boldsymbol{\xi}^T = [\xi, \eta]$ , c.f. Figure 4.2. In contrast to the continuous displacement field  $\mathbf{u}$ , the discretized nodal displacements are denoted as  $\mathbf{d}_I$ , such that the current deformation at a node  $I$  is calculated as

$$\mathbf{x}_I = \mathbf{X}_I + \mathbf{d}_I. \quad (4.15)$$

All displacement vectors are approximated equivalent to the geometry, with

$$\mathbf{u} = \sum_{I=1}^{n_{\text{en}}} N_I \mathbf{d}_I. \quad (4.16)$$

To compute the approximation of the deformation gradient  $\mathbf{F}$  or displacement gradient  $\mathbf{H}$ , based on the nodal displacements, a discretized formulation for  $\text{Grad}[\mathbf{u}]$  is required. This is achieved using (4.14)<sub>1</sub> and (4.16)

$$\text{Grad}[\mathbf{u}] = \text{Grad} \left[ \sum_{I=1}^{n_{\text{en}}} N_I \mathbf{d}_I \right] = \sum_{I=1}^{n_{\text{en}}} \text{Grad}[N_I] \mathbf{d}_I, \quad (4.17)$$

where  $\text{Grad}[N_I]$  can be reformulated as

$$\text{Grad}[N_I] = \frac{\partial N_I}{\partial \mathbf{X}} = \frac{\partial N_I}{\partial \boldsymbol{\xi}} \frac{\partial \boldsymbol{\xi}}{\partial \mathbf{X}} = \mathbf{J}^{-T} \frac{\partial N_I}{\partial \boldsymbol{\xi}}. \quad (4.18)$$

To facilitate the formulation, the commonly used B-matrix that contains the derivatives of the shape functions is introduced, here for a 2D truss with two nodes

$$\mathbf{B}_I = \begin{bmatrix} N_{I,\xi} (J_{11}^{-1} + J_{21}^{-1}) & 0 \\ 0 & N_{I,\eta} (J_{12}^{-1} + J_{22}^{-1}) \\ N_{I,\eta} (J_{12}^{-1} + J_{22}^{-1}) & 0 \\ 0 & N_{I,\xi} (J_{11}^{-1} + J_{21}^{-1}) \end{bmatrix}. \quad (4.19)$$

Note the switch to the matrix notation, where second-order tensors are written as a vector and fourth-order tensors are expressed as a matrix. As a last step the elemental matrices are defined to eliminate the need of the summation operator,

$$\mathbf{d}^{eT} = [ \mathbf{d}_1^T \mid \cdots \mid \mathbf{d}_{n_{\text{en}}}^T ], \quad (4.20)$$

$$\mathbf{B}^e = [ \mathbf{B}_1 \mid \cdots \mid \mathbf{B}_{n_{\text{en}}} ] \quad \text{and} \quad (4.21)$$

$$\mathbf{N}^e = \left[ \begin{array}{cc|ccc} N_1 & 0 & & & N_{n_{\text{en}}} & 0 \\ 0 & N_1 & & & 0 & N_{n_{\text{en}}} \end{array} \right]. \quad (4.22)$$

Finally one obtains the displacements  $\mathbf{u}$  and the displacement gradient  $\mathbf{F}$  for each point in an element as

$$\mathbf{u} = \mathbf{N}^e \mathbf{d}^e \quad \text{and} \quad \mathbf{F} = \mathbf{1} + \mathbf{B}^e \mathbf{d}^e. \quad (4.23)$$

The linearized virtual work for a single element is formulated as

$$\text{Lin}G^e = G^e + \Delta G^e. \quad (4.24)$$

Then, the two terms  $G^e$  and  $\Delta G^e$  are discretized by applying (4.23) to each one while using the matrix notation,

$$G^e = \delta \mathbf{d}^{eT} \left[ \int_{\mathcal{B}^e} \mathbf{B}^{eT} \mathbf{P} \, dV - \mathbf{r}^{e,t_{BC}} - \int_{\mathcal{B}^e} \mathbf{N}^{eT} \mathbf{f} \, dV \right] \quad \text{and} \quad (4.25)$$

$$\Delta G^e = \delta \mathbf{d}^{eT} \left[ \int_{\mathcal{B}^e} \mathbf{B}^{eT} \mathbb{A} \mathbf{B}^e \, dV \, \Delta \mathbf{d}^e + \int_{\mathcal{B}^e} \mathbf{N}^{eT} \rho_0 \mathbf{N}^e \, dV \, \Delta \ddot{\mathbf{d}}^e \right]. \quad (4.26)$$

Here the element residual vector  $\mathbf{r}^{e,t_{BC}} = \int_{\partial \mathcal{B}_e^e} \mathbf{N}^{eT} \mathbf{t}_{BC} \, dA$  represents the contribution of the tractions. From now on the traction contribution to the element is ignored, as it is applied using boundary elements or other specific procedures, which are not part of the scope of this work. At this point it is needed to introduce two additional numerical concepts to obtain a general FEM formulation. The first is the concept of numerical time integration, to deal with the time derivatives  $\Delta \ddot{\mathbf{d}}^e$  and  $\ddot{\mathbf{x}}$ . The second is the GAUSS integration, to get a general solution for the volume integrals of the element.

## 4.4 Numerical Time Integration

Just as the continuous body is split into finite elements, time is discretized into finite time steps. For each time step the equilibrium is solved. There are two general approaches for numerical time integration: explicit and implicit. Explicit time integration is easily implemented, as the solution at time  $t_{n+1}$  only depends on quantities of the last time step  $t_n$ . This approach is mainly limited by the choice of time step size. For a stable computation the time steps need to be chosen small enough. A general criterion for the time step  $\Delta t$  for nonlinear explicit problems is given in BELYTSCHKO, CHIAPETTA, and BARTEL [9] as  $\Delta t < \delta \frac{h}{c_L}$ . Herein  $h$  is the smallest element size,  $c_L$  the compressive wave speed for a linear elastic solid, and  $\delta$  a reduction parameter chosen according to the nonlinearity of the problem, with  $0.2 < \delta < 0.9$ . The compressive wave speed is calculated as  $c_L = \frac{3K(1-\nu)}{\rho(1+\nu)}$  with the modulus of compression  $K$ , the POISSON's ratio  $\nu$  and the density  $\rho$ . Implicit time integration schemes however depend upon values at time  $t_n$  as well as the unknown quantities of the current time  $t_{n+1}$ . This requires the solution of a nonlinear algebraic equation at every time step. The remarkable advantage in this approach is that the integration scheme can be constructed in such a way that the algorithm is unconditionally stable. As a result the time step size can be chosen much larger than in an explicit scheme. Practically, the time step size  $\Delta t$  still needs to be chosen according to the relevant frequencies.

### 4.4.1 Newmark Method

For the sake of stability and generality an implicit time integration scheme was chosen for this work, namely the NEWMARK method, see e.g. NEWMARK [80]. It is a well known and widely used method for approximating the dynamic response in structural

mechanics. It is used to solve the nonlinear discrete equation of motion, derived from the weak form of linear momentum

$$\mathbf{M}\ddot{\mathbf{u}} + \mathbf{R}^{\text{int}}(\mathbf{u}) = \mathbf{R}^{\text{ext}}, \quad (4.27)$$

where  $\mathbf{M}$  is the mass matrix,  $\mathbf{R}^{\text{int}}$  the vector of internal forces, and  $\mathbf{R}^{\text{ext}}$  the vector of time dependent external forces. The NEWMARK method is based on the following approximations for the displacements  $\mathbf{u}_{n+1}$  and velocities  $\dot{\mathbf{u}}_{n+1}$

$$\mathbf{u}_{n+1} = \mathbf{u}_n + \Delta t \dot{\mathbf{u}}_n + \frac{\Delta t^2}{2} [(1 - 2\beta)\ddot{\mathbf{u}}_n + 2\beta\ddot{\mathbf{u}}_{n+1}] \quad \text{and} \quad (4.28)$$

$$\dot{\mathbf{u}}_{n+1} = \dot{\mathbf{u}}_n + \Delta t [(1 - \gamma)\ddot{\mathbf{u}}_n + \gamma\ddot{\mathbf{u}}_{n+1}]. \quad (4.29)$$

The parameters  $\beta$  and  $\gamma$  are constants which control the behavior of the integration method. Based on mathematical analysis they are bounded as  $0 \leq \beta \leq 0.5$  and  $0 \leq \gamma \leq 1$ . The unknown accelerations  $\ddot{\mathbf{u}}_{n+1}$  are determined by the equation of linear momentum. The same equations can be reformulated, such that the current values of velocity and acceleration are written in terms of the unknown current displacements as

$$\ddot{\mathbf{u}}_{n+1} = \frac{1}{\beta\Delta t^2}(\mathbf{u}_{n+1} - \mathbf{u}_n) - \frac{1}{\beta\Delta t}\dot{\mathbf{u}}_n - \frac{1 - 2\beta}{2\beta}\ddot{\mathbf{u}}_n \quad \text{and} \quad (4.30)$$

$$\dot{\mathbf{u}}_{n+1} = \frac{\gamma}{\beta\Delta t}(\mathbf{u}_{n+1} - \mathbf{u}_n) + (1 - \frac{\gamma}{\beta})\dot{\mathbf{u}}_n + (1 - \frac{\gamma}{2\beta})\ddot{\mathbf{u}}_n. \quad (4.31)$$

This procedure harmonizes perfectly with the already applied NEWTON-RAPHSON method, where the current displacements are iteratively computed. In this work  $\beta = 0.25$  and  $\gamma = 0.5$  are chosen, which represents a constant acceleration within each time step. Furthermore, applying these values results in an unconditionally stable algorithm. It should be noted, that the algorithm is only energy conserving for linear elasticity. For more general information on FE dynamics approximations and the NEWMARK method see BATHE [8] and WRIGGERS [118].

#### 4.4.2 Application to the FEM Problem

The just presented NEWMARK method facilitates the computation of the sought-after nodal accelerations  $\ddot{\mathbf{d}}$  and the respective nodal velocities  $\dot{\mathbf{d}}$  at time  $t_{n+1}$  as

$$\ddot{\mathbf{d}} = \frac{\mathbf{d} - \hat{\mathbf{d}}}{\beta\Delta t^2} \quad \text{and} \quad \dot{\mathbf{d}} = \hat{\dot{\mathbf{d}}} + \Delta t \gamma \ddot{\mathbf{d}}, \quad (4.32)$$

where the predictors are defined as

$$\hat{\mathbf{d}} = \mathbf{d}_n + \Delta t \dot{\mathbf{d}}_n + \frac{\Delta t^2}{2} (1 - 2\beta) \ddot{\mathbf{d}}_n \quad \text{and} \quad (4.33)$$

$$\hat{\dot{\mathbf{d}}} = \dot{\mathbf{d}}_n + \Delta t (1 - \gamma) \ddot{\mathbf{d}}_n, \quad (4.34)$$

while dropping the index  $\bullet_{n+1}$  for the current values. It can be observed that the predictors only depend on time  $t_n$ , such that they are fixed to a constant value during

the NEWTON-RAPHSON iteration of each time step. Thus, the incremental nodal accelerations can be expressed as

$$\Delta \ddot{\mathbf{d}} = \frac{1}{\beta \Delta t^2} \Delta \mathbf{d}. \quad (4.35)$$

Applying this to the discretized linearized weak form (4.26), results in

$$\Delta G^e = \delta \mathbf{d}^{eT} \left[ \int_{\mathcal{B}^e} \mathbf{B}^{eT} \mathbb{A} \mathbf{B}^e dV + \frac{1}{\beta \Delta t^2} \int_{\mathcal{B}^e} \mathbf{N}^{eT} \rho_0 \mathbf{N}^e dV \right] \Delta \mathbf{d}^e. \quad (4.36)$$

## 4.5 Gauss Integration

To compute the derived terms in (4.25) and (4.36), the integrals need to be calculated. There are several numerical integration methods, e.g the SIMPSON's method or MONTE CARLO integration. For simple elements analytical integration can be applied. The derivation of a linear 1D truss element is given in Appendix A as example. In the FEM, the standard method is the GAUSS integration, as combined with the known shape functions and the parametric concept it results in a very efficient, accurate and easily implementable algorithm. Using the isoparametric concept to transform an integral, here exemplified for a 2D function  $g(\mathbf{X})$ , to the parameter space with (4.14)<sub>1</sub>, results in

$$\int_{\mathcal{B}^e} g(\mathbf{X}) dA = \int_{\mathcal{B}_\square} g(\boldsymbol{\xi}) \det[\mathbf{J}(\boldsymbol{\xi})] dA_\square = \int_{-1}^{+1} \int_{-1}^{+1} g(\xi, \eta) \det[\mathbf{J}(\xi, \eta)] d\xi d\eta. \quad (4.37)$$

Now applying the GAUSS integration, the integral can be approximated as a weighted sum of evaluated characteristic points of the function  $g$  in the domain

$$\int_{-1}^{+1} \int_{-1}^{+1} g(\boldsymbol{\xi}) \det[\mathbf{J}(\boldsymbol{\xi})] d\xi d\eta \approx \sum_{p=1}^{n_p} g(\xi_p, \eta_p) \det[\mathbf{J}(\xi_p, \eta_p)] w_p, \quad (4.38)$$

where  $n_p$  are the number of evaluated points,  $w_p$  the weight factors and  $\xi_p$  and  $\eta_p$  the coordinates of the respective GAUSS points. Table 4.1 presents the coordinates and

$n_p$	$p$	$\xi_p$	$w_p$	
1	1	0.0	2	
2	1	$-1/\sqrt{3}$	1	
	2	$+1/\sqrt{3}$	1	
3	1	$-\sqrt{3/5}$	5/9	
	2	0.0	8/9	
	3	$+\sqrt{3/5}$	5/9	

**Table 4.1:** GAUSS integration for one dimension.

weight factors up to  $n_p = 3$  for one-dimensional GAUSS integration. The strength of the GAUSS integration is that a one-dimensional polynomial of the order  $P$  can be exactly determined using  $n_p \geq \frac{P+1}{2}$  points. Higher-dimensional formulas, coordinates and weight factors for cuboids can be generated from this as a product of every coordinate direction.

## 4.6 Global FEM Formulation

This chapter started with the strong form and applied the variational principle to create the weak form of linear momentum. Then, this was used to derive a discretized and linearized weak form at the element level. To finalize this chapter on general FEM, first the commonly used elemental fields are defined and presented in easily implementable formulations, before this chapter is concluded by formulating the global FEM problem.

From the derived formulation of  $G^e$  (4.25), the elemental vector of internal forces  $\mathbf{r}^e$  is defined as the sum of its static and dynamic terms,  $\mathbf{r}^e = \mathbf{r}^{e,\text{stat}} + \mathbf{r}^{e,\text{dyn}}$ , with

$$\mathbf{r}^{e,\text{stat}} = \int_{\mathcal{B}^e} \mathbf{B}^{e\text{T}} \mathbf{P} \, dV \approx \sum_{p=1}^{n_p} \mathbf{B}_p^{\text{T}} \mathbf{P}_p \det[\mathbf{J}_p] w_p \quad \text{and} \quad (4.39)$$

$$\mathbf{r}^{e,\text{dyn}} = - \int_{\mathcal{B}^e} \mathbf{N}^{e\text{T}} \mathbf{f} \, dV \approx - \sum_{p=1}^{n_p} \mathbf{N}_p^{\text{T}} \mathbf{f}_p \det[\mathbf{J}_p] w_p. \quad (4.40)$$

In the same way, the linearized element stiffness matrix is defined as  $\mathbf{k}^e = \mathbf{k}^{e,\text{stat}} + \frac{1}{\beta \Delta t^2} \mathbf{k}^{e,\text{dyn}}$ ,

$$\mathbf{k}^{e,\text{stat}} = \int_{\mathcal{B}^e} \mathbf{B}^{e\text{T}} \mathbb{A} \mathbf{B}^e \, dV \approx \sum_{p=1}^{n_p} \mathbf{B}_p^{\text{T}} \mathbb{A}_p \mathbf{B}_p \det[\mathbf{J}_p] w_p \quad \text{and} \quad (4.41)$$

$$\mathbf{k}^{e,\text{dyn}} = \int_{\mathcal{B}^e} \mathbf{N}^{e\text{T}} \rho_0 \mathbf{N}^e \, dV \approx \sum_{p=1}^{n_p} \mathbf{N}_p^{\text{T}} \rho_0 \mathbf{N}_p \det[\mathbf{J}_p] w_p, \quad (4.42)$$

based on (4.36). Using these abbreviations, (4.24) is formulated as

$$\text{Lin}G^e = \delta \mathbf{d}^{e\text{T}} [\mathbf{k}^e \Delta \mathbf{d}^e + \mathbf{r}^e]. \quad (4.43)$$

As equilibrium is defined only for the global problem (4.6), it is necessary to define respective global measures

$$\mathbf{K} = \mathbf{A} \bigg|_{e=1}^{n_{\text{el}}} \mathbf{k}^e, \quad \mathbf{R} = \mathbf{A} \bigg|_{e=1}^{n_{\text{el}}} \mathbf{r}^e, \quad \mathbf{D} = \bigcup_{e=1}^{n_{\text{el}}} \mathbf{d}^e, \quad \delta \mathbf{D} = \bigcup_{e=1}^{n_{\text{el}}} \delta \mathbf{d}^e \quad \text{and} \quad \Delta \mathbf{D} = \bigcup_{e=1}^{n_{\text{el}}} \Delta \mathbf{d}^e, \quad (4.44)$$

where  $\mathbf{A}$  is the assembly operator and  $\bigcup$  a unification operator, as the nodal displacements shared by different elements are not added, but belong to the same degree of freedom. Now the expression (4.43) can be posed in global fields as

$$\text{Lin}G = \delta \mathbf{D}^{\text{T}} [\mathbf{K} \Delta \mathbf{D} + \mathbf{R}] = 0 \quad \Rightarrow \quad \mathbf{K} \Delta \mathbf{D} = -\mathbf{R}. \quad (4.45)$$

This finally is the standard FEM formulation, where the problem is iteratively solved for the displacement update  $\Delta \mathbf{D}$  until the norm  $|\Delta \mathbf{D}|$  or the norm of the residual  $|\mathbf{R}|$  is less than a specified threshold.

# 5 Material Modeling

The field of material modeling is vast and complex. This chapter gives a brief overview of the material models applied and derived in the work at hand. It starts by giving the general equation for an elastic, large strain material model. Then, modifications as stretch-rate sensitivity and damage are derived and respective numerical parameter studies presented. All numerical examples in this chapter are performed on a quasi 1D system of two truss elements in series, loaded with a constant displacement rate, unless otherwise specified. The stress is determined using the reaction force on the displacement boundary divided by the area. The strain is computed as the displacement divided by the system's reference length. The ultimately derived 1D material formulation is later used in the modeling of an effective fiber pullout, as regarded in Chapter 10.

## 5.1 Hyperelastic Material Law

The Neo-HOOKEan constitutive law yields a simple expression to model hyperelastic material behavior at large strains. It is sufficient to model and simulate materials in various engineering problems. For the case of a geometrically linear formulation, the Neo-HOOKE material model reduces to the classical law of linear elasticity. The formulation presented in this section is limited to isotropic materials, possessing the same properties in all spatial directions. In addition it allows for volume changes, resulting in a compressible material law. The strain energy density function is given as

$$\psi = \frac{\lambda}{2} \ln[J]^2 - \mu \ln[J] + \frac{\mu}{2} \text{tr}[\mathbf{C} - \mathbf{1}], \quad (5.1)$$

with the LAMÉ constants  $\lambda$  and  $\mu$ . The two LAMÉ constants are related to YOUNG's modulus and POISSON's ratio by

$$\lambda = \frac{\nu E}{(1 + \nu)(1 - 2\nu)} \quad \text{and} \quad \mu = \frac{E}{2(1 + \nu)}. \quad (5.2)$$

For more details see e.g. the book by BONET and WOOD [15]. The first derivative of the strain energy density function with respect to the deformation gradient yields the first PIOLA-KIRCHHOFF stress tensor

$$\mathbf{P} = \frac{\partial \psi}{\partial \mathbf{F}} = (\lambda \ln[J] - \mu) \mathbf{F}^{-T} + \mu \mathbf{F}. \quad (5.3)$$

Since the following material models are only used in combination with a truss element, the material law can be simplified to only one dimension. A uniaxial deformation state in  $x$ -direction and  $\nu = 0$  are assumed. From this follows  $J = F_{11}$ ,  $\lambda = 0$  and  $\mu = \frac{E}{2}$ , which simplifies the energy density function (5.1) to

$$\psi = \frac{1}{4} E (F_{11}^2 - 1 - 2 \ln[F_{11}]). \quad (5.4)$$

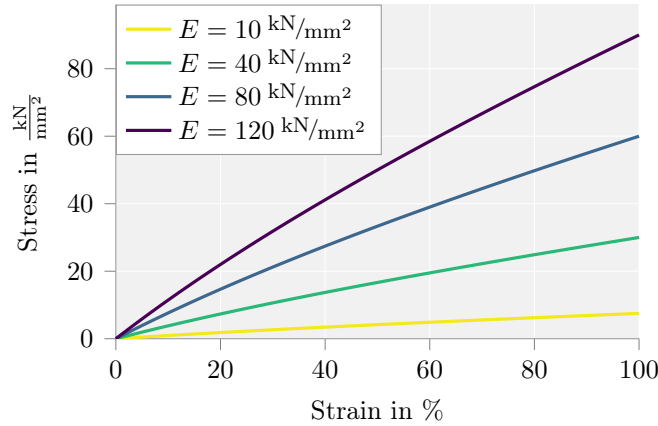


**Figure 5.1:** Parameter study of a 1D Neo-HOOKE material, presenting the variation of the YOUNG's modulus  $E$ .

In the same way, the expression for the first PIOLA-KIRCHHOFF stress tensor is reduced to

$$P_{11} = \frac{\partial \psi}{\partial F_{11}} = \frac{1}{2} E \left( F_{11} - \frac{1}{F_{11}} \right). \quad (5.5)$$

The respective consistent tangent modulus follows as

$$\mathbb{A}_{1111} = \frac{1}{2} E \left( 1 + \frac{1}{F_{11}^2} \right). \quad (5.6)$$

Hereafter all extended material formulations refer to this 1D material model. Indices are thus dropped without loss of accuracy, as all quantities of deformation, stress or tangent moduli relate to the local  $x$ -direction.

### 5.1.1 Parameter Study – Young's Modulus $E$

This simple 1D hyperelastic material model has a single parameter, the YOUNG's Modulus  $E$ . Figure 5.1 displays the influence of the parameter in a stress-strain diagram for up to 100 % strain. The geometrical nonlinearity of the finite strain formulation as well as the increase in stress with increasing stiffness is visible.

## 5.2 Stress as a Function of Stretch Rate

Under different loading rates, materials can exhibit distinct effective behavior. For high dynamic loading scenarios such as impact or explosion, inertia has a significant influence on the overall behavior. However, even at rates where inertia can be assumed to be negligible, a significant change in material behavior can be observed, as for example presented in the single-fiber tension test presented in Chapter 10. To capture this effect, a material formulation with a stress function depending on the rate of the deformation gradient is suggested. The previously introduced stress function (5.5) is extended by a multiplication with a dynamic increase factor. Now the stress  $P^*$  is not only a function of the deformation gradient  $\mathbf{F}$  but also of its rate  $\dot{\mathbf{F}}$ ,

$$P^*(F, \dot{F}) = P(F) \left( 1 + \Omega(\dot{F}) \right). \quad (5.7)$$

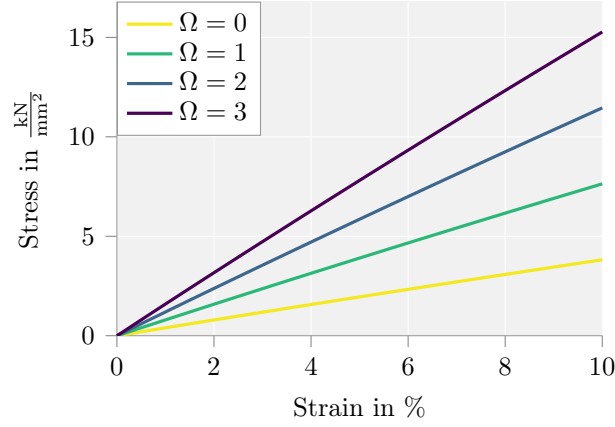


**Figure 5.2:** Parameter study of a 1D Neo-HOOKE material with stretch-rate sensitivity of the stress.  $E = 40 \text{ kN/mm}^2$ ,  $\dot{F} = 1 \text{ s}^{-1}$  are held constant, while the function  $\Omega$  (5.9) is modified.

The function  $\Omega(\dot{F})$  is a measure of the dynamic increase factor. To differentiate this formulation from the rate-independent Neo-HOOKE model within this chapter, the variables are denoted with an asterisk  $\bullet^*$ . The stretch rate is calculated as the average of the current and last time step, where the current value is determined by the forward difference method. This results in the formulation of the stretch rate as,

$$\dot{F}_{n+1} = \frac{F_{n+1} - F_n}{2\Delta t} + \frac{\dot{F}_n}{2}. \quad (5.8)$$

The average has been considered to slightly delay the response and thereby dynamically stabilize the model. Preliminary numerical test calculations have shown an improved robustness over the classical forward difference approach. For the implementation, two history fields containing  $F_n$  and  $\dot{F}_n$  are required. It should be noted that initial conditions have to be considered, when a constant rate is to be simulated.

### 5.2.1 Dynamic Increase Function

Experiments have shown that the dynamic increases in stress can often be well approximated by logarithmic functions, c.f. CUROSU [24]. The function  $\Omega$  has been chosen as a piecewise function. One part is a logarithmic function of the deformation gradient rate, the other part is constant. It has the property to only take values of zero and above,

$$\Omega = \begin{cases} \alpha^I \ln \left[ \frac{\dot{F}}{\alpha^{II}} \right] & \dot{F} \geq \alpha^{II} \\ 0 & \dot{F} < \alpha^{II} \end{cases}, \quad (5.9)$$

where the two parameters  $\alpha^I$  and  $\alpha^{II}$  respectively determine the slope and zero value of the logarithmic function. The goal is an increase in stress for high deformation rates.

## 5.2.2 Tangent Modulus

The tangent modulus is defined as the derivative of the first PIOLA-KIRCHHOFF stress (5.7) with respect to the deformation gradient,

$$\mathbb{A}^* = \frac{\partial P^*}{\partial F} = \mathbb{A}(1 + \Omega) + P \frac{\partial \Omega}{\partial F}. \quad (5.10)$$

To determine the derivative of the dynamic increase factor  $\Omega$  with respect to the deformation gradient, the chain rule is applied,  $\frac{\partial \Omega}{\partial F} = \frac{\partial \Omega}{\partial \dot{F}} \frac{\partial \dot{F}}{\partial F}$  with  $\frac{\partial \Omega}{\partial \dot{F}} = \frac{\alpha^I}{F}$  and  $\frac{\partial \dot{F}}{\partial F} = \frac{1}{2\Delta t}$ ,

$$\frac{\partial \Omega}{\partial F} = \begin{cases} \frac{\alpha^I}{2\Delta t F} & \Omega > 0 \\ 0 & \Omega = 0 \end{cases}. \quad (5.11)$$

## 5.2.3 Parameter Study – Dynamic Increase Factor $\Omega$

The influence of the dynamic increase factor  $\Omega$  together with its parameters  $\alpha^I$  and  $\alpha^{II}$  are analyzed for a constant stretch rate. To understand  $\Omega$  (5.9), one should first have a look at the influence of the two parameters on the function itself. The function has one characteristic point, given by  $\alpha^{II} > 0$ . It determines below which stretch rate value the logarithmic part of the function becomes negative.  $\alpha^I$  defines the slope of the function. To visualize the influence of the dynamic increase function on the simulation, a constant stretch rate of  $\dot{F} = 1 \text{ s}^{-1}$  is chosen, and  $\Omega$  changed by varying  $\alpha^{II}$ . Figure 5.2 visualizes the overall increase due to the stretch-rate sensitivity for a constant stretch rate up to 10% strain. The rate sensitivity of the stress can also be interpreted as an increase in effective stiffness, c.f. Figure 5.1.

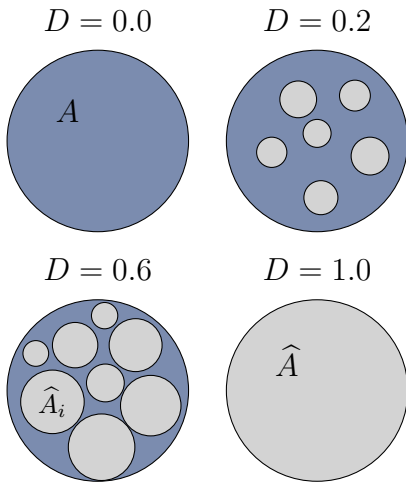


**Figure 5.3:** Visual representation of the damage parameter  $D$ , calculated as  $D = \hat{A}/A$ .

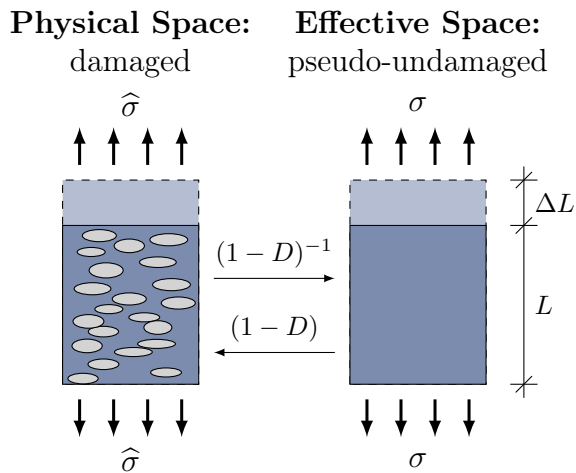


**Figure 5.4:** Strain equivalence principle.

## 5.3 Discontinuous Damage

As the governing mechanism for an effective fiber pullout model, a damage formulation has been chosen. In general, damage is an effect arising at small scales, be it the irreversible breaking of atomic bonds, the formation of microcracks or the plastic enlargement of microcavities. The presented damage approach regards damage as a homogenized quantity represented as a local material property. This section gives a brief derivation of isotropic discontinuous damage, for the 1D Neo-HOOKE material law presented in Section 5.1. To accentuate the variables related to damaged quantities, they are denoted with a hat  $\hat{\bullet}$ , within this chapter. Some general introductions to damage modeling are given in GROSS and SEELIG [37], LEMAITRE and CHABOCHE [54], LEMAITRE [57], and SOUZA NETO et al. [98]. More detailed applications are found in BALZANI and ORTIZ [4], BALZANI, HOLZAPFEL, and BRINKHUES [5], and LEMAITRE and DESMORAT [55], among others.

### 5.3.1 Damage Approach

Damage can be interpreted as a deterioration of the material stiffness, where the damage value determines the amount of stress which can be transmitted by the weakened material. Due to the generally assumed isotropy as well as the specifically used 1D formulation, damage is thus given as a scalar value  $0 \leq D \leq 1$ . This assumption is motivated by the idea that an undamaged cross section  $A$ , deteriorates successively by increasing the damaged area  $\hat{A} = \sum \hat{A}_i$  as illustrated in Figure 5.3. The damage value is then given by  $D = \hat{A}/A$ . This is called the effective stress concept, introduced by KACHANOV [48] and applied to finite strains in MIEHE [71] and SIMO [95]. This in turn is based on the strain equivalence principle by LEMAITRE [56]. It states that the strain of the damaged material under the applied stress  $\hat{\sigma}$  equals the strain of the undamaged material under the effective stress  $\sigma$ , visualized in Figure 5.4. As shown, the two states are linked by the reduction factor  $(1 - D)$ . Applying this to the Neo-HOOKE material

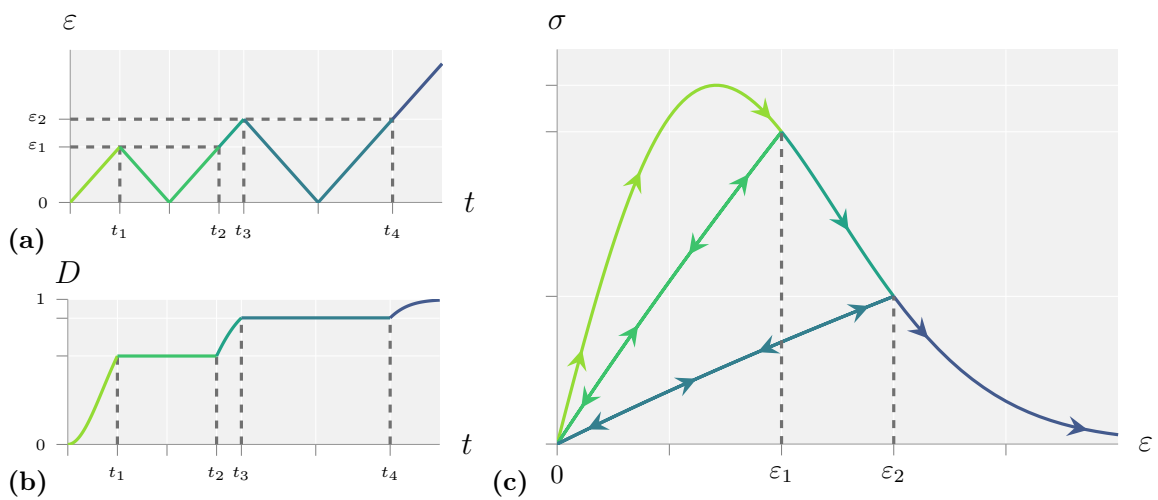


**Figure 5.5:** Qualitative example of the discontinuous damage approach, showing respectively (a) the applied strain  $\varepsilon$  over time  $t$ , (b) the evolution of the damage value  $D$  and (c) the resulting stress-strain diagram.

provides the expression for the damaged stress  $\widehat{P}$  with

$$\widehat{P} = P(1 - D). \quad (5.12)$$

The effective stress concept only describes the reduction of the stiffness by a damage factor. However, it does not include information about how the damage evolves with respect to the applied loading. This is given by an a priori chosen damage function.

### 5.3.2 Exponential Damage Function

In this work, an exponential damage function has been chosen

$$D = D_\infty \left( 1 - \exp \left( - \left( \frac{\psi_D}{D_{\text{rate}}} \right)^{D_{\text{shape}}} \right) \right), \quad (5.13)$$

where  $D_\infty \in [0, 1]$  is the maximum reachable damage, usually set close to 1. The second parameter  $D_{\text{rate}} > 0$  influences the velocity of the damage evolution. Smaller values of  $D_{\text{rate}}$  result in a faster damage process. The third parameter  $D_{\text{shape}}$  enables the modification of the shape of the function. Values below 1 will increase the damage rate at the beginning, while decreasing it for larger deformations. The variable  $\psi_D$  is an internal variable, representing the effective energy considered for damage. It is defined as the maximum value of  $\psi_0$  (c.f. (5.4)) that has been reached up to the current time. Thus, the damage evolves only when  $\psi_0 > \psi_D$ , then the variables are updated as  $\psi_D = \psi_0$ . This results in the discontinuous damage approach. Due to the chosen evolution criterion, damage can only increase over time, which makes it thermodynamically consistent. Figure 5.5 illustrates the discontinuous damage approach, by presenting an arbitrarily chosen loading history in Figure 5.5a, the respective damage evolution in Figure 5.5b and the resulting stress-strain plot in Figure 5.5c.

### 5.3.3 Tangent Modulus

To enable the iterative solving algorithm, the tangent modulus must be derived. It is defined as

$$\widehat{\mathbb{A}} = \frac{\partial \widehat{P}}{\partial F} = \frac{\partial P(1 - D)}{\partial F} = \mathbb{A}(1 - D) - P \frac{\partial D}{\partial F}. \quad (5.14)$$

Here the sensitivity of the damage with respect to the strain is required. First the chain rule is applied  $\frac{\partial D}{\partial F} = \frac{\partial D}{\partial \psi_D} \frac{\partial \psi_D}{\partial F}$  and the derivative of the damage with respect to the effective damage energy formulated

$$\frac{\partial D}{\partial \psi_D} = \frac{D_\infty D_{\text{shape}}}{D_{\text{rate}}} \exp \left( - \left( \frac{\psi_D}{D_{\text{rate}}} \right)^{D_{\text{shape}}} \right) \left( \frac{\psi_D}{D_{\text{rate}}} \right)^{D_{\text{shape}}-1}. \quad (5.15)$$

Then the derivative of the damage function with respect to the deformation gradient can be expressed as a conditional function,

$$\frac{\partial D}{\partial F} = \begin{cases} P \frac{\partial D}{\partial \psi_D} & \frac{\partial \psi_D}{\partial F} > 0 \\ 0 & \frac{\partial \psi_D}{\partial F} = 0 \end{cases}, \quad (5.16)$$

considering that for evolving damage  $\frac{\partial \psi_D}{\partial F} = \frac{\partial \psi_0}{\partial F} = P$ , while otherwise  $\frac{\partial \psi_D}{\partial F} = 0$ .

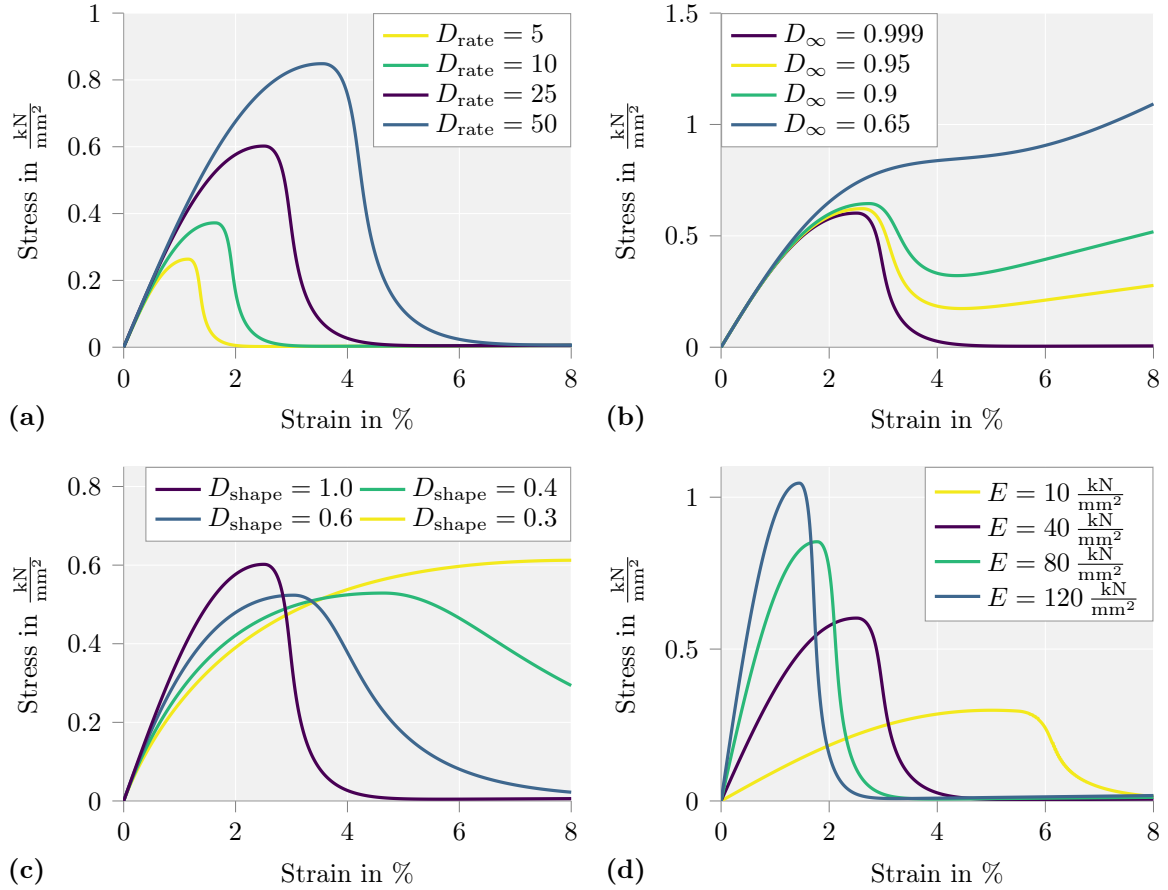


**Figure 5.6:** Parameter study of a 1D Neo-HOOKE material with damage formulation. Parameters used (purple line):  $E = 40 \frac{\text{kN}}{\text{mm}^2}$ ,  $D_{\text{rate}} = 25$ ,  $D_{\infty} = 0.999$ ,  $D_{\text{shape}} = 1$ . Each diagram shows the effect of varying a single parameter: (a)  $D_{\text{rate}}$ , (b)  $D_{\infty}$ , (c)  $D_{\text{shape}}$  and (d)  $E$ .

### 5.3.4 Parameter Study – $D_{\infty}$ , $D_{\text{rate}}$ , $D_{\text{shape}}$ , $E$

The damage evolution is controlled by three parameters  $D_{\infty}$ ,  $D_{\text{rate}}$  and  $D_{\text{shape}}$ .  $D_{\infty}$  sets the maximum damage value which can be reached by the damage function. For most applications, a total damage of  $D = 1$  can lead to numerical instabilities. A value of e.g.  $D_{\infty} = 0.999$  can be set to reduce the stress at maximum damage to 0.1%. The parameter  $D_{\text{rate}}$  governs the rate of damage. The larger the value, the slower the damage evolution. The third parameter  $D_{\text{shape}}$  modifies the overall shape of the function. Values below 1 will increase the damage rate at the beginning, while decreasing it for larger deformations. These effects of the damage parameters on the stress-strain curve as well as the influence of the stiffness  $E$  are depicted in Figure 5.6. The resulting plots in Figure 5.6a clearly demonstrate that a slower damage evolution yields a peak at a higher stress and strain level. Whereas the value of maximum damage controls mainly the post-peak behavior, as shown in Figure 5.6b. The shape parameter can greatly influence the overall damage behavior as presented in Figure 5.6c, allowing for a less rapid softening phase. Figure 5.6d shows a significant influence of stiffness values on the damage response.

## 5.4 Damage Formulation Combined with a Rate Sensitivity of Stress

Finally the two concepts of rate sensitivity and damage are combined in a single formulation. The stress is then calculated by

$$\widehat{P}^* = P(1 + \Omega)(1 - D). \quad (5.17)$$

From this follows the tangent modulus as

$$\widehat{\mathbb{A}}^* = \mathbb{A}(1 + \Omega)(1 - D) + P(1 - D)\frac{\partial \Omega}{\partial F} - P(1 + \Omega)\frac{\partial D}{\partial F}, \quad (5.18)$$

where the relevant quantities are defined in the previous sections in (5.5), (5.6), (5.9), (5.11), (5.13) and (5.16). This final model now includes discontinuous damage and an increase in stress at high stretch rates.

### 5.4.1 Varying Strain Rates

In Chapter 10 this model is used to match fiber pullout experiments under different strain rates. To visualize the effects of the damage value  $D$  in combination with the dynamic increase value  $\Omega$ , a small numerical study is conducted, comparing the stress-strain response for four different loading scenarios. The particular calculations are mainly defined by their displacement functions given as

$$\begin{aligned} 1 : & \quad \Omega = 0 \\ 2 : & \quad u_2(t) = \frac{u_{\max}}{t_{\max}} t \\ 3 : & \quad u_3(t) = \frac{u_{\max}}{t_{\max}^3} t^3 \\ 4 : & \quad u_4(t) = -6 \frac{u_{\max}}{t_{\max}^3} \left( \frac{1}{3} t^3 - \frac{1}{2} t^2 t_{\max} \right) \end{aligned} \quad (5.19)$$

where the functions' parameters are chosen such that  $u_i(t_{\max}) = u_{\max}$ . This way, by applying the same maximum displacement  $u_{\max}$ , one can compare equivalent deformation ranges. The value  $t_{\max}$  is then used to adjust the respective stretch rates. In scenario one, the shape of the loading function is not relevant, as this represents the simulation without stretch-rate effects. The functions (5.19) do not necessarily represent realistic loading conditions. Instead, they were chosen to highlight the combined effects of the strain rate sensitivity and the damage evolution. The resulting stress-strain answers are presented in Figure 5.7a with the respective stretch rate over strain diagram plotted in 5.7b. Two main effects can be noticed. First, consistent with the selected dynamic increase function (5.9), the graphs in 5.7a only deviate from simulation 1, for stretch rate values above the chosen threshold of  $\alpha^{\text{II}}$ . Second, the intersections of graphs in the stretch rate vs. strain diagram are retrieved in the stress-strain plot, as they represent a point with the same dynamic increase. To summarize, the proposed model parameters are listed in Table 5.1, providing an overview of the meaning and the permitted values.

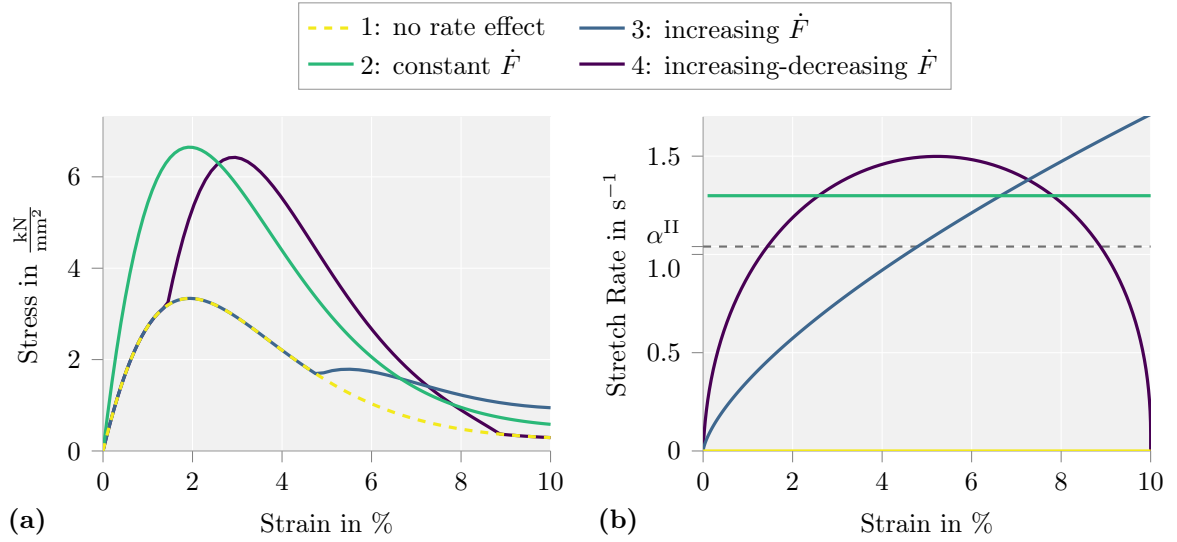


**Figure 5.7:** Combined damage and stretch-rate dependent material model for various loading conditions: (a) stress-strain response and (b) respective stretch rates. Loading functions given in (5.19), with  $u_{\max}/L = 0.1$ , 2:  $t_{\max} = 0.077$  s, 3:  $t_{\max} = 0.17$  s and 4:  $t_{\max} = 0.1$  s. All simulation are run with  $E = 40 \text{ kN/mm}^2$ ,  $D_{\infty} = 0.995$ ,  $D_{\text{rate}} = 100$ ,  $D_{\text{shape}} = 0.6$ ,  $\alpha^{\text{I}} = 4.48$  and  $\alpha^{\text{II}} = 1.04$ .

Parameter	Defines	Admissible Values
$E$	YOUNG'S modulus	$E > 0$
$\alpha^{\text{I}}$	slope of DIF-function	$\alpha^{\text{I}} \in \mathbb{R}$
$\alpha^{\text{II}}$	zero value of DIF-function	$\alpha^{\text{II}} > 0$
$D_{\infty}$	maximum damage value	$0 \leq D < 1$
$D_{\text{rate}}$	damage rate	$D_{\text{rate}} > 0$
$D_{\text{shape}}$	shape of $D$ -function	$D_{\text{shape}} \in \mathbb{R}$

**Table 5.1:** Overview of the parameters used in the material model.



## 6 Homogenization

The idea of homogenization methods is to reduce the complexity of a material's underlying microstructure and replace it with an effective material law by assuming a homogeneous body, c.f. Figure 6.1. This general concept is as old as material testing itself. When characteristic material properties as e.g. the YOUNG's modulus or the tensile strength are measured experimentally, the measured data is always the effective property of the specimen. Any engineering material, when observed at a sufficiently small scale, will present a distinctive microstructure. However, it is neither possible nor practical to consider every detail when the length scale of the microstructure is far below the scale of the technological application. For many materials it is possible to formulate a sufficiently accurate phenomenological model to describe the effective material behavior. Once the microstructure increases in complexity or the accuracy of the prediction is particularly significant, it becomes more difficult to find a function that properly describes the homogenized response for all relevant situations. This holds true especially for composite materials. Generally, a widely used solution consists of sophisticated homogenization methods that directly include more microstructural information. There are two major categories of homogenization methods, analytical and numerical homogenization. Analytical homogenization uses the information of the microstructure to develop a closed form solution for the effective material law. This is however only possible for rough approximations as e.g. small strains and linear elasticity or special cases of perfect periodicity and symmetry. The other option is to explicitly solve a boundary value problem and continuously compute effective macroscopic quantities. A recent overview of computational homogenization methods in general is given in GEERS et al. [33]. This work focuses on a first-order numerical homogenization procedure using the finite element method at both scales. Furthermore, the following convention will be used throughout this work. When dealing with multiscale problems, quantities related to the macroscale are indicated by a bar  $\bar{\bullet}$ , unless the association is unambiguous. This chapter provides the general ideas on which numerical homogenization is based. The following chapter then presents in detail the derivation of the proposed homogenization framework including microscale inertia.

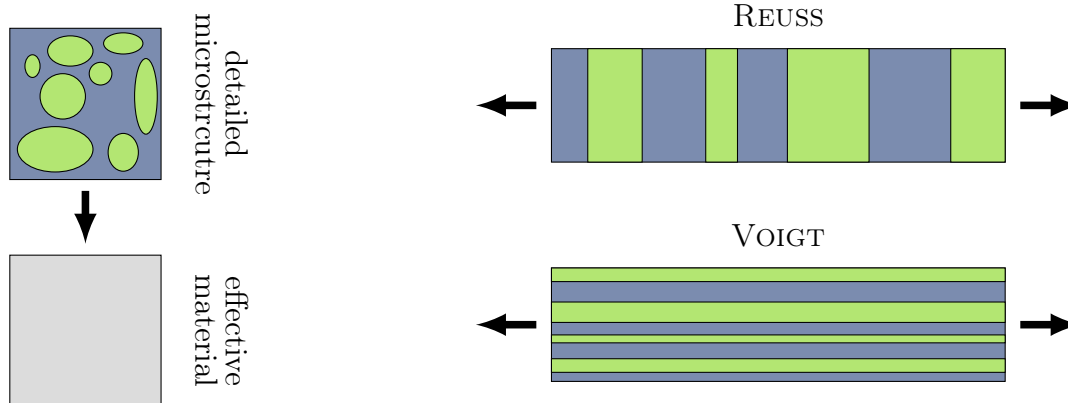


**Figure 6.1:** General idea of homogenization.

**Figure 6.2:** Physical representation of the VOIGT and REUSS bounds.

## 6.1 Analytical Homogenization

First steps in semi-analytical homogenization have been taken by VOIGT [112] and REUSS [87]. They both proposed simple approximations for linear elastic materials based on averaging theorems to obtain effective macroscopic values. VOIGT assumed the strain field within the microstructure to be uniform. This is obviously incorrect for most cases, as it does not allow the structure to find a state of equilibrium. However, following this assumption results in the formulation of the effective material tensor  $\bar{\mathbf{C}}$  as the volume average of the material tensor in each point of the microstructure

$$\bar{\mathbf{C}}_V = \langle \mathbf{C} \rangle. \quad (6.1)$$

In this work, the volume average of a microscale quantity  $\frac{1}{V} \int_{\mathcal{B}} \bullet dV$  is abbreviated by angle brackets  $\langle \bullet \rangle$ . In contrast to VOIGT's assumption, REUSS assumed the stress field of the microstructure to be uniform. Again, this does not represent an especially realistic scenario but leads to the formulation of the macroscopic material tensor as

$$\bar{\mathbf{C}}_R = \langle \mathbf{C}^{-1} \rangle^{-1}. \quad (6.2)$$

HILL [43] has proven that the results by VOIGT and REUSS are upper and lower bounds for the real effective material tensor for any linear elastic microstructure

$$\langle \mathbf{C}^{-1} \rangle^{-1} < \bar{\mathbf{C}} \leq \langle \mathbf{C} \rangle. \quad (6.3)$$

This inequality of tensorial values compares the respective eigenvalues. The physical interpretation of the VOIGT and REUSS bounds are visualized in Figure 6.2, as the REUSS bound gives the exact result for different material phases connected in series and the VOIGT bound for different phases connected in parallel to the loading direction. Unfortunately these bounds do not give a particularly narrow solution space especially for high contrast constituents. Thus improved bounds have been proposed by e.g. HASHIN and SHTRIKMAN [38, 39, 40]. Other approximations are e.g. the self-consistent scheme established by ESHELBY [30], or the mean-field approximation proposed by MORI and TANAKA [77, 109]. A quick overview of the different effective quantities for various volume fractions is given by LÖHNERT [65].

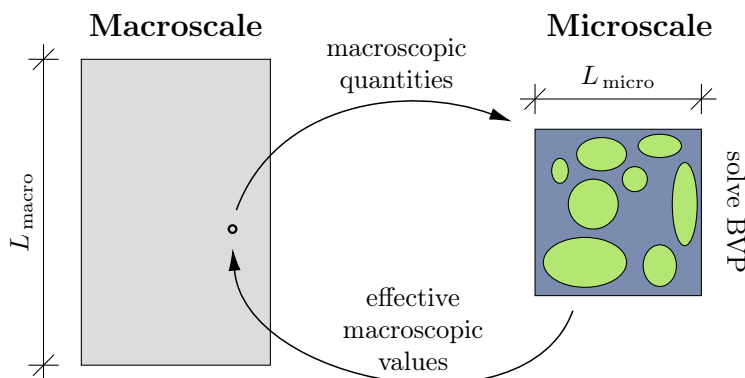


**Figure 6.3:** Schematic of the general  $\text{FE}^2$  method.

## 6.2 Computational Homogenization

The limitations of analytical approximation methods can generally be overcome by the application of computational homogenization. By now computational homogenization is a well-established field, with a wide range of methods and applications. A wide range of nonlinear phenomena can be incorporated by the application of large displacement settings at both scales. Here, the focus is on the  $FE^2$  method, that uses the finite element approach, presented in Chapter 4, on both scales. Its strength is the straightforward application of standard FE material models at the microscale, using the same FEM algorithms as applied in single-scale calculations and a relatively easy implementation at the macroscale. As visualized in the schematic in Figure 6.3, the  $FE^2$  method bilaterally links the two scales. Within this direct micro-macro homogenization each macroscopic integration point is represented by a microscale boundary value problem (BVP). The relevant macroscopic quantities are used as boundary conditions for the respective microscale computation. After solving the microscale problem, effective macroscopic values are computed based in the RVE results. When compared to a similar macroscale computation using a phenomenological material law, this approach certainly increases the computational cost notably. However, compared to a single-scale calculation, using the same fineness of microstructure discretization as is used at the RVE level, costs can be greatly reduced. In addition,  $FE^2$  lends itself perfectly to parallel computing. The parallelization of the  $FE^2$  simulation is trivial at the macroscopic element or GAUSS point loop, as the different microscale computations do not need to communicate with each other. A recapitulation of the  $FE^2$  method is presented in SCHRÖDER [92].

## 6.3 Representative Volume Element

Any multiscale method can only be as accurate as the chosen microscale discretization. The concept of a representative volume element has been introduced, although so far not further specified. The aim is to define a volume in such a way that it holds all relevant microstructural information of the full structure. For perfectly periodic materials in quasi-static calculations, the choice of RVE is evident. Deviations from this for dynamic multiscale computations are discussed later. By choosing the volume in such a way that multiple instances can recreate the whole microstructure, all relevant microstructural information is considered. This can then be called a unit cell, which is defined as the simplest repeating unit of the structure. In crystal structures where single discrete atoms are considered, there are a finite number of unit cells. Whereas in continuum models, there are infinite possibilities for choosing a unit cell. Combined with periodic boundary conditions they will all result in the same effective macroscale

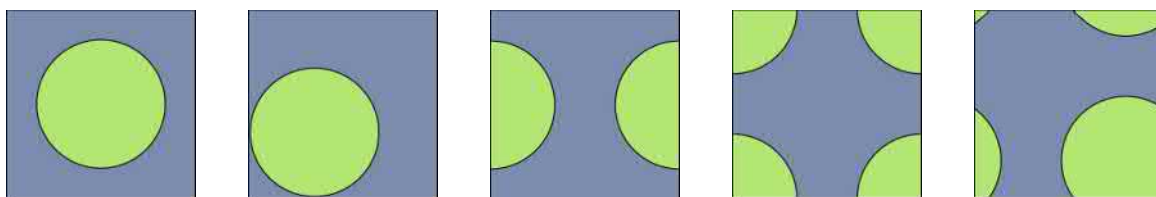


**Figure 6.4:** Some examples of possible unit cells for a periodic microstructure.

response. Example unit cells for a periodic microstructure with round inclusions are depicted in Figure 6.4. For non-periodic composite materials the choice of an adequate RVE is a lot more complex. An excellent overview of possible RVE definitions is found in GITMAN, ASKES, and SLUYS [34]. All definitions have in common that the RVE needs to include enough information to adequately approximate the macro response but still be sufficiently small compared to the macroscopic structural dimensions. A balance between the RVE's accuracy and the computational efficiency needs to be found. One solution to this problem is to use a simpler microstructure, but apply statistical analysis to ensure that the sample's geometry statistically matches that of the target microstructure. These are then called statistically similar RVEs (SSRVEs), which are further explained in BALZANI et al. [3], BALZANI et al. [6], SASAGAWA et al. [91], and SCHRÖDER et al. [93]. The shape of the RVE can be chosen at will. The most commonly chosen shape is a cube. For most periodic media it is the obvious choice to represent a possible unit cell. In addition, even for non-periodic microstructures the cube offers significant advantages in meshing and application of boundary conditions. However, other shapes might warrant consideration. As an example, the advantage of a spherical RVE is that the sphere has about 20% less surface area to volume ratio compared to a cube with an equivalent volume. This is of advantage, as it will reduce errors resulting from the influence of boundary conditions. In GLÜGE et al. [36] the difference between cubical and spherical RVEs are discussed in detail. It is shown that for non-periodic materials, spherical RVEs converge faster to a solution, reducing the number of required elements.

## 6.4 Separation of Scale

The fundamental assumption that the FE<sup>2</sup> method is based on, is a clear separation of the two scales. Generally speaking, this means that the relevant macroscopic dimensions must be significantly larger than the length of the microstructure,

$$L_{\text{macro}} \gg L_{\text{micro}}. \quad (6.4)$$

More specifically, the fluctuations of the macroscopic fields need to be larger than the size of the microscale problem, otherwise the projection of the macroscopic values onto the RVEs is not consistent.

Macroscopic displacement jumps such as cracks violate this principle. The proper incorporation of localization mechanisms at the microscale is not straightforward and needs special consideration, c.f. BOSCO et al. [16], KARAMNEJAD and SLUYS [50], and SONG and BELYTSCHKO [97], among others. Even simulations with large continuous macroscopic dimensions can violate the separation of scales, for example when high frequency loading is applied with a wavelength approaching the size of the microscale. When running simulations, it is essential to always keep in mind the assumptions that the framework is based on.

## 6.5 Large Strain Kinematics at Different Scales

All concepts introduced in Chapter 3 certainly apply to the large strain multiscale setting as well. The kinematic scale link utilized in this work applies the macroscopic

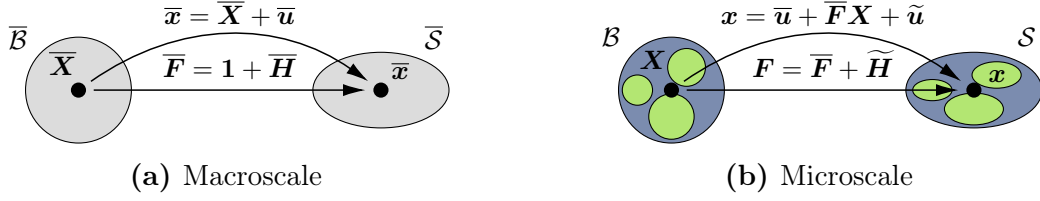


**Figure 6.5:** Large strain continuum mechanics on both scales.

displacement and macroscopic deformation gradient homogeneously onto the RVE. To facilitate the formulation, the origin of the microscopic coordinates is chosen to coincide with the geometrical center of the RVE, with

$$\int_{\mathcal{B}} \mathbf{X} \, dV = \mathbf{0}. \quad (6.5)$$

This choice of origin has no influence on the results. Now the microscopic deformation  $\mathbf{x}$  can be split into the sum of terms,

$$\mathbf{x} = \bar{\mathbf{u}} + \bar{\mathbf{F}}\mathbf{X} + \tilde{\mathbf{u}}. \quad (6.6)$$

Herein, two terms result directly from the macroscale: a constant part  $\bar{\mathbf{u}}$ , which describes the macroscopic rigid body translations, and a homogeneous part  $\bar{\mathbf{F}}\mathbf{X}$ , defined in terms of the macroscopic deformation gradient. The difference of these homogeneous deformations  $\bar{\mathbf{u}} + \bar{\mathbf{F}}\mathbf{X}$  to the actual deformations  $\mathbf{x}$  is the microscopic displacement fluctuation field  $\tilde{\mathbf{u}}$ . This is the field for which the microscopic BVP is solved. Now the microscopic displacements  $\mathbf{u}$  can be written as

$$\mathbf{u} = \bar{\mathbf{u}} + \bar{\mathbf{H}}\mathbf{X} + \tilde{\mathbf{u}}. \quad (6.7)$$

Analogously, the microscopic deformation gradient can be split as

$$\mathbf{F} = \bar{\mathbf{F}} + \tilde{\mathbf{H}} \quad \text{with} \quad \tilde{\mathbf{H}} = \partial_{\mathbf{X}}\tilde{\mathbf{u}}. \quad (6.8)$$

At the macroscale the kinematics are standard, see Figure 6.5, where the kinematic relations for both microscale and macroscale are summarized.

## 6.6 Kinematic Links to the Macroscale

As presented in equation (6.6), the microscale deformation is directly defined by the macroscopic displacements and the deformation gradient. However, defining  $\mathbf{x}$  based on the macroscale is only the first step. If no additional constraint is considered, the BVP will find an equilibrium where the microscopic fluctuations  $\tilde{\mathbf{u}}$  oppose the applied displacements, which results in zero effective displacement of the microstructure. This might not seem obvious at first. However, without any imposed constraint, the energetically most favorable position of each node will be its initial configuration, as any deviation from it requires energy, provided the structure is initially at rest. Thus resulting in a microscopic displacement fluctuation field of  $\tilde{\mathbf{u}} = -\bar{\mathbf{u}} - \bar{\mathbf{H}}\mathbf{X}$ , c.f. (6.7).

### 6.6.1 Deformation Gradient Constraint

The first constraint is well-established in first-order RVE homogenization frameworks. It postulates that the volume average of the microscopic deformation gradients must equal the macroscopic deformation gradient

$$\overline{\mathbf{F}} = \langle \mathbf{F} \rangle. \quad (6.9)$$

This choice is motivated by classical continuum mechanics, where the deformation gradient is considered to be uniformly distributed over an infinitesimal volume element. Applying this assumption on a homogenized microscale, the deformation is then given by  $\mathbf{x} = \overline{\mathbf{F}}\mathbf{X}$ . With no cavities or displacement jumps, the following gradient theorem holds true

$$\int_{\partial\mathcal{B}} \mathbf{X} \otimes \mathbf{N} \, dA = \int_{\mathcal{B}} \text{Grad}\mathbf{X} \, dV = \mathbf{1}V. \quad (6.10)$$

This can be used to define the macroscopic deformation gradient in terms of the microscale as

$$\overline{\mathbf{F}} = \overline{\mathbf{F}} \mathbf{1} \frac{V}{V} = \frac{\overline{\mathbf{F}}}{V} \int_{\mathcal{B}} \text{Grad}\mathbf{X} \, dV = \frac{1}{V} \int_{\partial\mathcal{B}} (\overline{\mathbf{F}}\mathbf{X}) \otimes \mathbf{N} \, dA = \frac{1}{V} \int_{\partial\mathcal{B}} \mathbf{x} \otimes \mathbf{N} \, dA. \quad (6.11)$$

Applying once more the gradient theorem, the equality of the constraint (6.9) is proven for the assumption of a homogeneous microscale

$$\overline{\mathbf{F}} = \frac{1}{V} \int_{\partial\mathcal{B}} \mathbf{x} \otimes \mathbf{N} \, dA = \frac{1}{V} \int_{\mathcal{B}} \text{Grad}\mathbf{x} \, dV = \frac{1}{V} \int_{\mathcal{B}} \mathbf{F} \, dV. \quad (6.12)$$

As shown in (6.11), the constraint can be defined in terms of the surface displacements. It enables the possibility to fulfill the constraint by simply choosing suitable boundary conditions. The trivial choice are linear displacement boundary conditions. These are imposed by setting the boundary fluctuations to zero

$$\tilde{\mathbf{u}}(\mathbf{X}) = \mathbf{0}, \quad \forall \mathbf{X} \in \partial\mathcal{B}. \quad (6.13)$$

Although easily implemented, this is a very restrictive constraint, generally resulting in a stiffer material response and with that in an overestimation of the composite stiffness. The most commonly used boundary conditions for RVEs are the periodic boundary conditions (PBC). PBCs produce especially good results for periodic microstructures, as they are able to capture the periodicity of displacements and stress. However, even for non-periodic structures periodic boundary conditions are able to produce satisfying and quickly converging results, c.f. PERIĆ et al. [85], SLUIS et al. [96], and TERADA et al. [110]. As depicted in Figure 6.6 for PBC, the boundary  $\partial\mathcal{B}$  is divided into two opposing surfaces,  $A^+$  and  $A^-$ , where  $A_i^+$  and  $A_i^-$  are pairs of parallel surfaces of equal size on opposite sides of the volume. The union of all  $A_i$  pairs recovers the total surface  $\partial\mathcal{B}$ . The displacement for each node at the boundary is directly coupled to a node on the opposite side of the volume as

$$\tilde{\mathbf{u}}(\mathbf{X}^+) = \tilde{\mathbf{u}}(\mathbf{X}^-), \quad \forall \mathbf{X}^+ \in A_i^+ \quad \text{and matching} \quad \mathbf{X}^- \in A_i^-. \quad (6.14)$$

This sets special requirements for the microscale mesh and geometry. For a straight-

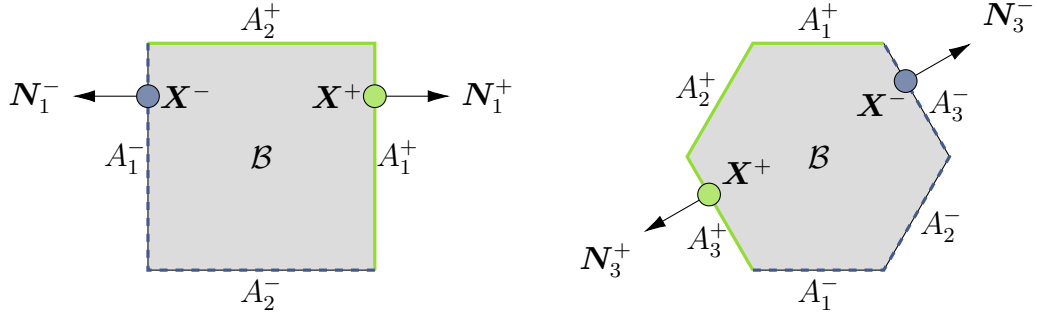


**Figure 6.6:** Visualization of periodic boundary conditions on differently shaped RVEs, based on VAZ JÚNIOR, SOUZA NETO, and MUÑOZ-ROJAS [111].

forward implementation, the nodes of the opposing faces need to coincide. This demands extra effort when creating unstructured meshes, as the boundary periodicity needs to be explicitly created. One apparent drawback of PBC is the simulation of microscopic defects, such as crack initialization or shear bands. Due to the a priori chosen periodicity of the boundary, localizations are forced into artificial paths. More advanced boundary conditions can be applied to compensate these disadvantages. For example NGUYEN et al. [81] present a method to apply PBC for non-periodic meshes. In BOSCO et al. [16] and COENEN et al. [20] the periodicity is modified to align itself with forming localizations to model these with as little boundary influence as possible. In this thesis, standard periodic boundary conditions are applied to the RVE to enforce the deformation gradient constraint.

### 6.6.2 Displacement Constraint

When dealing with a two-scale homogenization framework that considers the full balance of linear momentum on both scales, not only the macroscopic deformation gradient but also the macroscopic displacements are directly applied to the microstructure, c.f. (6.6). The deformation gradient constraint is not sufficient to fixate the rigid body motion of the microscale solution. Thus, a suitable scale link needs to be chosen for the macroscopic displacements as well. For instance, in quasi-static calculations, fluctuations of a node in the corner of the RVE are restricted, without influencing the results. This is however not possible for the dynamic case without artificially restricting the fluctuations. Homogenization schemes that incorporate inertia terms consistently at the microscale are new in comparison to quasi-static homogenization. There is still not a consensus in the community on the optimal choice of displacement constraints, as discussed in the following.

**Volume Integral Displacement Constraint** For this proposed dynamic homogenization framework, the macroscopic displacements are chosen as the volume average of the microscopic displacements

$$\bar{\mathbf{u}} = \langle \mathbf{u} \rangle, \quad (6.15)$$

following the work of BLANCO et al. [14], ROCA et al. [88], and SOUZA NETO et al. [99]. This constraint is required in addition to the deformation gradient constraint (6.9). Fulfilling the one will not automatically fulfill the other. In contrast to (6.9), (6.15) can not be reformulated in terms of the boundary displacements only. Hence, this

is called the volume integral displacement constraint or in short, the volume constraint (VC). By using the displacement split (6.7) and the definition of the origin of the local coordinate system (6.5), the volume constraint (6.15) can be reformulated to

$$\langle \tilde{\mathbf{u}} \rangle = \mathbf{0}. \quad (6.16)$$

It states that the constraint is fulfilled, once the volume average of the microscale fluctuations equal zero. Detailed information on the implementation follows in the next chapter.

**Surface Displacement Constraint** Another possible choice found in the literature is the application of the macroscale displacement only on the boundary of the RVE. The simple case is to apply DIRICHLET boundary conditions, c.f. (6.13). A more advanced option is to apply the macroscopic displacements as the surface average on the RVE as

$$\bar{\mathbf{u}} = \frac{1}{A} \int_{\partial\mathcal{B}} \mathbf{u} \, dA, \quad \text{or equivalently} \quad \frac{1}{A} \int_{\partial\mathcal{B}} \tilde{\mathbf{u}} \, dA = \mathbf{0}, \quad (6.17)$$

where  $A$  is the total surface area. Different examples can be found in LIU and REINA [62], PHAM et al. [86], and SRIDHAR et al. [102]. These particular examples all model resonant microstructures. Initial analysis of the applicability of the chosen volume integral displacement constraint for simple examples are presented in Chapters 8 and 9. There, the chosen volume constraint is compared to an approximation of the surface constraint (6.17) by setting the fluctuations of the corner nodes to zero. In this work it is thus called the fixed corner displacement constraint (FC).

## 6.7 Averaging Expressions

So far the kinematic macro-to-micro link was discussed. For a fully coupled FE<sup>2</sup> framework, it is necessary to obtain consistent averaging formulations to compute the effective macroscopic fields. The upscaling of the microscale behavior is classically achieved according to the principle of macro-homogeneity by HILL [44] and MANDEL [68], thus also famously known as the HILL-MANDEL principle. It states that the energy of the microscale has to be equivalent to the effective energy for the homogenized material. This ensures that no energy is lost or created when going from one scale to the other. To consistently extend quasi-static homogenization frameworks to the dynamic regime, an extended version of the HILL-MANDEL condition of macro homogeneity is adopted, presented in detail in BLANCO, SÁNCHEZ, SOUZA NETO, and FEIJÓO [14]. It is called the principle of multiscale virtual power, here formulated in terms of the the first PIOLA-KIRCHHOFF stress tensor  $\mathbf{P}$ , and the deformation gradient  $\mathbf{F}$ ,

$$\bar{\mathbf{P}} : \delta \bar{\mathbf{F}} - \bar{\mathbf{f}} \cdot \delta \bar{\mathbf{u}} = \langle \mathbf{P} : \delta \mathbf{F} - \mathbf{f} \cdot \delta \mathbf{u} \rangle, \quad (6.18)$$

where  $\mathbf{f}$  is the microscale body force vector and  $\bar{\mathbf{f}}$  the macroscale counterpart. The principle of multiscale virtual power specifies that the macroscopic virtual power needs to coincide with the volume average of the microscopic virtual power, while taking into account inertia and body forces at both scales. This can now be utilized to derive the homogenization expression for the effective stress and body forces. It is

shown in [61] that the extended HILL-MANDEL averaging relation can be applied in a discretized setting without introducing additional errors by scale transition. By expressing the microscale fields of  $\delta\mathbf{F}$  and  $\delta\mathbf{u}$  in terms of their macroscopic quantities and the respective microscale fluctuations by using (6.7) and (6.8), (6.18) can be reformulated as

$$\overline{\mathbf{P}} : \delta\overline{\mathbf{F}} - \overline{\mathbf{f}} \cdot \delta\overline{\mathbf{u}} = \langle \mathbf{P} : (\delta\overline{\mathbf{F}} + \text{Grad}[\delta\tilde{\mathbf{u}}]) - \mathbf{f} \cdot (\delta\overline{\mathbf{u}} + \delta\overline{\mathbf{F}}\mathbf{X} + \delta\tilde{\mathbf{u}}) \rangle. \quad (6.19)$$

Keep in mind that the variation of the deformation and displacement gradient are equal  $\delta\mathbf{F} = \delta\mathbf{H}$ . This formulation of the principle of multiscale virtual power can be used to derive all necessary averaging equations.

**Microscale Equilibrium** The macroscale test functions  $\delta\overline{\mathbf{F}}$  and  $\delta\overline{\mathbf{u}}$  are set to zero. The resulting expression is the microscale equilibrium equation

$$0 = \langle \mathbf{P} : \text{Grad}[\delta\tilde{\mathbf{u}}] - \mathbf{f} \cdot \delta\tilde{\mathbf{u}} \rangle, \quad (6.20)$$

which is nothing but the previously derived weak form (4.4) in terms of the microscale values. This makes sense, as  $\delta\overline{\mathbf{F}} = \mathbf{0}$  and  $\delta\overline{\mathbf{u}} = \mathbf{0}$  represent constant macroscopic values, i.e. a single macroscopic step in the NEWTON-RAPHSON iteration for which the microscopic equilibrium needs to be solved.

**Homogenized Stress** To obtain the expression of the macroscopic stress, the microscale virtual displacements  $\delta\mathbf{u}$  are set to zero along with the macroscopic virtual displacements  $\delta\overline{\mathbf{u}}$ . The stress averaging equation obtained from (6.19) is

$$\overline{\mathbf{P}} = \langle \mathbf{P} - \mathbf{f} \otimes \mathbf{X} \rangle. \quad (6.21)$$

By assuming zero body forces  $\mathbf{f}$ , the well-known quasi-static stress averaging equation is recovered

$$\overline{\mathbf{P}} = \langle \mathbf{P} \rangle. \quad (6.22)$$

**Homogenized Body Forces** Analogous to the stress, the averaging formulation of the microscopic body forces is obtained, by setting the microscale virtual displacements  $\delta\mathbf{u}$  as well as the macroscopic virtual deformation gradient  $\delta\overline{\mathbf{F}}$  to zero. The homogenization expression of the body forces is given by

$$\overline{\mathbf{f}} = \langle \mathbf{f} \rangle. \quad (6.23)$$

The body forces can be split into inertia forces  $\mathbf{f}^\rho$  and body forces related to e.g. gravitation  $\mathbf{f}^b$ , as  $\mathbf{f} = \mathbf{f}^b - \mathbf{f}^\rho$ . This obviously allows the averaging equation (6.23) to be formulated separately for the homogenized body forces

$$\overline{\mathbf{f}}^b = \langle \mathbf{f}^b \rangle \quad (6.24)$$

and the homogenized inertia forces

$$\overline{\mathbf{f}}^\rho = \langle \mathbf{f}^\rho \rangle = \langle \ddot{\mathbf{u}}\rho_0 \rangle. \quad (6.25)$$



# 7 Dynamic Homogenization Framework

This chapter is the heart of the thesis. Here, the general concept of computational homogenization is extended consistently to the dynamic regime on both scales. Key concepts are shortly presented and main points from the last chapter recapitulated. It follows the detailed derivation of the multiscale framework including inertia at the microscale. The derivation includes possible constraints for the microscale boundary value problem, using LAGRANGE multipliers to directly link the two scales kinematically. In addition, a closed form formulation of the consistent macroscopic tangent moduli is presented. This enables a numerically efficient computation. The derivation of the framework has previously been published in TAMSEN and BALZANI [106].

## 7.1 General Concepts

The basic idea of the homogenization framework for dynamics is to consider the full balance of linear momentum including the inertia terms at the microscale. This enables not only the analysis of full dynamic fields at the microscale but also a direct study of microscopic inertia effects on the macroscale. An FE<sup>2</sup> type of homogenization method is applied. However the extension to the dynamic regime requires additional considerations. By using appropriate averaging relations and kinematic links, a consistent scale bridging for dynamic loading is established. In order to properly differentiate the two scales, variables associated with the macroscale are further denoted with a bar  $\bar{\bullet}$ . A highlight of the framework is the considered finite strain setting, which enables the analysis of a wide range of material behavior and micromechanical effects under dynamic loading. A schematic illustration of the method is presented in Figure 7.1,

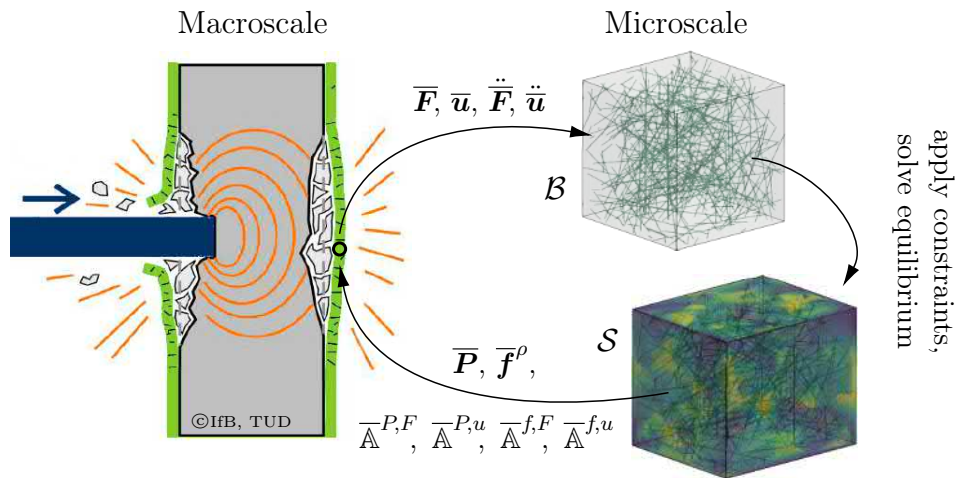


**Figure 7.1:** Overview of the FE<sup>2</sup> framework including microscale dynamics. Here, an example of macroscopic impact on SHCC is illustrated, based on TAMSEN and BALZANI [106].

using SHCC as an example. Note the quantities that are being transferred between the scales, required as a result of the microscale dynamic problem. The respective definitions are found in the following sections of this chapter.

### 7.1.1 Microscale Constraints and Homogenization Operators

To kinematically link the two scales within the full dynamic framework, both the macroscopic deformation gradient, the macroscopic displacements as well as their second time derivatives are projected onto the RVE. As discussed in Section 6.6, the microscopic kinematic quantities are chosen to be on average equivalent to the macroscale, resulting in the following two constraints applied on the microscopic volume

$$\overline{\mathbf{F}} = \frac{1}{V} \int_{\mathcal{B}} \mathbf{F} \, dV = \langle \mathbf{F} \rangle \quad \text{and} \quad (7.1)$$

$$\overline{\mathbf{u}} = \frac{1}{V} \int_{\mathcal{B}} \mathbf{u} \, dV = \langle \mathbf{u} \rangle. \quad (7.2)$$

Without having an effect on the results, the origin of the microscopic coordinates is chosen as the geometrical center of the RVE, with

$$\int_{\mathcal{B}} \mathbf{X} \, dV = \mathbf{0}. \quad (7.3)$$

This simplifies the expressions and enables the microscopic displacements  $\mathbf{u}$  to be written as a split in microscopic and macroscopic quantities, as

$$\mathbf{u} = \overline{\mathbf{u}} + \overline{\mathbf{H}} \mathbf{X} + \tilde{\mathbf{u}}. \quad (7.4)$$

This displacement split will be frequently used when deriving the macroscopic tangent moduli.

Based on the extended HILL-MANDEL principle of macro-homogeneity (6.18), two averaging relations have been derived in Section 6.7. There, macroscopic stress  $\overline{\mathbf{P}}$  and macroscopic body forces  $\overline{\mathbf{f}}$  are expressed in terms of the microscopic fields, as

$$\overline{\mathbf{P}} = \langle \mathbf{P} - \mathbf{f} \otimes \mathbf{X} \rangle \quad \text{and} \quad (7.5)$$

$$\overline{\mathbf{f}} = \langle \mathbf{f} \rangle. \quad (7.6)$$

This ensures that the virtual work of the macroscale coincides with its respective microscopic volume average, thus energetic consistency is achieved across the scales.

### 7.1.2 Time Integration

The examples of dynamic simulations in the following chapters all use the NEWMARK method to numerically approximate the time integration problem, as presented in Section 4.4. It allows the current acceleration of a node  $\ddot{\mathbf{d}}$  to be approximated by

$$\ddot{\mathbf{d}} = \frac{1}{\beta \Delta t^2} (\mathbf{d} - \hat{\mathbf{d}}), \quad (7.7)$$

c.f. (4.32) and (4.33), where the predictor  $\hat{\mathbf{d}}$  only depends on quantities of the last time step. Herein  $\beta$  is one of the two NEWMARK parameters influencing the type and

stability of the time integration. During the following derivation, the fact is used that the derivative of the NEWMARK formulation for  $\ddot{\mathbf{d}}$  (7.7) with respect to a quantity of the current time step can be reduced to

$$\frac{\partial \ddot{\mathbf{d}}}{\partial \bullet} = \frac{1}{\beta \Delta t^2} \frac{\partial (\mathbf{d} - \widehat{\mathbf{d}})}{\partial \bullet} = \frac{1}{\beta \Delta t^2} \frac{\partial \mathbf{d}}{\partial \bullet}. \quad (7.8)$$

The same can be applied for any quantity in a continuum formulation approximated in terms of the nodal displacements as e.g.  $\ddot{\mathbf{u}}$  or  $\ddot{\mathbf{F}}$ . This concept is applied for the dynamic quantities of both the microscale and macroscale, which is indicated by the use of the NEWMARK parameter  $\beta$  or  $\bar{\beta}$ , respectively. The numerical examples are all run with NEWMARK parameters of  $\gamma = 0.5$  and  $\beta = 0.25$  at both scales, resulting in an unconditionally stable algorithm. However it is possible to use parameters for each scale.

## 7.2 The Microscopic Problem

The derivation of the dynamic multiscale formulation starts at the microscale. In addition to the microscopic fields, the algorithmic treatment of the associated constraint conditions is given. This enables the consistent inclusion of the necessary kinematic links (7.1) and (7.2) to the macroscale into the framework.

### 7.2.1 Microscopic Balance of Linear Momentum

For a dynamic analysis, the microscopic balance of linear momentum is given by

$$\text{Div } \mathbf{P} + \mathbf{f} = \mathbf{0}, \quad (7.9)$$

c.f. (4.1). The body force vector  $\mathbf{f}$  can be decomposed into an inertia part  $\mathbf{f}^\rho$  and a body force vector representing e.g. the gravitational pull  $\mathbf{f}^b$ . As this framework is intended to model impact loading, gravitational forces are assumed to be negligible compared to the inertia forces in the computations. Thus, the relevant body force vector is defined as  $\mathbf{f} := \mathbf{f}^\rho = -\rho_0 \ddot{\mathbf{u}}$  with  $\rho_0$  referring to the density of the microscale constituents in the reference configuration. If gravitational forces have to be considered, they can be included in the standard way by the additional force vector  $\mathbf{f}^b = \rho_0 \mathbf{g}$ , where  $\mathbf{g}$  is the acceleration due to Earth's gravitational field. Since this force however does not depend on the displacements, it does not represent any specialty with view to the proposed homogenization framework and is thus omitted to avoid unnecessary complications.

Using standard FE procedures for the discretization and linearization of the weak form of the balance of linear momentum, the well-known equation

$$\delta \tilde{\mathbf{D}}^T \mathbf{K} \Delta \tilde{\mathbf{D}} = -\delta \tilde{\mathbf{D}}^T \mathbf{R} \quad (7.10)$$

is obtained, c.f. Chapter 4. Herein  $\mathbf{K}$  and  $\mathbf{R}$  are the global microscopic tangent stiffness matrix and the residuum vector, including terms associated to inertia. After incorporating DIRICHLET boundary conditions as for example kinematically linked nodes, the global vector of incremental nodal displacements  $\Delta \tilde{\mathbf{D}}$  is computed from

$\mathbf{K}\Delta\tilde{\mathbf{D}} = -\mathbf{R}$  for each NEWTON iteration step. Once convergence is achieved when the norm of the updates reaches a specified tolerance  $|\Delta\tilde{\mathbf{D}}| < tol$ , an equilibrium is assumed. Following the classical scheme, the global tangent stiffness matrix  $\mathbf{K}$  is assembled from the element matrix defined in Section 4.6 as

$$\mathbf{k}^e = \mathbf{k}^{e,\text{stat}} + \frac{1}{\beta\Delta t^2}\mathbf{k}^{e,\text{dyn}}, \quad \text{with} \quad (7.11)$$

$$\mathbf{k}^{e,\text{stat}} = \int_{\mathcal{B}^e} \mathbf{B}^{e\text{T}}\mathbb{A}\mathbf{B}^e dV \quad \text{and} \quad \mathbf{k}^{e,\text{dyn}} = \mathbf{m}^e = \int_{\mathcal{B}^e} \mathbf{N}^{e\text{T}}\rho_0\mathbf{N}^e dV. \quad (7.12)$$

Herein,  $\mathbf{N}^e$  is the classical element matrix of shape functions (4.22),  $\mathbf{B}^e$  denotes the classical B-matrix containing the derivatives of the shape functions (4.21), and  $\mathbb{A}$  is the matrix representation of the material tangent modulus, defined as the sensitivity of the microscopic stress with respect to the microscopic deformation gradient as  $\mathbb{A} = \partial_{\mathbf{F}}\mathbf{P}$ , from (4.10). Analogously, the global residuum vector  $\mathbf{R}$  is obtained by the assembly of the element-wise counterparts, given as

$$\mathbf{r}^e = \int_{\mathcal{B}^e} (\mathbf{B}^{e\text{T}}\mathbf{P} + \mathbf{N}^{e\text{T}}\rho_0\ddot{\mathbf{u}}) dV, \quad (7.13)$$

previously derived in (4.39) and (4.40). Herein,  $\mathbf{P}$  denotes the vector representation of the first PIOLA-KIRCHHOFF stresses. It can be noted that both,  $\mathbf{k}^e$  and  $\mathbf{r}^e$  have dynamic terms related to the density  $\rho_0$ , which directly enables the evaluation of inertia at the microscale.

## 7.2.2 Kinematic Links to the Macroscale

As depicted in Figure 7.1, the macroscopic displacements and deformation gradient and their time derivatives are used to define boundary conditions on the RVE. Inserting them into (7.4) is only the first step. As discussed in Section 6.6, if no additional constraint is considered, the BVP will find an equilibrium where the fluctuations  $\tilde{\mathbf{u}}$  oppose the applied displacements which results in zero effective displacement of the microstructure. Based on the work of BLANCO et al. [14], the two chosen kinematic links  $\bar{\mathbf{F}} = \langle \mathbf{F} \rangle$  and  $\bar{\mathbf{u}} = \langle \mathbf{u} \rangle$  are considered for this framework. The first constraint is generally known from quasi-static RVE homogenization frameworks. This is usually enforced by choosing appropriate boundary conditions, e.g., linear displacement or periodic boundary conditions. The second constraint is a necessary expansion for the dynamic microscopic problem. This link to the macroscopic displacements is essential in order to prevent the RVE from moving arbitrarily in space. In quasi-static calculations, fluctuations e.g. of a corner node in the RVE are restricted, which does not influence the results. The framework proposed here does not make any a priori assumptions about which part of the microstructure will be dynamically significant, as this cannot always be determined in advance for arbitrary problems. As shown in Section 6.6 the volume integral displacement constraint can be reduced to

$$\langle \tilde{\mathbf{u}} \rangle = \mathbf{0}, \quad (7.14)$$

which states that the constraint is fulfilled, once the volume average of the fluctuations equals zero. Some initial analysis on the effect of the constraint on the macroscale response, as well as on the overall numerical stability are presented in the following chapters.

### 7.2.3 Algorithmic Treatment of Kinematic Constraints

To enforce the volume displacement constraint in (7.14) on the whole RVE domain, it is proposed to use the method of LAGRANGE multipliers, c.f. e.g. BERTSEKAS [12]. Similar applications can be found in BLANCO et al. [13] and ROCA et al. [88]. To apply the constraint, the mechanical boundary value problem is recast in terms of the principle of minimum potential energy. By adding the potential  $\Pi^\lambda$  associated with the LAGRANGE multipliers  $\boldsymbol{\lambda}$  and the constraint (7.14) to the function of potential energy  $\Pi$ , one obtains

$$\Pi = \Pi^{\text{int}} + \Pi^{\text{ext}} + \Pi^\lambda, \quad \text{with} \quad \Pi^\lambda = \boldsymbol{\lambda} \cdot \int_{\mathcal{B}} \tilde{\mathbf{u}} \, dV. \quad (7.15)$$

In the following derivation, only the terms concerning the LAGRANGE multiplier will be regarded, as the other terms capturing the internal potential energy  $\Pi^{\text{int}}$  and the external potential energy  $\Pi^{\text{ext}}$  will result in the standard FE formulation (7.10) given above and derived in Section 4.6. However, note that due to the LAGRANGE term, the additional degrees of freedom  $\boldsymbol{\lambda}$  now appear in the global system of equations.

**Variation** The potential energy is varied once with respect to the displacement fluctuations  $\tilde{\mathbf{u}}$  and once with respect to the LAGRANGE multipliers  $\boldsymbol{\lambda}$ , i.e.

$$\delta_{\tilde{\mathbf{u}}} \Pi^\lambda = \boldsymbol{\lambda} \cdot \int_{\mathcal{B}} \delta \tilde{\mathbf{u}} \, dV \quad \text{and} \quad (7.16)$$

$$\delta_{\boldsymbol{\lambda}} \Pi^\lambda = \delta \boldsymbol{\lambda} \cdot \int_{\mathcal{B}} \tilde{\mathbf{u}} \, dV. \quad (7.17)$$

**Discretization** Using the shape function matrix (4.22) as the FE approximation of the fluctuation fields  $\tilde{\mathbf{u}} \approx \mathbf{N}^e \tilde{\mathbf{d}}^e$  and  $\delta \tilde{\mathbf{u}} \approx \mathbf{N}^e \delta \tilde{\mathbf{d}}^e$ , the discretized expressions can be written as

$$\delta_{\tilde{\mathbf{u}}} \Pi^\lambda = \boldsymbol{\lambda}^T \mathbf{A} \left[ \int_{\mathcal{B}^e} \mathbf{N}^e \, dV \delta \tilde{\mathbf{d}}^e \right] \quad \text{and} \quad (7.18)$$

$$\delta_{\boldsymbol{\lambda}} \Pi^\lambda = \delta \boldsymbol{\lambda}^T \mathbf{A} \left[ \int_{\mathcal{B}^e} \mathbf{N}^e \, dV \tilde{\mathbf{d}}^e \right], \quad (7.19)$$

where  $n_{\text{el}}$  is the total number of elements. To obtain the equivalent of the global volume integral in terms of the elements, the assembly operator  $\mathbf{A}$  is applied for the respective matrices. For better readability, a new element matrix is defined as

$$\mathbf{g}^{eT} = \int_{\mathcal{B}^e} \mathbf{N}^e \, dV. \quad (7.20)$$

This simplifies the formulations to

$$\delta_{\tilde{\mathbf{u}}} \Pi^\lambda = \boldsymbol{\lambda}^T \mathbf{A} \left[ \mathbf{g}^{eT} \delta \tilde{\mathbf{d}}^e \right] \quad \text{and} \quad (7.21)$$

$$\delta_{\boldsymbol{\lambda}} \Pi^\lambda = \delta \boldsymbol{\lambda}^T \mathbf{A} \left[ \mathbf{g}^{eT} \tilde{\mathbf{d}}^e \right]. \quad (7.22)$$

**Global Matrix Notation** To write the whole system of equations as a global problem, the global matrices are defined in terms of the element matrices, i.e.

$$\mathbf{G} = \mathbf{A} \mathbf{g}^e, \quad \tilde{\mathbf{D}} = \bigcup_{e=1}^{n_{el}} \tilde{\mathbf{d}}^e \quad \text{and} \quad \delta \tilde{\mathbf{D}} = \bigcup_{e=1}^{n_{el}} \delta \tilde{\mathbf{d}}^e, \quad (7.23)$$

where  $\mathbf{A}$  is the afore-mentioned assembly operator and  $\bigcup$  the unification operator, as the nodal displacement fluctuations shared by different elements are not added, as they belong to the same degree of freedom. Now the expressions (7.21) and (7.22) can be reformulated in global fields as

$$\delta_{\tilde{\mathbf{u}}} \Pi^\lambda = \boldsymbol{\lambda}^T \mathbf{G}^T \delta \tilde{\mathbf{D}} = \delta \tilde{\mathbf{D}}^T \mathbf{G} \boldsymbol{\lambda} \quad \text{and} \quad (7.24)$$

$$\delta_{\boldsymbol{\lambda}} \Pi^\lambda = \delta \boldsymbol{\lambda}^T \mathbf{G}^T \tilde{\mathbf{D}} = \mathbf{0}. \quad (7.25)$$

Since the LAGRANGE multiplier only appears in  $\Pi^\lambda$ , no terms result from the variation of  $\Pi^{\text{int}}$  and  $\Pi^{\text{ext}}$  with respect to  $\boldsymbol{\lambda}$ . It follows that the second expression has to vanish, see (7.25).

**Linearization** In order to solve the nonlinear global system of equations, the NEWTON-RAPHSON method is utilized. For that purpose, not only are the equations needed in weak form as in (7.24) and (7.25) but also their linearizations are required. They are used to iteratively compute the nodal displacement fluctuations as well as the LAGRANGE multipliers. Here the definition (4.8) of the  $\Delta$ -operator is used, stating that the linearization of a function  $f(x) = 0$  at  $\hat{x}$  can be expressed as  $\text{Lin} f = f|_{\hat{x}} + \Delta f|_{\hat{x}}$ , with  $\Delta f = \frac{\partial f}{\partial x}|_{\hat{x}} \Delta x$ . Applying this to the weak forms results in

$$\text{Lin} \delta_{\tilde{\mathbf{u}}} \Pi^\lambda = \delta \tilde{\mathbf{D}}^T \mathbf{G} \boldsymbol{\lambda} + \delta \tilde{\mathbf{D}}^T \mathbf{G} \Delta \boldsymbol{\lambda} \quad \text{and} \quad (7.26)$$

$$\text{Lin} \delta_{\boldsymbol{\lambda}} \Pi^\lambda = \delta \boldsymbol{\lambda}^T \mathbf{G}^T \tilde{\mathbf{D}} + \delta \boldsymbol{\lambda}^T \mathbf{G}^T \Delta \tilde{\mathbf{D}} = \mathbf{0}. \quad (7.27)$$

## 7.2.4 Global Discretized Microscopic Problem Including Constraint

From the linearized variations of  $\Pi^\lambda$  the global residua are defined

$$\mathbf{R}^{\tilde{\mathbf{u}}} = -\mathbf{G} \boldsymbol{\lambda} = \mathbf{A} \mathbf{r}^{\tilde{\mathbf{u}}^e} \quad \text{with} \quad \mathbf{r}^{\tilde{\mathbf{u}}^e} = -\mathbf{g}^e \boldsymbol{\lambda} \quad \text{and} \quad (7.28)$$

$$\mathbf{R}^\lambda = -\mathbf{G}^T \tilde{\mathbf{D}} = \sum_{e=1}^{n_{el}} \mathbf{r}^{\lambda^e} \quad \text{with} \quad \mathbf{r}^{\lambda^e} = -\mathbf{g}^{eT} \tilde{\mathbf{d}}^e. \quad (7.29)$$

Including all linearized variations of  $\Pi^{\text{int}} + \Pi^{\text{ext}} + \Pi^\lambda$  yields the discrete equation

$$\left[ \delta \tilde{\mathbf{D}}^T \mid \delta \boldsymbol{\lambda}^T \right] \left[ \begin{array}{c|c} \mathbf{K} & \mathbf{G} \\ \mathbf{G}^T & \mathbf{0} \end{array} \right] \left[ \begin{array}{c} \Delta \tilde{\mathbf{D}} \\ \Delta \boldsymbol{\lambda} \end{array} \right] = \left[ \delta \tilde{\mathbf{D}}^T \mid \delta \boldsymbol{\lambda}^T \right] \left[ \begin{array}{c} \mathbf{R} + \mathbf{R}^{\tilde{\mathbf{u}}} \\ \mathbf{R}^\lambda \end{array} \right] \quad (7.30)$$

as expansion of (7.10). After including DIRICHLET boundary conditions and applying standard arguments of variational calculus, the resulting discrete system of equations reads

$$\left[ \begin{array}{c|c} \mathbf{K} & \mathbf{G} \\ \mathbf{G}^T & \mathbf{0} \end{array} \right] \left[ \begin{array}{c} \Delta \tilde{\mathbf{D}} \\ \Delta \boldsymbol{\lambda} \end{array} \right] = \left[ \begin{array}{c} \mathbf{R} + \mathbf{R}^{\tilde{\mathbf{u}}} \\ \mathbf{R}^\lambda \end{array} \right]. \quad (7.31)$$

Note that in contrast to  $\mathbf{K}$ , the new tangent stiffness matrix is not necessarily positive definite, which needs to be taken into account when choosing and setting up a solver. In general, LAGRANGE multipliers have the disadvantage of adding new degrees of freedom to the system of equations. For the presented displacement constraint, only one extra degree of freedom is added for each spatial direction. This is due to the fact that the constraint is applied on the whole RVE, which avoids the approximation of the LAGRANGE multipliers as field variables. Thus, for three-dimensional problems,  $\boldsymbol{\lambda}$  will only add three additional degrees of freedom. Compared to the displacement fluctuations which are linked to the nodes and which may thus easily reach thousands of degrees of freedom, the number of three additional degrees of freedom over the whole RVE is negligible, making it computationally cheap.

### 7.2.5 Coupling of the Deformation Gradient

The constraint related to the deformation gradient (7.1) can be derived and applied in the same manner as just presented for (7.2). A detailed derivation is given in Appendix B. The only change in the final formulation is that the matrix  $\mathbf{g}_{(\mathbf{F})}^{eT}$  needs to be computed as the volume average of the element B-Matrix instead of the shape functions,

$$\mathbf{g}_{(\mathbf{F})}^{eT} = \int_{\mathcal{B}^e} \mathbf{B}^e \, dV. \quad (7.32)$$

Applying the constraint regarding the deformation gradient on the volume instead of enforcing it using periodic boundary conditions will lead to minimally invasive boundary conditions enabling e.g. arbitrary damage propagation at the microscale without artificial restrictions imposed by periodic boundaries. As shown in SOUZA NETO and FEIJÓO [100], such minimally invasive boundary conditions result in a softer constraint compared to periodic boundary conditions. To simplify the numerical examples in this paper, only the displacement constraint is applied and the constraint related to the deformation gradient is enforced by using periodic boundary conditions.

## 7.3 The Macroscopic Problem

This section starts by deriving the linearized and discretized balance equations required for solving the macroscopic dynamic boundary value problem within the dynamic multiscale framework. Subsequently the tangent moduli are addressed. In classical material simulations, the stress field depends only on the local deformations. There the general definition of the material tangent modulus is the current slope of the stress-stretch curve. For large strains this is calculated as the derivative of the first PIOLA-KIRCHHOFF stress tensor  $\mathbf{P}$  with respect to the deformation gradient  $\mathbf{F}$ , as  $\mathbb{A} = \frac{\partial \mathbf{P}}{\partial \mathbf{F}}$ . The same relation can be stated for the macroscopic values in a multiscale setting based on the microscopic fields. When considering dynamics, the local response is not only dependent on the deformation gradient but also on the macroscopic accelerations  $\ddot{\mathbf{u}}$  with (7.5), thus  $\overline{\mathbf{P}}(\overline{\mathbf{F}}, \ddot{\mathbf{u}})$ . Furthermore, the macroscopic inertia force  $\overline{\mathbf{f}}^\rho$  is computed based on the microscopic fields as well, c.f. (7.6). In the same way as the macroscopic stress, the macroscopic inertia force is therefore a function of two quantities,  $\overline{\mathbf{f}}^\rho(\overline{\mathbf{F}}, \ddot{\mathbf{u}})$ . The dependence of the material point on both  $\overline{\mathbf{F}}$  and  $\ddot{\mathbf{u}}$  is unusual. This modifies the

microscopic problem from a standard material formulation into a structural problem for the dynamic part. This results in a total of four distinct tangent moduli, as presented in the following section. The proposed tangent formulations consistently take into account the displacement constraint proposed in the previous section.

### 7.3.1 Macroscopic Boundary Value Problem

**Macroscopic Equilibrium Equation** The complete balance of linear momentum including inertia written in macroscopic notation is given by

$$\text{Div} [\bar{\mathbf{P}}] + \bar{\mathbf{f}} = \mathbf{0}. \quad (7.33)$$

Applying a test function  $\delta \bar{\mathbf{u}}$  on the entire domain  $\bar{\mathcal{B}}$  leads to the weak form of linear momentum

$$\int_{\bar{\mathcal{B}}} \delta \bar{\mathbf{u}}^T (\text{Div} [\bar{\mathbf{P}}] + \bar{\mathbf{f}}) dV = 0. \quad (7.34)$$

By applying the known properties  $\text{Div} [\bar{\mathbf{P}}] \cdot \delta \bar{\mathbf{u}} = \text{Div} [\bar{\mathbf{P}}^T \delta \bar{\mathbf{u}}] - \bar{\mathbf{P}} : \text{Grad} [\delta \bar{\mathbf{u}}]$  and the GAUSS theorem  $\int_{\bar{\mathcal{B}}} \text{Div} [\bar{\mathbf{P}}^T \delta \bar{\mathbf{u}}] dV = \int_{\partial \bar{\mathcal{B}}} \delta \bar{\mathbf{u}} \cdot \bar{\mathbf{t}} dA$ , the weak form is written as

$$\bar{G} := \int_{\bar{\mathcal{B}}} \delta \bar{\mathbf{F}} : \bar{\mathbf{P}} dV + \int_{\bar{\mathcal{B}}} \delta \bar{\mathbf{u}}^T \bar{\mathbf{f}}^\rho dV = 0. \quad (7.35)$$

Herein, zero traction forces are taken into account at the boundary. Analogous to the microscale, only body forces related to inertia, not gravity, are considered at the macroscale. Thus, the body force vector is set to  $\bar{\mathbf{f}} := \bar{\mathbf{f}}^\rho = \langle \mathbf{f}^\rho \rangle$ .

**Linearization** To solve the weak form of equilibrium by using the standard NEWTON-RAPHSON scheme, the linearized balance of linear momentum is obtained as

$$\text{Lin} \bar{G} = \bar{G} + \Delta \bar{G} = 0 \quad \text{with} \quad \Delta \bar{G} = \int_{\bar{\mathcal{B}}} \delta \bar{\mathbf{F}} : \Delta \bar{\mathbf{P}} dV + \int_{\bar{\mathcal{B}}} \delta \bar{\mathbf{u}}^T \Delta \bar{\mathbf{f}}^\rho dV. \quad (7.36)$$

Now the  $\Delta$ -operator (4.8) is applied to  $\Delta \bar{\mathbf{P}}(\bar{\mathbf{F}}, \ddot{\bar{\mathbf{u}}})$  and  $\Delta \bar{\mathbf{f}}^\rho(\bar{\mathbf{F}}, \ddot{\bar{\mathbf{u}}})$ , yielding

$$\Delta \bar{\mathbf{P}} = \frac{\partial \bar{\mathbf{P}}}{\partial \bar{\mathbf{F}}} : \Delta \bar{\mathbf{F}} + \frac{\partial \bar{\mathbf{P}}}{\partial \ddot{\bar{\mathbf{u}}}} \cdot \Delta \ddot{\bar{\mathbf{u}}} \quad \text{and} \quad (7.37)$$

$$\Delta \bar{\mathbf{f}}^\rho = \frac{\partial \bar{\mathbf{f}}^\rho}{\partial \bar{\mathbf{F}}} : \Delta \bar{\mathbf{F}} + \frac{\partial \bar{\mathbf{f}}^\rho}{\partial \ddot{\bar{\mathbf{u}}}} \cdot \Delta \ddot{\bar{\mathbf{u}}}. \quad (7.38)$$

Here the unusual property of the two-scale homogenization framework for dynamics is observed. As both the macroscopic stress and inertia force depend on the macroscopic deformation gradient as well as the macroscopic accelerations, the linearization results in distinct moduli. The respective sensitivities are defined as

$$\bar{\mathbb{A}}^{P,F} = \partial_{\bar{\mathbf{F}}} \bar{\mathbf{P}}, \quad \bar{\mathbb{A}}^{P,u} = \partial_{\ddot{\bar{\mathbf{u}}}} \bar{\mathbf{P}}, \quad \bar{\mathbb{A}}^{f,F} = \partial_{\bar{\mathbf{F}}} \bar{\mathbf{f}}^\rho \quad \text{and} \quad \bar{\mathbb{A}}^{f,u} = \partial_{\ddot{\bar{\mathbf{u}}}} \bar{\mathbf{f}}^\rho. \quad (7.39)$$

These moduli (7.39) are inserted into the linearized weak form which results in

$$\begin{aligned} \text{Lin} \bar{G} = & \int_{\bar{\mathcal{B}}} \delta \bar{\mathbf{F}} : \bar{\mathbf{P}} dV + \int_{\bar{\mathcal{B}}} \delta \bar{\mathbf{u}}^T \bar{\mathbf{f}}^\rho dV + \int_{\bar{\mathcal{B}}} \delta \bar{\mathbf{F}} : \bar{\mathbb{A}}^{P,F} : \Delta \bar{\mathbf{F}} dV \\ & + \int_{\bar{\mathcal{B}}} \delta \bar{\mathbf{F}} : \bar{\mathbb{A}}^{P,u} \cdot \Delta \ddot{\bar{\mathbf{u}}} dV + \int_{\bar{\mathcal{B}}} \delta \bar{\mathbf{u}}^T \bar{\mathbb{A}}^{f,F} : \Delta \bar{\mathbf{F}} dV + \int_{\bar{\mathcal{B}}} \delta \bar{\mathbf{u}}^T \bar{\mathbb{A}}^{f,u} \cdot \Delta \ddot{\bar{\mathbf{u}}} dV. \end{aligned} \quad (7.40)$$

**FE Discretization** The linearization of the weak form of the balance of linear momentum is now discretized in terms of finite elements. First, the linear increment

$$\begin{aligned} \Delta \bar{G} = & \int_{\mathcal{B}} \delta \bar{\mathbf{F}} : \bar{\mathbb{A}}^{P,F} : \Delta \bar{\mathbf{F}} \, dV + \int_{\mathcal{B}} \delta \bar{\mathbf{F}} : \bar{\mathbb{A}}^{P,u} \cdot \Delta \ddot{\bar{\mathbf{u}}} \, dV \\ & + \int_{\mathcal{B}} \delta \bar{\mathbf{u}}^T \bar{\mathbb{A}}^{f,F} : \Delta \bar{\mathbf{F}} \, dV + \int_{\mathcal{B}} \delta \bar{\mathbf{u}}^T \bar{\mathbb{A}}^{f,u} \cdot \Delta \ddot{\bar{\mathbf{u}}} \, dV \end{aligned} \quad (7.41)$$

is discretized using standard FE formulations. Then, to get rid of the dependence on the time derivatives, the numerical time integration in terms of (4.35) is used, which results in

$$\begin{aligned} \Delta \bar{G} = & \sum_{e=1}^{n_{\text{el}}} \delta \bar{d}_P^e \left( \int_{\mathcal{B}^e} \bar{B}_{ijP}^e \bar{\mathbb{A}}_{ijmn}^{P,F} \bar{B}_{mnQ}^e + \frac{1}{\beta \Delta t^2} \bar{B}_{ijP}^e \bar{\mathbb{A}}_{ijk}^{P,u} \bar{N}_{kQ}^e \right. \\ & \left. + \bar{N}_{iP}^e \bar{\mathbb{A}}_{imn}^{f,F} \bar{B}_{mnQ}^e + \frac{1}{\beta t^2} \bar{N}_{iP}^e \bar{\mathbb{A}}_{ik}^{f,u} \bar{N}_{kQ}^e \, dV \right) \Delta \bar{d}_Q^e. \end{aligned} \quad (7.42)$$

Herein, the matrix representation of the moduli in index notation has been used. Lowercase indices refer to the spatial dimension  $n_{\text{dm}}$ , whereas uppercase indices refer to the total degrees of freedom of an element  $n_{\text{edf}}$ . Again, standard element B-matrix  $\bar{\mathbf{B}}^e$  and shape function matrix  $\bar{\mathbf{N}}^e$  are considered. By extracting the nodal virtual and incremental displacements, this yields the definition of the full macroscopic element tangent stiffness matrix

$$\begin{aligned} \bar{k}_{PQ}^e = & \int_{\mathcal{B}^e} \left( \bar{B}_{ijP}^e \bar{\mathbb{A}}_{ijmn}^{P,F} \bar{B}_{mnQ}^e + \frac{1}{\beta \Delta t^2} \bar{B}_{ijP}^e \bar{\mathbb{A}}_{ijk}^{P,u} \bar{N}_{kQ}^e \right. \\ & \left. + \bar{N}_{iP}^e \bar{\mathbb{A}}_{imn}^{f,F} \bar{B}_{mnQ}^e + \frac{1}{\beta \Delta t^2} \bar{N}_{iP}^e \bar{\mathbb{A}}_{ik}^{f,u} \bar{N}_{kQ}^e \right) \, dV. \end{aligned} \quad (7.43)$$

Now the remaining part of the linearization (7.40), the residuum  $\bar{R}$ , is discretized as

$$\bar{R} = \sum_{e=1}^{n_{\text{el}}} \left( \delta \bar{d}_P \int_{\mathcal{B}^e} \bar{B}_{ijP}^e \bar{P}_{ij} \, dV + \delta \bar{d}_P \int_{\mathcal{B}^e} \bar{N}_{iP}^e \bar{J}_i^\rho \, dV \right). \quad (7.44)$$

By extracting the nodal virtual displacements, the element residuum is identified as

$$\bar{r}_P^e = \int_{\mathcal{B}^e} \left( \bar{B}_{ijP}^e \bar{P}_{ij} + \bar{N}_{iP}^e \bar{J}_i^\rho \right) \, dV, \quad (7.45)$$

where again matrix representation and index notation is used.

### 7.3.2 Consistent Macroscopic Tangent Moduli

For the dynamic homogenization framework, the four macroscopic tangent moduli (7.39) need to be determined, c.f. (7.43). To obtain the sought-after moduli in closed form, the derivation starts by taking the derivative of the incremental linearized weak form of linear momentum at the microscale with respect to the two relevant macroscopic quantities, the deformation gradient  $\bar{\mathbf{F}}$  and the acceleration  $\ddot{\bar{\mathbf{u}}}$ . Then the moduli are derived by considering the microscopic problem in its equilibrium state.

## Incremental Weak Forms Including Displacement Constraint

As will become apparent later, the derivatives of the microscopic nodal fluctuations with respect to the macroscopic deformation gradient and the acceleration  $\partial_{\bar{\mathbf{F}}}\tilde{\mathbf{D}}$  and  $\partial_{\ddot{\mathbf{u}}}\tilde{\mathbf{D}}$  will be required for the derivation of the tangents. For their calculation, the incremental linearized weak form of the microscale has to be expressed with respect to these two quantities. In order to account for the proposed displacement constraint, the potential associated with the LAGRANGE multipliers must be considered as well. This yields

$$\Delta G^{\tilde{\mathbf{u}}} = \int_{\mathcal{B}} \delta F_{ij} \mathbb{A}_{ijmn} \Delta F_{mn} dV + \int_{\mathcal{B}} \delta \tilde{u}_i \rho_0 \Delta \ddot{u}_i dV + \Delta \lambda_i \int_{\mathcal{B}} \delta \tilde{u}_i dV \quad \text{and} \quad (7.46)$$

$$\Delta G^\lambda = \delta \lambda_i \int_{\mathcal{B}} \Delta \tilde{u}_i dV, \quad (7.47)$$

c.f. (4.9), (7.16) and (7.17). Using the decompositions (6.7) and (6.8), equation (7.46) can be reformulated as

$$\begin{aligned} \Delta G^{\tilde{\mathbf{u}}} &= \int_{\mathcal{B}} \delta F_{ij} \mathbb{A}_{ijmn} \Delta \bar{F}_{mn} dV + \int_{\mathcal{B}} \delta F_{ij} \mathbb{A}_{ijmn} \Delta \tilde{H}_{mn} dV + \int_{\mathcal{B}} \delta \tilde{u}_i \rho_0 \Delta \ddot{\tilde{u}}_i dV \\ &\quad + \int_{\mathcal{B}} \delta \tilde{u}_i \rho_0 \Delta \ddot{\tilde{H}}_{ij} X_j dV + \int_{\mathcal{B}} \delta \tilde{u}_i \rho_0 \Delta \ddot{\tilde{u}}_i dV + \Delta \lambda_i \int_{\mathcal{B}} \delta \tilde{u}_i dV. \end{aligned} \quad (7.48)$$

**Derivatives of Incremental Weak Forms** By taking the derivatives of the increments (7.47) and (7.48) in the equilibrium state  $\Delta G = 0$ , a closed form formulation of the tangent moduli will be obtained subsequently. Thus, the associated derivatives are computed in the following. Note that, equivalently to (7.8), the  $\Delta$ -operator of a quantity  $\Delta \bullet$  can be dropped when taking its derivative with respect to a quantity  $\square$  of the current iteration step, as

$$\frac{\partial \Delta \bullet_{n+1}}{\partial \square_{n+1}} = \frac{\partial (\bullet_{n+1} - \bullet_n)}{\partial \square_{n+1}} = \frac{\partial \bullet_{n+1}}{\partial \square_{n+1}}. \quad (7.49)$$

**Derivative with Respect to  $\bar{\mathbf{F}}$**  Taking the derivatives of (7.48) and (7.47) with respect to the macroscopic deformation gradient, while considering (7.49) results in

$$\begin{aligned} 0_{kl} &= \int_{\mathcal{B}} \delta F_{ij} \mathbb{A}_{ijkl} dV + \int_{\mathcal{B}} \delta F_{ij} \mathbb{A}_{ijmn} \frac{\partial \tilde{H}_{mn}}{\partial \bar{F}_{kl}} dV + \frac{1}{\beta \Delta t^2} \int_{\mathcal{B}} \delta \tilde{u}_k \rho_0 X_l dV \\ &\quad + \frac{1}{\beta \Delta t^2} \int_{\mathcal{B}} \delta \tilde{u}_i \rho_0 \frac{\partial \tilde{u}_i}{\partial \bar{F}_{kl}} dV + \frac{\partial \lambda_i}{\partial \bar{F}_{kl}} \int_{\mathcal{B}} \delta \tilde{u}_i dV \quad \text{and} \end{aligned} \quad (7.50)$$

$$0_{kl} = \delta \lambda_i \int_{\mathcal{B}} \frac{\partial \tilde{u}_i}{\partial \bar{F}_{kl}} dV. \quad (7.51)$$

Using standard FE discretization yields

$$\begin{aligned} 0_{kl} &= \sum_{e=1}^{n_{el}} \delta \tilde{d}_P^e \left( \int_{\mathcal{B}^e} B_{ijP}^e \mathbb{A}_{ijkl} dV + \int_{\mathcal{B}^e} B_{ijP}^e \mathbb{A}_{ijmn} B_{mnQ}^e dV \frac{\partial \tilde{d}_Q^e}{\partial \bar{F}_{kl}} + \frac{1}{\beta \Delta t^2} \int_{\mathcal{B}^e} N_{kP}^e \rho_0 X_l dV \right. \\ &\quad \left. + \frac{1}{\beta \Delta t^2} \int_{\mathcal{B}^e} N_{iP}^e \rho_0 N_{iQ}^e dV \frac{\partial \tilde{d}_Q^e}{\partial \bar{F}_{kl}} + \int_{\mathcal{B}^e} N_{iP}^e dV \frac{\partial \lambda_i}{\partial \bar{F}_{kl}} \right) \quad \text{and} \end{aligned} \quad (7.52)$$

$$0_{kl} = \sum_{e=1}^{n_{el}} \delta \lambda_i \left( \int_{\mathcal{B}^e} N_{iP}^e dV \frac{\partial \tilde{d}_P^e}{\partial \bar{F}_{kl}} \right). \quad (7.53)$$

To simplify the notation, two new abbreviations are introduced at the element level as well as in the global notation

$$\mathbf{L} = \mathbf{A}_{e=1}^{n_{el}} \mathbf{l}^e \quad \text{with} \quad l_{Pij}^e = \int_{\mathcal{B}^e} B_{klP}^e \mathbb{A}_{kl ij} \, dV \quad \text{and} \quad (7.54)$$

$$\mathbf{Z} = \mathbf{A}_{e=1}^{n_{el}} \mathbf{z}^e \quad \text{with} \quad z_{Pij}^e = \int_{\mathcal{B}^e} \rho_0 N_{Pi}^e X_j \, dV. \quad (7.55)$$

An overview of these two and all upcoming abbreviations in this chapter can be found in Appendix C. Inserting them, in addition to (7.12) and (7.20) and rewriting equations (7.52) and (7.53) in global notation leads to the expressions

$$\mathbf{0} = \mathbf{L} + \frac{1}{\beta \Delta t^2} \mathbf{Z} + \left( \mathbf{K}^{\text{stat}} + \frac{1}{\beta \Delta t^2} \mathbf{M} \right) \frac{\partial \tilde{\mathbf{D}}}{\partial \mathbf{F}} + \mathbf{G} \frac{\partial \boldsymbol{\lambda}}{\partial \mathbf{F}} \quad \text{and} \quad (7.56)$$

$$\mathbf{0} = \mathbf{G}^T \frac{\partial \tilde{\mathbf{D}}}{\partial \mathbf{F}}. \quad (7.57)$$

By combining the nodal fluctuations and the LAGRANGE multipliers into one column matrix  $\mathbf{D}^*$ , additional new fields are defined as

$$\mathbf{D}^{*\text{T}} = \left[ \tilde{\mathbf{D}}^T \mid \boldsymbol{\lambda}^T \right], \quad (7.58)$$

$$\mathbf{L}^{\bar{\text{T}}} = \left[ \mathbf{L}^T + \frac{1}{\beta \Delta t^2} \mathbf{Z}^T \mid \mathbf{0} \right] \quad \text{and} \quad (7.59)$$

$$\mathbf{K}^* = \left[ \begin{array}{c|c} \mathbf{K}^{\text{stat}} + \frac{1}{\beta \Delta t^2} \mathbf{M} & \mathbf{G} \\ \hline \mathbf{G}^T & \mathbf{0} \end{array} \right]. \quad (7.60)$$

These definitions allow the two expressions (7.56) and (7.57) to be written as a single system of equations  $\mathbf{0} = \mathbf{L}^{\bar{\text{T}}} + \mathbf{K}^* \partial_{\mathbf{F}} \mathbf{D}^*$ . Then, the required derivative can be computed from

$$\frac{\partial \mathbf{D}^*}{\partial \mathbf{F}} = -\mathbf{K}^{*-1} \mathbf{L}^{\bar{\text{T}}}. \quad (7.61)$$

Note that  $\mathbf{K}^*$  is the microscopic tangent stiffness matrix in (7.31), which is already available from solving the microscopic boundary value problem, requiring no additional assembly.

**Derivative with Respect to  $\ddot{\mathbf{u}}$**  Analogously, the derivative of (7.48) and (7.47) with respect to  $\ddot{\mathbf{u}}$  can be obtained by applying (7.49), i.e. one obtains

$$\begin{aligned} 0_k &= \int_{\mathcal{B}} \delta F_{ij} \mathbb{A}_{ijmn} \frac{\partial \tilde{H}_{mn}}{\partial \ddot{u}_k} \, dV + \int_{\mathcal{B}} \delta \tilde{u}_k \rho_0 \, dV \\ &\quad + \frac{1}{\beta \Delta t^2} \int_{\mathcal{B}} \delta \tilde{u}_i \rho_0 \frac{\partial \tilde{u}_i}{\partial \ddot{u}_k} \, dV + \frac{\partial \lambda_i}{\partial \ddot{u}_k} \int_{\mathcal{B}} \delta \tilde{u}_i \, dV \quad \text{and} \end{aligned} \quad (7.62)$$

$$0_k = \delta \lambda_i \int_{\mathcal{B}} \frac{\partial \tilde{u}_i}{\partial \ddot{u}_k} \, dV. \quad (7.63)$$

Standard FE discretization using matrix representation and index notation yields

$$0_k = \sum_{e=1}^{n_{el}} \delta \tilde{d}_P^e \left( \int_{\mathcal{B}^e} B_{ijP}^e \mathbb{A}_{ijmn} B_{mnQ}^e dV \frac{\partial \tilde{d}_Q^e}{\partial \ddot{u}_k} + \int_{\mathcal{B}^e} N_{kP} \rho_0 dV \right. \\ \left. + \frac{1}{\beta \Delta t^2} \int_{\mathcal{B}^e} N_{iP}^e \rho_0 N_{iQ}^e dV \frac{\partial \tilde{d}_Q^e}{\partial \ddot{u}_k} + \int_{\mathcal{B}} N_{iP}^e dV \frac{\partial \lambda_i}{\partial \ddot{u}_k} \right) \quad \text{and} \quad (7.64)$$

$$0_k = \sum_{e=1}^{n_{el}} \delta \lambda_i \left( \int_{\mathcal{B}} N_{iP}^e dV \frac{\partial \tilde{d}_P^e}{\partial \ddot{u}_k} \right). \quad (7.65)$$

Applying the abbreviations previously defined in (7.12) and (7.20) and introducing another one

$$\mathbf{W} = \mathbf{A} \mathbf{w}^e \quad \text{with} \quad w_{Pi}^e = \int_{\mathcal{B}^e} \rho_0 N_{iP}^e dV, \quad (7.66)$$

simplifies the expressions to

$$\mathbf{0} = \mathbf{W} + \left( \mathbf{K}^{\text{stat}} + \frac{1}{\beta \Delta t^2} \mathbf{M} \right) \frac{\partial \tilde{\mathbf{D}}}{\partial \ddot{\mathbf{u}}} + \mathbf{G} \frac{\partial \boldsymbol{\lambda}}{\partial \ddot{\mathbf{u}}} \quad \text{and} \quad (7.67)$$

$$\mathbf{0} = \mathbf{G}^T \frac{\partial \tilde{\mathbf{D}}}{\partial \ddot{\mathbf{u}}}. \quad (7.68)$$

Again, the two equations are combined by joining the displacements and the LAGRANGE multipliers into a single matrix, c.f. (7.58) and (7.60). An additional field is considered

$$\mathbf{W}^{*\text{T}} = [ \mathbf{W}^T \mid \mathbf{0} ]. \quad (7.69)$$

By solving the resulting system of equations with respect to the required derivative  $\frac{\partial \mathbf{D}^*}{\partial \ddot{\mathbf{u}}}$ ,

$$\frac{\partial \mathbf{D}^*}{\partial \ddot{\mathbf{u}}} = -\mathbf{K}^{*-1} \mathbf{W}^* \quad (7.70)$$

is obtained

**Derivation of Tangent Moduli** In this subsection the four moduli will be derived by inserting the derivatives computed in the last subsection. Note that all moduli are only consistent for a microscopic equilibrium state. Thus, quadratic convergence of the macroscopic NEWTON-RAPHSON iteration is only ensured if the microscopic boundary value problem is solved for each macroscopic iteration step. After the last microscopic iteration, the consistent tangent moduli can be computed.

**Derivation of  $\overline{\mathbb{A}}^{P,F}$**  To derive the sensitivity of the macroscopic stresses with respect to the macroscopic deformation gradient, the derivative is rewritten in five simple steps, using the definition of the macroscopic stresses in terms of the microscopic fields (7.5), i.e.

$$\overline{\mathbb{A}}_{ijmn}^{P,F} = \frac{\partial \overline{P}_{ij}}{\partial \overline{F}_{mn}} = \frac{\partial \langle P_{ij} + \rho_0 \ddot{u}_i X_j \rangle}{\partial \overline{F}_{mn}}. \quad (7.71)$$

First, the chain rule  $\frac{\partial \mathbf{P}(\mathbf{F})}{\partial \bar{\mathbf{F}}} = \frac{\partial \mathbf{P}}{\partial \mathbf{F}} : \frac{\partial \mathbf{F}}{\partial \bar{\mathbf{F}}}$  and the micro-macro splits of the displacement (6.7) and deformation gradient (6.8) are applied

$$\bar{\mathbb{A}}_{ijmn}^{P,F} = \left\langle \mathbb{A}_{ijmn} + \mathbb{A}_{ijkl} \frac{\partial \tilde{H}_{kl}}{\partial \bar{F}_{mn}} + \rho_0 \frac{\partial \tilde{H}_{ik}}{\partial \bar{F}_{mn}} X_k X_j + \rho_0 \frac{\partial \tilde{u}_i}{\partial \bar{F}_{mn}} X_j \right\rangle. \quad (7.72)$$

Second, the time derivatives are dealt with using the definitions of the NEWMARK method,

$$\bar{\mathbb{A}}_{ijmn}^{P,F} = \left\langle \mathbb{A}_{ijmn} + \mathbb{A}_{ijkl} \frac{\partial \tilde{H}_{kl}}{\partial \bar{F}_{mn}} + \frac{1}{\beta \Delta t^2} \rho_0 \delta_{im} X_n X_j + \frac{1}{\beta \Delta t^2} \rho_0 \frac{\partial \tilde{u}_i}{\partial \bar{F}_{mn}} X_j \right\rangle. \quad (7.73)$$

Third, the FE discretization is inserted, yielding

$$\begin{aligned} \bar{\mathbb{A}}_{ijmn}^{P,F} = & \sum_{e=1}^{n_{el}} \left( \frac{1}{V} \int_{\mathcal{B}^e} \mathbb{A}_{ijmn} dV + \frac{1}{\beta \Delta t^2} \frac{1}{V} \int_{\mathcal{B}^e} \rho_0 \delta_{im} X_j X_n dV \right. \\ & \left. + \frac{1}{V} \int_{\mathcal{B}^e} \mathbb{A}_{ijkl} B_{klP}^e dV \frac{\partial \tilde{d}_P^e}{\partial \bar{F}_{mn}} + \frac{1}{\beta \Delta t^2} \frac{1}{V} \int_{\mathcal{B}^e} \rho_0 N_{Pi}^e X_j dV \frac{\partial \tilde{d}_P^e}{\partial \bar{F}_{mn}} \right). \end{aligned} \quad (7.74)$$

And fourth, by using the abbreviations  $\mathbf{L}$  (7.54) and  $\mathbf{Z}$  (7.55) and introducing the new field

$$\mathbb{Y}_{ijmn} = \rho_0 \delta_{im} X_j X_n, \quad (7.75)$$

equation (7.74) can be simplified to

$$\bar{\mathbb{A}}^{P,F} = \left\langle \mathbb{A} + \frac{1}{\beta \Delta t^2} \mathbb{Y} \right\rangle + \frac{1}{V} \left( \mathbf{L} + \frac{1}{\beta \Delta t^2} \mathbf{Z} \right)^T \frac{\partial \tilde{\mathbf{D}}}{\partial \bar{\mathbf{F}}}. \quad (7.76)$$

The fifth and last step is to plug in the result of the derivative of the microscopic nodal fluctuations with respect to the macroscopic deformation gradient (7.61). To consistently take the volume displacement constraint into account, the term  $\mathbf{L} + \frac{1}{\beta \Delta t^2} \mathbf{Z}$  is expanded following the abbreviation  $\mathbf{L}^{\bar{*}}$  (7.59), however this time applying the NEWMARK parameter  $\beta$  associated to the microscale. Therefore the resulting field is denoted as  $\mathbf{L}^*$ . The closed form formulation of the sensitivity of the macroscopic stress with respect to the macroscopic deformation gradient considering large strains and including the volume integral displacement constraint, is obtained as

$$\bar{\mathbb{A}}^{P,F} = \left\langle \mathbb{A} + \frac{1}{\beta \Delta t^2} \mathbb{Y} \right\rangle - \frac{1}{V} \mathbf{L}^{*\top} \mathbf{K}^{*-1} \mathbf{L}^{\bar{*}}. \quad (7.77)$$

This result has already been published in TAMSEN et al. [107] for a special scenario of dynamic homogenization, which did not consider the macroscopic displacements and thus not yet the volume displacement constraint.

**Derivation of  $\bar{\mathbb{A}}^{P,u}$**  The derivation of the sensitivity of the macroscopic stresses with respect to the macroscopic accelerations is analogous to that of  $\bar{\mathbb{A}}^{P,F}$ . Therefore

only the most relevant steps are shown. First, the derivative is rewritten using the definition of the macroscopic stresses in terms of the microscopic fields as

$$\bar{\mathbb{A}}_{ijk}^{P,u} = \frac{\partial \bar{P}_{ij}}{\partial \ddot{u}_k} = \frac{\partial \langle P_{ij} + \rho_0 \ddot{u}_i X_j \rangle}{\partial \ddot{u}_k}. \quad (7.78)$$

Then, using the chain rule, (6.7), (6.8), (7.8) and FE discretization, the equation reads

$$\begin{aligned} \bar{\mathbb{A}}_{ijk}^{P,u} = & \sum_{e=1}^{n_{el}} \left( \frac{1}{V} \int_{B^e} \rho_0 \delta_{ik} X_j \, dV + \frac{1}{V} \int_{B^e} \mathbb{A}_{ijmn} B_{mnP}^e \, dV \frac{\partial \tilde{d}_P^e}{\partial \ddot{u}_k} \right. \\ & \left. + \frac{1}{\beta \Delta t^2} \frac{1}{V} \int_{B^e} \rho_0 X_j N_{iP}^e \, dV \frac{\partial \tilde{d}_P^e}{\partial \ddot{u}_k} \right). \end{aligned} \quad (7.79)$$

Finally, using the previously introduced abbreviations (7.59),(7.60) and (7.69), in addition to the new field

$$\mathbf{V}_{ijk} = \rho_0 \delta_{ik} X_j \quad (7.80)$$

and inserting the derivative of the microscopic nodal fluctuations with respect to the macroscopic accelerations (7.70), the closed form tangent modulus is obtained as

$$\bar{\mathbb{A}}^{P,u} = \langle \mathbf{V} \rangle - \frac{1}{V} \mathbf{L}^{*\top} \mathbf{K}^{*-1} \mathbf{W}^*. \quad (7.81)$$

**Derivation of  $\bar{\mathbb{A}}^{f,F}$**  The derivation of the sensitivity of the macroscopic inertia with respect to the macroscopic deformation gradient is again similar to that of  $\bar{\mathbb{A}}^{P,F}$ . First, the derivative is rewritten as

$$\bar{\mathbb{A}}_{imn}^{f,F} = \frac{\partial \bar{f}_i^p}{\partial F_{mn}} = \frac{\partial \langle \rho_0 \ddot{u}_i \rangle}{\partial F_{mn}} \quad (7.82)$$

and by using (6.7), (6.8), (7.8) and FE discretization, the equation reads

$$\bar{\mathbb{A}}_{imn}^{f,F} = \sum_{e=1}^{n_{el}} \left( \frac{1}{\beta \Delta t^2} \frac{1}{V} \int_{B^e} \rho_0 \delta_{im} X_n \, dV + \frac{1}{\beta \Delta t^2} \frac{1}{V} \int_{B^e} \rho_0 N_{iP}^e \, dV \frac{\partial \tilde{d}_P^e}{\partial F_{mn}} \right). \quad (7.83)$$

Using the abbreviations (7.80), (7.69), (7.60), (7.59) and plugging in (7.61), the modulus is identified as

$$\bar{\mathbb{A}}^{f,F} = \frac{1}{\beta \Delta t^2} \langle \mathbf{V}^\top \rangle - \frac{1}{V} \frac{1}{\beta \Delta t^2} \mathbf{W}^{*\top} \mathbf{K}^{*-1} \mathbf{L}^*. \quad (7.84)$$

**Derivation of  $\bar{\mathbb{A}}^{f,u}$**  Analogously, the derivative is rewritten as

$$\bar{\mathbb{A}}_{ik}^{f,u} = \frac{\partial \bar{f}_i^p}{\partial \ddot{u}_k} = \frac{\partial \langle \rho_0 \ddot{u}_i \rangle}{\partial \ddot{u}_k}. \quad (7.85)$$

Then, using (6.7) and the FE discretization, the expression becomes

$$\overline{\mathbb{A}}_{ik}^{f,u} = \sum_{e=1}^{n_{el}} \left( \frac{1}{V} \int_{\mathcal{B}^e} \rho_0 \delta_{ik} dV + \frac{1}{V} \frac{1}{\beta \Delta t^2} \int_{\mathcal{B}^e} \rho_0 N_{iP}^e dV \frac{\partial \tilde{d}_P^e}{\partial \ddot{u}_k} \right). \quad (7.86)$$

Taking into account the global abbreviations and inserting (7.70), the final modulus is derived as

$$\overline{\mathbb{A}}^{f,u} = \langle \rho_0 \rangle - \frac{1}{V} \frac{1}{\beta \Delta t^2} \mathbf{W}^{*T} \mathbf{K}^{*-1} \mathbf{W}^*. \quad (7.87)$$

By dropping all terms including dynamics, identified by  $\beta$  or  $\bar{\beta}$ , the first tangent modulus in (7.77) takes the same form as e.g. found in MIEHE et al. [72]. Here, the closed form moduli (7.77), (7.81), (7.84) and (7.87) extend this consistently to the dynamic regime. An overview over the algorithm of the proposed framework is presented in Figure 7.2. All moduli and special fields defined during the derivation are summarized in Appendix C.

The following two chapters present academic problems investigating some general behavior of the dynamic multiscale framework, including the macroscopic convergence behavior and initial studies regarding the volume displacement constraint. Afterwards more practically oriented simulations regarding SHCC experiments are given.

### macroscopic problem

**loop** over all macroscopic elements

**loop** over element GAUSS points

microscopic problem

**input:**  $\overline{\mathbf{F}}, \overline{\mathbf{u}}, \ddot{\overline{\mathbf{F}}}, \ddot{\overline{\mathbf{u}}}$

**boundary conditions:**  $\mathbf{x} = \overline{\mathbf{u}} + \overline{\mathbf{F}} \mathbf{X} + \tilde{\mathbf{u}}$  with  $\langle \tilde{\mathbf{u}} \rangle = \mathbf{0}$  on  $\mathcal{B}$  Eq. (6.6),(7.14)

**loop** microscale iteration until  $|\Delta \mathbf{D}^*| < tol$

**compute** global microscopic fields:

$$\mathbf{K}, \mathbf{R}, \mathbf{R}^{\tilde{\mathbf{u}}}, \mathbf{R}^\lambda, \mathbf{G} \quad \text{Eq. (7.11),(7.13),(7.28),(7.29),(7.20)}$$

$$\text{solve } \mathbf{K}^* \Delta \mathbf{D}^* = \mathbf{R}^* \quad \text{Eq. (7.31)}$$

**update**  $\mathbf{D}^* \leftarrow \mathbf{D}^* + \Delta \mathbf{D}^*$

**compute** homogenized fields and moduli:

$$\overline{\mathbf{P}}, \overline{\mathbf{f}}^\rho, \overline{\mathbb{A}}^{P,F}, \overline{\mathbb{A}}^{P,u}, \overline{\mathbb{A}}^{f,F}, \overline{\mathbb{A}}^{f,u} \quad \text{Eq. (7.5),(7.6),(7.77),(7.81),(7.84),(7.87)}$$

**compute** matrices  $\overline{\mathbf{k}}^e$  and  $\overline{\mathbf{r}}^e$ , using GAUSS integration Eq. (7.43),(7.45)

**solve**  $\overline{\mathbf{K}} \Delta \overline{\mathbf{D}} = \overline{\mathbf{R}}$

**Figure 7.2:** Algorithm for single macroscopic iteration of the dynamic FE<sup>2</sup> framework with respective equation references. It should be noted that the overall structure of the standard FE procedure does not change, only some additional fields need to be computed. Furthermore, for the implementation of the microscopic problem, the macroscopic displacements  $\overline{\mathbf{u}}$  may be omitted from the code. It is the second derivative  $\ddot{\overline{\mathbf{u}}}$ , computed in the macroscopic problem, which influences the microscopic results.



## 8 Numerical Study – Layered Structure

Now that the framework for the two-scale homogenization procedure, including dynamics on both scales is derived, a first academic example is presented as a proof of concept. First, the macroscopic NEWTON iteration, based on the tangent moduli derived in Chapter 7 is analyzed. After demonstrating the quadratically converging macroscopic iteration behavior of the fully coupled simulation, an initial analysis of different RVE choices is conducted. As it turns out, for dynamic homogenization the definition of RVE is even more complex than for quasi-static cases. In order to assess the reliability of the homogenization framework, single-scale comparisons are calculated. Then, the concept of a unit cell as RVE is evaluated under dynamic conditions. Finally, a comparison of two different displacement constraints, including the proposed one, is presented. The analysis presented in this chapter has been published in TAMSEN and BALZANI [106].

### 8.1 Boundary Value Problem

A one-dimensional model of a layered structure with the total length of  $L$  is investigated. The studied heterogeneous material consists of two alternating phases, a soft light phase, and a stiff heavy phase. Each phase has a length of  $l_M$ , a YOUNG'S modulus  $E_1$  and  $E_2$ , and a density  $\rho_1$  and  $\rho_2$ , respectively. In all numerical simulations within this chapter the material properties are set to  $E_1 = 2 \cdot 10^3 \text{ N/mm}^2$ ,  $E_2 = 2 \cdot 10^5 \text{ N/mm}^2$ ,  $\rho_1 = 1 \cdot 10^3 \text{ kg/m}^3$  and  $\rho_2 = 1 \cdot 10^5 \text{ kg/m}^3$ . The POISSON'S ratio is chosen to be negligible, i.e.  $\nu = 10^{-6}$ , to enable a quasi-1D investigation. The left boundary is fixed. On the right end an impact load is applied in terms of a displacement boundary condition using the polynomial function  $\bar{u}(t) = \frac{2^8 \bar{u}_{\max}}{T^8} t^4 (t - T)^4$ , where  $\bar{u}_{\max}$  is the amplitude of the impact wave and  $T$  the duration in which the load is applied. Initially, the bar is at rest.

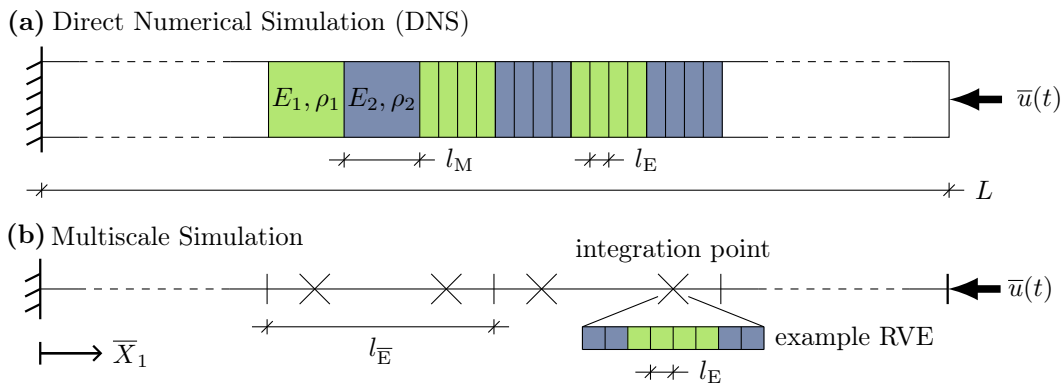


**Figure 8.1:** Illustration of the numerical calculations including (a) a 1D single scale FE Model and (b) the macroscopic model and the RVE of the FE<sup>2</sup> approach, based on TAMSEN and BALZANI [106].

The problem will be solved using both a standard single-scale finite element problem, referred to as direct numerical simulation (DNS), as well as the proposed dynamic FE<sup>2</sup> framework. Both are visualized in Figure 8.1. The DNS discretizes the microscopic phases at the macroscale into a large number of finite elements with a length of  $l_E$ . It thereby serves as overkill reference for the multiscale approach. The FE<sup>2</sup> simulations have a macroscopic element length of  $l_{\bar{E}}$  and make use of the same element length  $l_E$  at the microscale for better direct comparability of the microscopic fields to the DNS. To approximate the displacement fields of the elements, linear shape functions and two GAUSS points are used for all scales. As shown in Figure 8.1b, each microscopic RVE calculation is associated to a single macroscopic integration point. The corresponding parameters of each simulation, regarding geometry, material parameters and loading will be listed in the caption of each figure.

## 8.2 Consistency of the Numerical Framework

This example investigates the convergence behavior of the macroscopic NEWTON iteration. In Figure 8.2a, the distribution of macroscopic displacement fields is shown at three different time instances for both the DNS (in gray) and the FE<sup>2</sup> computation. As RVE, the basic unit cell of the type A (c.f. Figure 8.3) is considered. It can be seen that the dynamic multiscale framework approximates the overall behavior well and even captures some of the smaller waves arising due to the microstructure. A better representation of the wave propagation might be achieved by using finer time steps. However, this would generally make the problem converge faster as the initial values are already closer to the solution, defying the objective to properly test the tangent moduli. The convergence behavior of the three arbitrarily chosen time frames is depicted in Figure 8.2b. Quadratic convergence of the norm of the updates of the nodal displacements  $|\Delta D^*|$  is observed. This demonstrates that the macroscopic tangent

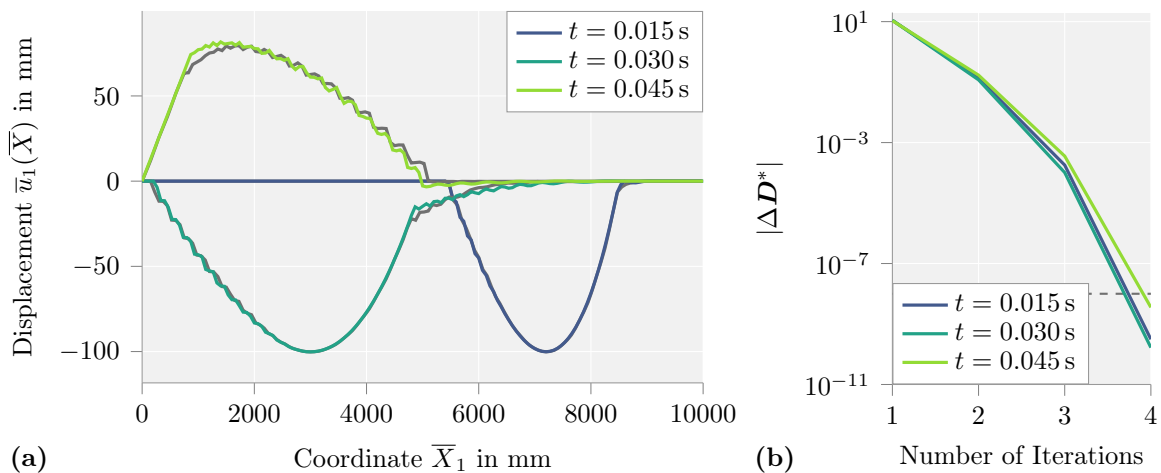


**Figure 8.2:** Analysis of algorithmic consistency: (a) Comparison of displacement fields and (b) Convergence of the macroscopic NEWTON iteration with a tolerance of  $10^{-8}$ . The simulation parameters are  $L = 10000$  mm,  $l_M = 10$  mm,  $l_{\bar{E}} = 33.33$  mm,  $\bar{u}_{\max} = 100$  mm,  $T = 0.01$  s,  $\Delta t = 5 \cdot 10^5$  s and basic unit cell type A as RVE, data from TAMSEN and BALZANI [106].

moduli, incorporating both microscale inertia forces as well as possible constraints, have been derived in a consistent manner.

### 8.3 Analysis of the Unit Cell Concept under Dynamic Loading

For quasi-static homogenization simulations of periodic microstructures using PBC, it is known that the resulting macroscopic answer as well as the corresponding microscopic fields are invariant with respect to the specific choice of unit cell. In contrast, in a dynamic setting the distribution of the mass relative to the geometrical center is relevant. An extreme example is shown in Figure 8.4. Here, the macroscopic displacement field presented in the first example in Figure 8.2a at  $t = 0.045$  is compared to a simulation using the unit cell type B as an RVE (c.f. Figure 8.3). To properly measure the influence of different RVE choices on the FE<sup>2</sup> simulation, an objective error measure  $\epsilon$  is considered. It is defined as the average difference of the macroscopic displacement fields  $\epsilon = \sum_i^{n_{\text{nodes}}} |\bar{u}_i^I(t_j) - \bar{u}_i^{II}(t_j)| / n_{\text{nodes}}$ . This measure can be evaluated for each time step and thus the average is once more computed over the number of time steps  $\epsilon_{\text{time}} = \sum_j^{n_{\text{timesteps}}} \epsilon_j / n_{\text{timesteps}}$ . In Figure 8.5a the difference of the unit cell type relative to each other is presented, whereas Figure 8.5b shows the error of each type compared to the DNS. To study the influence of the RVE size with respect to the

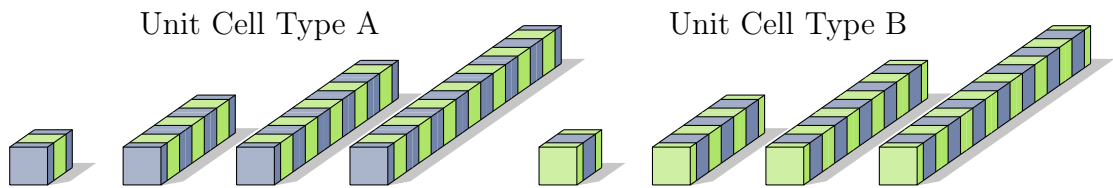


**Figure 8.3:** Selection of RVE choices with different numbers of basic unit cells, based on TAMSEN and BALZANI [106].

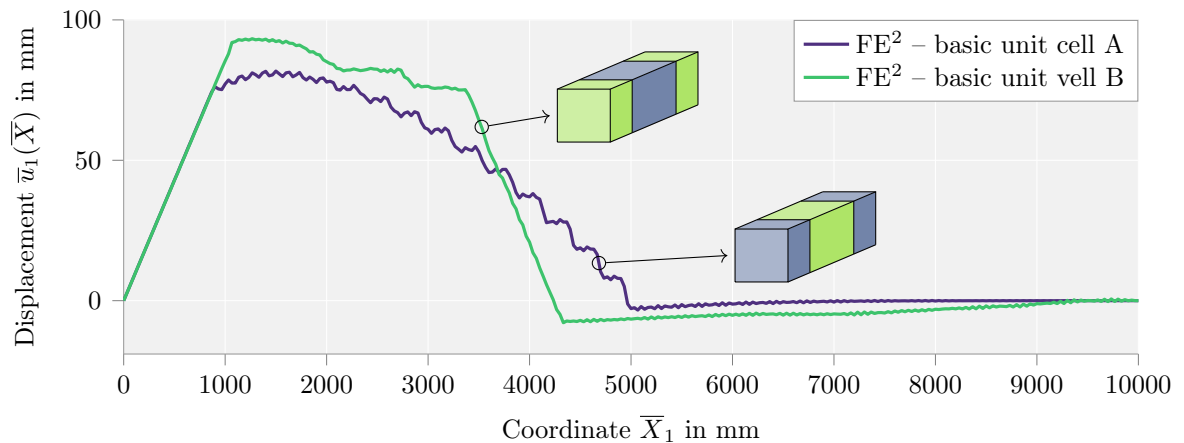


**Figure 8.4:** Comparison of macroscopic displacement fields for two different RVEs with different basic unit cells types. The simulation parameters are  $L = 10000$  mm,  $l_M = 10$  mm,  $l_{\bar{E}} = 33.33$  mm,  $\bar{u}_{\text{max}} = 100$  mm,  $T = 0.01$  s,  $t = 0.045$  s and  $\Delta t = 5 \cdot 10^5$  s. The data is published in TAMSEN and BALZANI [106].

unit cell choice, RVEs with multiple unit cells are considered, as depicted in Figure 8.3. Two effects can be observed: First, the difference in macroscopic displacements between different choices of unit cell type decreases when the number of unit cells per RVE is increased, c.f. Figure 8.5a. This indicates that the choice of a particular basic unit cell type does not matter as long as the RVE is chosen large enough. Second, the error  $\epsilon_{\text{time}}$ , which is computed as the difference to the DNS reference, increases when the size of the RVE relative to the macroscopic element length is too large. This is visualized in Figure 8.5b. Thus a violation of the scale separation assumption results in the observed increase in errors. However, the second effect can generally be neglected, as calculations with RVE sizes larger than the macroscopic element length have little practical application when applying homogenization methods. At this point, it is favorable to use domain decomposition approaches instead of a homogenization method in order to avoid the scale separation assumption.

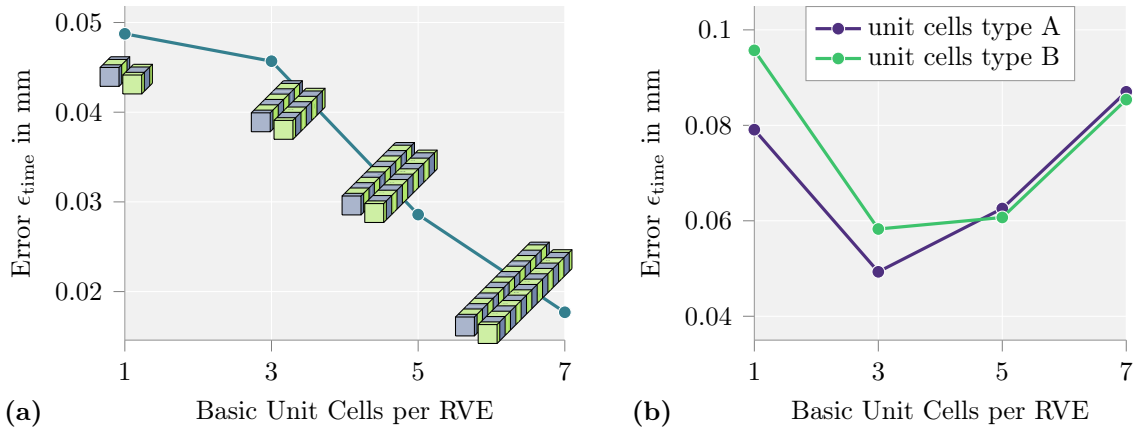


**Figure 8.5:** Analysis of different RVE choices: (a) direct comparison of RVEs with unit cell type A and B, shown with increasing numbers of basic unit cells per RVE (the error is computed as difference between the response of the two unit cell types, not with respect to the DNS), (b) error of unit cell type A and B, compared to DNS as reference. The simulation parameters are  $L = 10000$  mm,  $l_M = 2.5$  mm,  $l_{\bar{E}} = 20$  mm,  $\bar{u}_{\max} = 100$  mm,  $T = 0.01$  s,  $\Delta t = 5 \cdot 10^5$  s,  $n_{\text{timesteps}} = 400$ , from TAMSEN and BALZANI [106].

Number of Unit Cells per RVE		1	3	5	7
Unit Cell Type	$\bar{\mathbf{u}}$ -Link	Number of Time Steps			
A	$\bar{\mathbf{u}} = \langle \mathbf{u} \rangle$	1000	940	1000	1000
	$\tilde{\mathbf{u}}_{\text{corner}} = \mathbf{0}$	1000	671	634	1000
B	$\bar{\mathbf{u}} = \langle \mathbf{u} \rangle$	1000	456	1000	1000
	$\tilde{\mathbf{u}}_{\text{corner}} = \mathbf{0}$	944	420	192	166

**Table 8.1:** Number of time steps before either the simulation crashed (divergence of NEWTON iteration at microscale) or the intended complete set of 1000 time steps was successfully reached. Different choices of RVEs and constraints were analyzed.

## 8.4 Influence of Displacement Constraints

Finally the proposed displacement link  $\bar{\mathbf{u}} = \langle \mathbf{u} \rangle$  is compared to the standard boundary condition for quasi-static periodic homogenization, where the fluctuations at the RVE corner nodes is set to zero, i.e.  $\tilde{\mathbf{u}}_{\text{corner}} = \mathbf{0}$ . For the quasi-1D example considered here, this is equivalent to setting the integral over the surface equal to the corresponding macroscopic displacements, which has been taken into account in other dynamic homogenization schemes, see Section 6.6.2. The results are presented in Table ???. The same RVE choices investigated in Figure 8.5b are now compared for the two constraints. The number of time steps reached before either the calculations crashed (due to diverging NEWTON iterations at the microscale) or were finished successfully after the intended complete set of 1000 time steps are given. For this example, it is observed that using the proposed volume constraint  $\bar{\mathbf{u}} = \langle \mathbf{u} \rangle$  results in a more robust framework in terms of stability of the NEWTON-RAPHSON iterations. Furthermore, slightly smaller error values are obtained compared to the DNS reference. Especially the calculations using the unit cell type B in combination with the zero fluctuations of the corner nodes, underperformed the other scenarios. To understand the difference between the performance of the displacement links, it is necessary to examine the behavior at the RVE level.

Here the examples with the RVEs consisting of three periods of the unit cell B are further evaluated. Figure 8.6 compares the microscopic displacements for four relevant time instances just before the peak of the input wave passes through the RVEs. More specifically, the differences between the microscopic displacement fields  $\mathbf{u}$  of an RVE and the respective macroscopic displacements  $\bar{\mathbf{u}}$  are presented. To compare the DNS, an effective  $\bar{\mathbf{u}}$  has been computed as the average displacement over the associated length. Thereby, the quality of the microscopic fields can be analyzed independently from the macroscopic displacements. Using these results, the two different displacement constraint options can be effectively compared with the reference solution obtained from the DNS. The graphs show that the fixed corner constraint leads to artificially increased displacement intensities at the microscale due to the constricted boundary. These increased displacements eventually lead to extreme deformations in single elements at the microscale, crashing the simulation. The proposed volume integral displacement constraint however, leads to a softer constraint which results in a more robust computation while still enabling dynamic effects which agree well with the ones from the reference DNS. In the presented examples, the only rate dependent influences are inertia forces. In cases where rate dependent material properties are included, the influence of different displacement constraints on the overall simulation is expected to increase in favor of the proposed volume constraint.

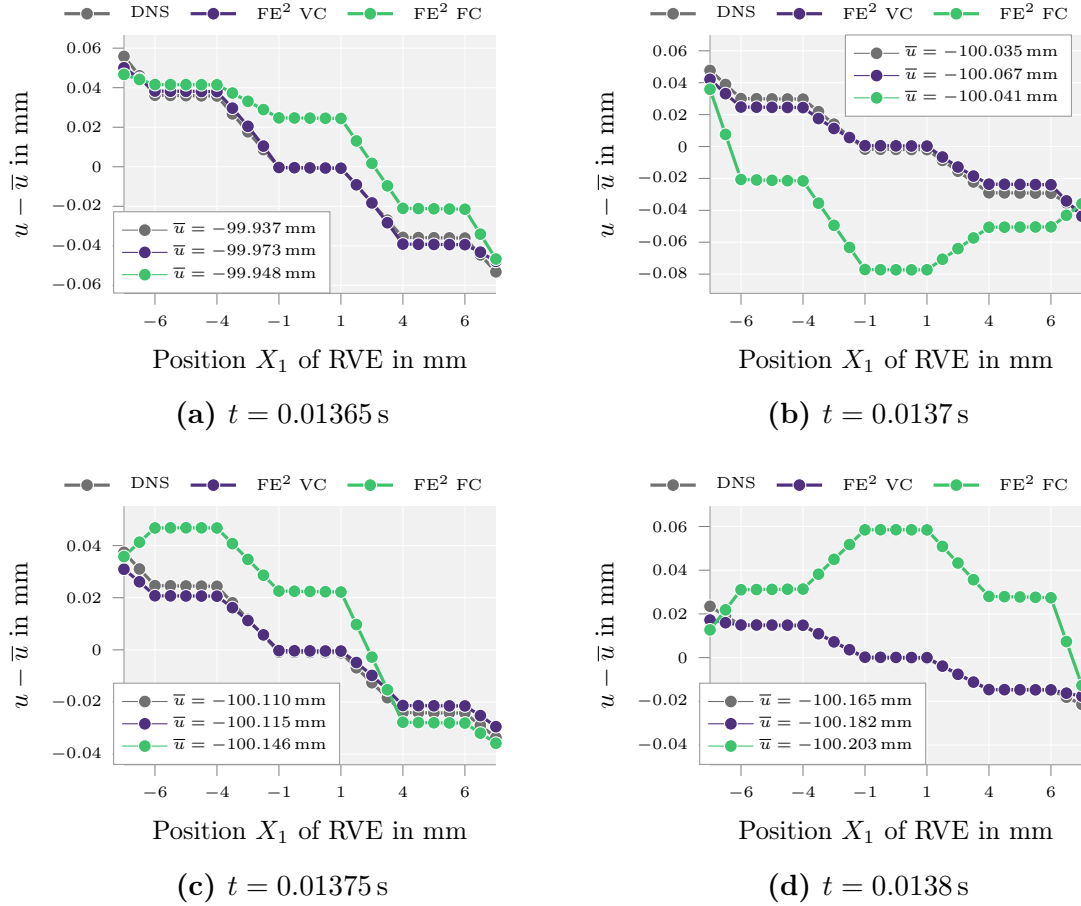


**Figure 8.6:** Comparison of microscopic displacement fields obtained from the FE<sup>2</sup> simulations with the DNS. The displacements have been normalized by  $\bar{u}$  (for the DNS, average displacement) in order to analyze the quality of microscopic displacements more or less independently of the macroscopic displacements. The two different displacement links, the volume constraint (VC) and the fixed corners (FC) are investigated. The simulation parameters are  $L = 10000$  mm,  $l_M = 2.5$  mm,  $l_E = 20$  mm,  $\bar{u}_{\max} = 100$  mm,  $T = 0.01$  s,  $\Delta t = 5 \cdot 10^5$  s, location of the macroscale integration point  $\bar{X}_1 = 7504, 23$  mm, section of the DNS displacement field from  $\bar{X}_1 = 7496.25$  mm to  $\bar{X}_1 = 7511.25$  mm, RVE with three periods of basic unit cell types B. Data from TAMSEN and BALZANI [106].

## 9 Numerical Study – Metamaterial

In the last chapter a simple example of a quasi-1D layered structure using the proposed homogenization framework was analyzed. The quadratic convergence was presented, showcasing the consistency of the tangent moduli. As a second example, a locally resonant microstructure is chosen. A brief overview of the results is published in TAMSEN and BALZANI [105]. This microstructure is characterized by an array of local resonators, in this case a heavy and stiff inclusion coated with a soft material which is placed in a relatively stiff matrix as shown in Figure 9.1. For the case of quasi-static loading the inclusion has no influence on the overall behavior. At certain loading frequencies however, the resonators lead to an effective wave attenuation. Such designed materials are classified as metamaterials, as they can exhibit properties such as an effective negative mass or bulk modulus, which are not found in natural materials. A loading frequency for which the traveling wave is completely absorbed is called a band gap, which was shown experimentally in LIU et al. [64]. The present example will mainly focus on the capability of the dynamic framework for capturing these resonant effects and then further investigate the influence of the microscopic boundary conditions on the effective macroscopic behavior. The conducted simulations are inspired by the work of LIU and REINA [63], in which the material presented in LIU et al. [64] was modeled. Note that the original material parameters reported for the experiment [64] apparently underestimate the stiffness and neglect the incompressibility of the rubber as published in STILL et al. [104]. Since the goal of this example is not to study properties of this specific metamaterial, the initially reported parameters are kept. A study of the influence of the incompressibility on this simulation can be found in KRUSHYNSKA, KOUZNETSOVA, and GEERS [53].

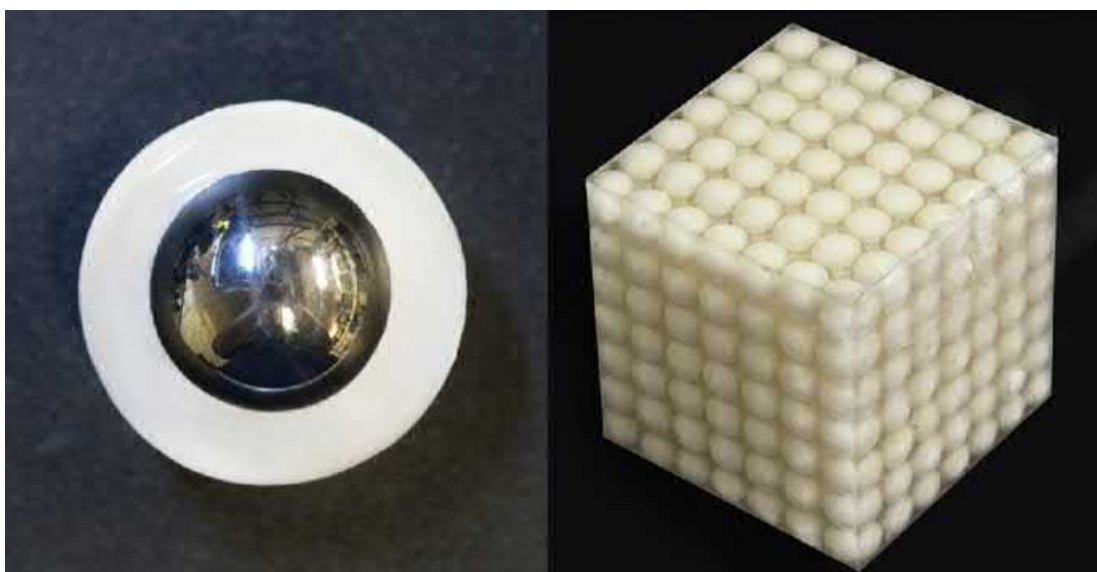


**Figure 9.1:** Acoustic metamaterial: Left, lead inclusion with rubber coating and right, the full composite consisting of multiple unit cells, from MA and SHENG [67].

## 9.1 Boundary Value Problem

An actual microstructure of a resonant metamaterial is shown in Figure 9.1, a round, coated inclusion in a matrix. To keep the computational cost of the DNS at a manageable level, the geometry is simplified as a cube, shown in Figure 9.2. The length of the cube is 20 mm, with an inclusion of 10 mm edge length and a soft layer of 2.5 mm. The material properties are listed in Table 9.1. The unit cell is meshed with  $5 \times 5 \times 5$  linear brick elements, resulting in 125 elements, with 8 nodes each, and a total of 216 nodes for one RVE. The DNS uses the same discretization for the respective unit cells. A study was conducted, using elements with quadratic shape functions, however the qualitative results were identical. Thus linear elements were chosen for the sake of a shorter computation time. The overall simulation is designed similar to in the first example (c.f. Figure 8.1) only the microstructure and loading function are changed. A displacement is applied at one end of a long row of unit cells and the induced wave is observed over time. The boundaries are fixed perpendicularly to the surface, such that transversal expansion or contraction is restricted, making it suitable to compare with the multiscale simulation, using the same assumption at the microscale. As in LIU and REINA [63], a harmonic sine wave  $u(t) = A(1 - \cos(2\pi ft))$  is applied, with the wave amplitude  $A$  and the frequency  $f$ . All presented simulations are run with  $A = 0.5$  mm, resulting in a maximum induced displacement of 1 mm. The length of the rod is adjusted according to the applied loading frequency, keeping the macroscopic element length in a constant relation to the wave period. In addition to variations in loading frequency and the macroscopic mesh resolution, three different microscopic conditions are compared: the two microscale constraints analyzed in the previous chapter, the fixed corners (FC) and the volume constraint (VC), and in addition a quasi-static microstructure (QS).

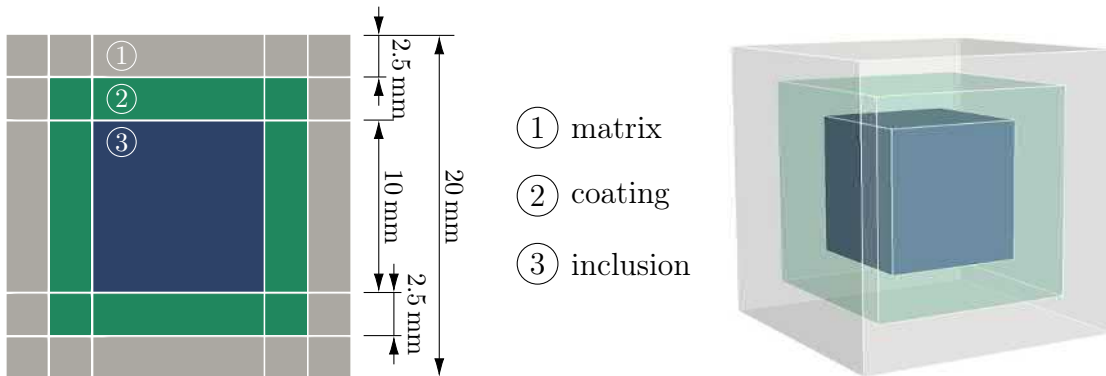


**Figure 9.2:** Finite element discretization of the approximated microstructure.

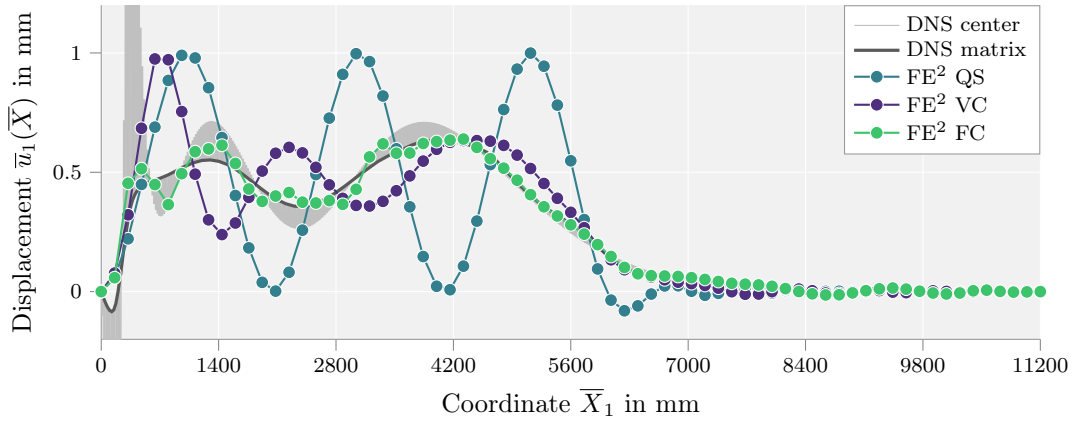
	YOUNG'S Modulus, $E$ N/mm <sup>2</sup>	POISSON'S Ratio, $\nu$ -	Density, $\rho_0$ kg/m <sup>3</sup>
Inclusion	40793.0	0.37	11600.0
Coating	0.118	0.469	1300.0
Matrix	4350.0	0.368	1180.0

**Table 9.1:** Overview of the material parameters of the different microstructural phases.

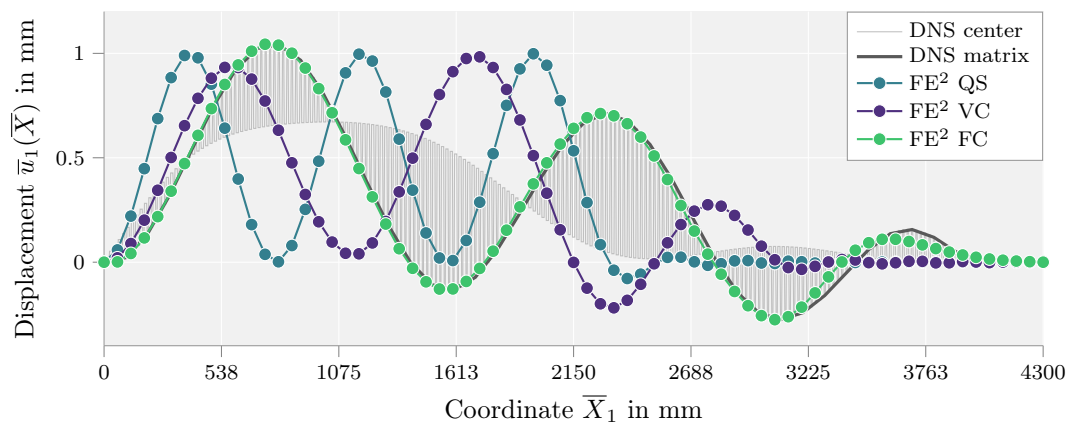
## 9.2 Initial Simulation

The analysis of this example begins by simply comparing the displacement fields of a DNS with the different microscopic conditions for two arbitrary loading frequencies: 500 Hz and 1302.33 Hz. The simulation with the 500 Hz loading is a rod with 560 unit cells in the direct simulation and thus has a total length of 11200 mm. The 1302.33 Hz simulation has 215 unit cells and a total length of 4300 mm. The  $\text{FE}^2$  calculations each uses  $\bar{n}_{\text{el}} = 70$  linear truss elements at the macroscale. Figure 9.3 shows the displacement in loading direction after three wave periods (1000 time steps), at  $t = 0.006$  s and  $t = 0.0023$  s, respectively. The gray lines show the displacement for the DNS, in light along the center line passing through each inclusion highlighting the movement of the internal microstructure, and in dark along a corner, showing only the matrix displacement. The points visualize the displacement of the  $\text{FE}^2$  macroscopic nodes for the three different microscale conditions.

First of all, it is observed that the wave amplitude for the quasi-static microstructure does not diminish, proving that the wave attenuation is a purely microdynamic effect.



(a)  $f = 500$  Hz,  $t = 0.006$  s,  $\Delta t = 6 \mu\text{s}$ ,  $L = 11200$  mm, DNS unit cells: 520,  $\bar{n}_{\text{el}} = 70$ .



(b)  $f = 1302.33$  Hz,  $t = 0.0023$  s,  $\Delta t = 2.3 \mu\text{s}$ ,  $L = 4300$  mm, DNS unit cells: 215,  $\bar{n}_{\text{el}} = 70$ .

**Figure 9.3:** Comparison of the displacement field after three wave periods, with an excitation amplitude of  $A = 0.5$  mm: for a DNS, an  $\text{FE}^2$  calculation with quasi-static microstructure (QS), an  $\text{FE}^2$  calculation applying the volume displacement constraint (VC) and an  $\text{FE}^2$  calculation using the fixed corner boundary (FC). Based on TAMSEN and BALZANI [105].

This showcases one of the unique features of the dynamic multiscale framework, as a single-scale calculation could not consider the dynamic effects of the scales separately. For this microstructure it is obvious that the microscopic boundary condition with the fixed nodes approximates the DNS significantly better, compared to the volume constraint. Both microscopic dynamic conditions show an overall wave attenuation in a similar range, although the effective wave speed of the displacement constraint appears to be slightly mismatched.

Finally, comparing the overall behavior of the two loading frequencies, one observes as expected a change in wave propagation for the dynamic microstructures. The quasi-static waves appear equivalent, as the total length and macroscale element size is adjusted in proportion to the loading frequency. Following the first observations, this microstructure is further used to analyze two additional aspects: the convergence behavior of the macroscale mesh and the resulting wave attenuation for different frequencies.

### 9.3 Macroscopic Mesh Study

The first aspect which is investigated is the sensitivity of the dynamic multiscale simulation with respect to the macroscopic mesh resolution. Figure 9.4 shows the simulation with an excitation frequency of 500 Hz at time  $t = 0.006$  s with five different mesh densities for the two regarded dynamic microscopic boundary constraints. The

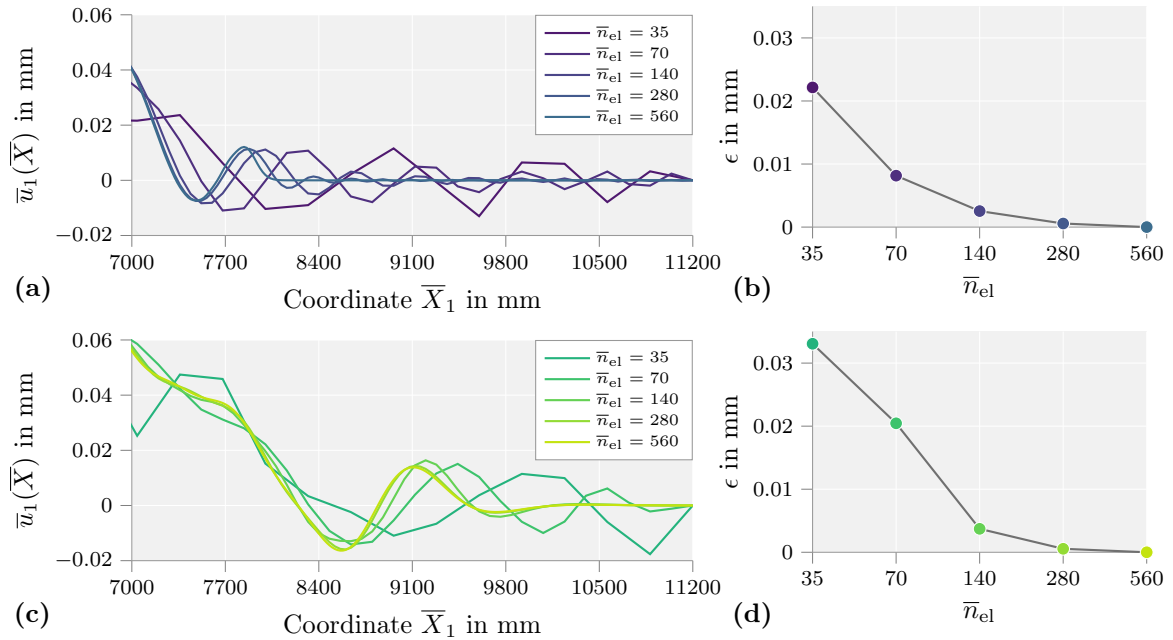


**Figure 9.4:** The displacement plot of the macroscopic problem is shown for different mesh resolutions: in (a) applying the volume constraint as well as in (c) the fixed corner constraint. Displayed is only the last section, focusing on the advancing wave front as here the differences can be observed best. In addition, the average nodal distance  $\epsilon = \frac{1}{n_{nel}} \sum_i^{n_{nel}} |\bar{u}_i^{560} - \bar{u}_i|$  for each mesh with respect to the finest discretization is plotted in (b) and (d), showing the convergence behavior.

simulation setup is identical to the one presented in Figure 9.3a. In addition to the displacement fields, an error measure  $\epsilon$  related to the finest discretization is given. This error is calculated as the average nodal distance of the inspected mesh to the corresponding nodes in the reference simulation, in this case the mesh with 560 macroscopic elements. The results clearly show a satisfactory convergence behavior for both constraints. This confirms that the differences between the two constraints as shown in Figure 9.3 are due to the boundary conditions influencing the inherent effective properties, and not a result of a poorly chosen mesh. Considering the complexity of the multiscale simulation involving a resonant microstructure, even a coarse discretization with  $n_{\text{el}} = 35$  performs remarkably well.

## 9.4 Sensitivity Regarding the Excitation Frequency

The aim of the second investigation is to understand the sensitivity of the structure with respect to the excitation frequency, which is the property that makes locally resonant materials interesting. This opportunity is also used to test two different methods for direct numerical analysis of wave attenuation. Again the two microscopic constraints are compared. Usually for this kind of frequency study a single unit cell is analyzed with respect to its eigenfrequencies, in order to calculate the theoretical band gaps. However, once additional nonlinear properties are considered, the complexity of the problem increases. LIU and REINA proposed in [63] a qualitative method based on the real-time evolution of the propagating wave. The maximum displacement along the bar is measured at a defined time, e.g. three wave periods  $t = 3T$ . The sections where maximum displacements in the resulting spectrum are relatively small can indicate the band gaps. To start, the proposed method above is demonstrated. To provide a comparable mesh size for the various loading situations, the macroscopic element length is adjusted proportional to the wave period as  $\bar{l} \approx 80000 f^{-1} \text{ mm/s}$ . The simulated bar at the macroscale was chosen sufficiently long with  $L = 140\bar{l}$ , to ensure no boundary interference at the considered times. Note that this analysis is sensitive to the selected time. For example, an evaluation for  $t = (x + 0.5)T$ ,  $\forall x \in \mathbb{N}$  will always result in

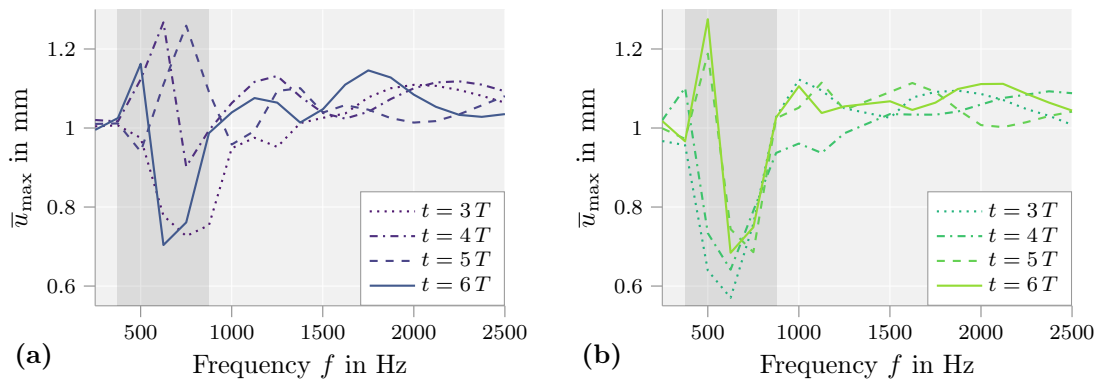


**Figure 9.5:** Maximum displacement recorded along the bar for a range of loading frequencies at four different times, comparing the two microscale boundary constraints (a) Volume Constraints and (b) Fixed Corner Constraint. The band gap is shaded in gray.  $A = 0.5 \text{ mm}$ ,  $\Delta t = T/300$ ,  $L = f^{-1} 1.11 \cdot 10^7 \text{ mm/s}$  and  $\bar{n}_{\text{el}} = 140$ .

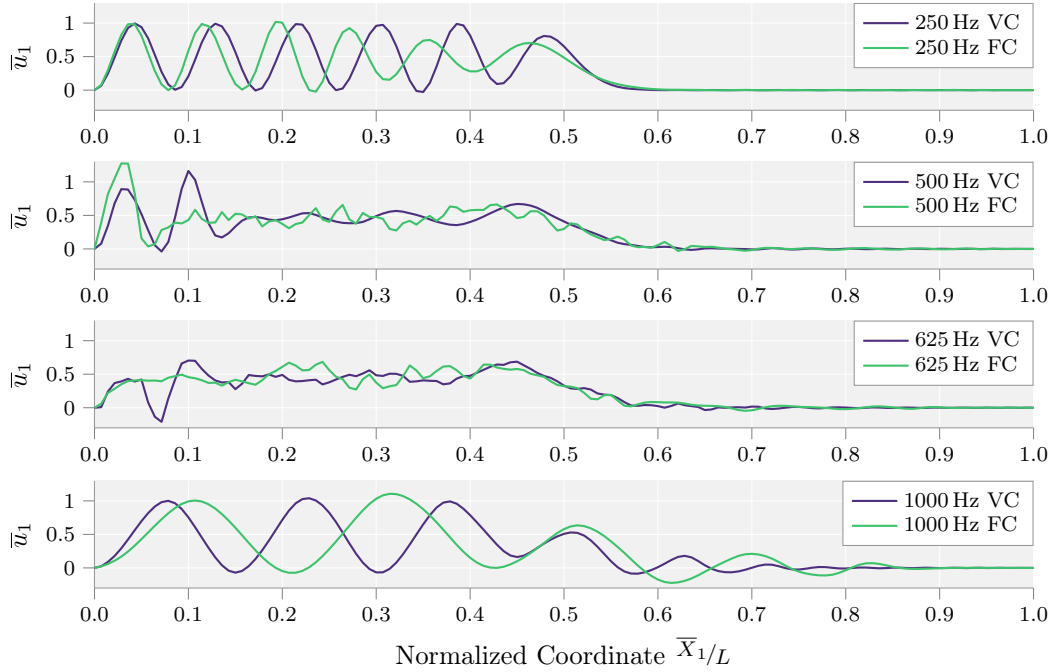


**Figure 9.6:** Full displacement field for four different excitation frequencies, plotted over the normalized bar length at  $t = 6T$ .

a maximum value of  $2A$  or larger, as this will automatically include the peak of the introduced wave. Thus,  $t = 3T$ ,  $t = 4T$ ,  $t = 5T$  and  $t = 6T$  have been chosen for the study. Figure 9.5 presents the recorded maximum displacements for frequencies ranging from 250 Hz to 2500 Hz in approximate 125 Hz increments. Both constraints exhibit a band gap between roughly 375 Hz and 875 Hz, highlighted in orange. The sensitivity with respect to the chosen time is apparent, as is shown by the peaks for the fixed corner constraint for 500 Hz at  $t = 6T$  as well as for the volume constraint for 625 Hz at  $t = 4T$ . To better understand these peaks, the displacement along the bar at  $t = 6T$  is presented in Figure 9.6 for four specific frequencies. Two frequencies lie just outside and two inside the band gap. Evidently, the waves within the band gap do not properly propagate but show a rather chaotic scattering behavior. The peaks previously observed in Figure 9.5 all occur close to the excitation boundary  $\bar{X}_1 = 0$  and do not travel along the specimen.

This observation leads to an alternative direct measurement of the band gap. Instead of plotting the maximum displacement of all nodes at a certain time, the maximum displacement of a specific node for a certain time interval is plotted. Figure 9.7 shows the resulting spectrum for nodes at  $\bar{X}_1 = 29\bar{l}$ ,  $\bar{X}_1 = 43\bar{l}$ ,  $\bar{X}_1 = 57\bar{l}$  and  $\bar{X}_1 = 71\bar{l}$  from  $t = 0$  to  $t = 9T$ . The observed band gap coincides nicely with the first method. However, the results for this method seem to be relatively invariant to the chosen location, in contrast to the initial method which is sensitive to the considered point in time. Furthermore, the differences between the two constraints have decreased. This indicates that the second method is more robust for directly measuring the band gaps.

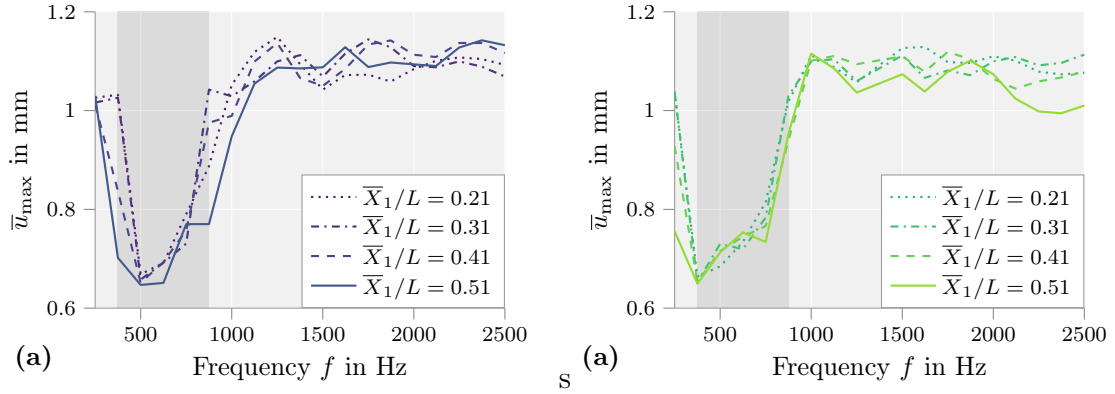


**Figure 9.7:** Maximum displacement recorded at four nodes from  $t = 0$  till  $t = 9T$ , comparing the two microscale boundary constraints (a) Volume Constraints and (b) Fixed Corner Constraint. The band gap is shaded in gray.  $A = 0.5$  mm,  $\Delta t = t/300$ ,  $L = f^{-1} 1.11 \cdot 10^7$  mm/s and  $\bar{n}_{\text{el}} = 140$ . Based on TAMSEN and BALZANI [105].

## 9.5 Remarks

It is evident that this framework is able to capture the resonant effect of the microstructure well, at least for the analyzed frequencies. This once more demonstrates its general capability of successfully capturing microdynamic effects. In contrast to the example of the layered structure, the boundary condition with the fixed nodes shows a better agreement with the DNS compared to the volume constraint. This is attributed to the fact that the macroscopic loading wave is transferred directly through the stiff matrix material. This is exactly the behavior that the fixed corner constraint is replicating. It seems that, just as with single-scale calculations, the microscale boundary conditions need to be chosen carefully according to the intended problem. Interestingly, the frequency analysis of the wave attenuation still demonstrates a good agreement of the two constraints. The following chapters will shift the focus from the general framework to the target material, strain-hardening cementitious composite.



# 10 Fiber-Matrix Bond Properties

In Chapter 2, the fiber-matrix bond has been introduced as one of the distinguishing features of SHCC. This chapter starts by giving a short overview of the theoretical background of fiber pullout. Then the testing setup used by CUROSU to obtain the experimental fiber data published in his doctoral thesis [24] is described. Following this, the measured data is presented and used to fit the material parameters of the proposed effective fiber pullout model given in Chapter 5. An overview of this is also published in TAMSEN et al. [108]. Finally, the calibrated fiber-matrix bond is then utilized to extrapolate fully embedded fiber properties to be used in the micromechanical simulation of SHCC.

## 10.1 Theoretical Background

Fiber-matrix composites can be generally characterized using the material properties of the two constituents. Homogenization methods for example can be used to predict the stiffness of the composite. When considering the fiber pullout however, the specific fiber-matrix interface must be analyzed in detail. Depending on the bond, the final result may vary from an easily pulled-out fiber up to a fiber rupture. The bond characteristic is influenced by physical and chemical adhesion, mechanical anchorage, friction, and inclination angle. To capture such bond behavior in detail, specific bond-slip laws can be formulated, which effectively consider the interface zone as a material of its own. Despite this range of factors influencing the pullout process, generalized fiber pullout can be classified into three distinct phases as shown in Figure 10.1.

**Bonded Phase** The first phase is the bonded phase, where the interface layer between the fiber and the matrix is fully intact and there are no relative slippage between the components. Deformation in this stage is considered elastic. By increasing the pullout force, shear stress is generated in the interface layer.

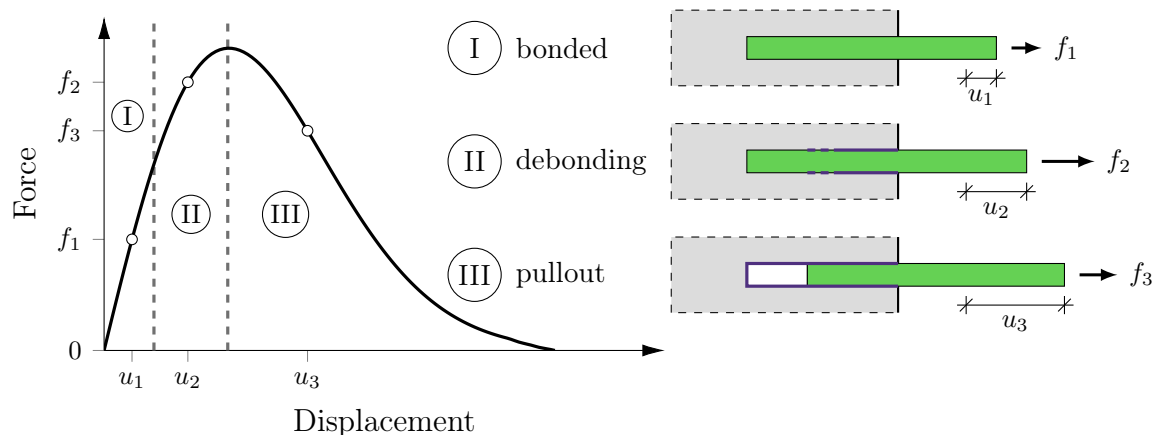


**Figure 10.1:** Sketch of the three general phases during fiber pullout.

**Debonding Phase** Once the shear stress in the interface reaches a critical value, microcracks start to propagate in the interfacial zone. Starting at the matrix surface, they gradually grow towards the embedded fiber tip. Some elastic deformation and initial sliding of the debonded section of the fiber are possible. The fiber is still anchored in the matrix until the cracks reach the end of the fiber.

**Pulling-Out Phase** When the cracks in the interface layer reach the fiber end, the embedded fiber can be pulled out. This usually coincides with the peak pullout load. This stage is characterized by frictional sliding. Depending on the composite, this phase can show behavior from strain softening, over an approximately constant friction up to strain hardening. Strain softening is observed when the interfacial zone is gradually damaged with increased slip, reducing friction and releasing shear stress. A constant friction leads to a force drop directly proportional to the remaining embedment length of the fiber. Strain hardening on the other hand is considered to be the result of fiber surface damage in soft polymer fibers, increasing the friction during slippage. In addition, mechanical interlocking due to possible matrix fragments in the fiber channel can have the same effect.

### 10.1.1 Embedment Length

Not only the material properties are relevant, but also the fiber geometry plays a significant role in the pullout process. This includes the diameter, inclination angle with respect to the loading direction and the actual shape of the fibers; e.g. steel fibers with hooked ends or soft fibers embedded with curvature. As the utilized model will only consider straight fibers of equal diameter, the most important geometrical variable to consider for modeling is the embedment length. This is a simplification, as the polymer microfibers deform during the mixing and casting process. Figure 10.2 shows a qualitative sketch of the change in force-displacement relation with increasing embedment length. Similar observations can be found e.g. in SHAN et al. [94]. The bonded phase does not change as the initiation of microcracking is invariant to the embedment length. In contrast, both the debonding and pulling-out phase are prolonged for larger embedment length. A direct result of the extended debonding phase is a higher maximum tensile stress  $f_{\max}$  in the fiber during pullout. This is the reason for a

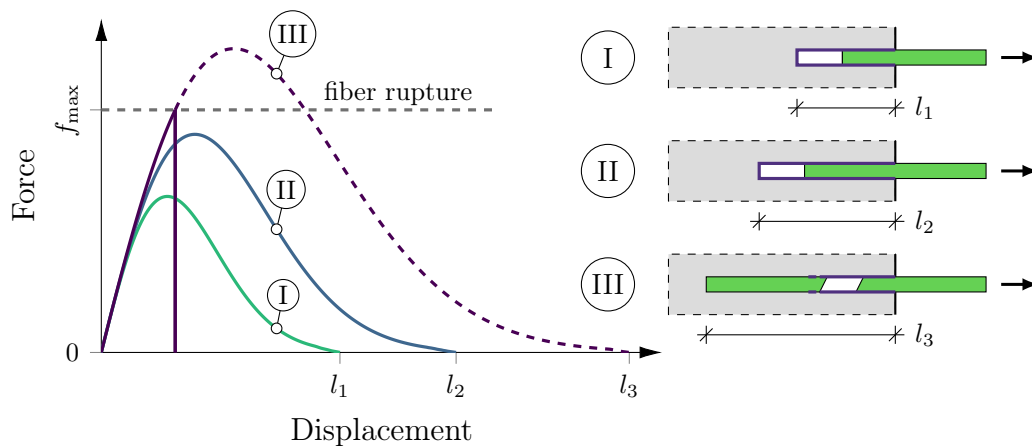


**Figure 10.2:** Sketch of the fiber pullout behavior for different embedment lengths.

shift from full fiber pullout to fiber rupture for longer embedment lengths. In addition, it explains why a weaker interface zone or shorter fibers might be advantageous for some composites, as it enables a more ductile failure compared to a brittle fracture.

## 10.2 Experimental Setup

The following experimental fiber pullout data was collected using amplified piezoelectric actuators incorporated in a steel frame, c.f. Figure 10.3. When a current is applied, the crystals expand. This leads to the transversal contraction of the frame, indicated by the arrows in Figure 10.3. The frame is fixed to the support at the top, while the bottom displacement is utilized to load the specimen in tension. The loading speed can be controlled with the applied current and is measured with the attached strain gauges. The setup has a maximum displacement of 1 mm and has been used for displacement speeds of 0.005 mm/s up to 50 mm/s. Two different tension tests are considered for the model calibration. The first is the single-fiber tension test and the second one is the single-fiber pullout test as depicted in Figure 10.4. The specimens are glued to steel bolts and screwed into the structure. A force sensor at the bottom of the specimen measures the force-time history of the process. The fibers used in the work of CUROSU [24] are the ultra high molecular weight polyethylene (UHMWP) fiber type SK62 from DYNAEEMA [29], further abbreviated as PE fibers. The reported properties are given in Table 10.1. Both tests are performed using 5 mm of free fiber length. The concrete matrix utilized for the fiber pullout test is a high strength concrete matrix, specifically designed to be used in combination with these fibers. Details on the composition of the concrete matrix are found in CUROSU [24, p.36]. All presented pullout tests were conducted with a 2 mm embedment length. Due to the maximum loading displacement of 1 mm, the data does not show the complete pullout process.

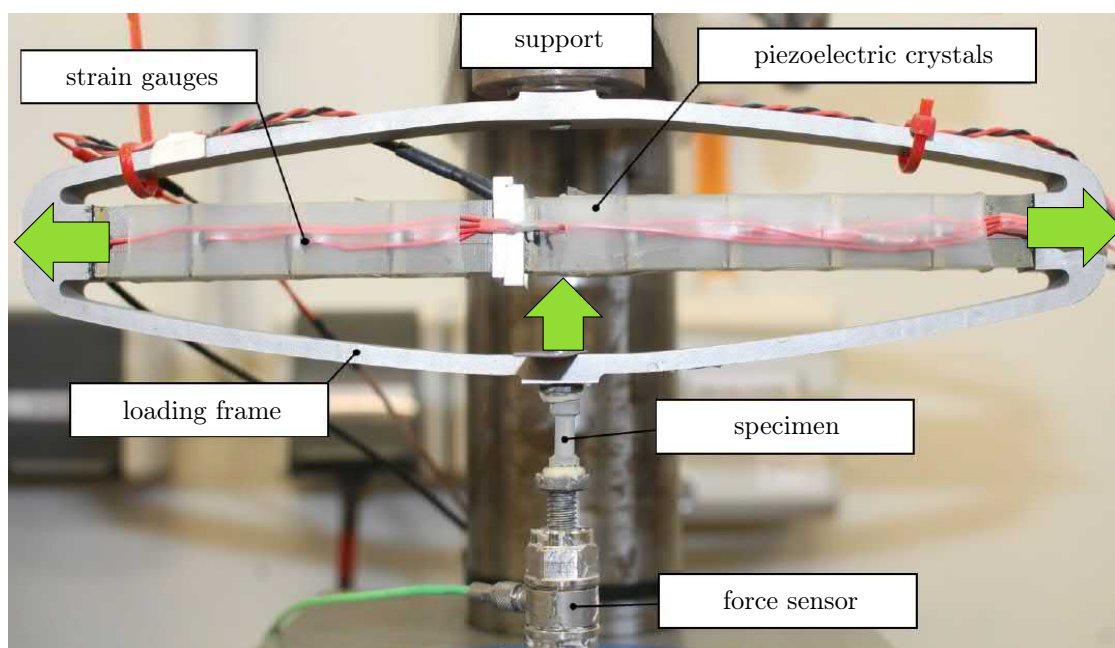


**Figure 10.3:** Experimental testing setup with a miniature concrete specimen, from CUROSU [24].

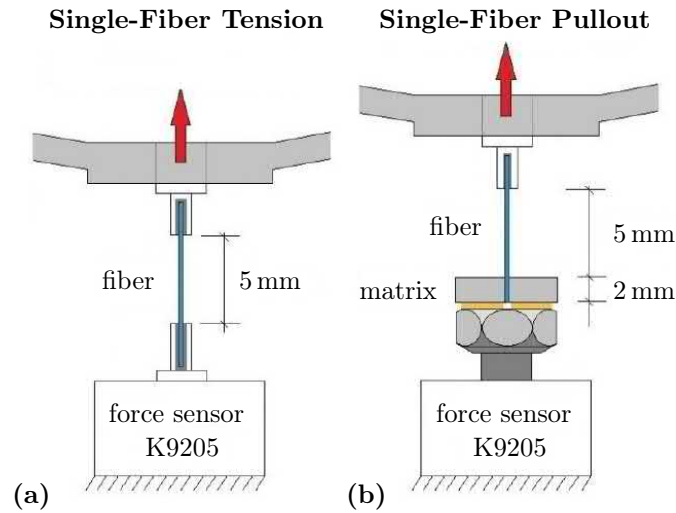


**Figure 10.4:** Experimental setup for (a) single-fiber tension and (b) pullout, from CUROSU [24].

Producer	DSM
Brand	DYNEEMA <sup>®</sup>
Material	UHMWPE
Diameter	20 $\mu\text{m}$
Density	970 $\text{kg}/\text{m}^3$
YOUNG's Modulus	80 $\text{kN}/\text{mm}^2$

**Table 10.1:** Material properties of the PE fibers, from DYNAEEMA [29].

### 10.3 Calibration of the Material Model

This section shows the step by step calibration of the material model presented in Section 5.4. The first step is the adjustment of the material stiffness  $E$  for the elastic fiber model. For this, the data of the single-fiber tension test is regarded. Numerically, this is an analysis purely based on the material model, without direct influence of the geometry. The numerical answer can be obtained with an FE program using only a single element without the need of solving a system of equations, or by directly computing the stress using the presented equation (5.7) for the relevant strains. The second step is to match the fiber pullout tests. Here the geometry is relevant, as the experimental data gives the structural response in a force-displacement plot. The experimental setup shown in Figure 10.4b is modeled using two truss elements with distinct parameters. The first 5 mm long element uses the material properties obtained from the single-fiber tension test representing the free fiber length. The second element is 2 mm long and considers the damage approach, representing the overall pullout procedure. In both steps the material parameters are first set according to the quasi-static results. Afterwards, the dynamic increase function is adjusted to match the experimental observations. As third and last step, the calibrated material properties for the 2 mm embedded fiber pullout are extrapolated to represent longer, fully embedded fibers.

### 10.3.1 Single-Fiber Tension Test

In this section, the quasi-static and dynamic material properties of the single fiber are investigated. Calibrating the elastic fiber model is a two step process, based on the data provided by CUROSU et al. [23] and CUROSU [24]. First, the effective quasi-static material stiffness is adjusted. Second, the sensitivity to the loading rate is determined. The presented strains are computed as the applied displacement divided by the initial element length.

**Quasi-Static Tension Test** In this series of experiments, five uniaxial tension tests were performed on single PE fibers. A clear nonlinear response for large displacements is shown. The loading rate of  $0.001\text{ s}^{-1}$  is considered to be quasi-static, thus free of stretch-rate effects. Based on this data the material stiffness parameter  $E$  is estimated, as the YOUNG's modulus of  $80\text{ kN/mm}^2$  given by the producer is only valid for the initial stiffness. Due to the nonlinearity of the fibers, a lower effective modulus needs to be chosen for the simulation. Figure 10.5 shows the experimental curves as well as the numerical material simulation with a chosen YOUNG's modulus of  $E = 50\text{ kN/mm}^2$ . The simulation has been fitted to match the experiments for low strain values, while accepting an overestimation of the stress for higher strains. Because the target application for this purely elastic material model is the simulation of the free fiber length in the pullout experiment, the initial stiffness is more relevant, due to the fact that the embedded part of the fibers will be pulled out before larger deformations occur in the free fiber length. In addition, due to the specific experimental testing setup, the measured stiffness has been slightly underestimated, as the deformation of the equipment is included in the strain measure.

**Dynamic Tension Test** To investigate the effect of the stretch rate on the fiber response, equivalent single-fiber tension tests were conducted at three increasing rates in addition to the quasi-static loading discussed previously. The experimental data for a total of 19 tension tests are shown in Figure 10.6a. Although the measurements show some scattering, a significant rate dependency is observed. To better quantify the dynamic increase, Figure 10.6b presents the stiffness calculated as the secant modulus

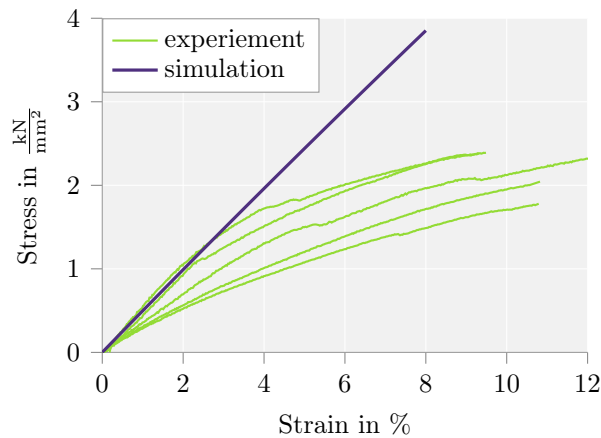


**Figure 10.5:** Quasi-static PE fiber tension tests. Comparison of numerical simulation and experimental results from CUROSU [24].

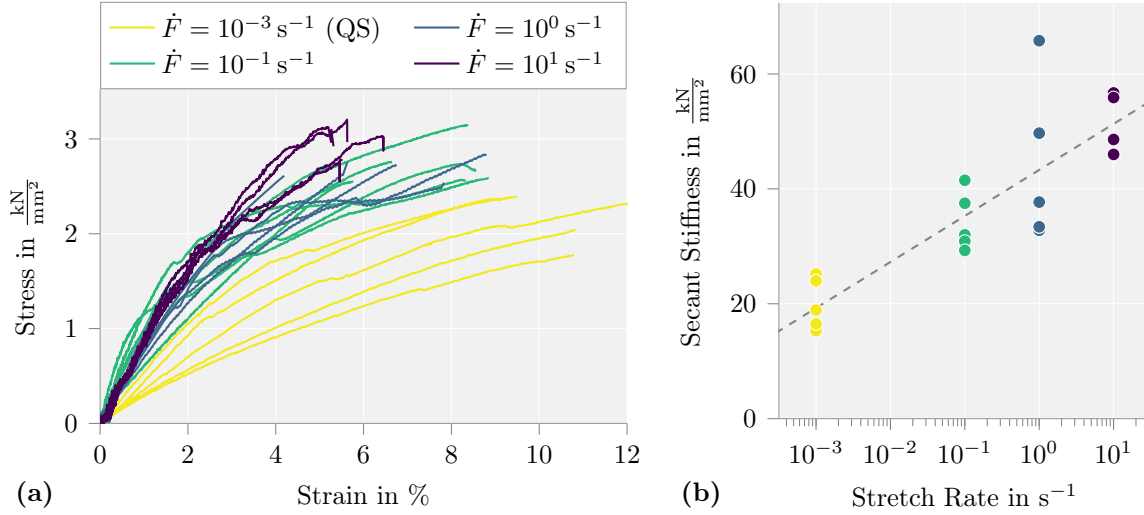


**Figure 10.6:** Experimental results of PE fiber tension tests at different loading rates: (a) stress-strain curves and (b) secant stiffness of the fibers at fracture plotted over the loading rate from [24], including logarithmic trend line.

from the measured tensile strength  $\sigma_{\max}$  in combination with the respective failure strain  $\varepsilon_{\max}$ . This should not be interpreted as the actual stiffness but it has been shown to be a good indicator of the dynamic influence. The dashed line is a logarithmic trend line, indicating that the dynamic increase might be well approximated using a logarithmic function. These results have been used to calibrate the hyperelastic material model including a stretch-rate dependent stress formulation, presented in Section 5.2. The material parameters are set to  $E = 50 \text{ kN/mm}^2$ ,  $\alpha^{\text{I}} = 0.19$  and  $\alpha^{\text{II}} = 1.8 \cdot 10^{-3}$ . The resulting stress-strain curves for the four stretch rates identical to the ones used in the experiments, are given in Figure 10.7a. To directly compare the simulation to the experiments, the dynamic increase factors (DIF) of the secant moduli are computed. The DIF is a well-known measure in dynamic experiments, and is generally defined as the regarded quantity including dynamic effects divided by a reference quantity considered static,  $\text{DIF} = \bullet_{\text{dyn}}/\bullet_{\text{ref}}$ . In contrast to the dynamic increase value  $\Omega$  defined in Section 5.2,  $\text{DIF} = 1$  represents no change due to dynamics,  $\text{DIF} > 1$  an increase and  $\text{DIF} < 1$  a decrease in the quantity. For the experimental quasi-static reference value, the average secant stiffness of  $E_{\text{sec}} = 20 \text{ kN/mm}^2$  of the five values for  $\dot{F} = 0.001 \text{ s}^{-1}$  has been used. To compute the respective secant moduli for the numerical data, approximate fracture strains have been chosen based on the observations of the experimental data. Fortunately, as a result of the relatively linear stress-strain response of the material model, the computed secant modulus is not particularly sensitive to the selected fracture strain. The resulting diagram plotting the dynamic increase of the simulated secant moduli as well as the experimentally measured ones is found in Figure 10.7b. The material model with the chosen parameters of  $\alpha^{\text{I}} = 0.19$  and  $\alpha^{\text{II}} = 1.8 \cdot 10^{-3}$  of the dynamic increase function, matches well with the experimental data.

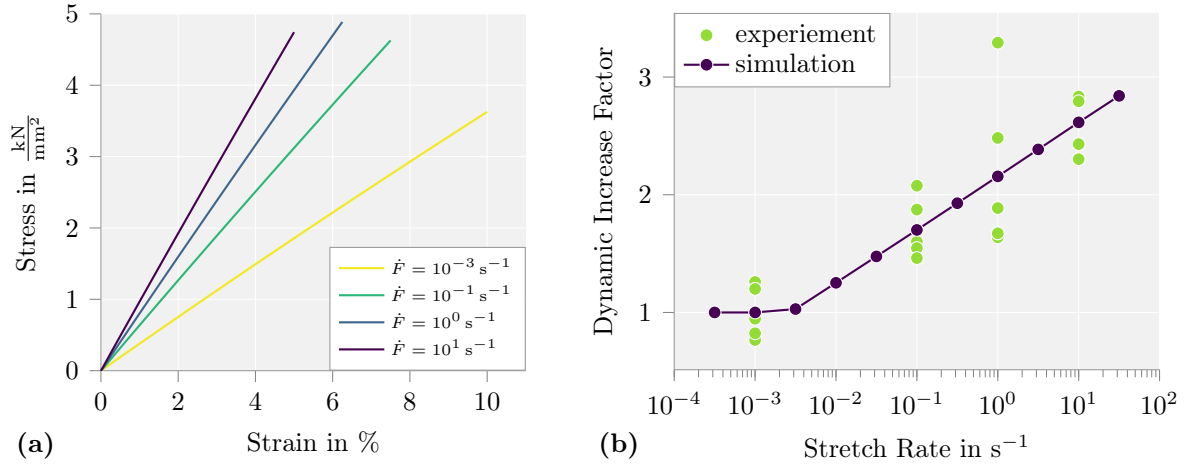


**Figure 10.7:** Simulation of single-fiber tension test with rate-dependent material properties, (a) stress-strain diagram, (b) the dynamic increase factor of the secant stiffness at fracture compared to experimental results from [24]. Data from TAMSEN et al. [108].

### 10.3.2 Single-Fiber Pullout Test

Now that the material parameters for the elastic free fiber length are set, this section deals with the calibration of the damage parameters for the embedded fiber material. As discussed in Section 10.1, fiber pullout is a highly complex procedure. The approach chosen in this work is to use a phenomenological model, based on a damage formulation to capture the relevant characteristics of the pullout process. It needs to be mentioned that this effective pullout model is a very simple approximation of the entire process. It does not consider the actual physical processes occurring during the respective periods and is a purely phenomenological approach. As will be discussed in detail in the next section, the material model is calibrated for a specific element length only. Changing the element length will directly affect the resulting material response, making it highly mesh dependent. However, the derivation and implementation of a more sophisticated fiber model, capturing the different phases in more detail, is beyond the scope of this work. The goal of our approach is to fine-tune the damage formulation such that it best matches the observed force-displacement curves from the experiments. By adjusting the damage parameters  $D_{\text{shape}}$  and  $D_{\text{rate}}$  to realize a very fast initial damage evolution followed by an progressively reduced damage rate, the observed pullout behavior can be approximately replicated.

**Quasi-Static Pullout Test** The pullout test conducted at a stretch rate of  $10^{-3} \text{ s}^{-1}$ , considered quasi-static, was performed seven times. Figure 10.8 shows the force-displacement data presented in [24] as well as the result of the numerical simulation. The experimental results scatter even more than those of the single-fiber tension test, due to the more complex interactions of fiber and matrix. However, the general phases described in the literature are easily identified. After an elastic phase, the fiber delamination leads to a peak in the force-displacement diagram at approximately 0.1 mm displacement. Then the fiber pullout initiates and is characterized by a mainly friction dominated phase. The effective material model was calibrated such that the peak of the pullout curve roughly matches that of the experimental data. An effort was made, such that the pullout phase exhibits a rather level force-displacement curve.

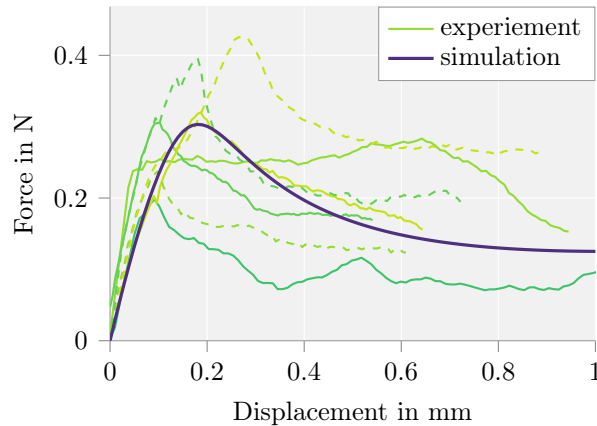


**Figure 10.8:** Quasi-static PE single-fiber pullout tests. Comparison of numerical simulation experimental results from [24].

The selected material parameters are  $E = 300 \text{ kN/mm}^2$ ,  $D_\infty = 0.998$ ,  $D_{\text{rate}} = 2.0$  and  $D_{\text{shape}} = 0.2$ . It might seem odd to increase the stiffness parameter  $E$  to values higher than the reported initial stiffness of the fiber. This is due to the choice of the damage values  $D_{\text{shape}}$  combined with  $D_{\text{rate}}$ , which results in a rapid increase in damage for small deformations, which needs to be compensated by an increase in stiffness. The advantage of the chosen parameters is that it enables the gentle softening curve, resulting in the sought-after pullout curve in Figure 10.8. This illustrates the fact that the chosen damage ansatz is only phenomenological and does not represent the complex physical processes during pullout. Even though the chosen material model is a drastic simplification, the presented effective model is able to capture relevant micromechanical aspects of the pullout behavior.

**Dynamic Pullout Test** Equivalent to the single-fiber tension test, the pullout test was performed using stretch rates of  $\dot{F} = 10^{-3} \text{ s}^{-1}$ ,  $\dot{F} = 10^{-1} \text{ s}^{-1}$ ,  $\dot{F} = 10^0 \text{ s}^{-1}$  and  $\dot{F} = 10^1 \text{ s}^{-1}$ . The experimental data together with the numerical simulations are presented in Figure 10.9. As expected, the scatter of the measured data increases with increasing loading rate. Analogous to the single-fiber tension test in Figure 10.6, a pronounced rate sensitivity of the fiber pullout behavior was observed, increasing the peak load and pullout force for higher stretch rates. The numerical simulation has been fitted to the experiments by adjusting the first dynamic increase parameter to  $\alpha^I = 0.08$ . An overview of the used parameters for the two simulated materials is given in Table 10.2.

It should be noted that the stretch rates for the numerical simulation have been applied as a displacement boundary condition. Due to the difference in material behavior of the free fiber length without a damage formulation and the embedded material responsible for the pullout effect, the stretch rates of the respective elements are neither constant nor equal. This leads to small instabilities in the calculations, indicated by the dotted lines for the simulations in Figure 10.9. The proposed phenomenological material model applied in the simulation seems to capture the experiments reasonably well. It should be noted however, that the experimental results show a general shift from a strain-softening behavior in the quasi-static regime, to a more pronounced strain-hardening behavior for higher pullout rates. Strain hardening during fiber pullout

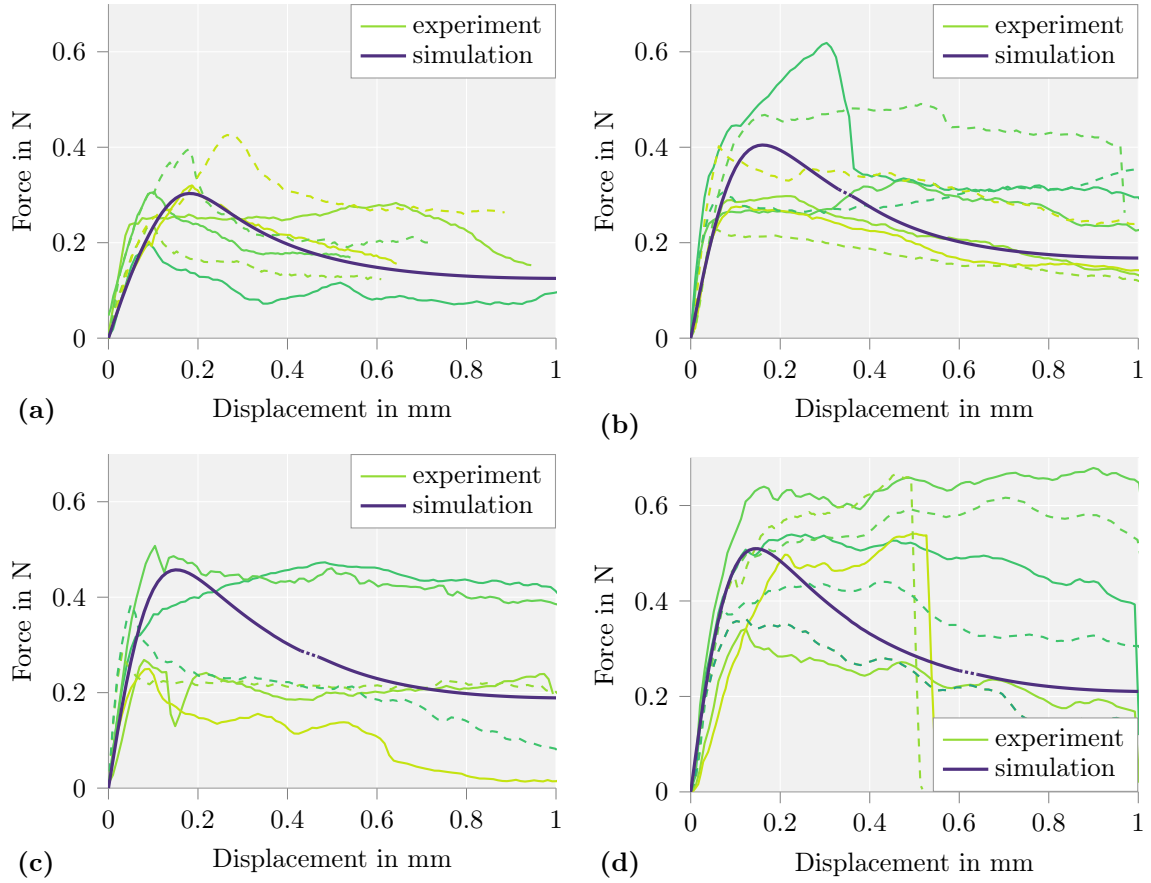


**Figure 10.9:** Simulation of single-fiber pullout test for different stretch rates: (a)  $0.001 \text{ s}^{-1}$ , (b)  $0.1 \text{ s}^{-1}$ , (c)  $1 \text{ s}^{-1}$  and (d)  $10 \text{ s}^{-1}$ . Experimental results from [24]. Numerical data based on TAMSEN et al. [108].

Parameter	Material 1	Material 2
	free fiber length	embedded fiber
$E$	$50 \text{ kN/mm}^2$	$300 \text{ kN/mm}^2$
$\alpha^I$	0.19	0.08
$\alpha^{II}$	$1.8 \cdot 10^{-3}$	$1.8 \cdot 10^{-3}$
$D_\infty$	—	0.998
$D_{\text{rate}}$	—	2.0
$D_{\text{shape}}$	—	0.2

**Table 10.2:** Overview of the parameters used in the pullout simulation.

can be explained e.g. by growing fiber surface damage with increasing slip distance, leading to higher frictional forces. The presented pullout model does not account for this detail.

### 10.3.3 Embedment Length

Up to this point, the material parameters have been adapted according to the available experimental data. However, the goal is not the simulation of a fiber pullout test. The steps so far are only for the calibration of the material parameters. Ultimately the material model is to be used in the microscale simulation of SHCC, wherein the fibers are fully embedded in the concrete matrix and have a length up to 12 mm. This is a challenge, as the implemented phenomenological fiber model has a major drawback. As briefly mentioned before, the calibrated material parameters only apply to the specific element length they were fitted for, in this case a 2 mm embedment. The problem is that data for longer, fully embedded fibers with the relevant material combination is currently not available. So far, when the length of the simulated fiber element is increased while keeping the parameters constant, the stress-strain response remains the same, whereas the force-displacement curve will change. Figure 10.10 shows the resulting force-displacement plots for increasing element length. A shift of the peak to larger displacements is observed. This is the result of lower values of the deformation gradient at the same displacement state. To be able to consider fully embedded fibers, it is necessary to extrapolate from the available experimental data, based on basic assumptions. The first assumption is that embedded fibers perform as if the crack is positioned in the center of the fiber and the debonding and pullout is occurring on one side of the crack only. As a matter of fact, the debonding would usually take place on both sides of the crack until the shorter embedment length is fully debonded. Then, a one sided pullout would commence. As the respective experimental data for dynamic two sided pullout is currently not at hand, the mentioned simplification is considered instead. This means that the material model calibrated in the last section for a 2 mm one sided pullout needs to be replicated using a 4 mm fiber element by adjusting the parameters accordingly. This has been achieved by doubling the stiffness to  $E = 600 \text{ kN/mm}^2$ , while increasing the damage rate to  $D_{\text{rate}} = 1$ . The maximum

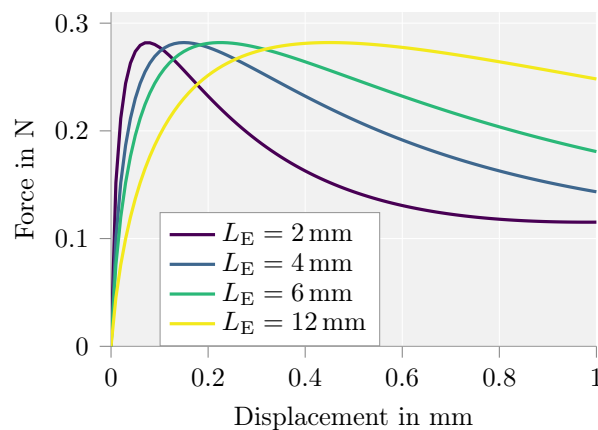


**Figure 10.10:** Quasi-static force-displacement function for different element length.

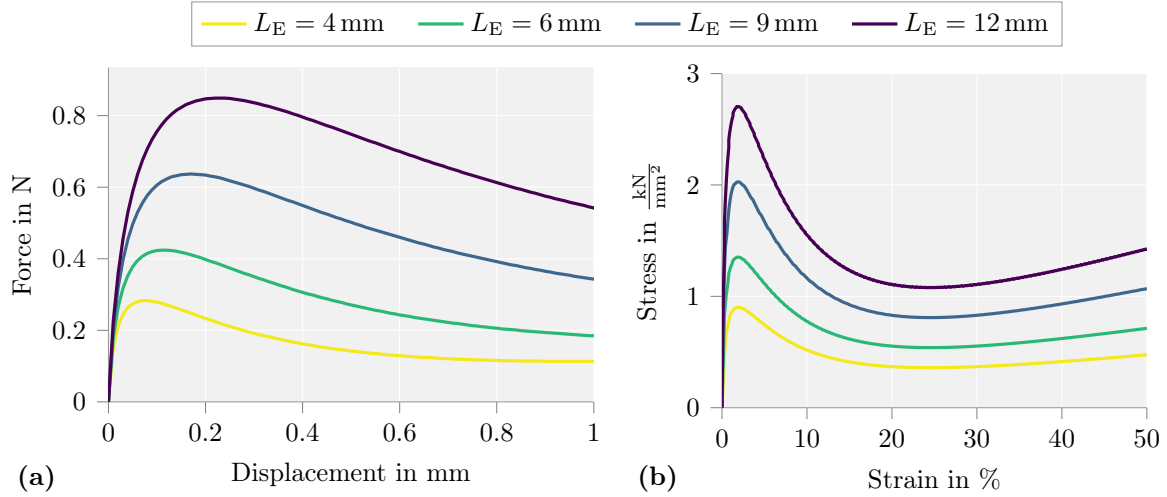


**Figure 10.11:** Proposed extrapolation of fiber embedment length by increase of material stiffness. Displayed are (a) the force-displacement and (b) stress-strain relationships for fiber length from 4 mm up to 12 mm.

damage has been adjusted slightly to  $D_\infty = 0.9982$ , to properly match the results of the single-fiber pullout test. These parameters now represent a fully embedded 4 mm fiber, based on the experimental data. The next step is to extrapolate the properties for longer fiber lengths. Physically, a change in the force-displacement answer is logical. However the initial stiffness is expected to remain the same, and the debonding and pullout should happen at a larger displacement and force. Figure 10.2 shows a qualitative sketch of the change with increasing embedment length. The depicted fiber rupture is not considered in the presented model. As Figure 10.10 shows, by increasing the element length, the effective initial stiffness is reduced. Thus, the second assumption is that longer fibers can be approximated by increasing the stiffness by a factor  $L/L_0$ , where  $L$  is the element length and  $L_0 = 4$  mm the reference length for which the simulation has been calibrated. This is a completely a priori chosen factor. The resulting force-displacement diagram and respective stress-strain curves are given in Figure 10.11. The general force-displacement behavior as discussed in Section 10.1 and visualized in Figure 10.2 is captured, c.f. Figure 10.11a. The plot of the resulting stress-strain curves is presented in Figure 10.11b. They show the expected increase in peak stress for equivalent strain values with increased fiber length.

### 10.3.4 Complete Fiber Pullout and Boundary Effects

Before continuing to the application of the fibers in multiscale SHCC computations, two more aspects need to be addressed. The first is the implementation of the full fiber pullout. The so far presented material model increases stress for any level of deformation, even when it is physically not reasonable anymore for a fiber pullout representation. The second aspect concerns fibers that intersect with the RVE boundary. Fibers that intersect with the boundary have a shorter element length than the target fibers, leading to unintended consequences in combination with introduced cracks.

**Full Fiber Pullout** The proposed model is based on the assumption of a crack located in the center of the fiber and the fiber being pulled out of the matrix on one of

the two sides. Following this, values of the deformation gradient above  $F = 1.5$  should represent a complete fiber pullout and thus not be allowed to carry loads any more (while disregarding for simplicity the elastic elongation in the fiber). This is achieved by reducing the stress  $P$  as well as the tangent modulus  $\mathbb{A}$  to approximately zero for values of  $F > 1.5$ . It is a very simplified form of an erosion method. The method needs to be combined with an internal history variable, such that if the simulated composite subsequently compresses after pullout and the assumed crack closes, the fiber should still be considered eroded.

**Boundary Effects** When considering a representative volume of a fiber-reinforced material, there are automatically fibers that intersect the boundary of the volume. As explained in the last section, a change in element length leads to an effective change in stiffness when comparing force-displacement relations. In combination with the undamaged matrix, this is not a problem. When assuming a homogeneous stretch state in the RVE, i.e. a linear displacement field, the differences in element length lead to equivalent stretch values in the respective fibers, as expected. However, once a crack is introduced, the displacement field of the matrix is no longer linear, as there is a jump in displacement around the crack. Nevertheless, the approximation of the fiber element is still linear as it has only knowledge about the two matrix nodes it is connected to. This results in different stretch states for distinct length of fiber elements, introducing an error due to boundary effects. This error results directly from the chosen representation of the entire fiber pullout as an effective material model. However it does not limit the possibility to study dynamic multiscale effects, thus making the model still acceptable for the chosen application.

**Numerical Example** To further visualize the results of the two discussed effects under quasi-static conditions, a small numerical study is conducted using a simplified single-scale simulation of an pre-cracked SHCC microstructure. As virtual specimen, a volume with the dimensions of  $10 \times 3 \times 3$  mm has been chosen, depicted in Figure 10.12a. The concrete matrix is represented by two quadratic brick elements separated by a

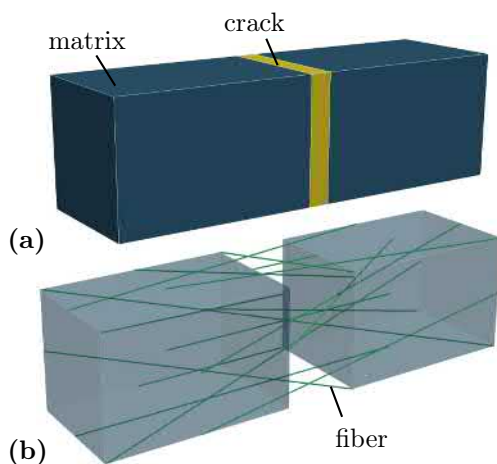


**Figure 10.12:** Simplified SHCC microstructure: (a) reference geometry with highlighted crack, (b) deformed specimen with visible fibers.

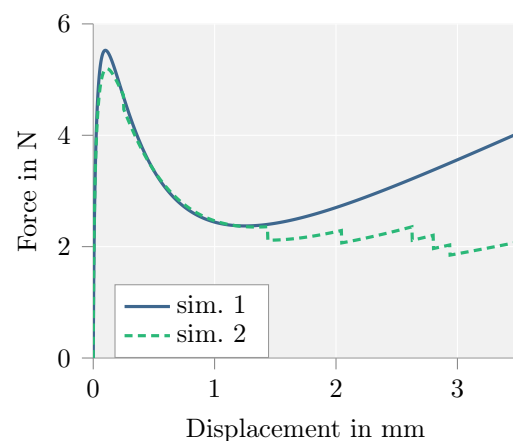


**Figure 10.13:** Pullout curves with and without a fixed reference length and activated full fiber pullout.

third, thin element acting as a crack in the matrix. The fibers bridging the crack shown in Figure 10.12b are approximated by truss elements directly connected to the nodes of the matrix. The boundaries are constrained perpendicular to the surface. A displacement boundary condition is applied at one end, loading the specimen in tension. The matrix material is approximated by a Neo-HOOKEan material law with a YOUNG's modulus of  $E = 35 \text{ kN/mm}^2$  and a POISSON's ratio of  $\nu = 0.3$ . To engage the fibers, the stiffness of the element representing the crack is set close to zero, with  $E = 10^{-7} \text{ kN/mm}^2$ . The truss elements are using the presented effective pullout model with parameters adjusted for an embedment length of 6 mm,  $E = 900 \text{ kN/mm}^2$ ,  $D_\infty = 0.9982$ ,  $D_{\text{rate}} = 1$  and  $D_{\text{shape}} = 0.2$ .

Two simulations were conducted, presented in Figure 10.13. They showcase the effect of the full fiber pullout as well as the effect of different element length. Simulation 1 is the standard computation with the full fiber pullout being inactive. The computation shows a relatively high force level for larger displacements, which is due to the fact that the short fibers quickly reach high stretch values. Comparing this to the simulation 2 where the full fiber pullout is active, the force level is reduced, as the short fibers are pulled out early. In addition, the subsequent fiber failures are clearly visible in the respective load drops throughout the simulation. The implementation of the full fiber pullout helps to reduce possible exaggerated stress levels emerging from short fibers. The observed load drops seem like a realistic depiction of a pullout curve for a fiber-matrix material, where the crack is certainly not located in the center of each crack-bridging fiber. While this is correct, this effect is unfortunately due to the previously mentioned boundary effect.



# 11 Simplified SHCC Simulation

The previous chapter handles the calibration of the material model to simulate an effective fiber pullout. The example in Figure 10.12 already shows a simplified simulation of a fiber-matrix composite, representing SHCC. However this is still a quasi-static, single-scale analysis. This chapter deals with simulations of a simplified SHCC microstructure in the proposed multiscale framework, including inertia forces at both scales. There are two sources of dynamic influence in this simulation. Firstly, the inertia forces on both scales, and secondly the chosen stretch-rate dependency of the stress in the fiber pullout model. By running simulations which consider various combinations of these two effects, a better understanding of the dynamic multiscale model for SHCC is obtained. In the following, a pre-cracked RVE is considered. Afterwards, the material model representing the crack is replaced by a model with the same initial stiffness as the matrix but including an erosion method. This enables the formation of the crack at a specific stress threshold.

## 11.1 Boundary Value Problem

Similar to the earlier dynamic multiscale examples in Chapters 8 and 9, a row of linear truss elements, representing a cylinder, is chosen as the macroscale problem. The cylinder has a length of  $L = 1$  m, a cross sectional area of  $A = 100$  cm<sup>2</sup>, a diameter of  $d = 11.28$  cm and it is discretized by 20 elements. As before, the macroscale cylinder is fixed at one end and loaded at the other via a displacement boundary condition, as depicted in Figure 11.1a. The microscale problem is shown in Figure 11.1b. The RVE is a rectangular cuboid with outer dimensions of  $10 \times 3 \times 3$  mm and discretized by 20 linear brick elements which represent the matrix of the composite. The elements in blue represent the concrete matrix, using a Neo-HOOKEan material model. The corresponding material parameters used in this chapter are  $E = 29$  kN/mm<sup>2</sup> and  $\nu = 0.3$ .

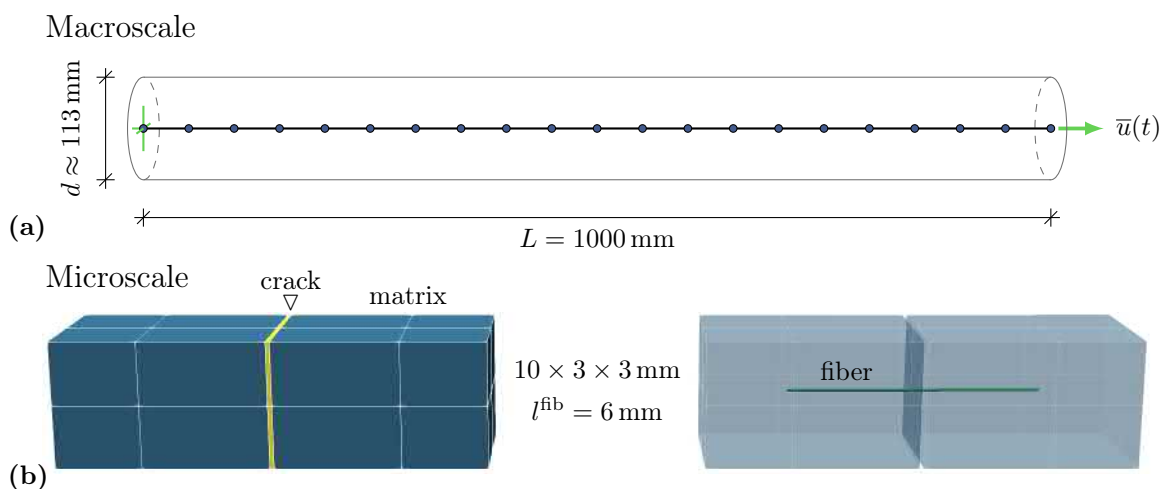


**Figure 11.1:** Multiscale boundary value problem of the simplified SHCC simulation, (a) macroscale and (b) microscale.

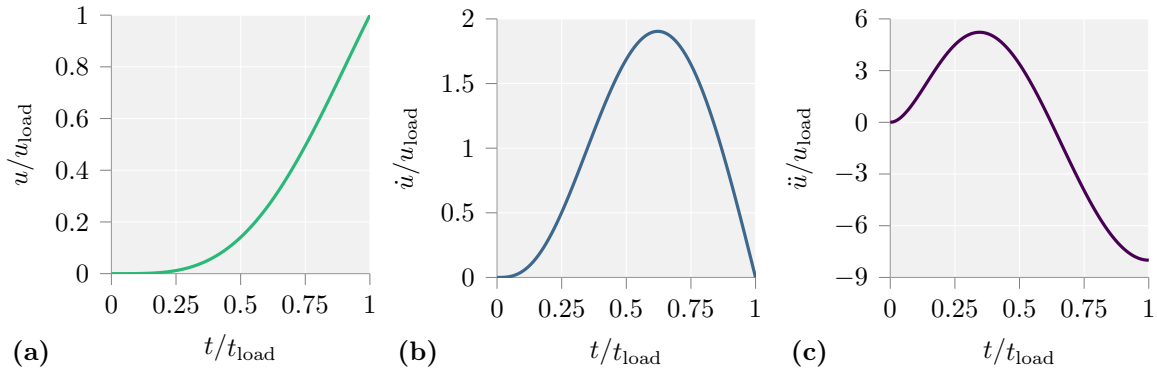


**Figure 11.2:** Normalized loading function (11.1) shown in (a) with its first and second time derivatives respectively in (b) and (c).

The yellow elements use the same material model, however with a very low YOUNG's modulus of  $E = 10^{-3} \text{ kN/mm}^2$ . They serve as a crack in the matrix. The crack has a width of  $l_{\text{cr}} = 0.1 \text{ mm}$ . The single embedded fiber is 6 mm long and located in the center of the RVE, oriented in loading direction. To approximate a realistic fiber-volume fraction the fiber cross section is chosen to be  $0.18 \text{ mm}^2$ , which is 2% of the RVE cross section. The material parameters calibrated in the last chapter for a 6 mm embedded fiber are adopted for this example.

As displacement boundary condition, a polynomial function

$$\bar{u}(t) = \frac{u_{\text{load}}}{t_{\text{load}}^8} t^4 (t - 2t_{\text{load}})^4, \quad (11.1)$$

has been chosen to roughly reflect an impact event. Two parameters control the function, such that the displacement  $u_{\text{load}}$  is reached at time  $t_{\text{load}}$ . For the following calculations the maximum displacement is kept constant at  $u_{\text{load}} = 100 \text{ mm}$ , which represents a maximum strain of 10% of the whole specimen. However, many examples will fail due to localized fiber pullout, before the maximum displacement is reached. As  $t_{\text{load}}$  is varied, it classifies the different loading scenarios, where the overall loading speed and acceleration increase with smaller values of  $t_{\text{load}}$ . Figure 11.2 displays the normalized displacement and respective velocity and acceleration over time for the chosen loading function. The displacement is continuously increased. The applied velocity is always positive during the simulation and reaches its maximum at about 3% strain. As would be expected for an impact load on a specimen at rest, there is an initial pulse of acceleration reaching its maximum value at approximately 0.4% overall strain. A function which more accurately resembles actual loading condition of impact tests is investigated in the next chapter. This chapter's focus is on the stress at the boundary where the load is applied. The recorded stress is the computed stress at the GAUSS points projected onto the boundary node, of the first element seen from the right in Figure 11.1b. It is presented in relation to the overall strain on the specimen  $\varepsilon(t) = \bar{u}(t)/L$ , which is just a more intuitive measure of the applied displacement.

## 11.2 Pre-Cracked Matrix

To investigate the respective dynamic effects, the first set of simulations apply a pre-cracked RVE which engages the fiber from the start. Three types of simulations

are compared here. The first one is a simulation considering only the stretch-rate dependency of the pullout. The second is a simulation only accounting for the inertia forces without the rate dependent fiber pullout. In the last one, both effects are combined. For each type various loading speeds are considered. Figure 11.3 shows a completely quasi-static problem as a base-line reference for strains up to 10%. As expected, the presented curve recovers the pullout behavior of the single fiber, c.f. Figure 10.11. A complete fiber pullout for this scenario will not be observed up to 33% overall strain, which corresponds to a deformation gradient of  $F = 1.5$  in the fiber elements of each RVE.

### 11.2.1 Stretch-Rate Dependent Stress

The first type of simulation investigates the influence of the stretch-rate dependency of the fiber model on the macroscopic system response. Figure 11.4 shows the stress-strain curves for different loading scenarios, ranging from  $t_{\text{load}} = 100$  s, to  $t_{\text{load}} = 1.25$   $\mu$ s. The overall simulation does not include any wave propagation since the inertia is not yet accounted for. Thus, the results can still be considered quasi-static in the sense that the stress, and with that the stretch, of each element is constant, even for a fast loading. The curves thus recover the shape of the quasi-static simulation in Figure 11.3 and only show an increase in stress, determined by the loading speed.

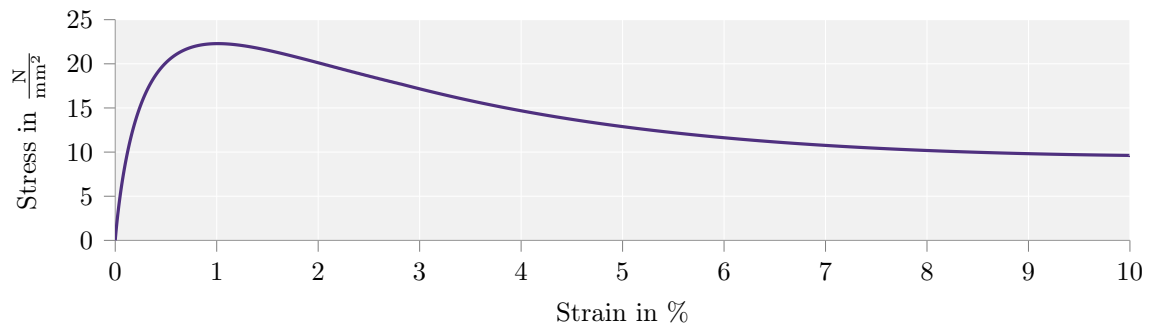


**Figure 11.3:** Stress-strain response for a quasi-static loading up to 10% strain.

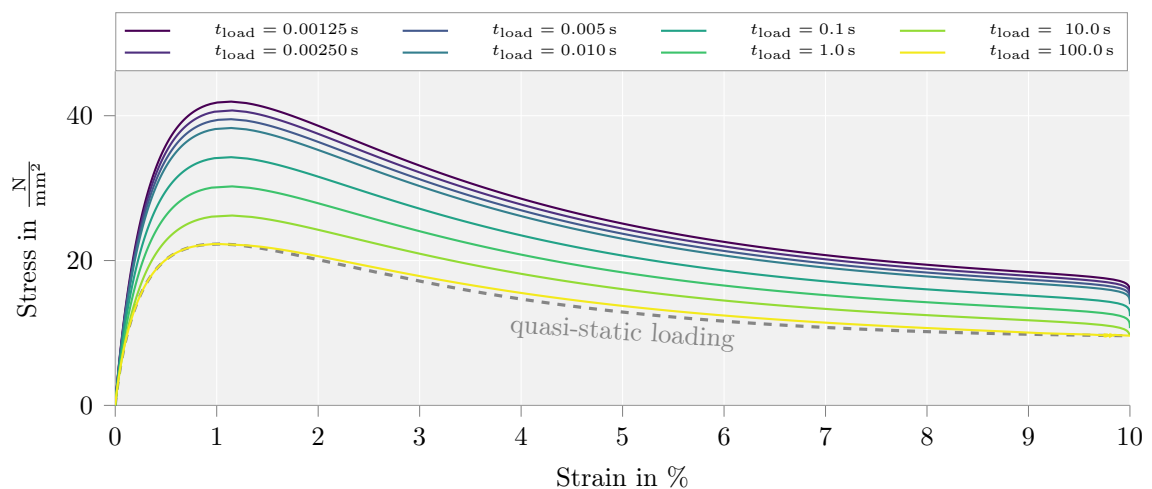


**Figure 11.4:** Stress-strain response for loading functions from  $t=100$  s up to  $t=0.00125$  s, only the rate dependency is considered.

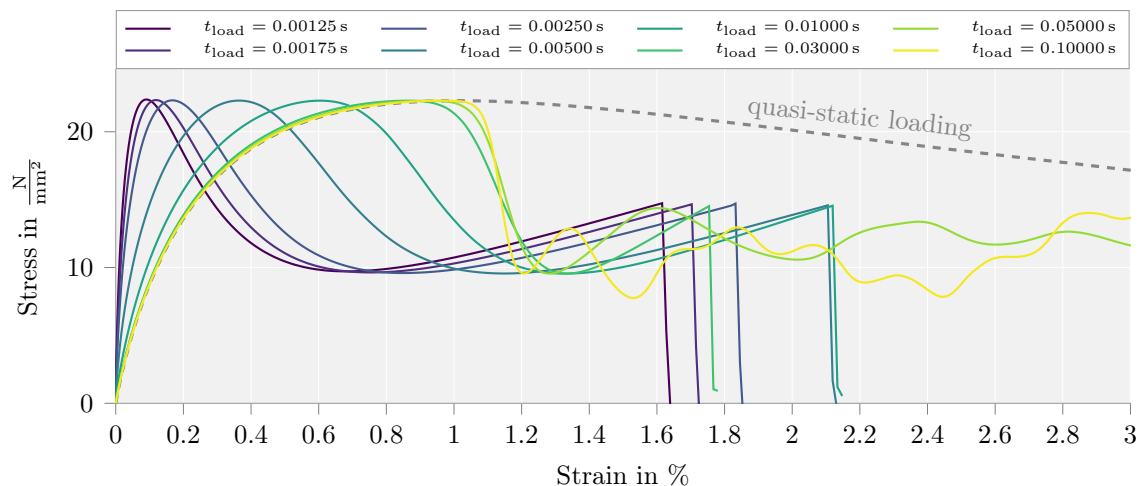


**Figure 11.5:** Stress-strain response for various loading speeds, only inertia is considered as dynamic influence.

### 11.2.2 Inertia Effects

The second type of simulation analyzes the effect of inertia on the macroscale material response. In contrast to the last problem, the applied load now travels as wave through the specimen, resulting in inhomogeneous loading conditions throughout the cylinder. Figure 11.5 presents the recorded nodal stress of the displacement boundary. For the three slowest analyzed loading speeds with the parameter  $t_{\text{load}} \geq 0.03$  s, all elements go into softening. Not until complete fiber pullout is reached with a fiber stretch of  $F > 1.5$ , is a failure in the first element observed. For faster loading rates, this behavior shifts towards a more localized pullout. Other elements still go into the debonding phase but the pullout is only observed in the first element. This effect is visible Figure 11.5 as the peak load is reached for smaller specimen strains with an increase in loading rate. To understand the presented behavior for faster applied displacements, one can imagine the inertia forces in the specimen as an effective increase in material stiffness for elements at rest. Since the load is applied as a displacement load on the node where the stress is measured, the first element is forced into the pulling-out phase before the wave is able to travel through the rest of the specimen, resulting in an early localization.

### 11.2.3 Full Dynamic Simulation

This section presents in Figure 11.6 the results of combining the stretch-rate and the inertia effects. As expected, by adding the stretch-rate dependent fiber model to the dynamic problem, the peak stress increases with loading speed as was already observed in Figure 11.4. However the resulting graphs are not just a multiplication of the purely inertial problem with a dynamic increase factor. The shapes of the plots change, suggesting a change in behavior. To visualize the effect and compare it to the two other settings, Figure 11.7 gives the value of the recorded peak stress  $\sigma_{\text{peak}}$  as well as the corresponding strain  $\varepsilon_{\text{peak}}$  with respect to the load function parameter  $t_{\text{load}}$ . The axis of parameter  $t_{\text{load}}$  is inverted, such that the effective applied loading speed increases when going from left to right. As presented in Figure 11.7b, the strain value corresponding to the peak load of the combined simulation is reached at a later stage,

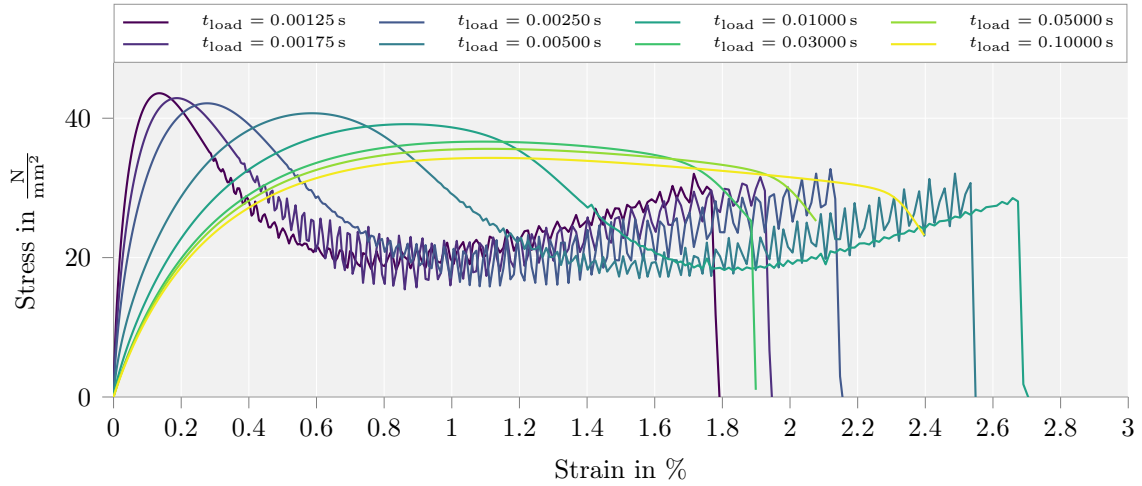


**Figure 11.6:** Stress-strain response for various loading functions, considering both the stretch-rate dependent fiber property as well as the inertia effects, with  $\Delta t = t_{\text{load}}/1000$ .

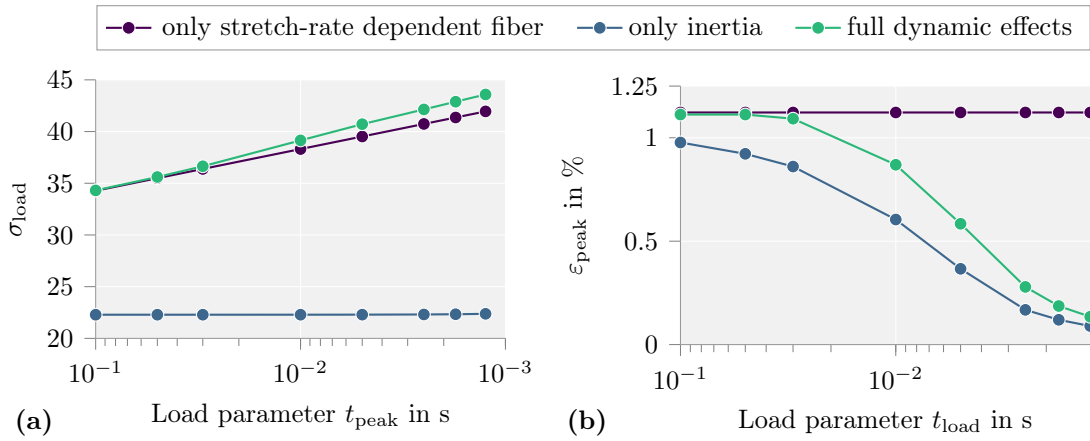


**Figure 11.7:** Comparing the peak stress (a) and respective strain value (b) of the three microstructural scenarios for various loading speeds.

compared to the inertia-only simulations. This means that a localization and with that structural failure is delayed. In addition, Figure 11.7a visualizes the peak loads. It is evident that the main increase is due to the chosen fiber model. Interestingly, even compared to the simulations which only consider the rate dependent fiber model, a further increase in peak load is observed. This is explained by localizations, which result in increased stretch rates in a single element leading in turn to the observed increase in measured stress. The oscillations recorded during the softening branch of the pullout arise at the microscale from inertia effects.

## 11.3 Matrix Cracking

So far all RVEs were considered to be pre-cracked. Nevertheless it is assumed that the cracking of the matrix is one of the mechanisms that adds to the specific energy absorbing properties of SHCC. The goal of this section is to investigate how a simplified cracking of the matrix affects the macroscopic behavior in a full dynamic multiscale simulation.

The simulation of proper crack propagation is a highly complex field and not in the scope of the current work. As a first approximation however, a simple erosion technique is implemented for the matrix, similar to the one used for the full fiber pullout, c.f. Section 10.3.4. Once the specified matrix material has reached a pre-set stress threshold  $\sigma_{cr}$  in loading direction, its stiffness is reduced to a small value, resulting in an effective crack. Because this threshold is defined at a local material point, this method is highly mesh dependent. This is not a desired quality, but can be tolerated as the focus lies on the qualitative material response. Due to the choice of truss elements directly connected to the matrix nodes, this method can not be applied arbitrarily to all matrix elements, as stress peaks at the shared nodes would lead to an erosion of the fiber anchorages. Consequently the crack location needs to be chosen before the computation, as seen with the pre-cracked examples. To reduce the impact of inaccuracies introduced by the simplified erosion method, only simulations using the same microscopic mesh will be compared.

Figure 11.8 compares the stress-strain path of the pre-cracked RVE for three different loading speeds with that of the cracking RVE. The tensile strength of the cracking matrix is set to  $\sigma_{cr} = 5 \text{ N/mm}^2$ . For  $t_{load} = 0.1 \text{ s}$ , the slowest regarded loading speed, the only relevant difference is a small peak at the start of the simulation. It captures the initial uncracked RVE stiffness up to the tensile strength of the concrete, then a sharp drop in stress is observed and the simulation follows the path of the pre-cracked matrix. This loading is slow enough that the cracking occurs quasi-simultaneously in all RVEs, with no observable dynamic effects for the macroscale. When the loading

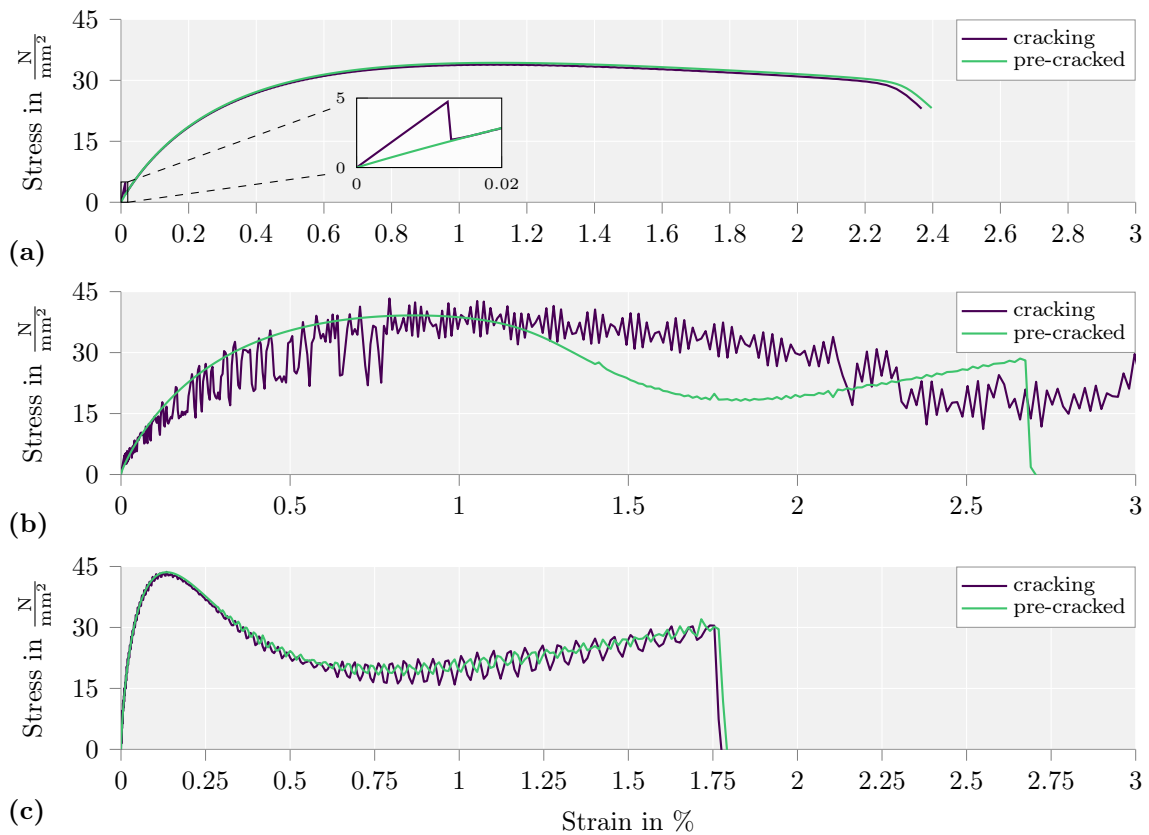


**Figure 11.8:** Comparing the stress-strain curves using a pre-cracked RVE vs. a cracking RVE, for (a)  $t_{load} = 0.1 \text{ s}$ , (b)  $t_{load} = 0.01 \text{ s}$  and (c)  $t_{load} = 0.00125 \text{ s}$ ,  $\Delta t = t_{load}/1000$ .

---

speed is increased to  $t_{\text{load}} = 0.01$  s, a macroscopic change in material behavior is seen, c.f. 11.8b. First, oscillations already appear during the debonding phase, as a result of the microdynamic effects. Second, the shape of the function changes to a more gradual overall pulling-out phase, a change already observed in Figure 11.7b when comparing inertia only and full dynamic effects for the pre-cracked matrix. This behavior occurs again due to a more dispersed pullout, instead the immediate localization in a single element. It is assumed that the combination of an increased initial stiffness and the stress increase due to the rate-dependency in the fiber after the brittle crack, lead to the delayed localization. Finally the quickest loading with  $t_{\text{load}} = 0.00125$  s, again results in the complete pullout only in the first element before the applied wave has had time to travel through the rest of the specimen. Some increased oscillations arising at the microscale are observed, however in this case they do not change the general behavior.



## 12 Split Hopkinson Bar Simulation

The previous chapter presented initial investigations of the dynamic multiscale framework with a fiber-matrix microstructure. The aim of this chapter is to replicate a specific dynamic experimental setup. This is used afterwards to show the possibilities that come with this kind of numerical tool. It enables the separate investigation of different dynamic effects, including rate dependent material behavior as well as microinertia and macroinertia. First of all, the material parameters of the fiber-matrix bond are adapted to the quasi-static experimental data. This mitigates the lack of data concerning the fully embedded fiber pullout, as well as possible discrepancies due to the simplified geometry of the microstructure. Secondly, the dynamic simulations are run, replicating the experimental loading conditions. Finally, this simulation is used to study the influence of dynamic loading on the macroscopic stress-strain relationship, by varying the loading function as well as the microscopic inertia and rate dependency. A brief presentation of the results is published in TAMSEN et al. [108].

### 12.1 Quasi-Static SHCC Tensile Experiment

This section presents the experimental setup and results for quasi-static loading. They are later used to calibrate the material parameters of the fiber model within the multiscale framework, before analyzing the dynamic effects in a subsequent section. The quasi-static testing setup is shown in Figure 12.1. The cylindrical specimen with a length of 50 mm and a diameter of 20 mm is glued at both ends to steel rings connected to steel stamps, which in turn are rigidly connected to the testing machine. Two linear variable different transformers measure axial deformations. This tensile experiment is deformation controlled, applying tensile stress with a displacement rate of 0.05 mm/s.



**Figure 12.1:** The testing setup for the quasi-static tensile test with SHCC, from CUROSU [24].

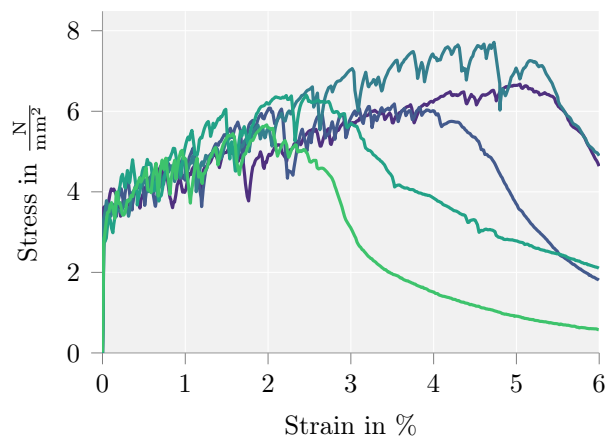


**Figure 12.2:** Experimental stress-strain curves of SHCC under quasi-static tensile loading, from CUROSU [24]. The strain-hardening and multiple cracking behavior is clearly observed.

The resulting stress-strain curves of five SHCC specimens are given in Figure 12.2. All paths show a general strain-hardening behavior, combined with multiple cracking up to 3 to 5 % strain, after which softening commences and with that the final structural failure. The initial matrix cracking is observed at a strain of approximately 0.015 % with a measured stress of around  $3.5 \text{ N/mm}^2$ . Subsequent cracks are visible by the load drops during the loading path. This is the classical multiple cracking behavior of SHCC.

## 12.2 Quasi-Static SHCC Tensile Simulation

To replicate the quasi-static experiment, a multiscale simulation analogue to the boundary value problem in Chapter 11 is used, c.f. 11.1a. The macroscale problem consists of five truss elements, each with a length of 10 mm and a diameter of 20 mm. The bar is fixed at one end and a displacement load is applied at the other. The resulting stress is measured at the boundary and the strain calculated as the applied displacement in respect to the specimen length. To ensure proper scale separation, a cubic RVE with an edge length of 1 mm is chosen, depicted within Figure 12.3a. Like in the last chapter, the RVE consists of linear brick elements, representing the matrix. The ones in the middle allow for matrix cracking. A single truss element in loading direction simulates the embedded fibers. Its two nodes coincide with those of matrix elements. The fiber parameters were adjusted to replicate the presented quasi-static experiments. The applied parameters are listed in the following:

$$\begin{aligned}
 & \text{for the matrix } E = 29 \text{ kN/mm}^2 \text{ and } \nu = 0.3, \\
 & \text{additionally for the crack } E_{\text{cr}} = 10^{-3} \text{ kN/mm}^2 \text{ and } \sigma_{\text{cr}} = 5 \text{ kN/mm}^2 \\
 & \text{and for the fiber } E = 40 \text{ kN/mm}^2, A = 0.05 \text{ mm}^2, \\
 & D_{\infty} = 0.9982, D_{\text{shape}} = 0.36 \text{ and } D_{\text{rate}} = 0.2.
 \end{aligned} \tag{12.1}$$

The resulting curve is presented in Figure 12.3. The overall fit is good, however due to the quasi-static loading, a homogeneous stress state is obtained. As there is no

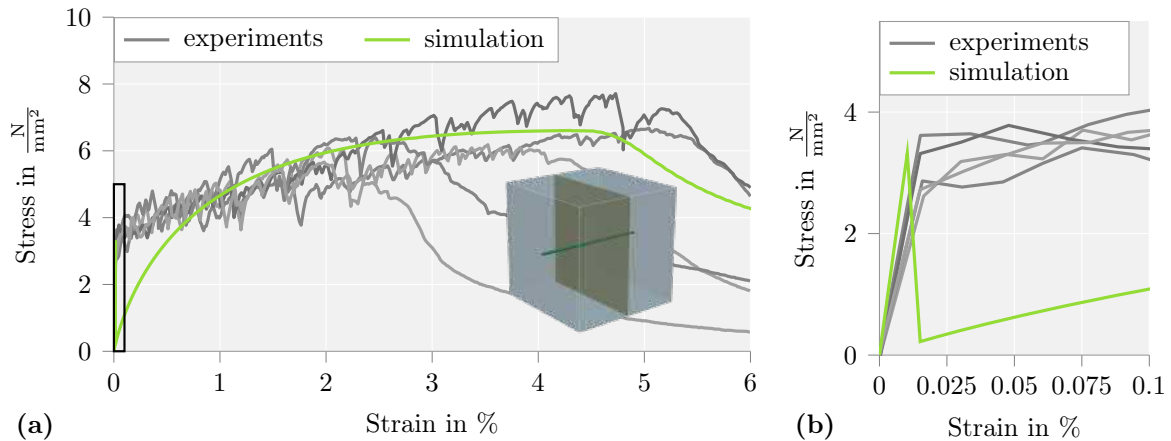


**Figure 12.3:** Results of the quasi-static multiscale simulation, compared to the experimental data. Part (a) shows the loading up to 6 % strain and depicts the selected RVE. Part (b) shows a zoomed in detail of part (a), focusing on the cracking of the matrix in the RVEs. Data from TAMSEN et al. [108].

natural variation in material parameters, all RVEs fracture simultaneously. The effect is clearly visible in Figure 12.3b, which depicts a zoomed in part of the beginning of the curve in Figure 12.3a. This explains the large discrepancy between the numerical solution and the experimental data up to 1% strain. Nevertheless, after the cracking of the matrix when the fibers are engaged, the general debonding behavior matches that of the experiment well.

## 12.3 Dynamic SHCC Tensile Experiment

The experimental test equipment to study SHCC under dynamic loads in this chapter is a split HOPKINSON tension bar. The general idea of this setup is to introduce an elastic wave into a metal bar and transmit this load into a test specimen glued to the end of the bar. A second bar is glued to the other side of the specimen to allow the wave to travel through. Using strain gauges, the applied, reflected and transmitted waves can be properly characterized and from this the material behavior deduced. There are various modifications of the original split HOPKINSON bar for tension loads, especially related to the way the load is applied. A review of several methods is found in XIA and YAO [119]. The specific setup used in CUROSU [24] and simulated in this work is a modified split HOPKINSON tension bar, by CADONI et al. [19]. The schematic in Figures 12.4 depicts the setup and identifies the individual parts. This particular system uses a pre-tension bar to generate the pulse load. A high strength steel bar is pulled on one end by a hydraulic jack, while the other end is fixed by a blocking device. By rupturing a brittle piece in the blocking device, stored elastic energy is suddenly released and transmitted into the input bar. This generates a tensile wave of trapezoidal shape of 240  $\mu\text{s}$  duration and a rise time of about 60  $\mu\text{s}$ . The generated pulse then propagates along the input bar with the wave velocity  $C_0$ , which for a solid can be approximated by

$$C_0 = \sqrt{\frac{E(1-\nu)}{\rho_0(1-\nu-2\nu^2)}}, \quad (12.2)$$

using the density  $\rho_0$  and the two elastic material parameter  $E$  and  $\nu$  of the respective material. The shape of the pulse remains unchanged while traveling along the bar.

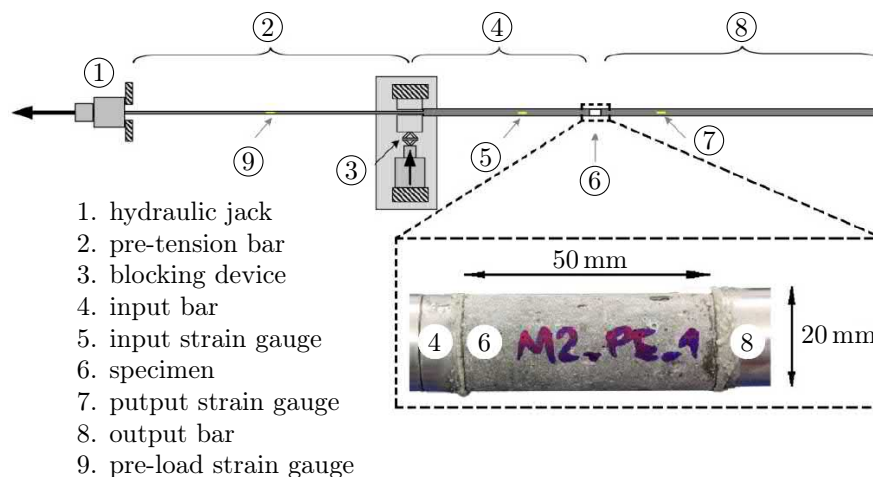


**Figure 12.4:** Split HOPKINSON tension bar setup, based on CUROSU [24].

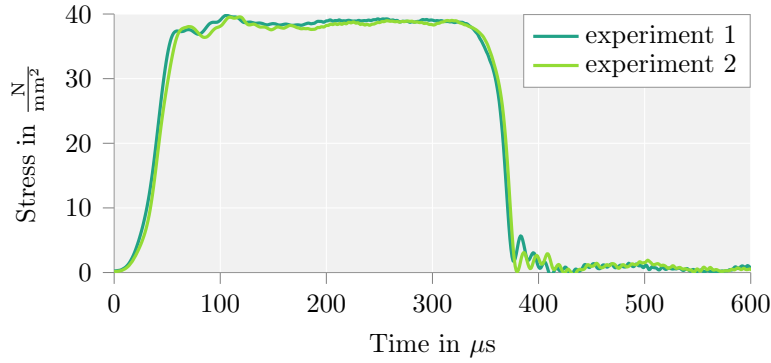


**Figure 12.5:** The characteristic trapezoidal loading pulse of the modified split HOPKINSON tension bar, as measured in the in input bar, from CUROSU [24].

Figure 12.5 shows two characteristic input waves, as measured by the strain gauge in the input bar. In this system, the two bars are made of aluminum and have a diameter of 20 mm. The input bar has a length of 3 m and the output bar a length of 6 m to ensure no interference due to wave reflections at the end of the bar. The specimen to be analyzed is sandwiched between the two bars and fixed with glue. It has the same diameter as the transmitter bars and in the analyzed experiment has a length of 50 mm, equivalent to the quasi-static test.

When the introduced wave reaches the specimen one part is reflected due to the impedance difference, while the rest travels through the specimen and propagates into the output bar. The two strain gauges on the input and output bars are used to measure the elastic deformations created on both bars by said incident, reflected and transmitted pulses, here respectively denoted as  $\varepsilon^I$ ,  $\varepsilon^R$  and  $\varepsilon^T$ . Applying the elastic, uniaxial stress wave propagation theory to the split HOPKINSON bar enables the calculation of the displacements  $u_1$  and  $u_2$  of the two faces of the specimen as well as the acting forces  $f_1$  and  $f_2$ . Following CADONI [18], the quantities are determined as

$$u_1(t) = C_0 \int_0^t (\varepsilon^I(t) - \varepsilon^R(t)) dt, \quad u_2(t) = C_0 \int_0^t \varepsilon^T(t) dt, \quad (12.3)$$

$$f_1(t) = E_0 A_0 C_0 (\varepsilon^I(t) - \varepsilon^R(t)) \quad \text{and} \quad f_2(t) = E_0 A_0 C_0 \varepsilon^T(t), \quad (12.4)$$

where  $E_0$ ,  $A_0$  and  $C_0$  are the YOUNG'S modulus, the cross section and the elastic wave speed of the aluminum bars. The stress and strain of the specimen can now be inferred by taking the average of the measured values at the boundaries between specimen and bars

$$\sigma(t) = \frac{f_1(t) + f_2(t)}{2A_S} \quad \text{and} \quad (12.5)$$

$$\varepsilon(t) = \frac{u_1(t) - u_2(t)}{L_S}, \quad (12.6)$$

with  $A_S$  denoting the cross section of the specimen and  $L_S$  its length. The resulting stress-strain plots of three specimens are presented in Figure 12.6. The quasi-static results are given in gray as comparison. It is evident that the measurements under dynamic loading show an increase in peak stress in addition to an earlier softening at

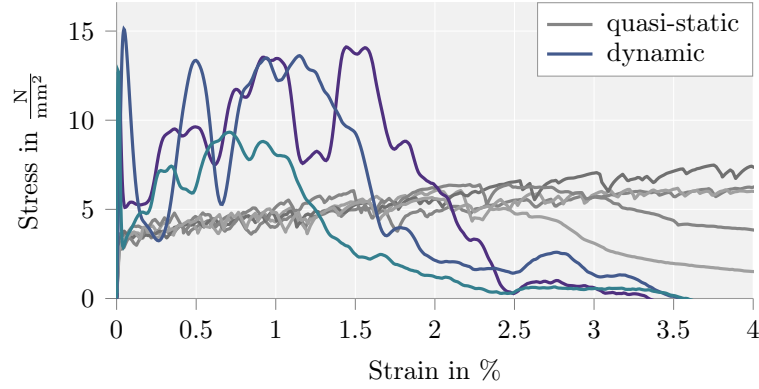


**Figure 12.6:** Experimental stress-strain curves for a tensile split HOPKINSON bar test with SHCC, from CUROSU [24]. The quasi-static results are given in gray as a comparison.

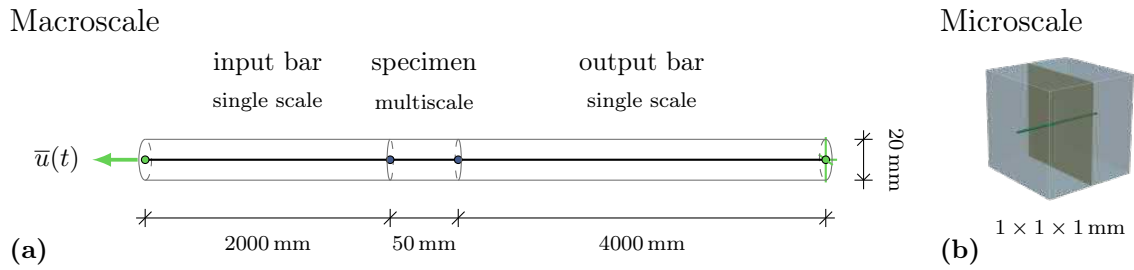


**Figure 12.7:** Schematic visualization of the boundary value problem representing the split HOPKINSON tension test. Part (a) depicts the macroscopic problem, part (b) the discretization of the SHCC microstructure applied in the multiscale simulation of the test specimen. Based on TAMSEN et al. [108].

around 1% strain. Especially noticeable is the first initial peak, corresponding to the first crack in the matrix.

## 12.4 Dynamic SHCC Tensile Simulation

This section replicates the split HOPKINSON bar experiment for the simplified SHCC RVE. The simulation is then used to analyze dynamic influences on the multiscale response.

### 12.4.1 Boundary Value Problem

To approximate the presented split HOPKINSON bar setup, a mixed simulation of single scale and multiscale elements is used. The input and output bars are simulated with standard truss elements, whereas the SHCC specimen is represented by the proposed dynamic multiscale method. The input bar is modeled with a length of 2 m, the output bar 4 m and the specimen 50 mm. A schematic is given in Figure 12.7a. To ensure a direct comparison to the quasi-static calculation, all macroscopic elements have a length of 10 mm. This results in a total of 605 macroscopic linear truss elements, of which five use the multiscale framework. The aluminum bars are modeled using a Neo-HOOKEan material formulation, with  $E = 69 \text{ kN/mm}^2$ ,  $\nu = 0.35$  and  $\rho_0 = 2700 \text{ kg/m}^3$ .

The simplified RVE used in the quasi-static calculation (c.f. Figure 12.7b) is chosen as microstructure. The applied microscale material parameters are the same as in the quasi-static calculation, c.f. (12.1). The following additional parameters for dynamics are used:

$$\begin{aligned} &\text{for the matrix and the crack } \rho_0 = 2100 \text{ kg/m}^3, \\ &\text{and for the fiber } \rho_0 = 980 \text{ kg/m}^3, \alpha^{\text{I}} = 0.08 \text{ and } \alpha^{\text{II}} = 0.51, \end{aligned} \quad (12.7)$$

where the parameters of the stretch-rate sensitivity are adopted from the fiber pullout analysis, c.f. Section 10.3.2. The most characteristic quality of the experiment to capture in the simulation is the applied loading wave.

**Loading Pulse** To properly represent the loading conditions of the experiment without the simulation of the whole pre-tension setup, the applied loading wave must be properly captured. To apply the known stress-time signals given in Figure 12.5 as a displacement boundary condition, they need to be converted to a displacement-time relation, which can be achieved by using the known material properties of the input bar. Assuming a linear stress-strain relationship, the stress signals are transformed into displacement data by a division with the bar's modulus of elasticity, a subsequent time integral of the resulting strains and a multiplication with the wave speed

$$u^{\text{inp}}(t) = \frac{C_0}{E_o} \int_0^t \sigma^{\text{inp}}(t) dt, \quad (12.8)$$

analogous to (12.3). Now  $u^{\text{inp}}(t)$  could be directly used as input signal of a boundary value problem. However, as it is advantageous to be able to not only replicate this single experiment but additionally analyze similar loading conditions with different loading speeds, the measured data is approximated by using suitable functions. A piecewise function  $\bar{u}^{\text{BC}}$  has been chosen to represent the applied load as a displacement boundary condition in the multiscale simulation. The three polynomial functions are

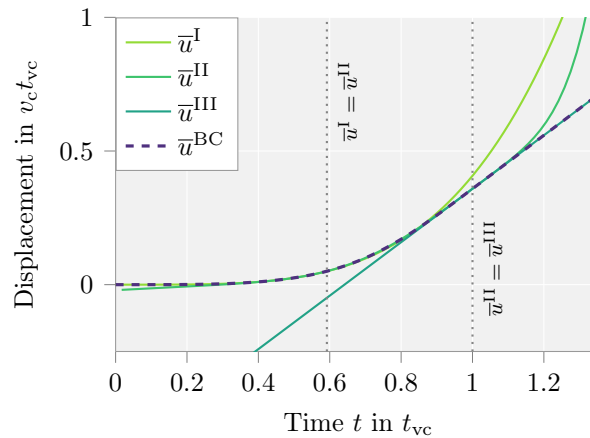


**Figure 12.8:** The piecewise displacement function replicating the experimental loading, normalized with respect to the parameters of the function.

defined as

$$\bar{u}^{\text{I}}(t) = \frac{14}{275} t v_c \left( \frac{2t}{t_{\text{vc}}} \right)^3, \quad (12.9)$$

$$\bar{u}^{\text{II}}(t) = \frac{t v_c}{275} \left[ 7 \left( \frac{2t}{t_{\text{vc}}} \right)^8 - 12 \left( \frac{2t}{t_{\text{vc}}} \right)^7 + 16 \left( \frac{2t}{t_{\text{vc}}} \right)^6 + 19 - \frac{34}{3} \left( \frac{2t}{t_{\text{vc}}} \right)^{-1} \right] \quad \text{and} \quad (12.10)$$

$$\bar{u}^{\text{III}}(t) = v_c \left( t - \frac{529}{825} t_{\text{vc}} \right). \quad (12.11)$$

The transitions between the respective functions are at  $\bar{u}^{\text{I}}(0.592 t_{\text{vc}}) = \bar{u}^{\text{II}}(0.592 t_{\text{vc}})$  and  $\bar{u}^{\text{II}}(t_{\text{vc}}) = \bar{u}^{\text{III}}(t_{\text{vc}})$ , such that the loading function is defined as

$$\bar{u}^{\text{BC}}(t) = \begin{cases} \bar{u}^{\text{I}}(t) & 0 \leq t \leq 0.592 t_{\text{vc}} \\ \bar{u}^{\text{II}}(t) & 0.592 t_{\text{vc}} < t \leq t_{\text{vc}} \\ \bar{u}^{\text{III}}(t) & t > t_{\text{vc}} \end{cases} \quad (12.12)$$

The four functions are visualized in Figure 12.8. Two parameters are used to shape the function, chosen to be easily identified by the experimentally measured data. The first parameter  $v_c$  gives the constant displacement velocity during the stress plateau, which is the slope of  $\bar{u}^{\text{III}}$ .  $t_{\text{vc}}$  defines the time the constant velocity is reached. For dynamic problems not only the displacements, but the velocity and accelerations are of relevance. It is therefore important to verify that the time derivatives of the displacement as are properly approximated. Figure 12.9 thus compares the chosen loading function  $\bar{u}^{\text{BC}}$  and its first and second time derivatives  $\dot{\bar{u}}^{\text{BC}}$  and  $\ddot{\bar{u}}^{\text{BC}}$  to the respective quantities of the two measured input waves. The loading parameters are set to  $t_{\text{vc}} = 60 \mu\text{s}$  and  $v_c = 3540 \text{ mm/s}$ . The chosen function approximates the observed experimental loading well. The actual loads are similar to the ones chosen a priori in the last chapter, c.f. 11.2. However, after the initial acceleration pulse at  $t = t_{\text{vc}}$  the load transitions into a phase of constant velocity. Changing the parameter  $t_{\text{vc}}$  modifies the rise time of the loading function. Reaching the stress plateau in a shorter time requires higher acceleration values, a longer rise time reduces the maximum acceleration. Varying  $v_c$ , results in a change in stress plateau as well as a change in maximum acceleration.

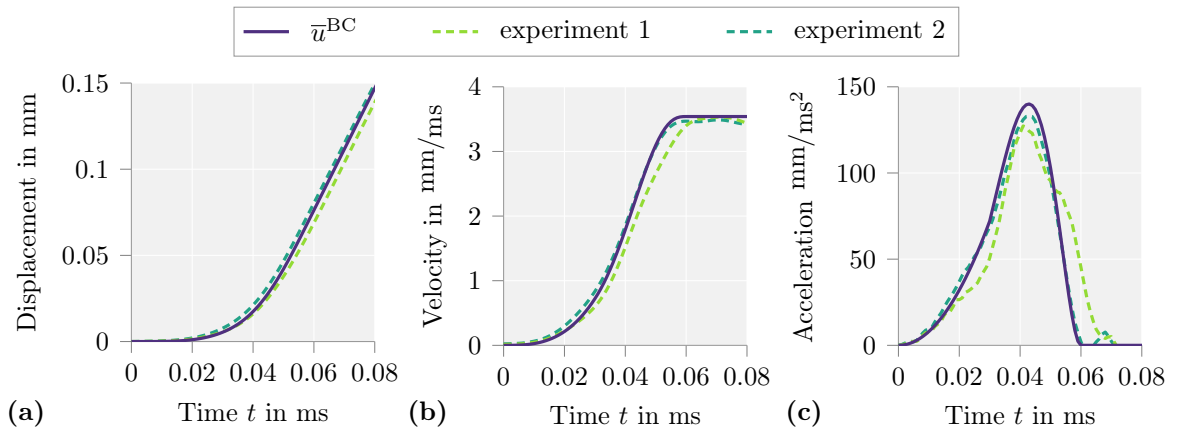


**Figure 12.9:** Loading function  $\bar{u}^{\text{BC}}$  (12.12) and its first two time derivatives, compared to the two measured experimental loads from CUROSU [24], with  $t_{\text{vc}} = 60 \mu\text{s}$  and  $v_c = 3540 \text{ mm/s}$ , from TAMSEN et al. [108].

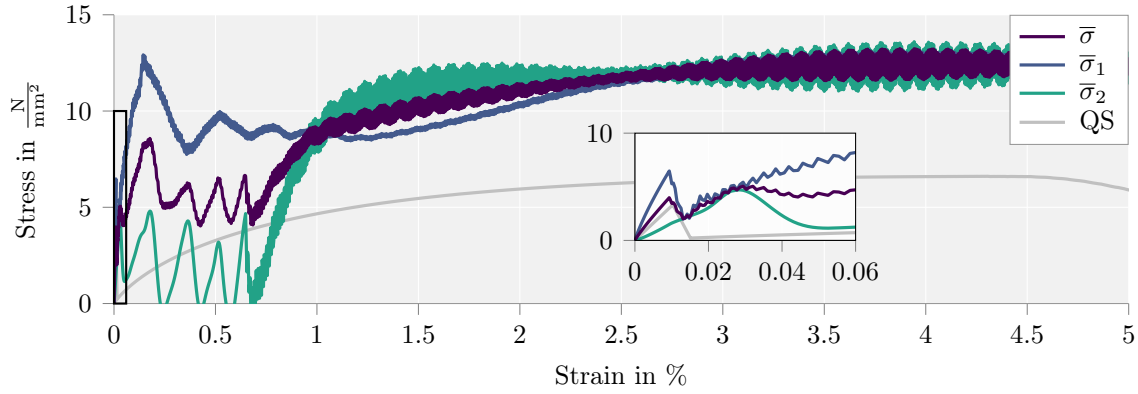


**Figure 12.10:** Results of the split HOPKINSON bar simulation. Stress-strain signals at both interfaces ( $\bar{\sigma}_1$ ,  $\bar{\sigma}_2$ ) as well as their average ( $\bar{\sigma}$ ). The zoom shows the initial cracking of the matrix. The quasi-static results (QS) are given as a reference.

## 12.4.2 Results

Analogously to the experiment, the stress and displacements are recorded during the simulation on the two interfaces between the test specimen and the bar. The strain  $\bar{\epsilon}$  is given as the overall strain of the specimen and the stress  $\bar{\sigma}$  as the average of the two signals  $\bar{\sigma}_1$  and  $\bar{\sigma}_2$ , c.f. (12.6) and (12.5). All three resulting stress-strain curves are given in Figure 12.10. The stress increase due to the dynamic loading is clearly visible when compared to the quasi-static results. Later on it will be analyzed in more detail. Another important qualitative difference to the quasi-static results is that the stress drop after the first crack is less pronounced. As the stress distribution in the sample is no longer homogeneous, it therefore leads to the cracking of the matrix at the microscale at different points in time for each RVE. Thus, the effect of multiple cracking can be observed. When comparing the two stress signals  $\bar{\sigma}_1$  and  $\bar{\sigma}_2$ , a difference is observed which is larger than just the time it would take for the loading wave to travel through the sample. The stress measured at the output bar only increases significantly once all cracks are formed. Afterwards, the stress equilibrium is reached. To further understand the process, first a study regarding the loading parameters is conducted. Then the influence of microinertia and the fiber models rate dependency are studied.

**Parameter Study –  $t_{cv}$**  To understand the influence of the applied loading, the parameter  $t_{vc}$  is varied. It sets the rise time of the loading pulse. A smaller  $t_{vc}$  value represents a faster rise time, thus more acceleration. By variation of this parameter it is possible to visualize the influence of the initial acceleration on the measured signal. The main difference is observed in the initial phase up to 1% strain, before stress equilibrium is reached. To better understand the effects, the two signals  $\bar{\sigma}_1$  and  $\bar{\sigma}_2$  are each analyzed in a separate plot, given in Figure 12.11. With increasing acceleration, i.e. a shorter rise time  $t_{vc}$ , the initial peak at the input face increases, as well as the subsequent macroscopic stress fluctuations. However, the transmitted stress at the output face does not change much. The only noticeable difference is a slight delay in stress increase for faster applied loads. This apparent delay is a simple result of the analyzed properties, as for a constant wave speed through the specimen the wave

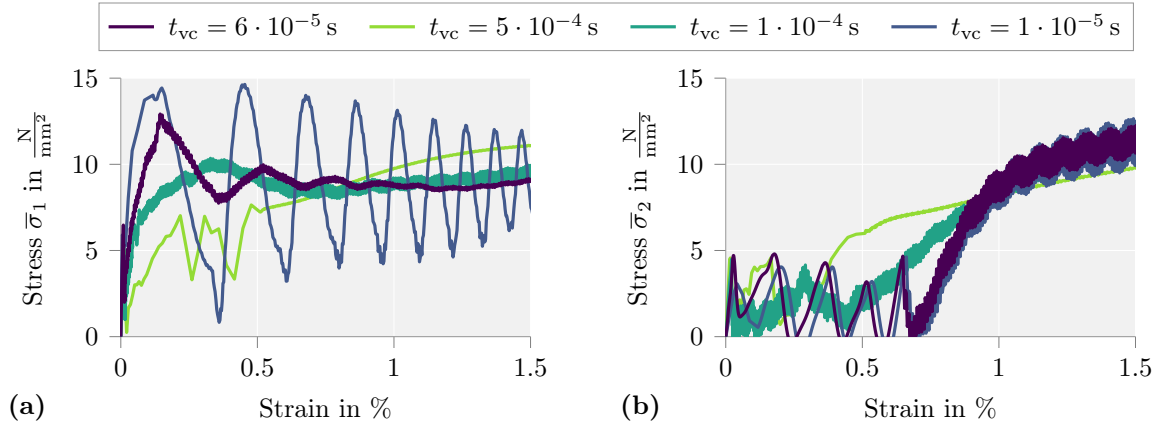


**Figure 12.11:** Analysis of the variation in rise time  $t_{cv}$  from  $5 \cdot 10^{-4} \text{ s}$  to  $10^{-6} \text{ s}$ , with  $v_c = 3540 \text{ mm/s}$ . Plot (a) depicts the signal  $\bar{\sigma}_1$  at the input face and (b) the respective signal  $\bar{\sigma}_2$  at the output face.

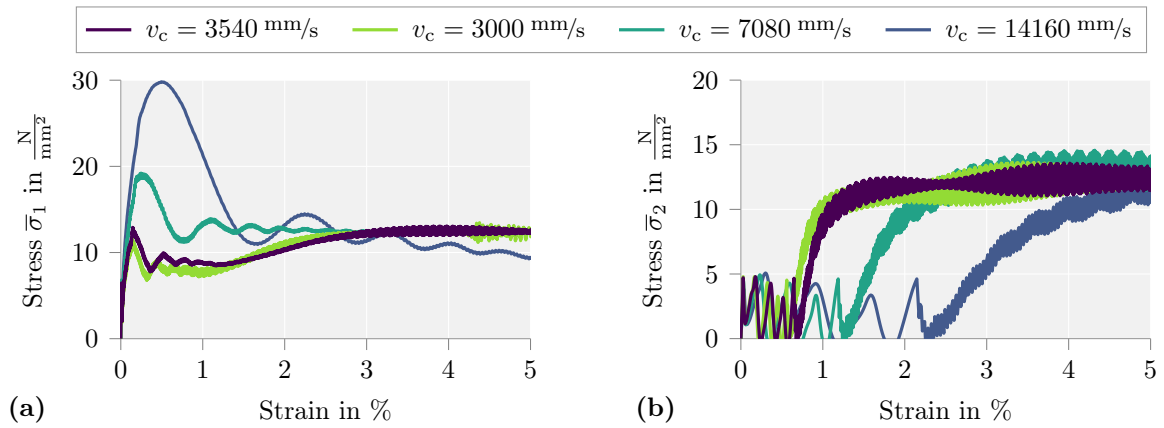


**Figure 12.12:** Analysis of the variation of  $v_c$  from  $2000 \text{ mm/s}$  to  $14160 \text{ mm/s}$ , with  $t_{cv} = 6 \cdot 10^{-5} \text{ s}$ . Plot (a) depicts the signal  $\bar{\sigma}_1$  at the input face and (b) the respective signal  $\bar{\sigma}_2$  at the output face.

front will reach the output face at larger overall strains when the load is applied more quickly.

**Parameter Study –  $v_{cv}$**  The second investigated loading parameter is  $v_c$ , it controls the constant loading velocity after the initial acceleration phase. Increasing the constant velocity leads to a higher stress level of the loading pulse, c.f. Figure 12.5. In spite of keeping the rise time  $t_{vc}$  constant, the maximum acceleration increases with increasing  $v_c$  as the higher speed needs to be reached in the same time frame. The resulting stress-strain curves are depicted in Figure 12.12. The two main effects of increasing the loading acceleration, as observed in the previous parameter study are again observed. For increased  $v_c$ , there is an initial stress peak at the input face and a delayed stress increase at the output face. In contrast to the variation of  $t_{cv}$ ,  $v_c$  changes not only the initial loading phase but the overall stress-strain curve, here displayed for strains up to 5%. The first stress peak observed in Figure 12.12a is a result of the stretch-rate sensitivity of the fibers and the macroscopic inertia. In addition, with increasing  $v_c$  the stress equilibrium is reached only at larger strains.

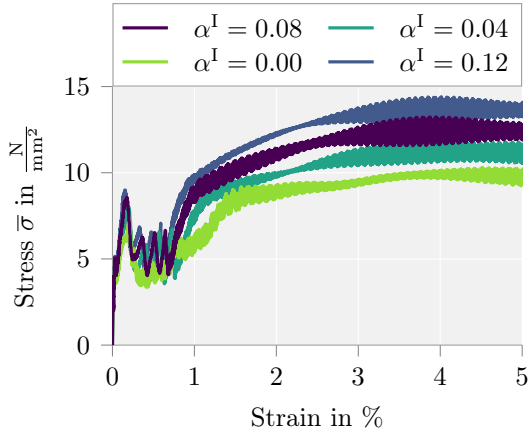


**Figure 12.13:** Analysis of the variation of the parameter  $\alpha^I$  from 0 to 0.12.

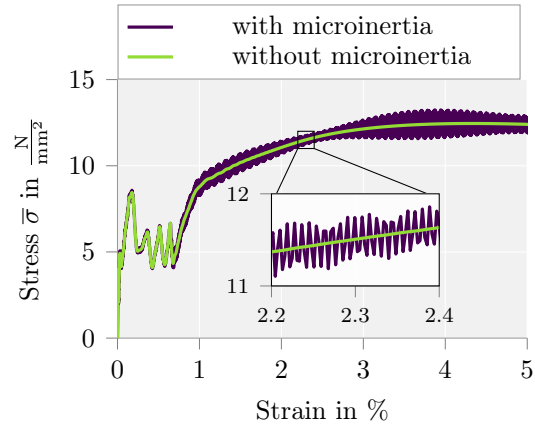


**Figure 12.14:** Analysis of the influence of microinertia on the macroscopic response.

**Parameter Study – Stretch-Rate Sensitivity of the Fiber** After showing the influence of the chosen loading conditions on the stress-strain curves, the dynamic influence of the microscale simulation on the macroscopic response is analyzed. First the stretch-rate sensitivity is studied. The full simulation, c.f. Figure 12.10 is compared to a simulation with no stretch-rate sensitivity as well as two simulations with a change in the parameter  $\alpha^I$ , as defined in (5.9). This time the stress average  $\bar{\sigma}$  of the two stress signals is given, as the overall change due to the stretch-rate sensitivity is invariant to the measured location. The results are presented in Figure 12.13. As expected, with increasing stretch-rate sensitivity of the fibers the macroscopic stress response increases as well.

**Parameter Study – Microinertia** Finally, the simulation is run without considering the inertia at the microscale and is again compared to the full simulation as presented in Figure 12.10. As before, the average of the measured stress at the specimen interfaces is given in Figure 12.14, including a zoomed in section to highlight the difference. It is clearly visible that in this simulation the overall macroscopic behavior is not significantly influenced by microscale inertia effects. This can be expected, as the chosen RVE combined with the microscopic material models do not allow for much dynamic activity. However, there are high frequency stress oscillations arising at the microscale once the crack has been formed. These are the results of the microcracks being able to freely open and close, as the fiber is anchored at the RVE boundary. This shows firstly the capability of the framework to capture these effects and secondly that even small dynamic action at the microscale can be detected at the macroscale.

## 12.5 Discussion

Comparing the experimental dynamic behavior in Figure 12.6 with the simulated dynamic tension test in Figure 12.10, shows that not all physically relevant effects have been captured. The initial stress recorded during the multiple cracking phase shows similar characteristics and stress levels as measured in the experiments. However the post-cracking behavior of the simulation is different, as the softening branch, indicating the fiber pullout, has not been reached for strains up to 5%. Although stress peaks

due to increased loading speed have been recorded at the input face, in contrast to the experiments this has not been recorded at the output face. Considering the simplicity of the applied micromechanical models as well as the oversimplified RVE geometry, some deviations were to be expected. Nonetheless, the simulations showed that general aspects as the stress increase due to inertia as well as stretch-rate dependent material behavior can be observed. In addition, the dynamic simulation was able to show multiple cracking.

The most obvious area to improve the physical representation of the SHCC simulation is the choice and complexity of the micromechanical models. Enabling an arbitrary crack path while capturing effects like crack-tip inertia, would allow for more meaningful crack analysis. Multiple cracking within a single RVE would then be possible. Furthermore, a fiber pullout model which is not only represented by a single truss element directly connected to the matrix nodes, would be able to introduce the tensile forces at the correct locations in the matrix. This would enable the analysis of the fiber-matrix bond separately from the fiber properties. Once the material models are more realistic and properly calibrated with a suitable set of experimental data, studies of e.g. fiber orientation with respect to the dynamic loading conditions could lead to valuable insights into the dynamic properties of the composite. One additional problem with the numerical simulation is the lack of parameter variation. The first cracking for fast loading will always initiate in the first element, c.f. Chapter 11. However, experimental specimens will initiate cracking at the weakest point. The crack location can have a significant influence on the measured stress due to inertia at the crack faces in a dynamic simulation. This is currently not trivially analyzed as a variation in local microscale parameters would be required.

Other effects leading to deviations of the simulation results from those of the experiments, which are not directly related to the micromechanical models could be e.g. the simplification of the macroscopic problem as row of truss elements. The current implementation assumes no deformation transversal to the loading direction. This would represent a very high degree of confinement at the microscale. Although the confinement effect is expected to increase with increased dynamic loading, it would not be homogeneous and not constant throughout the loading. As a first step to analyze the influence of this would be to assume the other extreme, zero stress perpendicular to the loading direction at the macroscale. In the long run, a full 3D computation could certainly answer the question of the influence of lateral confinement, which is expected to change depending on the size and geometry of the specimen. A second source of mismatch between the simulation and the experimental data, might be related to the difference in measurement location. In the simulation the stress was directly recorded at the interface as a projection of the adjacent element's GAUSS points. This is not possible in the experimental setup, therefore the stress and displacements are inferred from strain measurements of the input and output bar.

Despite of this list of potential improvements of the material models, this chapter has already shown the effectiveness of the developed framework as a tool to study the origin of measured dynamic effects.



## 13 Conclusion and Outlook

The aim of this work was to develop a computational multiscale framework to enable the simulation of SHCC under dynamic loading. The motivation was to analyze dynamic effects taking place at the microscale and observe their macroscopic influence.

After introducing the target material SHCC, this work started by giving a general introduction to the most important concepts later applied in the derivation of the dynamic multiscale framework. Basic concepts of continuum mechanics, as kinematic formulations, various stress measures and relevant balance equations were presented. The chapter was followed by an overview of the finite element method, including subsequently used approaches like the NEWMARK time integration scheme or GAUSS integration. Then the material models later applied to SHCC at the microscale were introduced. The focus was on the one-dimensional material model representing the fiber-matrix bond. Therefore the concept of damage and the stretch-rate dependent stress formulation were presented. The following chapter introduced the standard homogenization formulation for FE<sup>2</sup> modeling. Afterwards the core of this work was presented, i.e. the derivation of the proposed dynamic homogenization framework.

The proposed framework is based on the consistent incorporation of the inertia forces at the microscale. Energetic consistency is ensured by using an extended formulation of the HILL-MANDEL condition of macro-homogeneity, which is applied to derive the formulations of the macroscopic quantities of stress and inertia. One important aspect of dynamic two-scale models is the kinematic coupling of the macroscale and microscale. To ensure a consistent coupling of the displacements throughout the scales, a special volume integral displacement constraint was proposed and implemented. To enable an efficient numerical computation, the closed form tangent moduli were derived, taking into account both the inertia forces at the microscale as well as the volume displacement constraint.

In the next two chapters the proposed two-scale homogenization framework is applied onto two different microstructures. For the first example a simple layered structure of alternating stiff, heavy phases and soft, light phases was considered. Using specific material parameters, a quasi-one-dimensional simulation was realized. This allowed the analysis of the wave propagation in the layered microstructure, using macroscale truss elements. An equivalent single-scale calculation was performed, which served as a reference solution. Using this example, the quadratic convergence of the macroscopic NEWTON iteration could be shown. This validated the consistency of the computed macroscopic tangent moduli. The layered structure was further used to analyze the choice of RVE in a dynamic setting. By varying the choice of unit cell and in addition comparing computations with multiple unit cells, it was observed that the choice of RVE for dynamic homogenization is more complex than for the quasi-static case. Different unit cells can lead to distinct macroscopic results. By using multiple unit cells as RVE, the effect could be decreased. However, this again increases the calculation cost and can lead in extreme cases to errors arising from the violation of the clear separation of scales. At the same time, the proposed volume displacement constraint was compared to a second type of displacement constraint. The other constraint

set the displacement fluctuation of the corner nodes to zero, effectively applying the macroscopic displacement only at the boundary. The results for the layered structure of both constraints were similar. However, compared to the single-scale direct numerical calculation the volume integral displacement constraint showed a closer match of the displacement fields. More importantly, it resulted in a more robust computation. The second chosen example presents a more complex dynamic behavior at the microscale. It represents a locally resonant structure, where a dense and stiff core is coated with a soft phase and embedded in a stiff matrix, as it is found in some metamaterials. Similarly, a row of unit cells was subjected to an external displacement and the induced wave was observed while traveling along the bar. As in the previous example, a single-scale solution was computed to verify the homogenization framework. Different loading frequencies were applied and the effect of the locally resonant structure was clearly observed by a change in wave attenuation depending on the wave frequency. This was used to identify band gaps in the lower loading spectrum. Generally, conventional wave analysis may fail for nonlinear, history dependent material properties. Therefore such real-time analysis is advantageous. Furthermore, a practical feature of the dynamic framework was utilized, as the calculation could now be compared to an identical simulation without considering microinertia. The results proved that the wave attenuation was only due to the microinertia effects. As before, this example was used to compare the proposed displacement constraint to the fixed corners constraint. Although the volume integral constraint was able to detect the band gaps and showcase a comparable wave attenuation, the fixed corner constraint performed significantly better in matching the displacement field of the single scale calculation. Comparing this analysis to that of the layered structure, suggests that the proposed constraint is the more general one. However for specific dynamic microstructures such as the locally resonant material, a different choice which takes into account the expected dynamic material behavior can result in more realistic predictions. These two examples have shown that the proposed framework is both numerically stable as well as able to properly model structures with significant microscale inertia effects.

In the next sections, the focus of the work shifted to the material models required for an initial analysis of SHCC. Firstly, the fiber-matrix bond was studied and the parameters of the previously described material models were adapted to fit the experimental fiber pullout test for both quasi-static and dynamic conditions. Considering the simplicity of the used material models, the overall curves matched well. However, the pullout conditions in the experiment do not directly relate to the conditions within an SHCC specimen where the full fiber is embedded. Secondly, a simplified problem is used to analyze the general behavior of the fiber pullout within the multiscale framework. Material parameters loosely extrapolated from the pullout were used and a polynomial loading function chosen which approximated an impact. It was observed that with increasing loading speed the macroscopic behavior changed from a multiple cracking with uniform fiber debonding and pullout to a more localized failure at the loading face. By coupling the simulations which consider macroscopic and microscopic inertia with the stretch-rate sensitive fiber model, higher stress peaks were observed, suggesting a positive interaction of the two effects. In the last step, the boundary conditions were changed to replicate a specific split HOPKINSON bar test. A loading function was postulated, characterized by two parameters which can be directly measured. Therefore, a good representation of the stress pulses recorded in the experiments was

observed. Due to the lack of sufficient data to properly fit the pullout conditions of a fully embedded two sided fiber pullout, the material parameters were fit to replicate the quasi-static behavior of an SHCC tension test. Then, the dynamic split HOPKINSON bar simulation was run including the parameters of the rate dependency as observed in the dynamic fiber pullout test. By varying the loading parameters, the stretch-rate sensitivity, as well as running the simulation without microscopic inertia, the different effects related to the overall dynamic behavior could be studied separately. A direct comparison of the numerically computed results and the experimentally measured data showed that further improvement of the micromechanical models are needed to properly capture all relevant material effects. However, the qualitative trend of the simulation was in good agreement and the analysis showcased the power of this tool to investigate dynamic effects. Equipped with more realistic micromechanical models, the framework can be utilized to improve the composite by predicting the influence of microstructural properties under dynamic loading.

This work has shown that the developed homogenization framework is well capable of analyzing dynamic loading conditions on two scales, fulfilling the aim of this project. During the course of this research some interesting question have been touched but not further investigated. There are two main open research questions concerning the general dynamic homogenization framework. The first question is the optimal choice of RVE for dynamic loading. The second question is that of the choice of kinematic constraints to consistently link the two scales. The proposed displacement link showed promising results but further investigations are required. In addition, the coupling of the macroscopic deformation gradient could be implemented as a volume constraint as well, therefore not limiting the microscale problem to periodic boundary conditions. This would be especially valuable in combination with fracture simulations. To further improve the multiscale simulation of SHCC the objective is clear. The micromechanical models need to be improved. Especially the modeling of the matrix cracking and a more detailed fiber pullout will allow to capture further relevant effects. Finally the framework can be enhanced by improving the computational efficiency.

The most obvious step to quickly improve efficiency is the parallelization of the macroscopic FEM computation. This would not require any additional implementations compared to a parallel single scale computation. Another idea to save computation time for SHCC simulations is to apply the knowledge gained by the simplified examples. The direct results of microinertia in SHCC on the macroscopic problem seems to be negligible. This allows a reduction of the framework to a unilateral dynamic coupled system. The inertia effects at the microscale would be taken into account, as they significantly influence fracture simulations and pullout models. Therefore appropriate displacement constraints would still be required. However, the tangent modulus could be computed quasi-statically, saving the computational cost of computing the dynamic macroscopic tangent moduli. The macroscale inertia force would be computed classically, only based on macroscale acceleration values and a density simply based on the rule of mixture. Incorporating these improvements would facilitate the use of the framework on larger 3D macroscale problems, e.g. studying the effect of impact on a plate.



# A Large Strain Truss Element

In the following the derivation of a large strain truss element with linear shape functions for dynamics is presented using analytical integration. The derivation starts with the weak form for a single element

$$G^e = \int_{\mathcal{B}^e} \mathbf{P} \delta \mathbf{F} dV + \int_{\mathcal{B}^e} \delta \mathbf{u}^T \rho_0 \ddot{\mathbf{u}} dV, \quad (\text{A.1})$$

c.f. 4.3. The cross section  $A$  is assumed to be constant, thus the volume integral can be reduced to an integral over the reference length  $L$  along the local  $x$ -axis, multiplied by the area. Here values in the local base system of the element are denoted with a  $\hat{\bullet}$ . The constant cross section leads to the local deformation gradient and its variation

$$\hat{\mathbf{F}} = \begin{bmatrix} \hat{F}_{11} & 0 & 0 \\ 0 & 1 & 0 \\ 0 & 0 & 1 \end{bmatrix} \rightarrow \delta \hat{\mathbf{F}} = \begin{bmatrix} \delta \hat{F}_{11} & 0 & 0 \\ 0 & 0 & 0 \\ 0 & 0 & 0 \end{bmatrix}. \quad (\text{A.2})$$

Considering only homogeneous elements, the equation can be simplified to

$$G^e = A \int_L \hat{P}_{11} \delta \hat{F}_{11} d\hat{X} + A \int_L \delta \mathbf{u}^T \rho_0 \ddot{\mathbf{u}} d\hat{X}. \quad (\text{A.3})$$

The deformation gradient in local  $x$ -direction  $\hat{F}_{11}$  can be computed by dividing the current length  $l$  by the reference length  $L$  as  $\hat{F}_{11} = l/L \rightarrow \delta \hat{F}_{11} = \delta l/L$ . Assuming a linear interpolation between the two element nodes I and II, the displacement and acceleration fields can be approximated with their respective nodal values as  $\delta \mathbf{u}(\hat{X}) = \delta \mathbf{d}^I + \frac{\delta \mathbf{d}^{II} - \delta \mathbf{d}^I}{L} \hat{X}$  and  $\ddot{\mathbf{u}}(\hat{X}) = \ddot{\mathbf{d}}^I + \frac{\ddot{\mathbf{d}}^{II} - \ddot{\mathbf{d}}^I}{L} \hat{X}$ . Additionally, the variation of the current length can be defined in terms of the variation of the nodal displacements in the local coordinates  $\delta l = \delta \hat{d}_1^{II} - \delta \hat{d}_1^I$ . Now

$$\begin{aligned} G^e = & AP_{11} \int_L \frac{\delta \hat{d}_1^{II} - \delta \hat{d}_1^I}{L} d\hat{X} \\ & + A\rho_0 \int_L \left( \delta \mathbf{d}^{I^T} + \frac{\delta \mathbf{d}^{II^T} - \delta \mathbf{d}^{I^T}}{L} \hat{X} \right) \left( \ddot{\mathbf{d}}^I + \frac{\ddot{\mathbf{d}}^{II} - \ddot{\mathbf{d}}^I}{L} \hat{X} \right) d\hat{X}. \end{aligned} \quad (\text{A.4})$$

This integral can be solved analytically instead of using a GAUSS integration, yielding

$$\begin{aligned} G^e = & AP_{11} \left( \delta \hat{d}_1^{II} - \delta \hat{d}_1^I \right) \\ & + A\rho_0 L \left( \frac{1}{3} \delta \mathbf{d}^{I^T} \ddot{\mathbf{d}}^I + \frac{1}{6} \delta \mathbf{d}^{I^T} \ddot{\mathbf{d}}^{II} + \frac{1}{6} \delta \mathbf{d}^{II^T} \ddot{\mathbf{d}}^I + \frac{1}{6} \delta \mathbf{d}^{II^T} \ddot{\mathbf{d}}^{II} \right). \end{aligned} \quad (\text{A.5})$$

To facilitate the legibility of the formulation, the elemental vectors are defined as

$$\delta \hat{\mathbf{d}}^e{}^T = \left[ \delta \hat{\mathbf{d}}^I{}^T \mid \delta \hat{\mathbf{d}}^{II^T} \right], \quad \delta \mathbf{d}^e{}^T = \left[ \delta \mathbf{d}^I{}^T \mid \delta \mathbf{d}^{II^T} \right] \quad \text{and} \quad \ddot{\mathbf{d}}^e{}^T = \left[ \ddot{\mathbf{d}}^I{}^T \mid \ddot{\mathbf{d}}^{II^T} \right], \quad (\text{A.6})$$

and two auxiliary matrices  $\hat{\mathbf{a}}$  and  $\mathbf{B}$  as

$$\hat{\mathbf{a}} = \begin{bmatrix} -1 \\ 0 \\ 0 \\ 1 \\ 0 \\ 0 \end{bmatrix} \quad \text{and} \quad \mathbf{B} = \begin{bmatrix} \frac{1}{3} & 0 & 0 & | & \frac{1}{6} & 0 & 0 \\ 0 & \frac{1}{3} & 0 & | & 0 & \frac{1}{6} & 0 \\ 0 & 0 & \frac{1}{3} & | & 0 & 0 & \frac{1}{6} \\ \hline \frac{1}{6} & 0 & 0 & | & \frac{1}{3} & 0 & 0 \\ 0 & \frac{1}{6} & 0 & | & 0 & \frac{1}{3} & 0 \\ 0 & 0 & \frac{1}{6} & | & 0 & 0 & \frac{1}{3} \end{bmatrix}. \quad (\text{A.7})$$

This simplifies the equation to

$$G^e = A\hat{P}_{11}\delta\hat{\mathbf{d}}^e\hat{\mathbf{a}} + A\rho_0L\delta\mathbf{d}^{eT}\mathbf{B}\ddot{\mathbf{d}}^e. \quad (\text{A.8})$$

It should be noted that the first term only relates to the stress and is purely one-dimensional, only dependent on values of the local  $x$ -direction, due to the formulation of  $\hat{\mathbf{a}}$ , even though  $\delta\hat{\mathbf{d}}^e$  is three-dimensional. The second part is related to the accelerations and thus depends on displacements in all three spacial directions. Eventually the element formulation should be written in global coordinates, so  $\hat{\mathbf{d}}^e$  needs to be transformed to global bases. Defining the transformation matrix as  $\mathbf{T} = \begin{bmatrix} \mathbf{R} & | & \mathbf{0} \\ \hline \mathbf{0} & | & \mathbf{R} \end{bmatrix}$ , where  $\mathbf{R}$  is the rotation matrix that transforms local into global coordinates, leads to

$$G^e = \delta\mathbf{d}^{eT} \left( A\hat{P}_{11}\mathbf{T}\hat{\mathbf{a}} + A\rho_0L\mathbf{B}\ddot{\mathbf{d}}^e \right). \quad (\text{A.9})$$

This can be further simplified by defining  $\mathbf{T}\hat{\mathbf{a}} = \mathbf{a}$ , where  $\mathbf{a}^T = [ \mathbf{n}^T \mid \mathbf{n}^T ]$ , with  $\mathbf{n}$  being the current unit vector of the truss direction. It follows the linearization of  $G^e$ .

$$\text{Lin}G^e = G^e + \Delta G^e, \quad (\text{A.10})$$

with

$$\Delta G^e = \delta\mathbf{d}^{eT} \left( A\Delta\hat{P}_{11}\mathbf{a} + A\rho_0L\mathbf{B}\Delta\ddot{\mathbf{d}}^e \right). \quad (\text{A.11})$$

Reformulating  $\Delta\hat{P}_{11} = \frac{\partial\hat{P}_{11}}{\partial\hat{F}_{11}}\Delta\hat{F}_{11} = \hat{\mathbb{A}}_{1111}\Delta\hat{F}_{11}$  and applying the same concepts as before on  $\Delta\hat{F}_{11} = \frac{\Delta l}{L} = \frac{\Delta\hat{d}_1^I - \Delta\hat{d}_1}{L} = \frac{1}{L}\Delta\hat{\mathbf{d}}^e\hat{\mathbf{a}} = \frac{1}{L}\Delta\mathbf{d}^{eT}\mathbf{T}\hat{\mathbf{a}} = \frac{1}{L}\Delta\mathbf{d}^{eT}\mathbf{a}$ , then rewriting  $\Delta\ddot{\mathbf{d}}^e$ , by using the NEWMARK method as explained in Section 4.4, results in the final notation for the linear increment

$$\Delta G^e = \delta\mathbf{d}^{eT} \left( \hat{\mathbb{A}}_{1111} \frac{A}{L} \mathbf{a} \otimes \mathbf{a} + \frac{A\rho_0L}{\beta\Delta t^2} \mathbf{B} \right) \Delta\mathbf{d}^e. \quad (\text{A.12})$$

Using (A.9) and (A.12), the linearized element stiffness matrix and the respective right hand side residual vectors can now be defined as

$$\mathbf{k}^e = \hat{\mathbb{A}}_{1111} \frac{A}{L} \mathbf{a} \otimes \mathbf{a} + \frac{A\rho_0L}{\beta\Delta t^2} \mathbf{B} \quad \text{and} \quad (\text{A.13})$$

$$\mathbf{r}^e = -\hat{P}_{11}A\mathbf{a} - A\rho_0L\mathbf{B}\ddot{\mathbf{d}}^e, \quad (\text{A.14})$$

concluding the derivation of the element matrices of this two node truss.

# B Deformation Gradient Constraint

In Chapter 6 the two constraints (6.9) and (6.15) have been identified for the microscale boundary value problem within the multiscale framework. Section 7.2 presented the consistent derivation of the volume integral displacement constraint (6.15). Analogously, the derivation of the deformation gradient constraint  $\overline{\mathbf{F}} = \langle \mathbf{F} \rangle$  is presented here in detail.

## B.1 Lagrange Multipliers

The term  $\Pi^\lambda$  is added to the global energy function  $\Pi$ , which contains the LAGRANGE multipliers  $\lambda_2$ ,

$$\Pi = \Pi^{\text{int}} + \Pi^{\text{ext}} + \Pi^\lambda, \quad \text{with} \quad \Pi^\lambda = \lambda_2 \cdot \left( \frac{1}{V} \int_{\mathcal{B}} \widetilde{\mathbf{H}} \, dV \right). \quad (\text{B.1})$$

Using the micro-macro split (6.8), the constraint was rewritten as  $\widetilde{\mathbf{H}} = \mathbf{0}$ .

## B.2 Variation

The variation method is now applied to the whole energy function, which is varied once with respect to the displacement fluctuation  $\tilde{\mathbf{u}}$  and once with respect to the LAGRANGE multiplier  $\lambda_2$ . Here the focus is only on the new LAGRANGIAN energy part as the rest has been derived and is implemented in every standard FEM program.

$$\delta_{\tilde{\mathbf{u}}} \Pi^\lambda = \lambda_2 \cdot \frac{1}{V} \int_{\mathcal{B}} \delta \widetilde{\mathbf{H}} \, dV \quad \text{and} \quad (\text{B.2})$$

$$\delta_{\lambda_2} \Pi^\lambda = \delta_{\lambda_2} \Pi = \delta \lambda_2 \cdot \frac{1}{V} \int_{\mathcal{B}} \widetilde{\mathbf{H}} \, dV. \quad (\text{B.3})$$

## B.3 Discretization

Using  $\widetilde{\mathbf{H}} \approx \mathbf{B}^e \tilde{\mathbf{d}}^e$  and  $\delta \widetilde{\mathbf{H}} \approx \mathbf{B}^e \delta \tilde{\mathbf{d}}^e$  as FEM approximations, the equations can be rewritten as

$$\delta_{\tilde{\mathbf{u}}} \Pi^\lambda = \lambda_2^T \mathbf{A} \left[ \frac{1}{V} \int_{\mathcal{B}^e} \mathbf{B}^e \, dV \, \delta \tilde{\mathbf{d}}^e \right] \quad \text{and} \quad (\text{B.4})$$

$$\delta_{\lambda_2} \Pi^\lambda = \delta \lambda_2^T \mathbf{A} \left[ \frac{1}{V} \int_{\mathcal{B}^e} \mathbf{B}^e \, dV \, \tilde{\mathbf{d}}^e \right]. \quad (\text{B.5})$$

For better legibility a new element matrix is defined

$$\mathbf{g}_{\langle \mathbf{F} \rangle}^{eT} = \frac{1}{V} \int_{\mathcal{B}^e} \mathbf{B}^e \, dV. \quad (\text{B.6})$$

This simplifies the formulations to

$$\delta_{\tilde{\mathbf{u}}}\Pi^{\lambda_2} = \boldsymbol{\lambda}_2^T \mathbf{A} \begin{bmatrix} \mathbf{g}_{\langle \mathbf{F} \rangle}^{eT} \delta \tilde{\mathbf{d}}^e \end{bmatrix} \quad \text{and} \quad (\text{B.7})$$

$$\delta_{\lambda_2}\Pi^{\lambda_2} = \delta \boldsymbol{\lambda}_2^T \mathbf{A} \begin{bmatrix} \mathbf{g}_{\langle \mathbf{F} \rangle}^{eT} \tilde{\mathbf{d}}^e \end{bmatrix}. \quad (\text{B.8})$$

### B.3.1 Global Matrix Notation

To write the system of equation as a global problem the global matrix  $\mathbf{H}$  is defined as

$$\mathbf{G}_{\langle \mathbf{F} \rangle} = \mathbf{A} \begin{bmatrix} \mathbf{g}_{\langle \mathbf{F} \rangle}^e \end{bmatrix}, \quad (\text{B.9})$$

considering (7.23). This leads to the equations (B.7) and (B.8) in global fields as

$$\delta_{\tilde{\mathbf{u}}}\Pi^{\lambda_2} = \boldsymbol{\lambda}_2^T \mathbf{G}_{\langle \mathbf{F} \rangle}^T \delta \tilde{\mathbf{D}} = \delta \mathbf{D}^T \mathbf{G}_{\langle \mathbf{F} \rangle} \boldsymbol{\lambda}_2 \quad \text{and} \quad (\text{B.10})$$

$$\delta_{\lambda_2}\Pi^{\lambda_2} = \delta \boldsymbol{\lambda}_2^T \mathbf{G}_{\langle \mathbf{F} \rangle}^T \tilde{\mathbf{D}} = \mathbf{0}. \quad (\text{B.11})$$

### B.3.2 Linearization

To solve this nonlinear system of equations, a linearization is used to iteratively compute the displacement field as well as the LAGRANGE multipliers, yielding

$$\text{Lin } \delta_{\tilde{\mathbf{u}}}\Pi^{\lambda_2} = \delta \tilde{\mathbf{D}}^T \mathbf{G}_{\langle \mathbf{F} \rangle} \boldsymbol{\lambda}_2 + \delta \tilde{\mathbf{D}}^T \mathbf{G}_{\langle \mathbf{F} \rangle} \Delta \boldsymbol{\lambda}_2 \quad \text{and} \quad (\text{B.12})$$

$$\text{Lin } \delta_{\lambda_2}\Pi^{\lambda_2} = \delta \boldsymbol{\lambda}_1^T \mathbf{G}_{\langle \mathbf{F} \rangle}^T \tilde{\mathbf{D}} + \delta \boldsymbol{\lambda}_2^T \mathbf{G}_{\langle \mathbf{F} \rangle}^T \Delta \tilde{\mathbf{D}} = \mathbf{0}. \quad (\text{B.13})$$

## B.4 Residuum

From this two new global residuum vectors are defined

$$\mathbf{R}_2^{\tilde{\mathbf{u}}} = -\mathbf{G}_{\langle \mathbf{F} \rangle} \boldsymbol{\lambda}_2 = \mathbf{A} \begin{bmatrix} \mathbf{r}_2^{\tilde{\mathbf{u}}e} \end{bmatrix} \quad \text{with} \quad \mathbf{r}_2^{\tilde{\mathbf{u}}e} = -\mathbf{g}_{\langle \mathbf{F} \rangle}^e \boldsymbol{\lambda}_2 \quad \text{and} \quad (\text{B.14})$$

$$\mathbf{R}_2^{\lambda} = -\mathbf{G}_{\langle \mathbf{F} \rangle}^T \tilde{\mathbf{D}} = \sum_{e=1}^{n_{\text{el}}} \mathbf{r}_2^{\lambda e} \quad \text{with} \quad \mathbf{r}_2^{\lambda e} = -\mathbf{g}_{\langle \mathbf{F} \rangle}^{eT} \tilde{\mathbf{d}}^e. \quad (\text{B.15})$$

### B.4.1 Full System of Equations

Finally, these formulations can be applied to the presented system of equations in Section 7.2.4. This incorporates the deformation gradient constraint consistently into the framework.

# C Overview – Consistent Tangent Moduli

The four tangent moduli derived in Chapter 7 are given here as an overview. The respective abbreviations are listed in Table C.1 as well as Table C.2.

$$\bar{\mathbb{A}}^{P,F} = \left\langle \mathbb{A} + \frac{1}{\beta\Delta t^2} \mathbb{Y} \right\rangle - \frac{1}{V} \mathbf{L}^{*\text{T}} \mathbf{K}^{*-1} \mathbf{L}^{\bar{*}} \quad (\text{C.1})$$

$$\bar{\mathbb{A}}^{P,u} = \langle \mathbf{V} \rangle - \frac{1}{V} \mathbf{L}^{*\text{T}} \mathbf{K}^{*-1} \mathbf{W}^* \quad (\text{C.2})$$

$$\bar{\mathbb{A}}^{f,F} = \frac{1}{\beta\Delta t^2} \langle \mathbf{V}^{\text{T}} \rangle - \frac{1}{V} \frac{1}{\beta\Delta t^2} \mathbf{W}^{*\text{T}} \mathbf{K}^{*-1} \mathbf{L}^{\bar{*}} \quad (\text{C.3})$$

$$\bar{\mathbb{A}}^{f,u} = \langle \boldsymbol{\rho}_0 \rangle - \frac{1}{V} \frac{1}{\beta\Delta t^2} \mathbf{W}^{*\text{T}} \mathbf{K}^{*-1} \mathbf{W}^* \quad (\text{C.4})$$

Matrix	Size
$\mathbf{D}^* = \left[ \tilde{\mathbf{D}}^{\text{T}} \mid \boldsymbol{\lambda}^{\text{T}} \right]^{\text{T}}$	$(n_{\text{edf}} + n_{\text{lgr}}) \times 1$
$\mathbf{L}^* = \left[ \mathbf{L}^{\text{T}} + \frac{1}{\beta\Delta t^2} \mathbf{Z}^{\text{T}} \mid \mathbf{0} \right]^{\text{T}}$	$(n_{\text{edf}} + n_{\text{lgr}}) \times n_{\text{dm}}^2$
$\mathbf{L}^{\bar{*}} = \left[ \mathbf{L}^{\text{T}} + \frac{1}{\beta\Delta t^2} \mathbf{Z}^{\text{T}} \mid \mathbf{0} \right]^{\text{T}}$	$(n_{\text{edf}} + n_{\text{lgr}}) \times n_{\text{dm}}^2$
$\mathbf{W}^* = \left[ \mathbf{W}^{\text{T}} \mid \mathbf{0} \right]^{\text{T}}$	$(n_{\text{edf}} + n_{\text{lgr}}) \times n_{\text{lgr}}$
$\mathbf{K}^* = \left[ \begin{array}{c c} \mathbf{K} + \frac{1}{\beta\Delta t^2} \mathbf{M} & \mathbf{G} \\ \hline \mathbf{G}^{\text{T}} & \mathbf{0} \end{array} \right]$	$(n_{\text{edf}} + n_{\text{lgr}}) \times (n_{\text{edf}} + n_{\text{lgr}})$

**Table C.1:** Overview of the extended fields, with  $n_{\text{edf}}$  number of DOF at element level, denoting  $n_{\text{lgr}}$  the number of DOF of LAGRANGE constraint and with  $n_{\text{dm}}$  the spacial dimension.

Global		Element
Definition	Size	
$\mathbf{K} = \mathbf{A} \mathbf{k}^e$	$n_{\text{edf}} \times n_{\text{edf}}$	$k_{PQ}^e = \int_{\mathcal{B}^e} B_{ijP}^e \mathbb{A}_{ijkl} B_{klQ}^e dV$
$\mathbf{L} = \mathbf{A} \mathbf{l}^e$	$n_{\text{edf}} \times n_{\text{dm}}^2$	$l_{Pij}^e = \int_{\mathcal{B}^e} B_{klP}^e \mathbb{A}_{kl ij} dV$
$\mathbf{M} = \mathbf{A} \mathbf{m}^e$	$n_{\text{edf}} \times n_{\text{edf}}$	$m_{PQ}^e = \int_{\mathcal{B}^e} N_{iP}^e \rho_0 N_{iQ}^e dV$
$\mathbf{W} = \mathbf{A} \mathbf{w}^e$	$n_{\text{edf}} \times n_{\text{dm}}$	$w_{Pi}^e = \int_{\mathcal{B}^e} \rho_0 N_{iP}^e dV$
$\mathbf{Z} = \mathbf{A} \mathbf{z}^e$	$n_{\text{edf}} \times n_{\text{dm}}^2$	$z_{Pij}^e = \int_{\mathcal{B}^e} \rho_0 N_{iP}^e X_j dV$
$\mathbf{G} = \mathbf{A} \mathbf{g}^e$	$n_{\text{edf}} \times n_{\text{dm}}$	$g_{Pi}^e = \int_{\mathcal{B}^e} N_{iP}^e dV$
$\mathbf{V}$	$n_{\text{dm}}^2 \times n_{\text{dm}}$	$V_{ijk} = \rho_0 \delta_{ik} X_j$
$\mathbb{Y}$	$n_{\text{dm}}^2 \times n_{\text{dm}}^2$	$\mathbb{Y}_{ijkl} = \rho_0 \delta_{ik} X_l X_j$

**Table C.2:** Overview of the used fields at element and global level, denoting with  $n_{\text{edf}}$  the number of DOF at element level and with  $n_{\text{dm}}$  the spacial dimension.

# List of Figures

2.1	Multiple cracking in SHCC, from ZHAN et al. [120]. . . . .	5
2.2	Tensile stress-strain curves, comparing the quasi-static and dynamic behavior of SHCC, from CUROSU et al. [25]. . . . .	6
2.3	Energy-absorbing fiber-matrix mechanisms, based on ANDERSON [1] and ZOLLO [121]. . . . .	6
2.4	Global material failure of SHCC, based on CUROSU [24]. . . . .	6
2.5	Segmented fiber for a micro-CT scan in a 3.5 mm thin SHCC specimen, from LORENZONI et al. [66] . . . . .	7
2.6	Overview of the projects within the Research Training Group GRK 2250/1, based on CUROSU et al. [26]. This research is part of project B1. . . . .	8
3.1	Motion of the body $\mathcal{B}$ . . . . .	12
3.2	Infinitesimal elements in the reference and current configuration. . . . .	13
4.1	Example of a finite element approximation $\mathcal{B}^h$ of the real body $\mathcal{B}$ for a coarse mesh with $n_{el} = 4$ and a finer mesh with $n_{el} = 15$ . . . . .	19
4.2	Isoparametric mapping for a quadrilateral element. . . . .	20
5.1	Parameter study of a 1D Neo-HOOKE material, presenting the variation of the YOUNG's modulus $E$ . . . . .	28
5.2	Parameter study of a 1D Neo-HOOKE material with stretch-rate sensitivity of the stress. $E = 40 \text{ kN/mm}^2$ , $\dot{F} = 1 \text{ s}^{-1}$ are held constant, while the function $\Omega$ (5.9) is modified. . . . .	29
5.3	Visual representation of the damage parameter $D$ , calculated as $D = \hat{A}/A$ . . . . .	30
5.4	Strain equivalence principle. . . . .	30
5.5	Qualitative example of the discontinuous damage approach, showing respectively (a) the applied strain $\varepsilon$ over time $t$ , (b) the evolution of the damage value $D$ and (c) the resulting stress-strain diagram. . . . .	31
5.6	Parameter study of a 1D Neo-HOOKE material with damage formulation. Parameters used (purple line): $E = 40 \text{ kN/mm}^2$ , $D_{rate} = 25$ , $D_{\infty} = 0.999$ , $D_{shape} = 1$ . Each diagram shows the effect of varying a single parameter: (a) $D_{rate}$ , (b) $D_{\infty}$ , (c) $D_{shape}$ and (d) $E$ . . . . .	33
5.7	Combined damage and stretch-rate dependent material model for various loading conditions: (a) stress-strain response and (b) respective stretch rates. Loading functions given in (5.19), with $u_{max}/L = 0.1, 2$ : $t_{max} = 0.077 \text{ s}$ , $3$ : $t_{max} = 0.17 \text{ s}$ and $4$ : $t_{max} = 0.1 \text{ s}$ . All simulation are run with $E = 40 \text{ kN/mm}^2$ , $D_{\infty} = 0.995$ , $D_{rate} = 100$ , $D_{shape} = 0.6$ , $\alpha^I = 4.48$ and $\alpha^{II} = 1.04$ . . . . .	35
6.1	General idea of homogenization. . . . .	37
6.2	Physical representation of the VOIGT and REUSS bounds. . . . .	37
6.3	Schematic of the general FE <sup>2</sup> method. . . . .	38

6.4	Some examples of possible unit cells for a periodic microstructure. . .	39
6.5	Large strain continuum mechanics on both scales. . . . .	41
6.6	Visualization of periodic boundary conditions on differently shaped RVEs, based on VAZ JÚNIOR et al. [111]. . . . .	43
7.1	Overview of the FE <sup>2</sup> framework including microscale dynamics. Here, an example of macroscopic impact on SHCC is illustrated, based on TAMSEN and BALZANI [106]. . . . .	47
7.2	Algorithm for single macroscopic iteration of the dynamic FE <sup>2</sup> framework with respective equation references. It should be noted that the overall structure of the standard FE procedure does not change, only some additional fields need to be computed. Furthermore, for the implementation of the microscopic problem, the macroscopic displacements $\bar{\mathbf{u}}$ may be omitted from the code. It is the second derivative $\ddot{\bar{\mathbf{u}}}$ , computed in the macroscopic problem, which influences the microscopic results. . . . .	61
8.1	Illustration of the numerical calculations including (a) a 1D single scale FE Model and (b) the macroscopic model and the RVE of the FE <sup>2</sup> approach, based on TAMSEN and BALZANI [106]. . . . .	63
8.2	Analysis of algorithmic consistency: (a) Comparison of displacement fields and (b) Convergence of the macroscopic NEWTON iteration with a tolerance of $10^{-8}$ . The simulation parameters are $L = 10000$ mm, $l_M = 10$ mm, $l_{\bar{\mathbb{E}}} = 33.33$ mm, $\bar{u}_{\max} = 100$ mm, $T = 0.01$ s, $\Delta t = 5 \cdot 10^5$ s and basic unit cell type A as RVE, data from TAMSEN and BALZANI [106]. . . . .	64
8.3	Selection of RVE choices with different numbers of basic unit cells, based on TAMSEN and BALZANI [106]. . . . .	65
8.4	Comparison of macroscopic displacement fields for two different RVEs with different basic unit cells types. The simulation parameters are $L = 10000$ mm, $l_M = 10$ mm, $l_{\bar{\mathbb{E}}} = 33.33$ mm, $\bar{u}_{\max} = 100$ mm, $T = 0.01$ s, $t = 0.045$ s and $\Delta t = 5 \cdot 10^5$ s. The data is published in TAMSEN and BALZANI [106]. . . . .	65
8.5	Analysis of different RVE choices: (a) direct comparison of RVEs with unit cell type A and B, shown with increasing numbers of basic unit cells per RVE (the error is computed as difference between the response of the two unit cell types, not with respect to the DNS), (b) error of unit cell type A and B, compared to DNS as reference. The simulation parameters are $L = 10000$ mm, $l_M = 2.5$ mm, $l_{\bar{\mathbb{E}}} = 20$ mm, $\bar{u}_{\max} = 100$ mm, $T = 0.01$ s, $\Delta t = 5 \cdot 10^5$ s, $n_{\text{timesteps}} = 400$ , from TAMSEN and BALZANI [106]. . . . .	66

8.6	Comparison of microscopic displacement fields obtained from the FE <sup>2</sup> simulations with the DNS. The displacements have been normalized by $\bar{\mathbf{u}}$ (for the DNS, average displacement) in order to analyze the quality of microscopic displacements more or less independently of the macroscopic displacements. The two different displacement links, the volume constraint (VC) and the fixed corners (FC) are investigated. The simulation parameters are $L = 10000$ mm, $l_M = 2.5$ mm, $l_{\bar{E}} = 20$ mm, $\bar{u}_{\max} = 100$ mm, $T = 0.01$ s, $\Delta t = 5 \cdot 10^5$ s, location of the macroscale integration point $\bar{X}_1 = 7504, 23$ mm, section of the DNS displacement field from $\bar{X}_1 = 7496.25$ mm to $\bar{X}_1 = 7511.25$ mm, RVE with three periods of basic unit cell types B. Data from TAMSEN and BALZANI [106]. . . . .	68
9.1	Acoustic metamaterial: Left, lead inclusion with rubber coating and right, the full composite consisting of multiple unit cells, from MA and SHENG [67]. . . . .	69
9.2	Finite element discretization of the approximated microstructure. . .	70
9.3	Comparison of the displacement field after three wave periods, with an excitation amplitude of $A = 0.5$ mm: for a DNS, an FE <sup>2</sup> calculation with quasi-static microstructure (QS), an FE <sup>2</sup> calculation applying the volume displacement constraint (VC) and an FE <sup>2</sup> calculation using the fixed corner boundary (FC). Based on TAMSEN and BALZANI [105]. .	71
9.4	The displacement plot of the macroscopic problem is shown for different mesh resolutions: in (a) applying the volume constraint as well as in (c) the fixed corner constraint. Displayed is only the last section, focusing on the advancing wave front as here the differences can be observed best. In addition, the average nodal distance $\epsilon = \frac{1}{n_{\text{nel}}} \sum_i^{n_{\text{nel}}}  \bar{u}_i^{560} - \bar{u}_i $ for each mesh with respect to the finest discretization is plotted in (b) and (d), showing the convergence behavior. . . . .	72
9.5	Maximum displacement recorded along the bar for a range of loading frequencies at four different times, comparing the two microscale boundary constraints (a) Volume Constraints and (b) Fixed Corner Constraint. The band gap is shaded in gray. $A = 0.5$ mm, $\Delta t = T/300$ , $L = f^{-1} 1.11 \cdot 10^7$ mm/s and $\bar{n}_{\text{el}} = 140$ . . . . .	73
9.6	Full displacement field for four different excitation frequencies, plotted over the normalized bar length at $t = 6T$ . . . . .	74
9.7	Maximum displacement recorded at four nodes from $t = 0$ till $t = 9T$ , comparing the two microscale boundary constraints (a) Volume Constraints and (b) Fixed Corner Constraint. The band gap is shaded in gray. $A = 0.5$ mm, $\Delta t = t/300$ , $L = f^{-1} 1.11 \cdot 10^7$ mm/s and $\bar{n}_{\text{el}} = 140$ . Based on TAMSEN and BALZANI [105]. . . . .	75
10.1	Sketch of the three general phases during fiber pullout. . . . .	77
10.2	Sketch of the fiber pullout behavior for different embedment lengths. .	78
10.3	Experimental testing setup with a miniature concrete specimen, from CUROSU [24]. . . . .	79
10.4	Experimental setup for (a) single-fiber tension and (b) pullout, from CUROSU [24]. . . . .	80

10.5	Quasi-static PE fiber tension tests. Comparison of numerical simulation and experimental results from CUROSU [24]. . . . .	81
10.6	Experimental results of PE fiber tension tests at different loading rates: (a) stress-strain curves and (b) secant stiffness of the fibers at fracture plotted over the loading rate from [24], including logarithmic trend line.	82
10.7	Simulation of single-fiber tension test with rate-dependent material properties, (a) stress-strain diagram, (b) the dynamic increase factor of the secant stiffness at fracture compared to experimental results from [24]. Data from TAMSEN et al. [108]. . . . .	83
10.8	Quasi-static PE single-fiber pullout tests. Comparison of numerical simulation experimental results from [24]. . . . .	84
10.9	Simulation of single-fiber pullout test for different stretch rates: (a) $0.001\text{ s}^{-1}$ , (b) $0.1\text{ s}^{-1}$ , (c) $1\text{ s}^{-1}$ and (d) $10\text{ s}^{-1}$ . Experimental results from [24]. . . . .	85
10.10	Quasi-static force-displacement function for different element length. . . . .	86
10.11	Proposed extrapolation of fiber embedment length by increase of material stiffness. Displayed are (a) the force-displacement and (b) stress-strain relationships for fiber length from 4 mm up to 12 mm. . . . .	87
10.12	Simplified SHCC microstructure: (a) reference geometry with highlighted crack, (b) deformed specimen with visible fibers. . . . .	88
10.13	Pullout curves with and without a fixed reference length and activated full fiber pullout. . . . .	88
11.1	Multiscale boundary value problem of the simplified SHCC simulation, (a) macroscale and (b) microscale. . . . .	91
11.2	Normalized loading function (11.1) shown in (a) with its first and second time derivatives respectively in (b) and (c). . . . .	92
11.3	Stress-strain response for a quasi-static loading up to 10% strain. . . . .	93
11.4	Stress-strain response for loading functions from $t = 100\text{ s}$ up to $t = 0.00125\text{ s}$ , only the rate dependency is considered. . . . .	93
11.5	Stress-strain response for various loading speeds, only inertia is considered as dynamic influence. . . . .	94
11.6	Stress-strain response for various loading functions, considering both the stretch-rate dependent fiber property as well as the inertia effects, with $\Delta t = t_{\text{load}}/1000$ . . . . .	95
11.7	Comparing the peak stress (a) and respective strain value (b) of the three microstructural scenarios for various loading speeds. . . . .	95
11.8	Comparing the stress-strain curves using a pre-cracked RVE vs. a cracking RVE, for (a) $t_{\text{load}} = 0.1\text{ s}$ , (b) $t_{\text{load}} = 0.01\text{ s}$ and (c) $t_{\text{load}} = 0.00125\text{ s}$ , $\Delta t = t_{\text{load}}/1000$ . . . . .	96
12.1	The testing setup for the quasi-static tensile test with SHCC, from CUROSU [24]. . . . .	99
12.2	Experimental stress-strain curves of SHCC under quasi-static tensile loading, from CUROSU [24]. The strain-hardening and multiple cracking behavior is clearly observed. . . . .	99

12.3	Results of the quasi-static multiscale simulation, compared to the experimental data. Part (a) shows the loading up to 6% strain and depicts the selected RVE. Part (b) shows a zoomed in detail of part (a), focusing on the cracking of the matrix in the RVEs. Data from TAMSEN et al. [108]. . . . .	100
12.4	Split HOPKINSON tension bar setup, based on CUROSU [24]. . . . .	101
12.5	The characteristic trapezoidal loading pulse of the modified split HOPKINSON tension bar, as measured in the input bar, from CUROSU [24]. . . . .	102
12.6	Experimental stress-strain curves for a tensile split HOPKINSON bar test with SHCC, from CUROSU [24]. The quasi-static results are given in gray as a comparison. . . . .	103
12.7	Schematic visualization of the boundary value problem representing the split HOPKINSON tension test. Part (a) depicts the macroscopic problem, part (b) the discretization of the SHCC microstructure applied in the multiscale simulation of the test specimen. Based on TAMSEN et al. [108]. . . . .	103
12.8	The piecewise displacement function replicating the experimental loading, normalized with respect to the parameters of the function. . . . .	104
12.9	Loading function $\bar{u}^{BC}$ (12.12) and its first two time derivatives, compared to the two measured experimental loads from CUROSU [24], with $t_{vc} = 60 \mu\text{s}$ and $v_c = 3540 \text{ mm/s}$ , from TAMSEN et al. [108]. . . . .	105
12.10	Results of the split HOPKINSON bar simulation. Stress-strain signals at both interfaces ( $\bar{\sigma}_1, \bar{\sigma}_2$ ) as well as their average ( $\bar{\sigma}$ ). The zoom shows the initial cracking of the matrix. The quasi-static results (QS) are given as a reference. . . . .	106
12.11	Analysis of the variation in rise time $t_{cv}$ from $5 \cdot 10^{-4} \text{ s}$ to $10^{-6} \text{ s}$ , with $v_c = 3540 \text{ mm/s}$ . Plot (a) depicts the signal $\bar{\sigma}_1$ at the input face and (b) the respective signal $\bar{\sigma}_2$ at the output face. . . . .	107
12.12	Analysis of the variation of $v_c$ from $2000 \text{ mm/s}$ to $14160 \text{ mm/s}$ , with $t_{cv} = 6 \cdot 10^{-5} \text{ s}$ . Plot (a) depicts the signal $\bar{\sigma}_1$ at the input face and (b) the respective signal $\bar{\sigma}_2$ at the output face. . . . .	107
12.13	Analysis of the variation of the parameter $\alpha^I$ from 0 to 0.12. . . . .	108
12.14	Analysis of the influence of microinertia on the macroscopic response. . . . .	108

# List of Tables

4.1	GAUSS integration for one dimension. . . . .	24
5.1	Overview of the parameters used in the material model. . . . .	35
8.1	Number of time steps before either the simulation crashed (divergence of NEWTON iteration at microscale) or the intended complete set of 1000 time steps was successfully reached. Different choices of RVEs and constraints were analyzed. . . . .	66
9.1	Overview of the material parameters of the different microstructural phases. . . . .	70
10.1	Material properties of the PE fibers, from DYNAEEMA [29]. . . . .	80
10.2	Overview of the parameters used in the pullout simulation. . . . .	85
C.1	Overview of the extended fields, with $n_{\text{edf}}$ number of DOF at element level, denoting $n_{\text{lgr}}$ the number of DOF of LAGRANGE constraint and with $n_{\text{dm}}$ the spacial dimension. . . . .	119
C.2	Overview of the fields at element and global level, denoting with $n_{\text{edf}}$ the number of DOF and with $n_{\text{dm}}$ the spacial dimension. . . . .	120

---

# References

- [1] T. ANDERSON. *Fracture Mechanics - Fundamentals and Applications*. CRC Press, 2005.
- [2] F. DE ANDRADE SILVA, R. D. T. FILHO, J. DE ALMEIDA MELO FILHO, and E. DE MORAES REGO FAIRBAIRN. “Physical and mechanical properties of durable sisal fiber-cement composites”. In: *Construction and Building Materials* 24 (2010), pp. 777–785.
- [3] D. BALZANI, L. SCHEUNEMANN, D. BRANDS, and J. SCHRÖDER. “Construction of two- and three-dimensional statistically similar RVEs for coupled micro-macro simulations”. In: *Computational Mechanics* 54.5 (2014), pp. 1269–1284.
- [4] D. BALZANI and M. ORTIZ. “Relaxed incremental variational formulation for damage at large strains with application to fiber-reinforced materials and materials with truss-like microstructures”. In: *International Journal for Numerical Methods in Engineering* 92.6 (2012), pp. 551–570.
- [5] D. BALZANI, G. HOLZAPFEL, and S. BRINKHUES. “Modeling of damage in soft biological tissues and application to arterial walls”. In: *Computational Plasticity XI - Fundamentals and Applications, COMPLAS XI* (Jan. 2011), pp. 764–775.
- [6] D. BALZANI, D. BRANDS, and J. SCHRÖDER. “Construction of Statistically Similar Representative Volume Elements”. In: *Plasticity and Beyond: Microstructures, Crystal-Plasticity and Phase Transitions*. Ed. by J. SCHRÖDER and K. HACKL. Vienna: Springer Vienna, 2014, pp. 355–412.
- [7] Y. BAŞAR and D. WEICHERT. *Nonlinear continuum mechanics of solids : fundamental mathematical and physical concepts*. Berlin, Heidelberg: Springer, 2000.
- [8] K. BATHE. *Finite-Elemente-Methoden*. Berlin, Heidelberg: Springer, 2002.
- [9] T. BELYTSCHKO, T. CHIAPETTA, and R. L. BARTEL. “Efficient large-scale non-linear transient analysis by finite elements”. In: *International Journal for Numerical Methods in Engineering* 10 (1976), pp. 579–596.
- [10] T. BELYTSCHKO, W. LIU, and B. MORAN. *Nonlinear finite elements for continua and structures*. Chichester , Weinheim: Wiley, 2004.
- [11] A. BENSOUSSAN, J.-L. LIONS, and G. PAPANICOLAOU. *Asymptotic analysis for periodic structures*. Amsterdam: North-Holland Publishing Company, 1978.
- [12] D. P. BERTSEKAS. *Constrained optimization and lagrange multiplier methods*. Athena Scientific, 1996.
- [13] P. J. BLANCO, A. CLAUSSE, and R. A. FEIJÓO. “Homogenization of the Navier-Stokes equations by means of the Multi-scale Virtual Power Principle”. In: *Computer Methods in Applied Mechanics and Engineering* 315 (2017), pp. 760–779.
- [14] P. BLANCO, P. SÁNCHEZ, E. DE SOUZA NETO, and R. FEIJÓO. “Variational Foundations and Generalized Unified Theory of RVE-Based Multiscale Models”. In: *Archives of Computational Methods in Engineering* 23 (2016), pp. 191–253.

- 
- [15] J. BONET and R. D. WOOD. *Nonlinear Continuum Mechanics for Finite Element Analysis*. 2nd ed. Cambridge University Press, 2008.
- [16] E. BOSCO, V. KOUZNETSOVA, E. COENEN, M. GEERS, and A. SALVADORI. “A multiscale framework for localizing microstructures towards the onset of macroscopic discontinuity”. In: *Computational Mechanics* 54 (2014), pp. 299–319.
- [17] S. BRÛLÉ, E. H. JAVELAUD, S. ENOCH, and S. GUENNEAU. “Experiments on Seismic Metamaterials: Molding Surface Waves”. In: *Physical Review Letters* 112 (2014), p. 133901.
- [18] E. CADONI. “Dynamic characterization of orthogneiss rock subjected to intermediate and high strain rates in tension”. In: *Rock Mechanics and Rock Engineering* 43 (2010), pp. 667–676.
- [19] E. CADONI, A. MEDA, and G. PLIZZARI. “Tensile behaviour of FRC under high strain-rate”. In: *Materials and Structures* 42 (2009), pp. 1283–1294.
- [20] E. COENEN, V. KOUZNETSOVA, and M. GEERS. “Novel boundary conditions for strain localization analyses in microstructural volume elements”. In: *International Journal for Numerical Methods in Engineering* 90 (2012), pp. 1–21.
- [21] R. V. CRASTER, J. KAPLUNOV, and A. V. PICHUGIN. “High-frequency homogenization for periodic media”. In: *Proceedings of the Royal Society A* 466 (2010), pp. 2341–2362.
- [22] S. A. CUMMER and D. SCHURIG. “One path to acoustic cloaking”. In: *New Journal of Physics* 9 (2007), p. 45.
- [23] I. CUROSU, V. MECHTCHERINE, and O. MILLON. “Effect of fiber properties and matrix composition on the tensile behavior of strain-hardening cement-based composites (SHCCs) subject to impact loading”. In: *Cement and Concrete Research* 82 (2016), pp. 23–35.
- [24] I. CUROSU. “Influence of fiber type and matrix composition on the tensile behavior of strain-hardening cement-based composites (SHCC) under impact loading”. PhD thesis. Technische Universität Dresden, 2017.
- [25] I. CUROSU, V. MECHTCHERINE, D. FORNI, and E. CADONI. “Performance of various strain-hardening cement-based composites (SHCC) subject to uniaxial impact tensile loading”. In: *Cement and Concrete Research* 102 (2017), pp. 16–28.
- [26] I. CUROSU, V. MECHTCHERINE, M. HERING, and M. CURBACH. “Mineral-bonded composites for enhanced structural impact safety - Overview of the format, goals and achievements of the research training group GRK 2250”. In: *10th International Conference on Fracture Mechanics of Concrete and Concrete Structures* (2019).
- [27] I. CUROSU et al. “Impaktsicherheit von Baukonstruktionen durch mineralisch gebundene Komposite: Materialebene”. In: *Beton- und Stahlbetonbau* (2020).
- [28] A. DRECHSLER, R. FRENZEL, A. CASPARI, S. MICHEL, M. HOLZSCHUH, A. SYNYSKA, I. CUROSU, M. LIEBSCHER, and V. MECHTCHERINE. “Surface modification of poly(vinyl alcohol) fibers to control the fiber-matrix interaction in composites”. In: *Colloid and Polymer Science* 297 (2019), pp. 1079–1093.

- 
- [29] D. DYNAEEMA. *Fact Sheet - Ultra High Molecular Weight Polyethylene fiber from DSM Dynameema*. Online. CIS YA100. 2010.
- [30] J. D. ESHELBY and R. E. PEIERLS. “The determination of the elastic field of an ellipsoidal inclusion, and related problems”. In: *Proceedings of the Royal Society of London. Series A. Mathematical and Physical Sciences* 241.1226 (1957), pp. 376–396.
- [31] J. FISH, W. CHEN, and G. NAGAI. “Non-local dispersive model for wave propagation in heterogeneous media: multi-dimensional case”. In: *International Journal for Numerical Methods in Engineering* 54 (2002), pp. 347–363.
- [32] M. GEERS, V. KOUZNETSOVA, and W. BREKELMANS. “Multi-scale computational homogenization: Trends and challenges”. In: *Journal of Computational and Applied Mathematics* 234 (2010), pp. 2175–2182.
- [33] M. G. D. GEERS, V. G. KOUZNETSOVA, K. MATOUŠ, and J. YVONNET. “Homogenization methods and multiscale modeling: Nonlinear problems”. In: *Encyclopedia of Computational Mechanics Second Edition*. American Cancer Society, 2017, pp. 1–34.
- [34] I. GITMAN, H. ASKES, and L. SLUYS. “Representative volume: Existence and size determination”. In: *Engineering Fracture Mechanics* 74 (2007), pp. 2518–2534.
- [35] R. GLÜGE. “Beiträge zur analytischen und numerischen Homogenisierung in der Materialmodellierung”. Habilitation. Otto-von-Guericke-Universität Magdeburg, 2016.
- [36] R. GLÜGE, M. WEBER, and A. BERTRAM. “Comparison of spherical and cubical statistical volume elements with respect to convergence, anisotropy, and localization behavior”. In: *Computational Materials Science* 63 (2012), pp. 91–104.
- [37] D. GROSS and T. SEELIG. *Bruchmechanik: Mit einer Einführung in die Mikro-mechanik*. Springer, Berlin, 2007.
- [38] Z. HASHIN and S. SHTRIKMAN. “A variational approach to the theory of the elastic behaviour of polycrystals”. In: *Journal of the Mechanics and Physics of Solids* 10.4 (1962), pp. 343–352.
- [39] Z. HASHIN and S. SHTRIKMAN. “On some variational principles in anisotropic and nonhomogeneous elasticity”. In: *Journal of the Mechanics and Physics of Solids* 10.4 (1962), pp. 335–342.
- [40] Z. HASHIN and S. SHTRIKMAN. “A variational approach to the theory of the elastic behaviour of multiphase materials”. In: *Journal of the Mechanics and Physics of Solids* 11.2 (1963), pp. 127–140.
- [41] A. A. HERAVI, I. CUROSU, and V. MECHTCHERINE. “A gravity-driven split Hopkinson tension bar for investigating quasi-ductile and strain-hardening cement-based composites under tensile impact loading”. In: *Cement and Concrete Composites* 105 (2020), p. 103430.
- [42] M. HERING et al. “Impaktsicherheit von Baukonstruktionen durch mineralisch gebundene Komposite: Bauteilebene”. In: *Beton- und Stahlbetonbau* (2020).
- [43] R. HILL. “The elastic behaviour of a crystalline aggregate”. In: *Proceedings of the Physical Society, Section A* 65 (1952), pp. 349–354.

- [44] R. HILL. “On constitutive macro-variables for heterogeneous solids at finite strain”. In: *Proceedings of the Royal Society A* 326 (1972), pp. 131–147.
- [45] G. HOLZAPFEL. *Nonlinear Solid Mechanics*. Chichester: Wiley, 2000.
- [46] R. HU and C. OSKAY. “Multiscale nonlocal effective medium model for in-plane elastic wave dispersion and attenuation in periodic composites”. In: *Journal of the Mechanics and Physics of Solids* 124 (2019), pp. 220–243.
- [47] T. HUI and C. OSKAY. “A high order homogenization model for transient dynamics of heterogeneous media including micro-inertia effects”. In: *Computer Methods in Applied Mechanics and Engineering* 273 (2014), pp. 181–203.
- [48] L. KACHANOV. “Time of the Rupture Process under Creep Conditions”. In: *Izvestiia Akademii Nauk SSSR, Otdelenie Teckhnicheskikh Nauk* 8 (1958), pp. 26–31.
- [49] M. KADIC, T. BÜCKMANN, R. SCHITTNY, and M. WEGENER. “Experiments on cloaking in optics, thermodynamics and mechanics”. In: *Philosophical Transactions of the Royal Society A* 373 (2015), p. 20140357.
- [50] A. KARAMNEJAD and L. J. SLUYS. “A dispersive multi-scale crack model for quasi-brittle heterogeneous materials under impact loading”. In: *Computer methods in applied mechanics and engineering* 278 (2014), pp. 423–444.
- [51] C. KETTENBEIL and G. RAVICHANDRA. “Experimental investigation of the dynamic behavior of metaconcrete”. In: *International Journal of Impact Engineering* 111 (2018), pp. 199–207.
- [52] R. KHAJEHTOURIAN and M. I. HUSSEIN. “Dispersion characteristics of a nonlinear elastic metamaterial”. In: *AIP Advances* 4 (2014), p. 124308.
- [53] A. O. KRUSHYNSKA, V. G. KOUZNETSOVA, and M. G. D. GEERS. “Towards optimal design of locally resonant acoustic metamaterials”. In: *Journal of the MEchanics and Physics of Solids* 71 (2014), pp. 179–196.
- [54] J. LEMAITRE and J. CHABOCHE. *Mechanics of solid materials*. Cambridge University Press, 1990.
- [55] J. LEMAITRE and R. DESMORAT. *Engineering Damage Mechanics - ductile, Cree, Fatigue and Brittle Failures*. Springer, Berlin, Heidelberg, 2005.
- [56] J. LEMAITRE. *Evaluation of dissipation and damage in metals submitted to dynamic loading*. Tech. rep. Office National d’Études et de Recherches Aéronautiques, 1971.
- [57] J. LEMAITRE. *A Course on Damage Mechanics*. Springer-Verlag Berlin Heidelberg, 1996.
- [58] J. LI and C. T. CHAN. “Double-negative acoustic metamaterial”. In: *Physical Review E* 70.5 (5 2004), p. 055602.
- [59] P. LI, H. BROUWERS, and Q. YU. “Influence of key design parameter of ultra-high performance fibre reinforced concrete on in-service bullet resistance”. In: *International Journal of Impact Engineering* 136 (2020), p. 103434.
- [60] V. C. LI. “On Engineered Cementitious Composites (ECC) A Review of the Material and Its Applications”. In: *Journal of Advanced Concrete Technology* 1.3 (2003), pp. 215–230.

- 
- [61] C. LIU and C. REINA. “Discrete averaging relations for micro to macro transition”. In: *Journal of Applied Mechanics* 83.8 (2016), p. 081006.
- [62] C. LIU and C. REINA. “Variational coars-graining procedure for dynamic homogenization”. In: *Journal of the Mechanics and Physics of Solids* 104 (2017), pp. 187–206.
- [63] C. LIU and C. REINA. “Dynamic homogenization of resonant elastic metamaterials with spacetime modulation”. In: *Computational Mechanics* 64.1 (2018), pp. 147–161.
- [64] Z. LIU, X. ZHANG, Y. MAO, Y. Y. ZHU, Z. YANG, C. T. CHAN, and P. SHENG. “Locally resonant sonic materials”. In: *Science* 289.5485 (2000), pp. 1734–1736.
- [65] S. LÖHNERT. “Computational homogenization of microheterogeneous materials at finite strains including damage”. PhD thesis. Universität Hannover, 2004.
- [66] R. LORENZONI, I. CUROSU, F. LÉONARD, S. PACIORNIK, V. MECHTCHERINE, F. A. SILVA, and G. BRUNO. “Combined mechanical and 3D-microstructural analysis of strain-hardening cement-based composites (SHCC) by in situ X-ray microtomography”. In: *Cement and Concrete Research* (2020). under review.
- [67] G. MA and P. SHENG. “Acoustic metamaterials: From local resonances to broad horizons”. In: *Science Advances* 2.2 (2016).
- [68] J. MANDEL. *Plasticité classique et viscoplasticité*. Udine: Springer, 1971.
- [69] J. MARSDEN and T. HUGHES. *Mathematical Foundations of Elasticity*. Prentice-Hall, 1983.
- [70] I. MERTA and E. TSCHEGG. “Fracture energy of natural fibre reinforced concrete”. In: *Construction and Building Materials* 40 (2013), pp. 991–997.
- [71] C. MIEHE. “Discontinuous and continuous damage evolution in Odgen-type large-strain elastic materials”. In: *European Journal of Mechanics Series A Solids* 14.5 (1995), pp. 697–720.
- [72] C. MIEHE, J. SCHOTTE, and J. SCHRÖDER. “Computational micro-macro transitions and overall moduli in the analysis of polycrystals at large strains”. In: *Computational Materials Science* 16 (1999), pp. 372–382.
- [73] G. W. MILTON and J. R. WILLIS. “Minimum variational principles for time-harmonic waves in a dissipative medium and associated variational principles of Hashin-Shtrikman type”. In: *Proceedings of the Royal Society A: Mathematical, Physical and Engineering Sciences* 466.2122 (2010), pp. 3013–3032.
- [74] M. MINIACI, A. KRUSHYNSKA, F. BOSIA, and N. M. PUGNO. “Large scale mechanical metamaterials as seismic shields”. In: *New Journal of Physics* 18 (2016), p. 083041.
- [75] S. J. MITCHELL, A. PANDOLFI, and M. ORTIZ. “Effect of brittle fracture in a metaconcrete slab under shock loading”. In: *Journal of Engineering Mechanics* 142.4 (2016).
- [76] A. MOLINARI and S. MERCIER. “Micromechanical modelling of porous materials under dynamic loading”. In: *Journal of the Mechanics and Physics of Solids* 49 (2001), pp. 1497–1516.

- [77] T. MORI and K. TANAKA. “Average stress in matrix and average elastic energy of materials with misfitting inclusions”. In: *Acta Metallurgica* 21.5 (1973), pp. 571–574.
- [78] H. NASSAR, Q.-C. HE, and N. AUFRAY. “On asymptotic elastodynamic homogenization approaches for periodic media”. In: *Journal of the Mechanics and Physics of Solids* 88 (2016), pp. 274–290.
- [79] S. NEMAT-NASSER and A. SRIVASTAVA. “Overall dynamic constitutive relations of layered elastic composites”. In: *Journal of the Mechanics and Physics of Solids* 59.10 (2011), pp. 1953–1965.
- [80] N. NEWMARK. “A Method of Computation for Structural Dynamics”. In: *ASCE Journal of Engineering Mechanics Division* 85 (1959), pp. 67–94.
- [81] V.-D. NGUYEN, E. BÉCHET, C. GEUZAINÉ, and L. NOELS. “Imposing periodic boundary conditions on arbitrary meshes by polynomial interpolation”. In: *Computational Materials Science* 55 (2022), pp. 390–406.
- [82] J. J. NOTKIN and S. GULKIN. *Mechanik*. Tessloff, 1971.
- [83] T. F. W. VAN NULAND, P. B. SILVA, A. SRIDHAR, M. G. D. GEERS, and V. G. KOUZNETSOVA. “Transient analysis of nonlinear locally resonant metamaterials via computational homogenization”. In: *Mathematics and Mechanics of Solids* 24.10 (2019), pp. 3136–3155.
- [84] R. OGDEN. *Non-Linear Elastic Deformations*. Ellis Horwood and John Wiley, 1984.
- [85] D PERIĆ, E. DE SOUZA NETO, R. FEIJÓO, M. PARTOVI, and A. CARNEIRO MOLINA. “On micro-to-macro transitions for multi-scale analysis of non-linear heterogeneous materials: unified variational basis and finite element implementation”. In: *International Journal for Numerical Methods in Engineering* 87 (2010), pp. 149–170.
- [86] K. PHAM, G. KOUZNETSOVA V, and M. GEERS. “Transient computational homogenization for heterogeneous materials under dynamic excitation”. In: *Journal of the Mechanics and Physics of Solids* 61 (2013), pp. 2125–2146.
- [87] A. REUSS. “Berechnung der Fließgrenze von Mischkristallen auf Grund der Plastizitätsbedingung für Einkristalle.” In: *ZAMM - Journal of Applied Mathematics and Mechanics / Zeitschrift für Angewandte Mathematik und Mechanik* 9.1 (1929), pp. 49–58.
- [88] D. ROCA, O. LLOBERAS-VALLS, J. CANTE, and J. OLIVER. “A computational multiscale homogenization framework accounting for inertia effects: Application to acoustic metamaterials modelling”. In: *Computer methods in applied mechanics and engineering* 330 (2018), pp. 415–446.
- [89] M. H. SAGHAFI and H. SHARIATMADAR. “Enhancement of seismic performance of beam-column joint connections using high performance fiber reinforced cementitious composites”. In: *Construction and Building Materials* 180 (2018), pp. 665–680.
- [90] C. SARTORI, S. MERCIER, N. JACQUES, and A. MOLINARI. “Constitutive behavior of porous ductile materials accounting for micro-inertia and void shape”. In: *Mechanics of Materials* 80 (2015), pp. 324–339.

- 
- [91] T. SASAGAWA, M. TANAKA, R. OMOTE, and D. BALZANI. “Construction of statistically similar representative volume elements for discontinuous fiber composites”. In: *Composite Structures* 203 (2018), pp. 193–203.
- [92] J. SCHRÖDER. “Plasticity and Beyond - Microstructures, Crystal-Plasticity and Phase Transitions (CISM Lecture Notes 550, Eds. J. Schröder, K. Hackl)”. In: Springer, 2013. Chap. A numerical two-scale homogenization scheme: the FE<sup>2</sup>-method.
- [93] J. SCHRÖDER, D. BALZANI, and D. BRANDS. “Approximation of random microstructures by periodic statistically similar representative volume elements based on lineal-path functions”. In: *Archive of Applied Mechanics* 81 (2011), pp. 975–997.
- [94] H. SHAN, J. XIAO, and Q. CHU. “Investigation on Bond-Slip Behavior of Z-Pin Interfaces in X-Cor Sandwich Structures Using Z-Pin Pull-Out Test”. In: *Applied Composite Materials* 26 (2019), pp. 299–316.
- [95] J. SIMO. “On a fully three-dimensional finite-strain viscoelastic damage model: Formulation and computational aspects”. In: *Computer Methods in Applied Mechanics and Engineering* 60.2 (1987), pp. 153–173.
- [96] O. VAN DER SLUIS, P. SCHREURS, W. BREKELMANS, and H. MEIJER. “Overall behaviour of heterogeneous elastoviscoplastic materials: effect of microstructural modelling”. In: *Mechanics of Materials* 32 (2000), pp. 449–462.
- [97] J.-H. SONG and T. BELYTSCHKO. “Multiscale aggregating discontinuities method for micro-macro failure of composites”. In: *Composites Part B: Engineering* 40.6 (2009), pp. 417–426.
- [98] E. DE SOUZA NETO, D. PERIĆ, and D. OWEN. “Continuum modelling and numerical simulation of material damage at finite strains”. In: *Archives of Computational Methods in Engineering* 5 (1998), p. 311.
- [99] E. DE SOUZA NETO, P. BLANCO, P. SÁNCHEZ, and R. FEIJÓO. “An RVE-based multiscale theory of solids with micro-scale inertia and body force effects”. In: *Mechanics of Materials* 80 (2015), pp. 136–144.
- [100] E. A. DE SOUZA NETO and R. A. FEIJÓO. “Variational foundations of large strain multiscale solid constitutive models: kinematical formulation”. In: *Advanced Computational Materials Modeling*. John Wiley and Sons, Ltd, 2010. Chap. 9, pp. 341–378.
- [101] L. O. DE SOUZA, L. M. S. DE SOUZA, and F. DE ANDRADE SILVA. “Mechanics of natural curauá textile-reinforced concrete”. In: *Magazine of Concrete Research* (2019), pp. 1–12.
- [102] A. SRIDHAR, V. KOUZNETSOVA, and M. GEERS. “Homogenization of locally resonant acoustic metamaterials towards an emergent enriched continuum”. In: *Computational Mechanics* 57 (2016), pp. 423–435.
- [103] A. SRIDHAR, V. G. KOUZNETSOVA, and M. G. D. GEERS. “A general multi-scale framework for the emergent effective elastodynamics of metamaterials”. In: *Journal of the Mechanics and Physics of Solids* 111 (2018), pp. 414–433.

- [104] T. STILL, M. OUDICH, G. K. AUERHAMMER, D. VLASSOPOULOS, B. DJAFARI-ROUHANI, G. FYTAS, and P. SHENG. “Soft silicone rubber in phononic structures: Correct elastic moduli”. In: *Physical Review B* 88.9 (2013), p. 094102.
- [105] E. TAMSEN and D. BALZANI. “Influence of Micro-Inertia on the Macroscale - A Fully-Coupled Direct Homogenization Framework for Dynamics”. In: *Proceedings in Applied Mathematics and Mechanics* 20.1 (2020), e202000195.
- [106] E. TAMSEN and D. BALZANI. “A General, Implicit, Finite-Strain FE<sup>2</sup> Framework for the Simulation of Dynamic Problems on Two Scales”. In: *Computational Mechanics* (2021).
- [107] E. TAMSEN, W. WEBER, and D. BALZANI. “First steps towards the direct micro-macro simulation of reinforced concrete under impact loading”. In: *Proceedings in Applied Mathematics and Mechanics* 18.1 (2018), e201800181.
- [108] E. TAMSEN, I. CUROSU, V. MECHTCHERINE, and D. BALZANI. “Computational Micro-Macro Analysis of Impact on Strain-Hardening Cementitious Composites (SHCC) Including Microscopic Inertia”. In: *Materials* 13.21 (2020). Submitted, p. 4934.
- [109] K. TANAKA and T. MORI. “Note on volume integrals of the elastic field around an ellipsoidal inclusion”. In: *Journal of Elasticity* 2.3 (1972).
- [110] K. TERADA, M. HORI, T. KYOYA, and N. KIKUCHI. “Simulation of the multi-scale convergence in computational homogenization approaches”. In: *International Journal of Solids and Structures* 37 (2000), pp. 2285–2311.
- [111] M. VAZ JÚNIOR, E. DE SOUZA NETO, and P. MUÑOZ-ROJAS. *Advanced computational materials modeling : from classical to multi-scale techniques*. Weinheim: Wiley-VCH, 2011.
- [112] W. VOIGT. “Ueber die Beziehung zwischen den beiden Elasticitätsconstanten isotroper Körper”. In: *Annalen der Physik* 274.12 (1889), pp. 573–587.
- [113] Z. WANG and C. SUN. “Modeling micro-inertia in heterogeneous materials under dynamic loading”. In: *Wave Motion* 36 (2002), pp. 473–485.
- [114] J. R. WILLIS. *Dynamics of composites*. Springer Vienna, 1997.
- [115] J. R. WILLIS. “The construction of effective relations for waves in a composite”. In: *Comptes Rendus Mécanique* 340.4 (2012), pp. 181–192.
- [116] E. WÖLFEL, C. SCHEFFLER, I. CUROSU, and V. MECHTCHERINE. “Single fibre pull-out tests of polypropylene and glass fibres in cement-based matrices at high loading rates”. In: *18th European Conference on Composite Materials*. 2018.
- [117] E. WÖLFEL and C. SCHEFFLER. “Interphases in polypropylene and glass fiber reinforced cementitious model composites under dynamic loading”. In: *10th International Conference on Fracture Mechanics of Concrete and Concrete Structures*. Ed. by G. PIJAUDIER-CABOT, P. GRASSL, and C. LA BORDERIE. 2019.
- [118] P. WRIGGERS. *Nichtlineare Finite-Element-Methoden*. Berlin, Heidelberg: Springer, 2001.
- [119] K. XIA and W. YAO. “Dynamic rock tests using split Hopkinson (Kolsky) bar system - A review”. In: *Journal of Rock Mechanics and Geotechnical Engineering* 7 (2015), pp. 27–59.

- 
- [120] K. ZHAN, J. YU, Y. WANG, and K. YU. “Development of Cementitious Composites with Tensile Strain Capacity up to 10%”. In: *Strain-Hardening Cement-Based Composites*. Ed. by V. MECHTCHERINE, V. SLOWIK, and P. KABELE. Springer Netherlands, 2018, pp. 147–153.
- [121] R. F. ZOLLO. “Fiber-reinforced Concrete: an Overview after 30 Years of Development”. In: *Cement and Concrete Composites* 19 (1997), pp. 107–122.

**Mitteilungen aus dem Institut für Mechanik  
RUHR-UNIVERSITÄT BOCHUM  
Nr. 185**

**ISBN 978-3-935892-63-6**